

Jörg Höyland

# Challenges for large wind turbine blades

Thesis for the degree of Philosophiae Doctor

Trondheim, November 2010

Norwegian University of Science and Technology  
Faculty of Engineering Science and Technology  
Department of Engineering Design and Materials



**NTNU – Trondheim**  
Norwegian University of  
Science and Technology

**NTNU**

Norwegian University of Science and Technology

Thesis for the degree of Philosophiae Doctor

Faculty of Engineering Science and Technology  
Department of Engineering Design and Materials

© Jörg Höyland

ISBN 978-82-471-2417-8 (printed ver.)  
ISBN 978-82-471-2418-5 (electronic ver.)  
ISSN 1503-8181

Doctoral theses at NTNU, 2010:216

Printed by NTNU-trykk

# Acknowledgements

This work was carried out at the Norwegian University of Science and Technology (NTNU), at the Department of Engineering Design and Materials (IPM) over a five year period from 2004 to 2009. It was performed in the Plastics and Composites Group and was funded by the Research Council of Norway and IPM. The funding is greatly appreciated and made this thesis possible. This work would not have been possible without the help and guidance of others and I would therefore like to thank everyone involved.

I would like to thank my academic supervisors Professor Andreas Echtermeyer and Associate Professor Nils Petter Vedvik for their guidance and support. I am grateful for your inspiration and enthusiasm during this thesis. I admire the way you always found time for valuable help and discussions. Further, I would like to thank Asbjørn Solberg, Halvard Støwer, Bjarne Stolpnæssæter and the rest of the technical staff at IPM for their help in planning and conducting the laboratory experiments. I am also very grateful to my former and present colleagues at IPM for their support and assistance. In addition, I would like to thank the graduate students Sigurd Backe and Morten R. Jacobsen for their invaluable help in the lab.

I wish to express my gratitude to my colleges at SmartMotor AS for their support during the finishing of this thesis.

Special thanks goes to my friends Øystein Spangelo and Erik Sletten. When the computer analyses seemed to work against me, Øystein provided both help and motivation. His help in editing the language in this thesis was also of great value. When my mind became too filled with composite and wind turbine theory, Erik pulled me out of the office and into the real world. I highly value our climbing and skiing trips together.

Finally and most importantly, I wish to express my deepest gratitude to Charlotte Lie and my family for your valuable support during the entire PhD-study. Without you I would never have finished this thesis.

Trondheim, November 2010

Jörg Höyland



# Abstract

With global climate problems receiving increasingly international political attention, most European nations are looking for sources of renewable energy. Wind turbines are a promising source of renewable energy and their numbers have steadily increased since the introduction of the modern wind turbine in the 1970s. The largest units today have a rated power of 7 MW and blades ranging up to 62.5 m in length. Offshore wind turbines have access to stronger winds with less turbulence, thereby increasing the energy output of each unit. Offshore turbines will also have a lesser environmental impact than onshore turbines. It is believed that the development of offshore wind turbines will encourage the development of even longer blades.

The main spar geometry of a 100 m wind turbine blade was established in order to evaluate how the use of carbon and glass fiber composites would affect the design. A hybrid solution using UD carbon fiber for global stiffness and  $\pm 45^\circ$  glass fiber plies for buckling resistance was also developed. The ultimate loads were calculated for blades with pitch control and blades experiencing failure of pitch control during the 1-year and 50-year extreme gust. The DNV-OS-J102 standard for wind turbines was used in the calculation of safety factors for both loads and material strength criteria. The distribution of  $\pm 45^\circ$  anti-buckling plies by buckling analysis is extremely time consuming and therefore a program for automatic ply distribution was developed. The Matlab program interacted with the FEM software Abaqus, defining input files and extracting results, and proved to be highly efficient. The results from the FEM analyses were combined with a simple cost model in order to evaluate both the weight and cost of the different spar solutions.

Important weight reductions can be obtained by optimizing the performance of the composite laminate in the spar. Several sub-models of the 100 m spar were created with the aim of optimizing the spar's buckling performance. The angle and distribution of both the  $\pm 45^\circ$  and UD plies were systematically altered in order to increase the buckling load. The introduction of ply homogenization and core material in the flange was also evaluated and yielded the largest increases of buckling load. The results from the optimized sub-models were implemented in a 100 m spar and found to decrease the amount of  $\pm 45^\circ$  plies by 50 %.

A 6 m scaled main spar of glass fiber composite was produced by resin infusion. The spar was tested in a 4-point bending test and designed to fail by buckling of the top flange. In order to control the location of the buckling failure, an artificial imperfection was introduced in the middle of the top flange during manufacturing. The imperfection is representative for imperfections found during manufacturing of wind turbine spars. In addition to measuring force and global deflection, 25 strain gages were installed to monitor the spar.

Finally, a FEM analysis of the 6 m spar was developed and correlated with the experimental results. By implementing the imperfection in the compression spar and the use of non-linear analysis, the strain patterns from the test results were successfully reproduced.



# Table of Contents

<b>ACKNOWLEDGEMENTS</b>	<b>I</b>
<b>ABSTRACT</b>	<b>III</b>
<b>TABLE OF CONTENTS</b>	<b>V</b>
<b>SYMBOLS</b>	<b>IX</b>
<b>ABBREVIATIONS</b>	<b>XI</b>
<b>LIST OF FIGURES</b>	<b>XIII</b>
<b>1 INTRODUCTION</b>	<b>1</b>
1.1 Background .....	1
1.2 Challenges for future blades .....	3
1.3 Objectives .....	4
1.4 Outline of the thesis .....	4
<b>2 WIND TURBINE BLADE STRUCTURE</b>	<b>7</b>
2.1 General introduction .....	7
2.2 Aerodynamic shell .....	8
2.3 Main spar .....	9
2.4 Assembly of wind turbine blade .....	10
<b>3 AERODYNAMICS OF WIND TURBINE BLADES</b>	<b>11</b>
3.1 Physical principles of wind energy conversion .....	11
3.2 Airfoil terminology .....	12
3.3 Airfoil aerodynamics .....	13
3.4 Airfoil behavior .....	16
3.4.1 Moderate angles of attack .....	16
3.4.2 High angles of attack .....	17
3.5 Properties of a wind turbine rotor blade .....	19
3.5.1 Wind turbine characteristics .....	19
3.5.2 Choosing the number of rotor blades .....	20
3.5.3 Design tip speed ratio of the rotor .....	22
3.5.4 Power curve of a wind turbine .....	23

3.6	Important properties of wind turbine airfoils. . . . .	24
3.6.1	Available airfoils for wind turbines . . . . .	25
3.6.2	Blade twist . . . . .	25
3.6.3	Rotor blade chord length. . . . .	27
3.6.4	Thickness to chord ratio . . . . .	28
3.6.5	Spar width. . . . .	29
<b>4</b>	<b>LOADS ON A WIND TURBINE BLADE</b>	<b>31</b>
4.1	Gravity and inertia loads . . . . .	31
4.1.1	Gravitational loads. . . . .	32
4.1.2	Centrifugal loads . . . . .	32
4.1.3	Gyroscopic loads . . . . .	32
4.2	Aerodynamic loads . . . . .	32
4.3	Extreme wind loads. . . . .	33
<b>5</b>	<b>WIND TURBINE DESIGN CRITERIA</b>	<b>37</b>
5.1	Material safety factors . . . . .	37
5.2	Composite failure criteria. . . . .	38
5.3	Buckling analysis of wind turbine spar . . . . .	39
5.4	Wrinkling of sandwich structures . . . . .	43
5.5	Tower clearance . . . . .	44
<b>6</b>	<b>COMPOSITE MANUFACTURING METHODS</b>	<b>47</b>
6.1	Wet hand lay-up . . . . .	47
6.2	Filament winding. . . . .	48
6.3	Prepreg technology. . . . .	49
6.4	Resin infusion technology . . . . .	51
6.4.1	Vacuum Assisted Resin Transfer Method (VARTM) . . . . .	52
6.4.2	Vacuum Assisted Process (VAP) . . . . .	57
6.4.3	Controlled Atmospheric Pressure Resin Infusion (CAPRI). . . . .	60
6.5	Future development of composite manufacturing process . . . . .	62
<b>7</b>	<b>MECHANICAL PROPERTIES OF COMPOSITE MATERIALS IN FEM ANALYSIS</b>	<b>63</b>
7.1	Mechanical properties of glass fiber composite. . . . .	64
7.2	Mechanical properties of carbon fiber composite. . . . .	65
7.3	Mechanical properties of core material . . . . .	66
<b>8</b>	<b>FEM ANALYSIS OF A 100 M MAIN SPAR DURING EXTREME LOAD</b>	<b>67</b>
8.1	Introduction. . . . .	67
8.2	Main spar geometry . . . . .	70



8.3	Loads and boundary conditions . . . . .	73
8.4	Mesh . . . . .	74
8.5	Composite lay-up modelling in Abaqus CAE . . . . .	75
8.6	Non-linear analysis in Abaqus . . . . .	77
8.7	Design of 100 m main spar . . . . .	78
8.7.1	Distribution of reinforcements . . . . .	78
8.7.2	Automatic anti-buckling ply distribution . . . . .	82
8.8	Results of 100 m main spar design . . . . .	85
8.9	Simple cost estimate of spar flanges . . . . .	88
8.10	Blades with pitch control . . . . .	89
8.11	Degradation of composite ply properties . . . . .	94
8.12	Conclusions from FEM analysis of 100m main spar . . . . .	97
<b>9</b>	<b>OPTIMIZING BUCKLING RESISTANCE</b>	<b>99</b>
9.1	Optimization models . . . . .	99
9.1.1	Bending model . . . . .	100
9.1.2	Compression model . . . . .	103
9.2	Optimizing the glass fiber anti-buckling plies . . . . .	104
9.2.1	Defining the optimization analysis . . . . .	104
9.2.2	Results from the anti-buckling ply optimization . . . . .	106
9.2.3	Non-linear analysis of optimized laminates . . . . .	109
9.2.4	Implementing optimized anti-buckling plies in 100 m main spar . . . . .	110
9.3	Optimization of the UD carbon plies . . . . .	112
9.3.1	Defining the UD ply optimization analysis . . . . .	113
9.3.2	Results from UD carbon ply optimization . . . . .	114
9.3.3	Implementing optimized UD plies in a 100 m main spar . . . . .	118
9.4	Discussion of optimization results . . . . .	119
<b>10</b>	<b>TESTING OF A 6 M SCALED MAIN SPAR SECTION</b>	<b>121</b>
10.1	Geometry definition . . . . .	122
10.2	Manufacture of specimen . . . . .	124
10.3	Experimental setup for the 6 m spar . . . . .	125
10.4	Measuring equipment . . . . .	127
10.5	Test data . . . . .	128
<b>11</b>	<b>FEM ANALYSIS OF 6 M MAIN SPAR SECTION</b>	<b>135</b>
11.1	Geometry, materials and boundary conditions . . . . .	135
11.1.1	Geometry . . . . .	135
11.1.2	Boundary conditions . . . . .	136
11.1.3	Mesh . . . . .	137
11.2	Initial FEM analysis . . . . .	139

11.3 Calibration of FEM analysis . . . . .	141
11.3.1 Corner stiffness . . . . .	141
11.3.2 Including the imperfection . . . . .	142
11.3.3 Poisson’s ratio . . . . .	145
11.3.4 Peel-strain in bond . . . . .	145
11.4 Comments on the FEM analysis . . . . .	146
<b>12 CONCLUSIONS AND FUTURE WORK</b>	<b>147</b>
12.1 Overall conclusions . . . . .	147
12.2 Detailed conclusions . . . . .	147
12.3 Future work . . . . .	149
<b>REFERENCES</b>	<b>151</b>
<b>APPENDIX A: 100 M MAIN SPAR GEOMETRY</b>	<b>157</b>
<b>APPENDIX B: PLY DEFINITIONS FROM FEM ANALYSIS OF 100 M MAIN SPAR</b>	<b>159</b>
<b>APPENDIX C: STRESS PLOTS FROM 100 M SPAR ANALYSES</b>	<b>177</b>
<b>APPENDIX D: RESULTS FROM BUCKLING OPTIMIZATION</b>	<b>181</b>
<b>APPENDIX E: ABAQUS PLY DEFINITION FOR OPTIMIZATION MODEL</b>	<b>195</b>
<b>APPENDIX F: GEOMETRY OF 6 M SPAR</b>	<b>197</b>
<b>APPENDIX G: ABAQUS PLY DEFINITION FOR 6 M SPAR</b>	<b>199</b>
<b>APPENDIX H: WEB LINKS</b>	<b>201</b>

# Symbols

## Arabic

$A$	Area
$c$	Chord length
$c_{opt}$	Optimal chord length
$C_l$	Lift coefficient
$C_d$	Drag coefficient
$C_m$	Pitching moment
$C_{PR}$	Rotor power coefficient
$D$	Drag force
$D_d$	Largest tip deflection when passing tower
$D_i$	Smallest distance from blade tip to tower in unloaded condition
$E_1$	Axial E-modulus of composite in 1-direction
$E_2$	Transverse E-modulus of composite in 2-direction
$E_3$	Transverse E-modulus of composite in 3-direction
$E_c$	E-modulus core material
$E_f$	E-modulus face sheet
$E_k$	Kinetic energy
$F$	Force
$F_k$	Characteristic load
$F_{1t}, F_{2t}, F_{3t}$	Tensile strength along the principal ply directions
$F_{1c}, F_{2c}, F_{3c}$	Compression strength along the principal ply directions
$G_{12}$	Shear modulus in 1-2 plane
$G_{13}$	Shear modulus in 1-3 plane
$G_{23}$	Shear modulus in 2-3 plane
$G_c$	Shear modulus core material
$I$	2nd moment of inertia
$L$	Lift force
$l$	Characteristic length of flow
$m$	Mass
$M$	Pitching moment
$P$	Power
$P_0$	Power of undisturbed air stream
$P$	Pressure
$P_o$	Atmospheric pressure
$Q$	Volume flow
$r$	Local blade length
$Re$	Reynolds number
$S_6$	In-plane shear strength
$U$	Wind speed
$U_{DW}$	Design wind speed
$U_{in}$	Cut-in velocity for wind turbine
$U_{out}$	Cut-out velocity for wind turbine
$U_{rated}$	Wind speed for turbine rated power
$U_{rel}$	Relative wind speed

$U_{rot}$	Wind speed in the plane of rotation
$U_{tan}$	Tangential velocity of rotor blade tip
$U_{wind}$	Far field wind speed
$V_f$	Fiber volume fraction for composite material
$V_{ref}$	Reference wind speed
$v$	Velocity
$\nu_{12}$	Poisson's ratio in 1-2 plane
$\nu_{13}$	Poisson's ratio in 1-3 plane
$\nu_{23}$	Poisson's ratio in 2-3 plane
$z$	Number of rotor blades

### **Greek**

$\alpha$	Angle of attack
$\beta$	Design buckling load
$\gamma_f$	Load factor
$\gamma_m$	Material safety factor
$\gamma_n$	Consequence of failure factor
$\kappa$	Fiber permability
$\lambda$	Tip-speed ratio
$\lambda_D$	Design tip-speed ratio
$\mu$	Dynamic viscosity of fluid
$\rho$	Density
$\sigma_{Hoff}$	Critical sandwich face sheet stress by Hoff

## Abbreviations

AOA	Angle of attack
CAD	Computer Assisted Design
CAPRI	Controlled Atmospheric Pressure Resin Infusion
CFD	Computational Fluid Dynamics
DLC	Design Load Case
DNV	Det Norske Veritas, Norway
EADS	European Aeronautic Defense and Space Company
EVA	Ethylene vinyl acetate
FEM	Finite Element Method
GRP	Glass fiber Reinforced Plastic
IEC	International Electrotechnical Commission
IFE	Institutt for Energiteknikk, Norway
MDF	Medium Density Fiberboard
NACA	National Advisory Committee for Aeronautics, USA
PREPREG	Pre-impregnated composite fibers
PTFE	Polytetrafluoroethylene (Teflon)
SCRIMP	Seeman Composite Resin INFusion Moulding Process
SEM	Scanning Electron Microscope
UD	Unidirectional
VAP	Vacuum Assisted Process
VARTM	Vacuum Assisted Resin Transfer Method



# List of figures

<b>Figure 1-1</b>	Turbines from Vestas from 1981 to 2002 (www.vestas.dk). . . . .	1
<b>Figure 1-2</b>	Offshore wind turbine concepts by Hywind and Sway. . . . .	2
<b>Figure 1-3</b>	Blade length vs. weight (Brøndsted, 2005). . . . .	3
<b>Figure 2-1</b>	Components of a wind turbine blade and their load carrying functions (E. Lund, 2005). . . . .	7
<b>Figure 2-2</b>	Loads carried by the wind turbine blade structures (P. Brøndsted 2005). . . . .	7
<b>Figure 2-3</b>	Section of a typical wind turbine blade (B. F. Sørensen, 2004). . . . .	8
<b>Figure 2-4</b>	Cross section of wind turbine blade showing typical ply angles in different sections of the blade (based on P. Brøndsted 2005). . . . .	8
<b>Figure 2-5</b>	Section of wind turbine blade with internal main spar (Kühlmeier, 2006). . . . .	9
<b>Figure 2-6</b>	Bonding of wind turbine blade at LM Glasfiber. The close up view shows the thick structural adhesive applied to the joints (G. Gardier, 2008). . . . .	10
<b>Figure 3-1</b>	Flow conditions due to the extraction of mechanical energy from a free-stream air flow (E. Hau, 2006). . . . .	12
<b>Figure 3-2</b>	Airfoil definitions. . . . .	13
<b>Figure 3-3</b>	Relative velocity for a rotating wind turbine blade. . . . .	13
<b>Figure 3-4</b>	Pressure and airflow around an airfoil. . . . .	13
<b>Figure 3-5</b>	Pressure field around a wind turbine airfoil (based on E. Hau, 2006). . . . .	14
<b>Figure 3-6</b>	Forces on an airfoil from oncoming airflow. . . . .	14
<b>Figure 3-7</b>	Experimentally measured curves for coefficient of lift ( $C_l$ ), drag ( $C_d$ ) and pitching moment ( $C_m$ ) for the Risø-A1-18 Airfoil (Risø, 2001). . . . .	16
<b>Figure 3-8</b>	a) Smooth laminar flow b) Trailing edge stall c) Fully developed stall over the entire airfoil. . . . .	16
<b>Figure 3-9</b>	Stall behavior of the airfoils NACA 009 (A) and Risø A1-21 (B). Data from F. White (1994) and F. Bertagnolio (2001). . . . .	17
<b>Figure 3-10</b>	Coefficient drag of DU 96-w-180 airfoil measured at TU Delft. Data reproduced from R. Rooij (2004). . . . .	18
<b>Figure 3-11</b>	Drag coefficient distribution along wind turbine blade at $90^\circ$ angle of attack. Reproduced from N. N. Sørensen et al. (2004). . . . .	19

<b>Figure 3-12</b>	Flapwise bending moment calculations for a 100 m wind turbine blade using the assumptions of constant drag coefficient and variable drag coefficient along the blade. Wind speed is the 50-year gust of 70 m/s. ....	19
<b>Figure 3-13</b>	Influence of the number of blades on the rotor power and the optimum tip speed (Hau, 2006). ....	21
<b>Figure 3-14</b>	Rotor solidity as a function of the design tip-speed ratio ( $\lambda_D$ ), calculated for the NACA 4415 airfoil (Hau, 2006). ....	22
<b>Figure 3-15</b>	Rotor power coefficient versus tip-speed ratio ( $\lambda$ ) for different design tip-speed ratios ( $\lambda_D$ ), calculated for the NACA 4415 airfoil (Hau, 2006). 23	
<b>Figure 3-16</b>	Normalized effect curve of a wind turbine (NVE, 2007). ....	24
<b>Figure 3-17</b>	Influence of rotor blade twist on the rotor power coefficient. Curve a: optimal twist, curve b: linear twist, curve c: no twist (E. Hau, 2006). ....	26
<b>Figure 3-18</b>	Chord distribution along a 100m blade given by Equation 3-13. ....	27
<b>Figure 3-19</b>	a) Root section of a LM blade b) Root section of an Enercon blade (LM and Enercon). ....	28
<b>Figure 3-20</b>	Thickness to chord ratio along the blade length. ....	29
<b>Figure 3-21</b>	Definition of main spar width as a percentage of chord length. ....	29
<b>Figure 3-22</b>	Main spar width along blade. ....	29
<b>Figure 4-1</b>	Gravitational and inertia forces on a wind turbine blade (E. Hau, 2006). 31	
<b>Figure 4-2</b>	Different wind loads on a wind turbine blade (E. Hau, 2006). ....	33
<b>Figure 4-3</b>	Flapwise bending moment for the 100m blade. ....	34
<b>Figure 4-4</b>	a) Wind speed during 50-year gust. b) Wind speed during extreme operating gust for a wind turbine. c) A more realistic shape of the wind speeds during the 50-year gust. ....	35
<b>Figure 4-5</b>	Load cases for FEM simulation of 100 m main spar ....	36
<b>Figure 5-1</b>	Typical stress-strain relationship in laminate containing 0°, ±45° and 90° laminates. $\epsilon_{corr}$ is the corrected failure strain for the 0° ply. This value is to be used in the maximum strain criterion if the analysis method does not account for ply degradation (reproduced from DNV-OS-J102-2006 standard). ....	39
<b>Figure 5-2</b>	Representative shape of the first linear eigenvalue buckling mode of a main spar. ....	40
<b>Figure 5-3</b>	Failure modes by bifurcation buckling. a) Unstable or brittle post-buckling behavior. b) Neutral post-buckling behavior (plastic failure). c) Stable post-buckling behavior (ductile failure). ....	41



<b>Figure 5-4</b>	Limit point buckling. Structure becomes less stiff with increased load and reaches a smooth maximum at which the deformations increase in an uncontrolled way.....	41
<b>Figure 5-5</b>	Buckling load is defined as the load where ply stresses (checked on ply level) are above the design criteria for stresses (purple area). ....	42
<b>Figure 5-6</b>	Fiber stress in a UD carbon and $\pm 45^\circ$ glass fiber ply for a node in the buckling region during a non-linear analysis. ....	43
<b>Figure 5-7</b>	Wrinkling of sandwich structure (reproduced from DNV-OS-C501-2003). ....	43
<b>Figure 5-8</b>	Blade deflection when hit by the 50-year gust ( $70 \text{ m/s}$ ). Depending on the blade pitch it is either in danger of striking the tower (a) or free to deflect (b). ....	45
<b>Figure 5-9</b>	a) Wind turbine without tilted or pre-bent rotor. b) Tilted rotor plane. c) Blade with pre-bending. d) Coned rotor. ....	45
<b>Figure 6-1</b>	Concept of wet hand-lay-up (SP Systems, 2001).....	48
<b>Figure 6-2</b>	Concept of filament winding (SP Systems, 2001).....	49
<b>Figure 6-3</b>	Filament winding at Risø using glass fiber tape (P. Brøndsted, 2005) . . .	49
<b>Figure 6-4</b>	Vacuum consolidation of prepreg (SP Systems, 2001).....	50
<b>Figure 6-5</b>	a) Consolidation of low temperature prepreg using only vacuum and an oven (SP Systems, 2001). b) Autoclave for consolidating of laminates (SP Systems, 2001).....	50
<b>Figure 6-6</b>	Concept of vacuum infusion (based on SP Systems, 2001).....	52
<b>Figure 6-7</b>	Resin in fusion of wind turbine blade ( <a href="http://www.stanford.edu">www.stanford.edu</a> ) . . . . .	53
<b>Figure 6-8</b>	Distribution medium manufactured by Aerovac. ....	54
<b>Figure 6-9</b>	SCRIMP infusion process using a distribution medium on top of the preform (based on Hughes,2005). ....	54
<b>Figure 6-10</b>	a) CFM mat by Coldbond. b) Composite with CFM as interlaminar flow medium. ....	55
<b>Figure 6-11</b>	a) Picture of Diab Core with resin tracks. b) Holes at resin track intersection. ....	55
<b>Figure 6-12</b>	Pressure distribution across preform directly after complete infusion (reproduced from C. Niggemann et al., 2008).....	56
<b>Figure 6-13</b>	Thickness change over the preform length after infusion and cure (reproduced from W. Li et al., 2004).....	57
<b>Figure 6-14</b>	Infusion setup using the Saertex VAP membrane ( <a href="http://www.saertex.de">www.saertex.de</a> )... .	58

<b>Figure 6-15</b>	a) The Saertex VAP membrane. White side is the PTFE membrane and light blue is the reinforcing nylon layer. b) The pores of the VAP membrane are so small that only air and gas can escape ( <a href="http://www.saertex.de">www.saertex.de</a> ). c) SEM picture of the membrane (Hughes, C.J., 2005).	58
<b>Figure 6-16</b>	Cross-section of the 50 ply test plate showing a complete wet-through.	60
<b>Figure 6-17</b>	Thickness reduction of preform during debulking (Reproduced from C. Niggemann et al, 2008).	61
<b>Figure 6-18</b>	Setup of Boeing's controlled atmospheric pressure resin infusion process (Hughes, 2005).	61
<b>Figure 7-1</b>	Tensile testing of glass fiber specimen at NTNU/SINTEF fatigue laboratory.	63
<b>Figure 8-1</b>	Wind turbine blade with aerodynamic outer shell and main spar (Jensen et al., 2005).	67
<b>Figure 8-2</b>	a) Asymmetric distribution of UD plies in top and bottom flange. b) Symmetric distribution of UD plies in flanges.	69
<b>Figure 8-3</b>	Modelling matrix for the 100m main spar.	70
<b>Figure 8-4</b>	Definition of chord length and thickness to chord ratio for the 100m wind turbine blade.	71
<b>Figure 8-5</b>	NACA 64-series wing profiles used to define the wind turbine blade. b) Definition of main spar width.	72
<b>Figure 8-6</b>	a) Main spar sections. b) CAD model of main spar created in SolidWorks.	72
<b>Figure 8-7</b>	Boundary conditions at main spar root and pressure load on upper and lower surfaces. Purple arrows show the applied pressure load on the top and bottom flanges. Orange and blue arrows show the boundary conditions at the root, where nodes are restrained in all six degrees of freedom	74
<b>Figure 8-8</b>	Mesh refinement study of 100 m spar. Number of elements across the flange, spar corners and shear web is varied.	75
<b>Figure 8-9</b>	100 m spar mesh at the root area.	76
<b>Figure 8-10</b>	Abaqus ply editor is used to check ply orientation of the top flange in the 100 m spar analysis. a) 45° ply orientation b) 0° ply orientation.	76
<b>Figure 8-11</b>	a) A sudden change in shell normals will cause Abaqus to fail in applying a single ply in the selected region. b) At sharp corners a single ply needs to be divided into two individual plies in order to achieve correct shell section definitions.	77
<b>Figure 8-12</b>	Equilibrium path during a typical unstable static response.	77

<b>Figure 8-13</b>	Design procedure of a main spar.....	79
<b>Figure 8-14</b>	Stress plot of UD ply on the top flange of the main spar. Spar is subjected to the $70^m/s$ extreme gust primary load case and plies have been optimized. Spar deflections have been removed for clarity. ....	80
<b>Figure 8-15</b>	Axial compressive stress along the length of the spar for a UD ply. Spikes indicate location of UD and $\pm 45^\circ$ ply drops.....	80
<b>Figure 8-16</b>	a) Continuous areas violating strength criterion in UD ply (pink color). b) Separate areas violating the strength criterion. ....	81
<b>Figure 8-17</b>	Manual and automatic placement of plies for a wind turbine blade at LM Fiberglass (Plastics Technology, 2008). ....	81
<b>Figure 8-18</b>	Procedure of optimization software for distribution of $\pm 45^\circ$ anti-buckling plies.....	84
<b>Figure 8-19</b>	Distribution of $\pm 45^\circ$ and UD plies before and after optimization of a flange. Blue lines are $\pm 45^\circ$ plies and red lines are UD plies.....	85
<b>Figure 8-20</b>	Spar deflection of carbon fiber spar with no stiffness criterion (S-NS-C), carbon spar with stiffness criterion (S-S-C) and glass fiber spar with no stiffness criterion (S-NS-G).....	86
<b>Figure 8-21</b>	Price of carbon spar (S-S-C model) and hybrid spar (S-S-H model) as a function of carbon price. The price of a stiff glass fiber spar (S-S-G model) is plotted for comparison.....	89
<b>Figure 8-22</b>	Load cases for a 100m pitch controlled wind turbine blade. ....	90
<b>Figure 8-23</b>	Flapwise bending moment along main spar for blade with and without pitch control during 50-year extreme gust. ....	91
<b>Figure 8-24</b>	Deflection of spar with pitch control during 50-year extreme gust ( $70^m/s$ ). ....	92
<b>Figure 8-25</b>	Price of main spar flanges as a function of carbon price for blades with pitch control. ....	92
<b>Figure 8-26</b>	Relative reduction in transverse and shear modulus due to reduction in matrix Young's modulus for CFRP T300/5208 baseline ply (reproduced from S. W. Tsai,1988). ....	95
<b>Figure 8-27</b>	Spar buckling load and deflection as material properties are increasingly degraded in analysis 1 through 4. In analysis 4 (reduction of $G_{12}$ ) the spar failed to reach design load and a deflection result is therefore not included. ....	96
<b>Figure 9-1</b>	Buckling optimizations models for the top flange by a) L. Kühlmeier (2006) and b) E. Lund (2005).....	100
<b>Figure 9-2</b>	Sections from 22, 50 and 90 m used in the optimization study. ....	100

<b>Figure 9-3</b>	a) Load distribution of model. b) Linking beam edges to the reference point. . . . .	101
<b>Figure 9-4</b>	Linear eigenvalue buckling shape of the bending model simulation of the 50 m section. Buckling shape is present only in the middle of the spar. . . . .	102
<b>Figure 9-5</b>	Mesh refinement at the middle of the spar beam (some elements from the outer parts have been removed for clarity). . . . .	102
<b>Figure 9-6</b>	Boundary conditions of compression model. . . . .	103
<b>Figure 9-7</b>	Shape of the first linear buckling mode of the compression model. The buckling mode appears almost across the entire flange. Constraints are not included for clarity. . . . .	103
<b>Figure 9-8</b>	Example of top flange ply definition. UD carbon ply in the middle covered by four glass fiber plies for buckling resistance. . . . .	105
<b>Figure 9-9</b>	Color coding of the ply definition of the spar. . . . .	105
<b>Figure 9-10</b>	Optimal ply definitions of the 50 m section from the bending and compression model. Images of the 22 m and 90 m sections are included in Appendix D. . . . .	107
<b>Figure 9-11</b>	The Brazier effect causes ovalization or flattening of the beam cross section (reproduced from L. Kühlmeier, 2006). . . . .	108
<b>Figure 9-12</b>	Brazier buckling on beam cross section with insufficient amount of $\pm 45^\circ$ plies in the tension flange. . . . .	108
<b>Figure 9-13</b>	Axial stress plots of top flange for a 100 m spar with ply lay-up based on results from bending model. a) UD ply. b) $\pm 45^\circ$ ply. . . . .	111
<b>Figure 9-14</b>	Axial stress plots of top flange for a 100 m spar with ply lay-up based on results from compression model. a) UD ply. b) $\pm 45^\circ$ ply. . . . .	112
<b>Figure 9-15</b>	a) Traditional single skin design of flanges. b) Sandwich concept by J. Jensen et al. (2005). . . . .	112
<b>Figure 9-16</b>	a) $\pm 45^\circ$ plies surrounding the UD plies. B.) Homogenized laminate with $\pm 45^\circ$ plies distributed amongst the UD plies. . . . .	113
<b>Figure 9-17</b>	Change in linear eigenvalue buckling load due to UD carbon fiber ply angle. . . . .	115
<b>Figure 9-18</b>	Change in deflection due to UD carbon fiber ply angle. . . . .	115
<b>Figure 9-19</b>	Change in buckling load (0.5 mm imperfection) due to UD carbon fiber ply angle. Buckling load is found by using nonlinear analysis. . . . .	115
<b>Figure 9-20</b>	Change in linear eigenvalue buckling load due to addition of core material in flange. . . . .	116
<b>Figure 9-21</b>	Change in deflection due to addition of core material in flange. . . . .	116

<b>Figure 9-22</b>	Change in buckling load (0.5 mm imperfection) due to addition of core material in flange. Buckling load is found by using nonlinear analysis.....	116
<b>Figure 9-23</b>	Buckling load found by non-linear analysis (0.5 mm imperfection) for sections with and without homogenization of the laminate. Percentage above bars show change in buckling load due to homogenization. ....	117
<b>Figure 9-24</b>	Distribution of core material in the bottom flange of hybrid (NLH) spar. Core material is placed in flanges only except for the corners at the 4 root sections.....	118
<b>Figure 10-1</b>	a) Concrete base of Sleipner A offshore platform. b) Finite Element model of concrete base.....	121
<b>Figure 10-2</b>	Cross section of 6 m spar. ....	122
<b>Figure 10-3</b>	Tapering of core material in shear web of wind turbine spar (reproduced from F. M. Jensen et al., 2006).....	123
<b>Figure 10-4</b>	Introduction of imperfection in top flange by adding an extra ply of 100 mm wide UD ply.....	123
<b>Figure 10-5</b>	a) In-plane resin infusion with blockage of air. b) Through thickness infusion with break-zone. ....	124
<b>Figure 10-6</b>	3-point bending test of 1 m long spar in order to verify shear strength of bonds.....	125
<b>Figure 10-7</b>	4-point bending test set-up of 6 m spar. ....	125
<b>Figure 10-8</b>	Experimental setup of the 6 m spar at the NTNU/SINTEF fatigue laboratory. ....	126
<b>Figure 10-9</b>	Loading yoke on the 6 m spar. ....	126
<b>Figure 10-10</b>	a) Placement of spar, pulleys and actuator. b) Pulley mounted on hydraulic actuator cross head. ....	126
<b>Figure 10-11</b>	Strain gages on the top flange seen from above. ....	127
<b>Figure 10-12</b>	Strain gages and tracking points mounted on to top flange of the spar. Circular marks are used by the 3D digitizer to measure their position in space. ....	128
<b>Figure 10-13</b>	Spar deflection vs. load from the two load cells. ....	128
<b>Figure 10-14</b>	Comparison of strain on top and bottom flange in the middle of the specimen. ....	129
<b>Figure 10-15</b>	Axial strains along spar centerline.....	129
<b>Figure 10-16</b>	Comparing axial strains above and below the spar centerline (ref. Figure 10-11). ....	130

<b>Figure 10-17</b>	Tensile and compressive strains caused by the imperfection in the top flange. See also Figure 10-4 for information about imperfection. .	130
<b>Figure 10-18</b>	Transverse strain of 6 m spar.....	131
<b>Figure 10-19</b>	a) Spar cross-section when unloaded. b) Spar cross-section as load is increased. The Brazier effect will try to flatten the flanges, thereby causing additional transverse strains in the flanges. ....	131
<b>Figure 10-20</b>	Transverse to axial strain ratio with increasing load. ....	132
<b>Figure 10-21</b>	a) Ideal bonding of shear web and flange. b) Large gap between parts causing the adhesive to drain away due to insufficient thixotropy. ....	132
<b>Figure 10-22</b>	Failure of bond between shear web and flange at the left side of the spar. ....	133
<b>Figure 11-1</b>	Dimensions and material definition of spar cross section shell model.	135
<b>Figure 11-2</b>	Shell element reference plane offset in order to abstract the spar geometry. ....	136
<b>Figure 11-3</b>	Overview of FEM geometry of 6 m spar with boundary conditions. Loading blocks are included in the analysis in order to correctly apply the end support and load. Details of boundary conditions are shown in Figure 11-4.....	136
<b>Figure 11-4</b>	a) Boundary conditions at the symmetry plane of the spar. Zero displacement are prescribed for the nodes in the z-direction together with no rotation about the x and y-axis. b) MDF loading block restrained in the x and z-direction. Force is applied as a body load. c) MDF support block at spar end. No translation in x and y-direction for the centerline. Note that spar is rotated 180° about z-axis for clarity. ....	137
<b>Figure 11-5</b>	Mesh refinement study of spar. a) Adjustment of element width across spar flange. b) Adjustment of element width across shear web. c) Adjustment of element length along spar. ....	138
<b>Figure 11-6</b>	Mesh of the middle part of the 6 m spar. Boundary conditions at the spar center and loading block are shown as small arrows. ....	139
<b>Figure 11-7</b>	Deflection of 6 m spar at 24.85 kN load. The transparent plot shows the shape of the unloaded spar for comparison. ....	139
<b>Figure 11-8</b>	Field plot of minimum axial stress in 6 m spar. Note that at the center of the spar the middle part of the top flange experiences the largest compressive stresses. ....	140
<b>Figure 11-9</b>	a) Spar deflection from experiment and FEM analysis. b) Compressive strain on top flange in the middle of the spar. ....	140

<b>Figure 11-10</b>	a) Axial strain along spar centerline. b) Transverse strain at location 0 mm on top flange.....	140
<b>Figure 11-11</b>	a) Spar cross section represented by shell elements. b) New definition of shear web in order to increase the compliance of the corners of the shell element model. See also Figure 11-14.....	141
<b>Figure 11-12</b>	a) Axial compressive strain ( $\epsilon_1$ ) along spar centerline and the effect of corners with increased compliance. b) Relative displacement of node on top flange (n1) compared to node at flange/web intersection (n2).....	142
<b>Figure 11-13</b>	Influence of corners with increased compliance on transverse strain $\epsilon_2$ . ....	142
<b>Figure 11-14</b>	Displacement of nodes in order to reproduce the imperfection (50 mm from spar center). ....	143
<b>Figure 11-15</b>	A more realistic representation of how the imperfection affects the UD plies. The 0.83 mm displacement of the UD plies at the imperfection is evened out through the thickness of the laminate. ...	143
<b>Figure 11-16</b>	a) Axial stresses of UD plies in flanges at moment of spar failure (24.85 kN). An imperfection size of 0.6mm is used. b) Close-up of increased compressive stresses at imperfection.....	144
<b>Figure 11-17</b>	The effect of imperfection size on the axial strain pattern. ....	144
<b>Figure 11-18</b>	Effect of imperfection on the prediction of the transverse strain $\epsilon_2$ . ...	144
<b>Figure 11-19</b>	The effect of adjusting the Poisson's ratio on the transverse strains ( $\epsilon_2$ ). ....	145
<b>Figure 11-20</b>	Maximum in-plane strain at the intersection between shear web and top flange. The strain vectors suggest that peel-strains were present in the bond between the top flange and shear webs due to the buckling shape of the top flange.....	146
<b>Figure 12-1</b>	Axial stresses in UD carbon ply for carbon fiber spar with no stiffness criterion. ....	177
<b>Figure 12-2</b>	Axial stresses in UD carbon ply for carbon fiber spar with stiffness criterion. ....	177
<b>Figure 12-3</b>	Axial stresses in UD glass ply for glass fiber spar with no stiffness criterion. ....	177
<b>Figure 12-4</b>	Axial stress in top flange UD ply during 50-year gust.....	178
<b>Figure 12-5</b>	Axial stress in top flange $\pm 45^\circ$ ply during 50-year gust. ....	178
<b>Figure 12-6</b>	Axial stress in bottom flange UD ply during 50-year gust. ....	178
<b>Figure 12-7</b>	Axial stress in bottom flange $\pm 45^\circ$ ply during 50-year gust.....	178

**Figure 12-8** Axial stress in top flange UD ply during 50-year gust.....179  
**Figure 12-9** Axial stress in top flange  $\pm 45^\circ$  ply during 50-year gust. ....179  
**Figure 12-10** Axial stress in bottom flange UD ply during 50-year gust. ....179  
**Figure 12-11** Axial stress in bottom flange  $\pm 45^\circ$  ply during 50-year gust.....179  
**Figure 12-12** Axial stress in top flange UD ply during 50-year gust.....180  
**Figure 12-13** Axial stress in top flange  $\pm 45^\circ$  ply during 50-year gust. ....180  
**Figure 12-14** Axial stress in bottom flange UD ply during 50-year gust. ....180  
**Figure 12-15** Axial stress in bottom flange  $\pm 45^\circ$  ply during 50-year gust.....180



# 1 Introduction

## 1.1 Background

Acknowledging the fact that fossil fuel resources are limited and that nuclear power presents a potential environmental and safety hazard, governments in Europe have begun pursuing the further development of renewable energy sources. Norway has been very fortunate to have large sources of hydropower, but for many countries this option has not been available. For these countries the renewable energy from wind turbines is a promising solution. Once installed, a wind turbine does not result in any hazardous emissions, nor does it release any CO<sub>2</sub> into the atmosphere. The only forms of negative impact are noise and visual disturbance during operation. Some negative impact on wildlife and flora are possible, but careful selection of sites can reduce this to a minimum. Looking at the life-cycle energy balance, a wind turbine typically recovers the energy needed to build it within 6 to 12 months. With an expected lifetime of approximately 20 years, this results in a energy yield factor of between 20 and 40 (Hayman et al., 2008).

In February 2007 the European Union made a strong commitment to increase the total share of renewable energy in primary energy consumption to 20 % by 2020 (S. P. Breton, 2008). Ever since the modern wind turbine industry was established in the 1970s, the size of wind turbines has been increasing steadily. The main motivation for increasing the size of wind turbines is that the cost of energy production decreases with larger wind turbines (Berggreen, 2005). A rule-of-thumb is that a doubling of the rotor blade length will approximately quadruple the energy available for the wind. Figure 1-1 shows the increase in turbine size from 1981 to 2002 for the turbine manufacturer Vestas. The largest wind turbines today have a diameter of 130 m with an output of 5 MW. This is probably close to the limit for the size of onshore turbines for practical reasons. Infrastructure will make it difficult or impossible to transport longer blades from the manufacturer to the site.

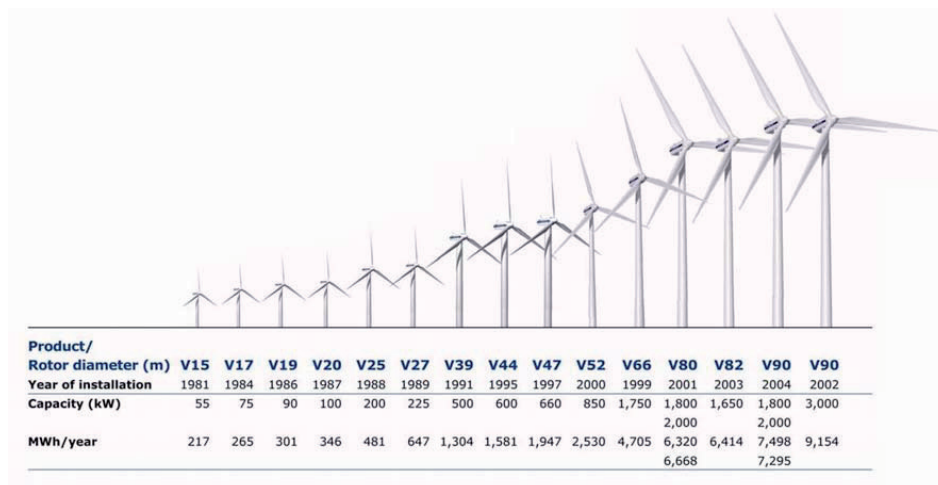


Figure 1-1 Turbines from Vestas from 1981 to 2002 (www.vestas.dk).

In their commitment for renewable energy, the European Union has set as a goal that 50 GW should come from offshore wind energy. Reaching this goal will mean a development of the offshore section similar to the development seen in the onshore section in the last 13 years (EWEA, 2007). There are several advantages to offshore wind turbines, compared to onshore installations. In many European countries the establishment of onshore wind turbine parks has been met with increased scepticism, due to conflicts with human interests and/or wildlife preservation. Moving the installation sufficiently far offshore will nearly eliminate the issues with visual impact and noise, in addition to greatly reducing the effect on wildlife. Offshore sites also offer stronger winds with less turbulence, resulting in an increased productivity of each unit. Onshore turbines have limitations to blade tip speed in order to reduce the noise during operation. Without the tip speed limit, offshore turbines may allow the use of different turbine designs, thereby increasing the efficiency. Manufacturers in Denmark and Germany have pioneered the development of offshore wind turbines, but these have been limited to shallow waters where the wind turbine tower has been fixed on the ocean bed. In Norway the two companies Hywind and Sway have set out to develop concepts for floating wind turbines, who are more suitable for the deeper waters along the Norwegian coast.



**Figure 1-2** Offshore wind turbine concepts by Hywind and Sway.

Without the limitations of infrastructure and allowing for new blade designs, offshore turbines will encourage the development of even longer blades. Another advantage of increasing turbine size is the fact that foundation cost does not rise in proportion to turbine size and that the cost of many components is also largely independent of turbine size (for example electronic control system). Even though the cost of generated power per kilowatt-hour for wind turbines has decreased greatly over the years, wind turbines are still dependent on economic incentives in order to be competitive (Hayman et al., 2008). Larger wind turbines, together with the better wind resources offshore might reduce the production cost sufficiently for wind turbines to deliver energy at a competitive price.

## 1.2 Challenges for future blades

The basic upwind rotor-tower design has remained unchanged with the increased blade length. A rough approximation is that the blade deflections increase with the cube of the blade length, making blade stiffness an increasingly important factor. On a global scale, the blade has to be sufficiently stiff such that it will not collide with the tower during operational and extreme wind loads (50-year gust). Locally, the blade has to be stiff enough to ensure that the shape of the aerodynamic profile is kept as stable as possible. Most wind turbine blades are made of glass fiber, but the larger deflections of future blades might force manufacturers to use carbon fiber in order to get sufficiently stiff blades.

A simple rule of scaling is that the blade weight increases cubically with the blade length. But Figure 1-3, showing data from the different manufacturers, implies that the industry trend is somewhat lower ( $R^{2.66}$ ). The data points outside the trend curve (blades with a length of more than 50 m) are due to new designs that push the margins for blade materials and the blade structure. This has been achieved through improved analysis of the loads in the blade, more accurate failure analysis and non-linear buckling stability predictions. Future blades, perhaps reaching lengths of 80 to 100 m, will have to keep pushing the design envelope in order to limit their weight. This will demand even better design tools and engineering solutions. Saving weight will not only reduce blade material costs, but will also generate savings throughout the rest of the turbine as loads on tower, gear, etc. are reduced. One consequence of the minimum material design approach is that the blade structure will become thin walled and thereby more susceptible to buckling.

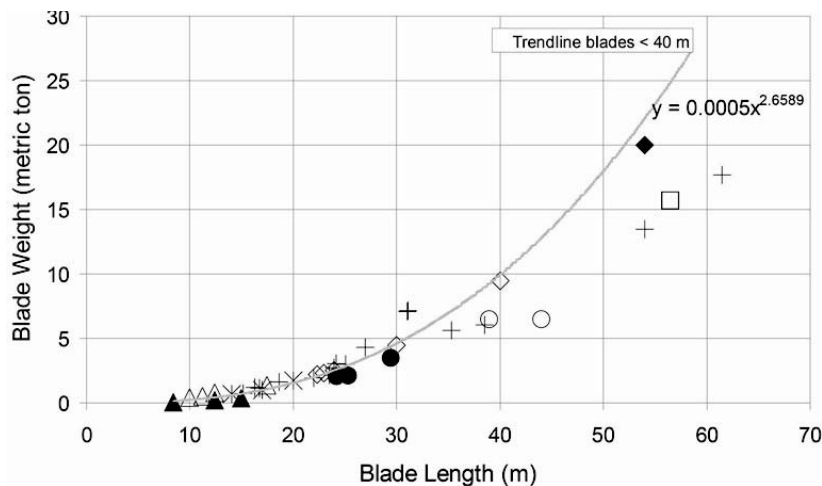


Figure 1-3 Blade length vs. weight (Brøndsted, 2005).

Typically, blade manufacturers improve their products incrementally. New materials are used in existing blade designs in order to reduce weight and blade lengths are increased in small increments. It is highly unlikely that a blade manufacturer will try something radical, for example to double the length of its blades. For large blades the cost of failure

is too high for such an approach to be justified. The author hopes that the FEM analysis presented here will reveal design trends that can guide and inspire in the development of future blades.

### 1.3 Objectives

This thesis explores the design of large wind turbine blades for offshore applications. A 100 m long blade was chosen as an extreme example to demonstrate limits of existing designs and to explore solutions for the anticipated next generation of blades. The objective was to find a possible design for such large blades. Emphasis was put on the design of the spar as the main load bearing component. This was to be done in two major steps:

- Development of optimization strategies for finding the best laminate lay-up. Optimization should be done by finite element analysis of spar designs based on glass, carbon and hybrid laminates. The analysis should focus on the critical failure modes strength and buckling.
- Confirmation of the accuracy of the finite element analysis by building a large but scaled spar to check predicted theoretical results against experimental evidence.

### 1.4 Outline of the thesis

The thesis is organized in chapters as follows:

In chapters 2 through 7 an introduction to important topics concerning wind turbine blades and composites is given. Chapter 2 presents the theory of aerodynamics for a wind turbine blade and how this affects its design. Chapter 3 deals with the loads a wind turbine has to be designed for, focusing on loads relevant in the flapwise direction. In chapters 4 and 5, the basic structure and design criteria for blades are presented. Manufacturing methods have a great influence on the properties of composite materials and the most common methods are presented in chapter 6. The manufacturing method of resin infusion is presented in detail. Mechanical properties of the composites used in this thesis are presented in chapter 7. Values from both experimental testing and calculations based micro mechanical models are presented and discussed.

In chapter 8 the FEM analysis of a 100 m main spar is presented. Various approaches to material distribution and stiffness criteria have been used. Also, the use of glass fiber and carbon fiber has been evaluated. Both linear and non-linear simulations have been used to evaluate the model's static and buckling performance. The influence of laminate eccentricity on buckling has been explored. Finally, a model containing plies with optimized buckling performance is evaluated.

In chapter 9, an optimization study is performed on a partial model of the spar in order to improve laminate buckling performance. In addition to fiber angle, the ratio of anti-buckling plies surrounding the top and bottom of a UD (unidirectional) laminate is

altered to find the best solution. Two different models for evaluating buckling performance are compared. Different approaches are also used to improve the buckling performance of the UD plies. Both linear and non-linear buckling analysis are performed. The most promising results from the optimization studies are applied to a 100 m spar to verify the results from the down-scaled optimization analysis.

In chapter 10, the testing of a 6m long scaled main spar is presented. The spar was tested by four point bending and designed to fail by buckling. 25 strain gages were used to monitor the axial and transverse strains in the spar. An imperfection has purposely been included in the spar in order to control the location of the buckling failure.

In chapter 11 a FEM analysis of the 6 m spar is developed and correlated to the data from the physical test in chapter 10. Results from both linear and non-linear FEM analysis are compared.

In chapter 12, overall conclusions and recommendations for further work are provided.

## Chapter 1 Introduction

## 2 Wind turbine blade structure

### 2.1 General introduction

A wind turbine blade is typically made up of an outer shell and a main spar (Figure 2-1). The outer shell gives the blade its aerodynamic profile and carries the edgewise loads, while the main spar carries the flapwise loads. Near the root the blade cross section changes from a wing profile to a circular profile. Edgewise loads are transferred to the main spar which in turn transfers all the blade loads to the turbine hub. Usually the spar and aerodynamic shells are manufactured separately and then adhesively bonded together, but blade manufacturer Bonus Siemens have also patented a blade manufacturing process where the entire blade is manufactured in one piece (European patent EP 1 859 920 B1).

The loads on the main spar come from the lift generated by the outer shell and bends the blade in the flapwise direction. Figure 2-2 shows that the main spar flange on the suction side is in compression loading, while the flange on the pressure side is in tension. The edgewise loads mainly come from the aerodynamic loads and gravity. As the blade rotates, the leading and trailing edge alternate between being in compression and tension.

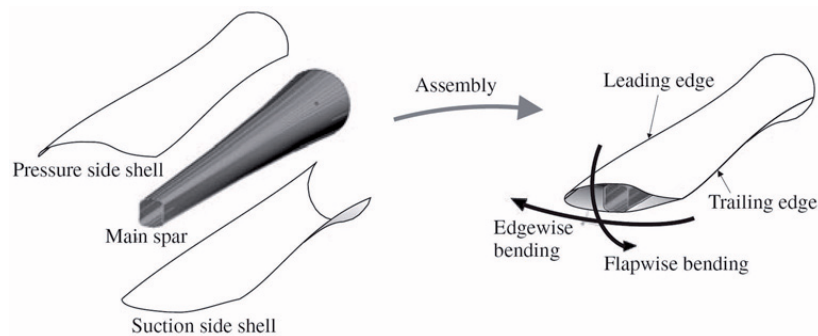


**Figure 2-1** Components of a wind turbine blade and their load carrying functions (E. Lund, 2005).

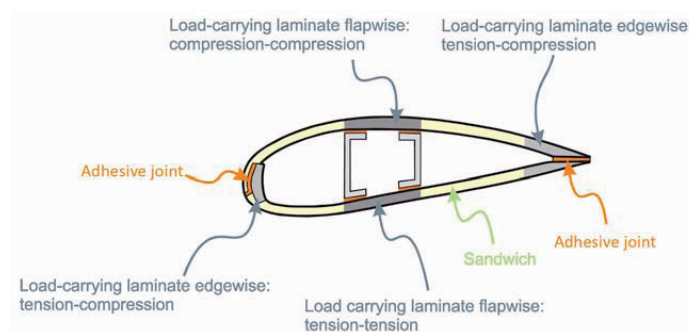


**Figure 2-2** Loads carried by the wind turbine blade structures (P. Brøndsted 2005).

## 2.2 Aerodynamic shell

The outer shell is often produced in two different sections and then bonded together around the main spar (Figure 2-1). To ensure that the shell keeps its shape under the pressure loads, a sandwich construction is used to increase stiffness and buckling resistance (Figure 2-3). The shell also transfers the blade's torque and gravity loads by shear to the leading and trailing edges. In a common blade design the sandwich parts of the aerodynamic shell are transferred into monolithic composite laminates in the areas where the shell is adhesively bonded to the main spar (O. Thomsen, 2006). The shell consists mainly of  $\pm 45^\circ$  plies, with unidirectional laminate at the trailing and leading edges to carry the edgewise forces and bending moments (E. Lund, 2005 and L. Kühlmeyer, 2006). Figure 2-4 shows the cross section of a wind turbine blade and some information about the fiber lay-up and sandwich sections.

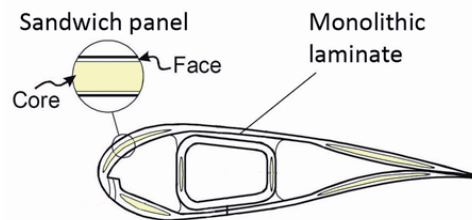


Figure 2-3 Section of a typical wind turbine blade (B. F. Sørensen, 2004).

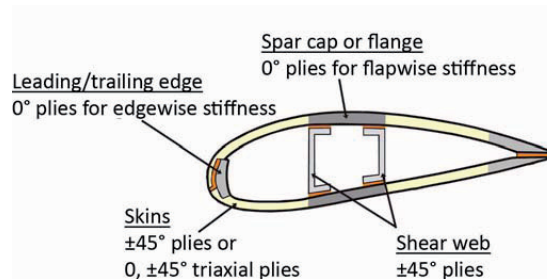


Figure 2-4 Cross section of wind turbine blade showing typical ply angles in different sections of the blade (based on P. Brøndsted 2005).

The aerodynamic shells are today made by either prepreg technology or resin infusion. In a prepreg material the glass or carbon fiber have been pre-impregnated with an epoxy resin that has a consistence before curing similar to toffee. The laminates are laid down in the mold, covered by a polymer film and a vacuum is applied under the film such that the laminate is compressed by the outside atmospheric pressure. The resin is cured by heating it up to 80-120 °C. The benefit of prepreg technology is that very high fiber volume fractions can be achieved. The drawback of prepreg is its high cost. When using resin infusion the reinforcements are laid down as dry fabrics in the mold covered by a polymer film like the prepreg. The vacuum is used to transport a low viscosity resin through the fiber reinforcement. The challenge is to assist the resin flow such that a



complete wet-out of the fibers is achieved. Compared to prepreg, composites made by resin infusion achieve a slightly lower fiber volume fraction but at a lower cost. A more detailed description of these two methods is presented in Chapter 6.

### 2.3 Main spar

The function of the main spar is to transfer the loads from the aerodynamic shell to the wind turbine hub. It is mainly subjected to flapwise bending and shear loads, thus performing like a beam. The main spar usually extends from the blade root to a position close to the blade tip. Figure 2-2 illustrates the loads on the main spar, with the flange on the suction side in compression and the other flange in tension. The fluctuations in compression and tension loads on the flanges are due to fluctuations in wind speed. It is important to note that the edgewise forces on the blade are in tension-compression due to the rotation of the blade, making fatigue resistance highly important at this location.

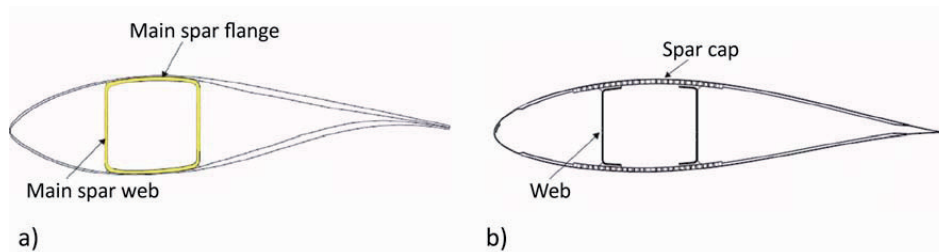


**Figure 2-5** Section of wind turbine blade with internal main spar (Kühlmeier, 2006).

The primary function of the flange is to carry the flapwise bending loads. This laminate is usually made as a thick monolithic composite laminate. In most blades today the flanges are made of glass fiber composites, but in some large blades hybrid glass/carbon composites have been used (Mason, 2004). The carbon fibers are used to enhance the bending stiffness of the blade. The flanges are mainly made of unidirectional plies to provide for bending stiffness and some  $\pm 45^\circ$  plies are included to provide for buckling resistance. The spar is usually constructed by using either a main spar or a spar cap construction. In a main spar construction a rectangular beam containing the flanges and shear webs is made as one piece (Figure 2-5a). The spar is made on a mandrel by both manual lay-up and tape winding. The composite in the mandrel is then allowed to cure under vacuum at elevated temperatures, depending on the resin system used. After cure the mandrel is extracted and the aerodynamic shell is then bonded around the spar. In a spar cap construction the flanges of the main spar are included in the outer aerodynamic shell (Figure 2-5b). The spar cap has the same function as the flanges and is basically made with the same material distribution. The shear webs are produced separately and are included as internal webs/stiffeners when the two aerodynamic shells are bonded together. Blade manufacturer Vestas used a main spar solution until the merging with NEG Micon in 2004. After the merger the technology in both companies was evaluated and resulted in that future blades would be based on Vestas aerodynamic profiles and that NEG Micon's spar cap solution would be used (L. Kühlmeier, 2006).

The function of the internal webs/shear stiffeners is to carry the flapwise shear forces resulting from the flapwise bending of the wind turbine blade. The internal webs/stiffeners can be made as monolithic composite laminates or as a sandwich plate with a polymeric or balsa core. Often the sandwich design is chosen in order to increase resistance against in-plane shear buckling (O. Thomsen, 2006). The laminate is often biaxial with the fibers oriented  $\pm 45^\circ$  relative to the blade length coordinate.

#### 2.4 Assembly of wind turbine blade

After production of the main spar and aerodynamic shells the components are bonded together. Since the edgewise forces alternate between compression and tensile for each rotation of the blade, this demands an adhesive with very good fatigue performance. Also, when bonding such large structures together, it is difficult to achieve a joint with narrow tolerances. Typically the industry operates with an adhesive joint thickness between 2 and 20 mm for large blades. For this reason the adhesive has a thick putty-like consistency such that it will fill all the gaps. Figure 2-6 shows a blade at the LM factory being bonded together. The close-up view shows the thixotropic adhesive applied to the lower half of the blade.

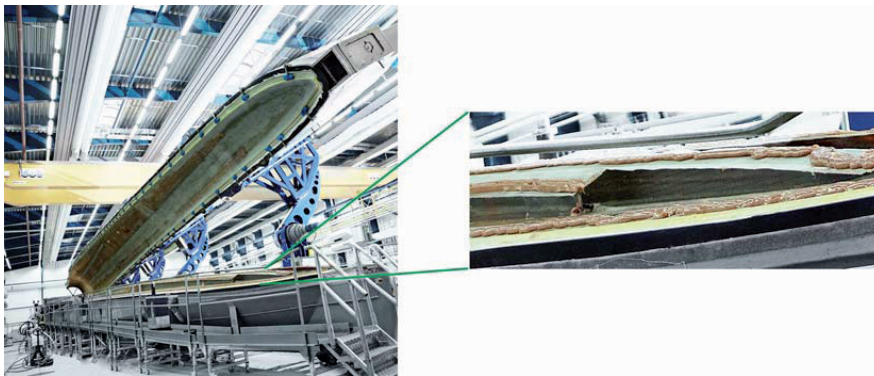


**Figure 2-6** Bonding of wind turbine blade at LM Glasfiber. The close up view shows the thick structural adhesive applied to the joints (G. Gardier, 2008).

## 3 Aerodynamics of wind turbine blades

The primary function of a wind turbine's rotor is to convert the kinetic energy of moving air to mechanical energy, i.e. rotating the hub. The performance of a wind turbine depends on a wide range of factors. Airfoil geometry, design wind-speed and rotor characteristics are some of the most important factors. The following chapter gives a brief introduction to the principle of wind energy conversion and the most important issues related to the rotor design of a horizontal-axis turbine. For a more thorough description the reader is referred to E. Hau (2006).

### 3.1 Physical principles of wind energy conversion

The extraction of mechanical energy from a rotating disc-shaped wind turbine follows its own set of basic rules and the first person to recognize this was Albert Betz in 1922 (E. Hau, 2006). By applying elementary physical principles he showed that there is a limit to the amount of mechanical energy one can extract from moving air. The kinetic energy of air with a mass  $m$  and moving at a speed  $v$  is expressed as:

$$E_k = \frac{1}{2}mv^2 \quad [\text{Nm}] \quad (3-1)$$

Considering a cross-sectional area  $A$  the power of the air (with density  $\rho$ ) moving through this area is given by:

$$P = \frac{1}{2}\rho v^3 A \quad [\text{W}] \quad (3-2)$$

To see how much energy can be extracted from the wind one needs to look at the free-stream airflow at the rotor (Figure 3-1). Here,  $v_1$  is the undelayed free-stream velocity (wind velocity) before it reaches the rotor and  $v_2$  is the flow velocity behind the rotor. As mechanical energy is extracted from the wind stream, the wind's kinetic energy drops correspondingly. Because the mass flow is the same, this means that the flow velocity behind the rotor must decrease. A reduced velocity also means a widening of the cross section (from  $A_1$  to  $A_2$  in Figure 3-1) because the same mass flow must pass through it. It is therefore necessary to consider the flow conditions in front and behind the rotor.

The mechanical energy that the rotor extracts from the airflow corresponds to the power difference of the air stream before and after the rotor:

$$P = \frac{1}{2}\rho(A_1v_1^3 - A_2v_2^3) \quad [\text{W}] \quad (3-3)$$

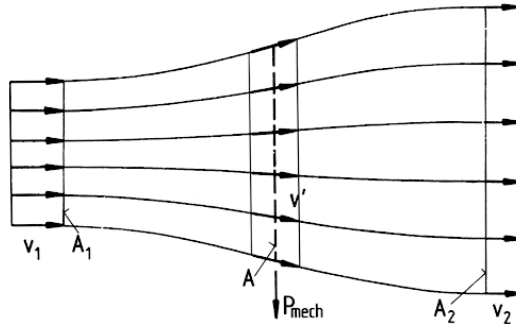


**Figure 3-1** Flow conditions due to the extraction of mechanical energy from a free-stream air flow (E. Hau, 2006).

The power of undisturbed air flowing through the same cross-sectional area  $A$  is:

$$P_0 = \frac{1}{2} \rho v_1^3 A \quad [\text{W}] \quad (3-4)$$

The rotor power coefficient is the ratio between the mechanical power extracted by the rotor and that of the undisturbed air-stream. This is called the rotor power coefficient  $C_{PR}$ :

$$C_{PR} = \frac{P}{P_0} \quad (3-5)$$

A. Betz showed that the rotor power coefficient depends on the ratio between the air velocities before and after the rotor. There is a limit to the amount of mechanical energy that can be extracted from the wind because the change of the velocity behind the rotor affects the wind velocity before the rotor. It follows that the maximum theoretical rotor power coefficient is  $C_{PR}=0.593$ . Betz was the first person to derive this important value and it is therefore called the “Betz limit”.

### 3.2 Airfoil terminology

Modern horizontal axis wind turbines use airfoils to generate power. When air passes over the airfoil shaped blade, lift is generated, in turn spinning the rotor and generating power. The shape of a blade is a function of desired aerodynamic performance and strength considerations. The outer sections of the blade use a thin and highly efficient airfoil, while at the root section a thicker and less efficient airfoil is used due to structural considerations. Several terms are used to describe an airfoil. The most forward and rearward points of the airfoil are called the leading edge and trailing edge (Figure 3-2). A straight line connecting the leading and trailing edges is called the chord ( $c$ ) of the airfoil. The thickness of the airfoil is the maximum distance between the upper and lower surfaces, measured perpendicular to the chord line. The angle of attack (AOA) of an airfoil is defined as the relative angle  $\alpha$  between the chord line and the incoming airflow.

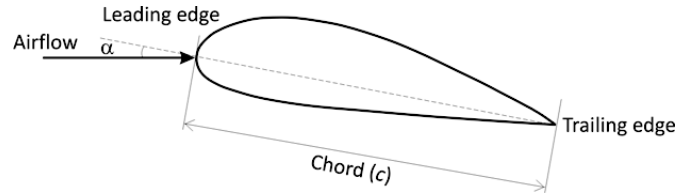


Figure 3-2 Airfoil definitions.

During operation the wind approaching the blade profile constitutes a vectorial sum of the far field wind speed perpendicular to the rotor plane ( $U_{wind}$ ) and the head wind due to the rotational movement of the blade through the air ( $U_{rot}$ ). Figure 3-3 shows how the vectorial sum of the rotational speed ( $U_{rot}$ ) and wind speed ( $U_{wind}$ ) combines into the airfoils relative velocity  $U_{rel}$  with an angle of attack  $\alpha$ .

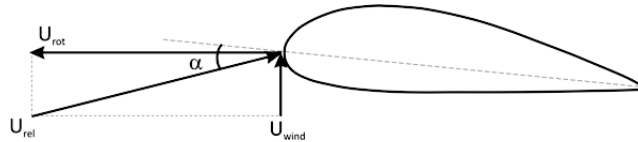


Figure 3-3 Relative velocity for a rotating wind turbine blade.

### 3.3 Airfoil aerodynamics

The physical explanation of the lift force generated by an airfoil is that the shape of the airfoil forces the streamlines to curve around the geometry as shown in Figure 3-4. Basic fluid mechanics (equation 3-6) show that a pressure gradient is necessary in order to curve the streamlines (M. O. Hansen, 2000).  $r$  is the curvature of the streamline and  $V$  the speed. Far away from the airfoil the air is at atmospheric pressure  $P_o$ , thus there must be a lower than atmospheric pressure on the upper side of the airfoil and a higher than atmospheric pressure on the lower side of the airfoil. This pressure difference results in a lifting force acting on the airfoil. At normal operation the flow is attached to the airfoil surface, i.e. a smooth flow over the airfoil (Figure 3-4).

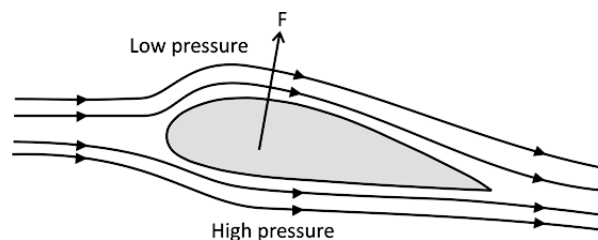


Figure 3-4 Pressure and airflow around an airfoil.

$$\frac{\partial P}{\partial r} = \rho \frac{V^2}{r} \quad (3-6)$$

Figure 3-5 shows the pressure distribution over the airfoil. The resulting force  $F$  over the airfoil surface can be resolved into two forces and a moment that acts along the chord at a distance of  $c/4$  from the leading edge (Figure 3-6). These forces and moment are defined as:

- Lift force  $L$ : defined to be perpendicular to the direction of the oncoming airflow. This force is a result of the unequal pressure on the upper and lower airfoil surfaces
- Drag force  $D$ : defined to be parallel to the direction of the oncoming airflow. This force is due to viscous friction between the air and airfoil surface, and to unequal pressure on the airfoil surfaces facing toward and away from the oncoming flow.
- Pitching moment  $M$ : defined to be about an axis perpendicular to the airfoil cross-section at 25 % of chord length (blade center). This moment is generated because the resulting force does not act through the airfoil's geometric center.

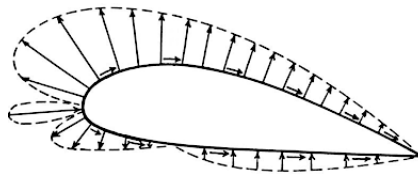


Figure 3-5 Pressure field around a wind turbine airfoil (based on E. Hau, 2006).

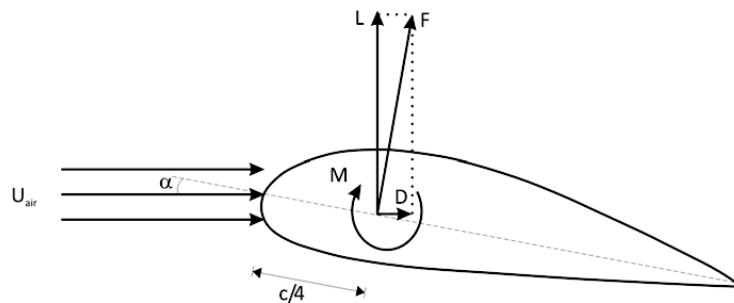


Figure 3-6 Forces on an airfoil from oncoming airflow.

The flow over an airfoil can be characterized by a number of non-dimensional parameters. The most important is the Reynolds number ( $Re$ ) which characterizes the flow conditions. It takes into account the size of the airfoil, the airflow speed and airflow viscosity. The Reynolds number is defined by:

$$\text{Re} = \frac{\rho U l}{\mu} = \frac{\text{Inertial force}}{\text{Fluid viscosity}} \quad (3-7)$$

where  $\rho$  is the fluid density,  $\mu$  is fluid viscosity,  $U$  is the velocity and the  $l$  length that characterizes the scale of the flow. For an airfoil,  $l$  is the chord length  $c$ .

When designing an airfoil, two-dimensional coefficients are often used to describe the properties of the airfoil. These coefficients describe the lift, drag and moment of an airfoil and are defined as:

The two-dimensional lift coefficient

$$C_l = \frac{L/l}{\frac{1}{2}\rho U^2 c} \quad (3-8)$$

The two-dimensional drag coefficient

$$C_d = \frac{D/l}{\frac{1}{2}\rho U^2 c} \quad (3-9)$$

The pitching moment coefficient

$$C_M = \frac{M}{\frac{1}{2}\rho U^2 A c} \quad (3-10)$$

where  $c$  is the airfoil chord length,  $l$  is the airfoil span,  $A$  is the projected airfoil area ( $c \times l$ ),  $\rho$  is the air density and  $U$  the velocity of the airfoil through the air. Figure 3-7 shows the experimentally measured coefficient values for the Risø-A1-18 airfoil. Especially the coefficients of lift and drag are important for evaluating the performance of an airfoil.

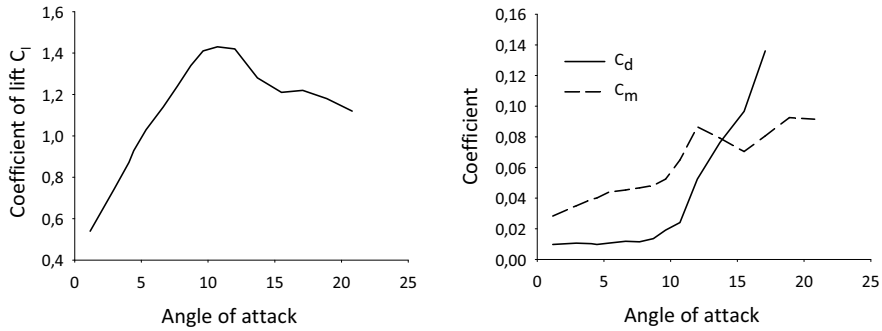


**Figure 3-7** Experimentally measured curves for coefficient of lift ( $C_l$ ), drag ( $C_d$ ) and pitching moment ( $C_m$ ) for the Risø-A1-18 Airfoil (Risø, 2001).

### 3.4 Airfoil behavior

#### 3.4.1 Moderate angles of attack

At a low angle of attack, the rear surfaces of the airfoil have an adverse pressure gradient, but not enough to cause significant boundary-layer separation. The flow pattern is smooth with excellent lift and low drag (Figure 3-8a). As the angle of attack is increased, the upper surface adverse becomes stronger and generally a separation bubble develops at the trailing edge and creeps forward on the upper surface (Figure 3-8b). At a certain angle ( $\alpha = 15$  to  $20^\circ$ ) the flow is completely separated from the upper surface (Figure 3-8c) and the airfoil is said to be stalled. Lift drops markedly, drag increases and the airfoil is no longer flyable. It is important to note that airfoil geometry greatly influences how stall is developed. For some airfoils the separation bubble will not creep towards the leading edge, but leap. This means that stall occurs more rapidly, resulting in a sudden loss of lift (Frank White, 1994). But stall can also develop at the leading edge of the airfoil, separating the entire boundary layer and causing an instantaneous loss of lift. Figure 3-9 illustrates the very different stall behavior of the airfoils NACA 009 and Risø A1-21. For NACA 009, stall occurs instantaneous at  $14^\circ$ , whilst for airfoil Risø A1-21 the stall starts at  $11^\circ$ , but develops more gradually and results in a smoother loss of lift.

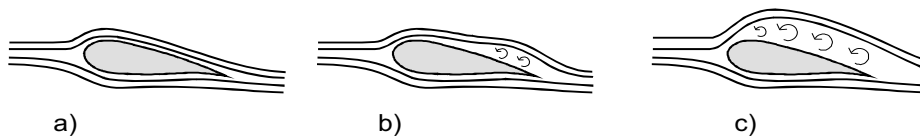


**Figure 3-8** a) Smooth laminar flow b) Trailing edge stall c) Fully developed stall over the entire airfoil.



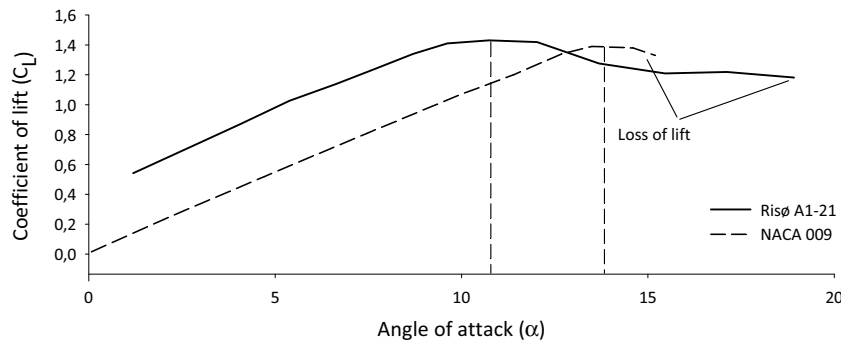


**Figure 3-9** Stall behavior of the airfoils NACA 009 (A) and Risø A1-21 (B). Data from F. White (1994) and F. Bertagnolio (2001).

### 3.4.2 High angles of attack

When designing wind turbine blades, one of the important load cases is when the turbine is parked due to high winds and is suddenly struck by a 50-year extreme gust of  $70 \text{ m/s}$ . The blade loads can be found by calculating the drag force from the wind striking the blade which is parked at  $90^\circ$  to the oncoming flow (Jensen et al., 2005).

The aero elastic design codes used for designing the blades use airfoil tables for lift and drag to compute the forces on the blade (N. N. Sørensen et al., 2004). Very limited data exists for airfoils at high angles of attack (above  $40$  degrees), making these computations uncertain. Calculating the drag coefficient at these high angles of attack has been shown to be quite challenging for Computational Fluid Dynamics (CFD) software, often highly overpredicting the drag coefficient. Sørensen et al. (2004) shows that for a flat plate positioned  $90^\circ$  onto the airflow, a 2D Navier-Stokes solver will predict a drag coefficient of around 3.3, while experimental results yield 1.98. Work done by R. Rooij et al. (2004) at the Delft University of Technology measured the drag and lift coefficient of the DU 96-W-180 airfoil for  $360^\circ$  angle of attack in a wind tunnel. Figure 3-10 shows the measured coefficient of drag for the DU 96-W-180 airfoil between  $0^\circ$  and  $180^\circ$  and it can be seen that at  $90^\circ$  the drag coefficient is approximately 1.9. The airfoil tested had a thickness to chord ratio of approximately 12 % and such a thin airfoil logically corresponds well to the drag coefficient for a flat plate (1.98).

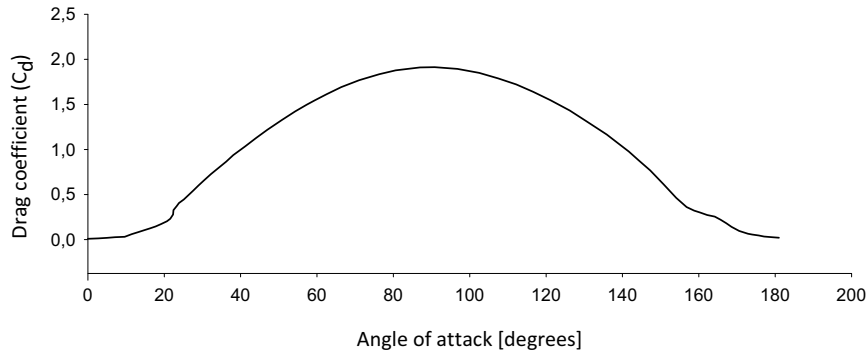


**Figure 3-10** Coefficient drag of DU 96-w-180 airfoil measured at TU Delft. Data reproduced from R. Rooij (2004).

Often in practical applications and in simplified load models a constant drag across the whole profile is assumed (N. N. Sørensen, 2004 and J. Jensen, 2005). Measurements in wind tunnels and CFD analysis puts this integrated drag value between 1.16 and 1.32 along the blade length (N. N. Sørensen, 2004). The fact that the cross section is varying from a cylinder at the root, through thick airfoil sections at the inner part of the blade to thin sections at the blade, suggests that the drag coefficient changes along the blade. Also geometric properties like twist and taper will affect the distribution of the drag coefficient along the blade. In order to perform realistic calculations of forces and moments on the blade it is necessary to know the drag distribution along the blade.

Sørensen et al. (2004) used a 3-dimensional CFD analysis software (EllipSys3D) to investigate the drag coefficient distribution at 90° angle of attack along four different wind turbine blades: the LM8.2 blade, the LM19.1 blade and two modern blades intended for use on megawatt size turbines. The simulations yielded a drag around 0.6 to 0.9 in the root region, which is in good agreement with the value 0.7 found for cylinders with the same aspect ratio (3-4). At the tip, where thin airfoils are used, high drag coefficient values were found from 1.6 to 2.2. This corresponds well to the drag of a flat plate 1.98. Figure 3-11 shows that there is a smooth transition along the blade between the low  $C_d$  values at the root and the high values at the tip. This is believed to be due to the tapering and twist of the blades.

### 3.5 Properties of a wind turbine rotor blade

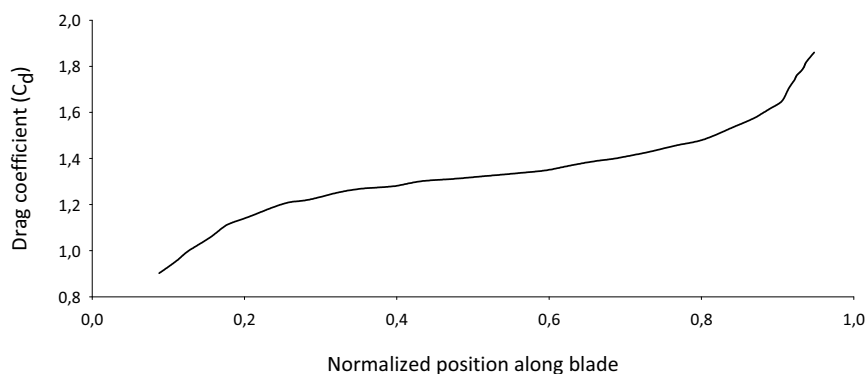


**Figure 3-11** Drag coefficient distribution along wind turbine blade at  $90^\circ$  angle of attack. Reproduced from N. N. Sørensen et al. (2004).

Using equation 3-9 the flapwise bending moment along a 100 m blade was calculated to see how the assumptions of constant drag ( $C_d=1.35$ ) and variable drag affects the calculations of the flapwise bending moments (Figure 3-12). It can be seen that the assumption of constant drag underpredicts the root bending moment by 38 %.

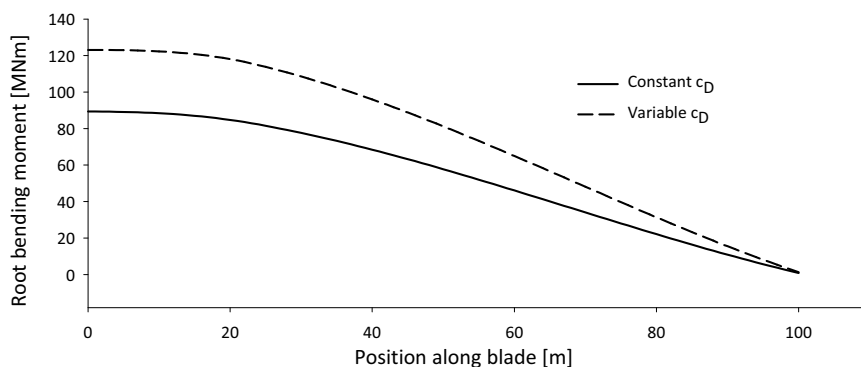


**Figure 3-12** Flapwise bending moment calculations for a 100 m wind turbine blade using the assumptions of constant drag coefficient and variable drag coefficient along the blade. Wind speed is the 50-year gust of  $70 \text{ m/s}$ .

## 3.5 Properties of a wind turbine rotor blade

### 3.5.1 Wind turbine characteristics

When determining the different properties of a wind turbine blade, these properties are often evaluated against how they affect the performance of the wind turbine. For this comparison two definitions are often used: the tip speed-ratio  $\lambda$  and the rotor power coefficient  $C_{PR}$ .

The tip speed ratio  $\lambda$  is defined as the ratio between the tangential velocity of the rotor blade tip and the speed of wind:

$$\lambda = \frac{U_{\text{tan}}}{U_{\text{wind}}} = \frac{\text{tangential velocity of the rotor blade tip}}{\text{speed of wind}} \quad (3-11)$$

Rotor power coefficient  $C_{PR}$  is the ratio of power the turbine is able to extract from the available wind power:

$$C_{PR} = \frac{P}{\frac{1}{2}\rho U_{\text{wind}}^3 A} = \frac{\text{Rotor power}}{\text{Power of the wind}} \quad (3-12)$$

where  $P$  is the rotor power output,  $\rho$  the density of air,  $U_{\text{wind}}$  the speed of the wind and  $A$  the area swept by the rotor.

### 3.5.2 Choosing the number of rotor blades

The number of rotor blades is the most obvious characteristic of a wind turbine and is frequently discussed. Figure 3-13 shows the influence of the number of blades on the rotor power coefficient.

When comparing to a one bladed rotor, it can be seen that there is approximately a 17 % increase in rotor power coefficient when using four blades. But the difference between a three bladed and four bladed rotor is relatively small, only 1.5 %. This is due to that rotors with a lower number of blades rotate faster, thus compensating for their disadvantages of a smaller physical blade area. The marginal increase in rotor power coefficient does therefore not justify the cost of equipping a wind turbine with a fourth blade. Figure 3-13 also shows that the power increase from one to two blades is 10 %, while the difference from two to three blades is only 3-4 %. It is apparent that a low number of rotor blades, i.e. two or three, are the preferred solution for a wind turbine. In general, a power gain of only a few percent does not justify the cost of an additional blade. It seems like a two bladed wind turbine system might be the preferred choice since it yields a power output only 3-4 % less than a three bladed rotor, but saves the cost of the third blade. Also the weight savings will generate additional savings throughout the wind turbine system.

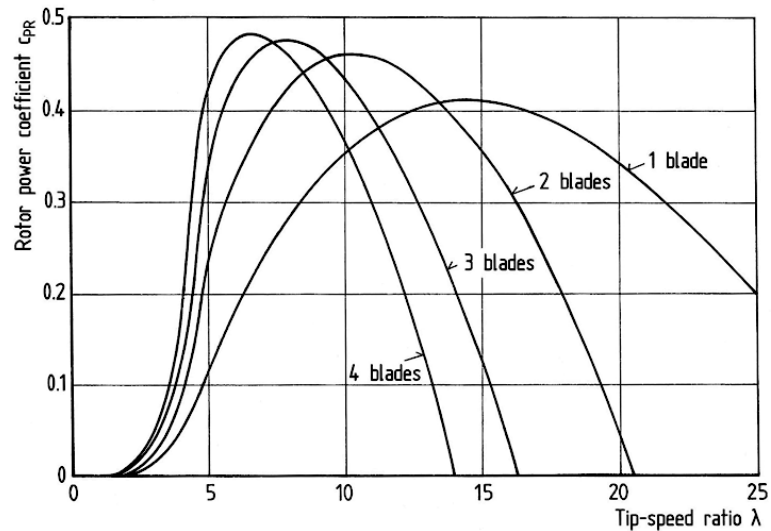


**Figure 3-13** Influence of the number of blades on the rotor power and the optimum tip speed (Hau, 2006).

This would be true, if it not were for other important criteria that have to be met. In an open atmosphere, wind speed and turbulence are always unevenly distributed in space over the rotor-swept area. Many gusts strike the rotor not as a whole, but only one side or only partially. One can imagine that the rotor blades beat into the gusts and that the local air speed along the blade suddenly changes. This has a significant effect on a rotating system and can increase the fatigue effect by up to 50 %. These effects cause the difference between the aerodynamically symmetric three bladed rotor and the two or one bladed rotors to be substantial. The aerodynamical unsymmetrical one or two bladed rotors experience high dynamic loads and require additional complexity in the other components of the wind turbine.

Also rotors that have a high tip speed, i.e. one or two bladed rotors, cause a noise emission that today is unacceptable at most sites. The visual impact of one or two bladed rotors are also a disadvantage when comparing to three bladed rotors. This is due to that their higher rpm is perceived as disturbing by persons living in their vicinity. This is due to the fact that the human eye and brain have evolved to react to movements and will automatically try to interpret these. A fast rotating wind turbine will therefore be perceived as more disturbing than a slower rotating three bladed rotor.

All this has made a three bladed rotor a standard among the wind turbine manufacturers today. But as larger blades are developed and with the increased interest in offshore wind farms, the two-bladed rotor may become attractive again. The choice of rotors is therefore a question of optimizing the power output and consideration of the total system.

### 3.5.3 Design tip speed ratio of the rotor

Selecting the rotor tip speed is a complicated matter where a number of factors have to be taken into consideration. Some factors argue for a high tip speed, whilst others favor lower tip speeds. It is important to note that the tip speed one chooses to design for, affects the whole wind turbine as a system and not only the blades.

A high design tip speed ratio means that the desired power can be generated by a lower torque, which in turn means a reduced weight of the rotor, shaft and gearbox. Another argument for a high tip speed ratio is that with increasing tip speed ratio, the required rotor solidity initially decreases rapidly (Figure 3-14). Less rotor solidity means less material is required for the rotor blades, thus in principle, lower cost. But practical experience shows that rotors with very high tip speed need technologically complex and expensive rotor blades. The strength and stiffness requirements can only be met by using very expensive materials (Hau, 2006).

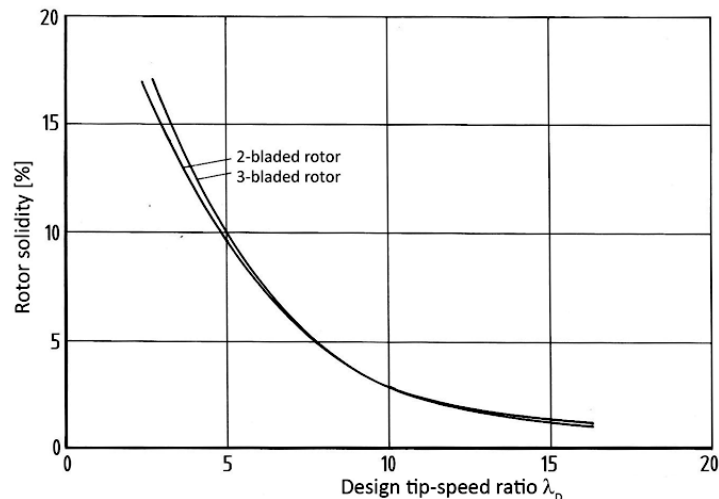


**Figure 3-14** Rotor solidity as a function of the design tip speed ratio ( $\lambda_D$ ), calculated for the NACA 4415 airfoil (Hau, 2006).

Another important question is to what extent the design tip speed has an effect on the achievable power coefficient. In Figure 3-15 the power coefficient vs. the tip speed ratio is plotted for three different design tip speed ratios  $\lambda_D$  (5, 10 and 15). It can be seen that the maximum power coefficient of the rotor changes only very little in the usual range for high-speed rotors. It is only for tip speed ratios below 5, i.e. for low speed rotors, that the  $C_{PR}$ -value drops rapidly. Thus from a point of view of energy yield, there is no reason to strive for very high tip speed ratios.

A very important aspect to be considered when choosing the tip speed ratio is the aerodynamic noise emission from the rotor. The common denominator for all sounds of aerodynamic origin, is that they increase sharply with increasing airflow velocity. Noise emissions increase by about the 5th power of the flow velocity, which, in turn, is essentially determined by the tangential velocity of the rotor blade tips (Hau, 2006). The major part of the rotor noise, as well as the rotor power, emanates from the outer 25 % of the blade and therefore the geometry of the blade tips is of special importance (Hau, 2006). One may therefore conclude that designing for very high tip speed ratios is no longer justified. Today it is common with  $\lambda_D$  of 6-8 for three-bladed rotors.

In practical terms, approximately  $80 \text{ m/s}$  is regarded as the maximum blade tip speed. It cannot be higher as it becomes too difficult to design blade tips from an lift/drag and noise point of view as one gets close to the speed of sound (the local air speed at the tip is accelerated).

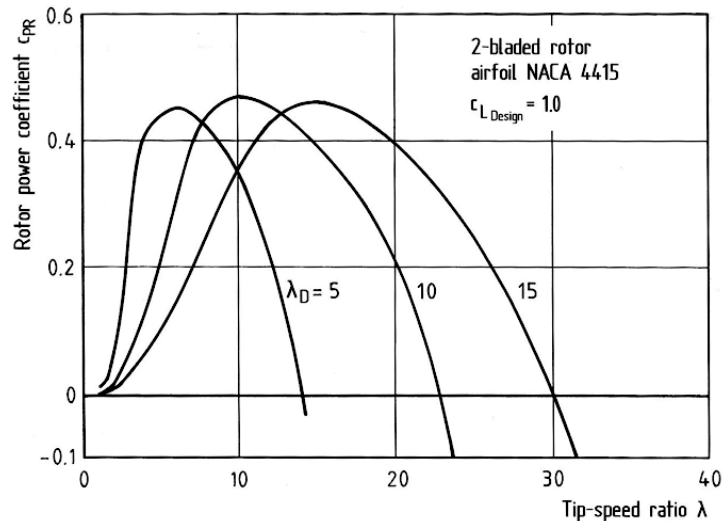


**Figure 3-15** Rotor power coefficient versus tip speed ratio ( $\lambda$ ) for different design tip speed ratios ( $\lambda_D$ ), calculated for the NACA 4415 airfoil (Hau, 2006).

### 3.5.4 Power curve of a wind turbine

A turbine's electrical power output versus wind speed is referred to as the power curve (Figure 3-16). It is calculated based on the rotor power characteristics ( $C_{PR}$ -curves), the design wind speed, wind spectrum at the planned location and the efficiency of the mechanical-electrical energy conversion system. Figure 3-16 shows the normalized power curve for a wind turbine at different wind speeds.  $U_{in}$  is the cut-in velocity ( $4 \text{ m/s}$ ) where the wind turbine starts to deliver electrical power to the grid. At this speed the rotor must deliver enough power to compensate for the power loss in the generator and to cover internal consumption.  $U_{rated}$  is the wind speed (approximately  $15 \text{ m/s}$ ) where the rated generator power is reached. Above this wind speed the blades will be

pitched such that they are less effective and the turbine has a constant power production.  $U_{out}$  is the cut-out velocity ( $25 \text{ m/s}$ ) where the turbine is shut down due to high winds. The power curve is the wind turbine's certificate of performance and has to be guaranteed by the manufacturer.

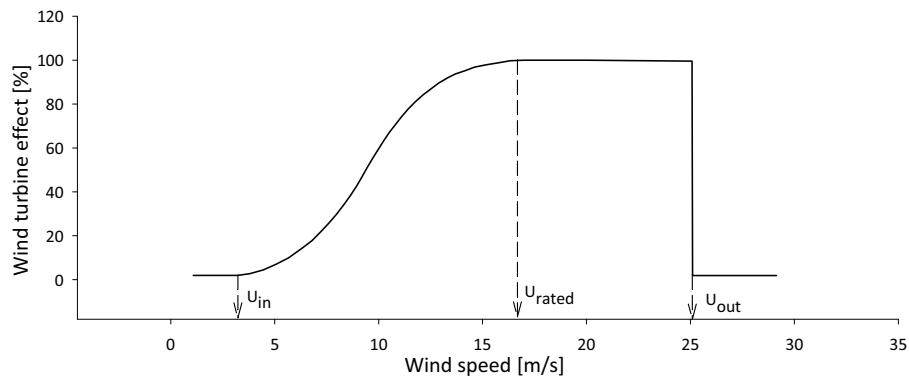


Figure 3-16 Normalized effect curve of a wind turbine (NVE, 2007).

### 3.6 Important properties of wind turbine airfoils

When designing a wind turbine blade it is important to choose airfoils with the right characteristics. Some properties are in conflict with each other and are given different importance at the different blade regions. Table 3-1 shows the complex matrix of blade properties for a wind turbine blade. At the root of the blade, structural properties are very important, whilst at the mid and tip parts, the aerodynamic performance is important. Also geometric compatibility is important to ensure a smooth transition from one airfoil to another (P. Fuglsang, 2004). A main design driver is that the blade does not lose its efficiency as dust, dirt and bugs accumulates on the leading edge. Therefore sensitivity against leading edge roughness is of high importance at the outer sections of the blade. A wind turbine with airfoils that are sensitive to leading edge roughness would after short operational time be considerably less effective. Stopping the wind turbine and cleaning the blades is not an option because it would mean loss in production and increased maintenance cost. When constructing wind turbines near populated areas, one has to limit the noise emissions from the turbine. Therefore, low airfoil noise properties are very important for the outer sections of the wind turbine blade. For wind turbines offshore, this criterion is of lesser importance.



**Table 3-1** Desirable airfoil properties for wind turbine airfoils and the importance to the different blade regions (Fuglsang, 2004).

Property	Root	Mid part	Tip
Thickness-to-cord ratio (t/c)	>27	27-21	21-15
Structure	+++	++	+
Geometrical compatibility	++	++	++
Maximum lift insensitive to leading edge roughness		+	+++
Design lift close to maximum $c_L$ of profile		+	+++
Maximum $c_L$ and post stall behavior		+	+++
Low airfoil noise		+	+++

### 3.6.1 Available airfoils for wind turbines

In the early development of wind turbines, airfoils developed for aircraft wings were used. This was justified by the flow velocity of the aerodynamically important outer part of the wind turbine blade being comparable to the flying speeds of light airplanes (Hau, 2006). But the requirements of a rotor blade is not in every way identical that of an aircraft wing. In order to further develop the wind turbine it was necessary to develop airfoils specifically for wind turbine blades.

Today the American NACA-series are still predominant with the 230-, 63- and 64-series in widespread use. The trend is that special aerodynamic profiles will be used and considerable research is put in development of these profiles. Recent wind turbines like Enercon E-112 and Vestas V90 use such innovative profiles. Danish blade manufacturer LM has recently built their own wind tunnel in order to improve their airfoil simulation tools and further optimize the performance of their airfoils (LM, web link 01).

### 3.6.2 Blade twist

The increase in relative air speed from the root to the blade tip requires the blade to be twisted such that the airfoil sections have an optimal aerodynamic performance along the blade. Blade twist is defined as the angle between the local airfoil chord and the blade tip. The optimal blade twist can only be determined for one tip speed ratio ( $\lambda$ ), i.e. for one operating point ( $\lambda_D$ ). As a rule this is determined for the rated power operating point, and for all other wind speeds the blade twist will be non optimal. For manufacturing reasons the sections near the blade hub often have less of a twist as would be desired from an aerodynamic point of view. Since the power generated at this section is relative small compared to the outer sections, compromises between aerodynamics, structure and mechanical engineering/design are more easily done here.

When designing a wind turbine the optimum twist for the blade sections are calculated using beam element method (BEM) or aero-elastic calculations. Practically the twist varies from 12 to 15 degrees at the root section, to  $-1^\circ$  or  $-2^\circ$  at the blade tip. Figure 3-17 shows the influence of different twist variations on a blade's performance. The challenge is to determine how much twist a blade should have. From a manufacturing point of view a blade should have no twist. The figure shows that choosing to have no twist, leads to a considerable reduction in power and for large turbines this is not an acceptable compromise. But it can be seen that the difference between an optimized twist and a linear twist is small. Therefore, when developing a simplified FEM analysis, a linear distribution of the twist is a reasonable approximation.

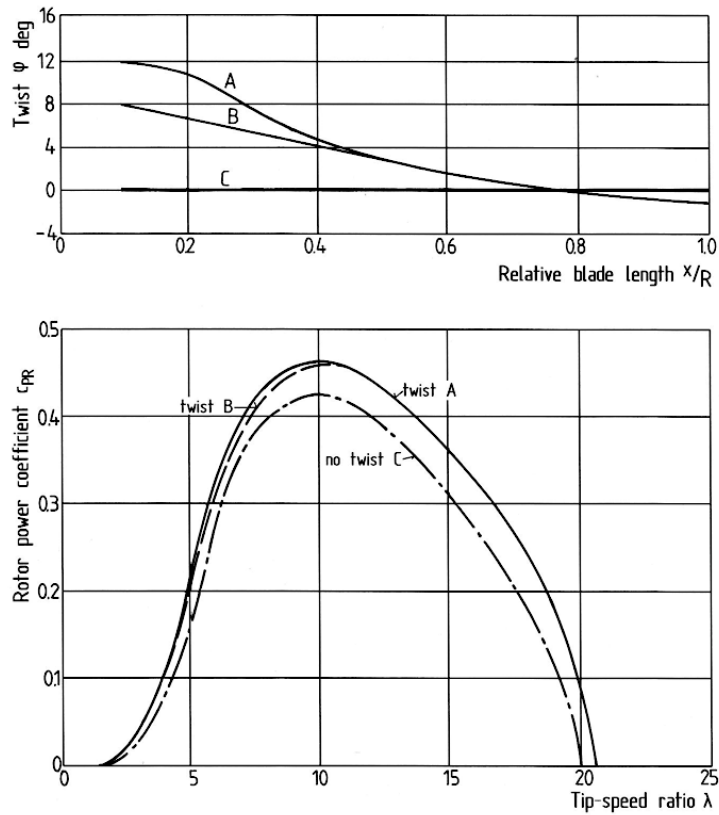


**Figure 3-17** Influence of rotor blade twist on the rotor power coefficient. Curve a: optimal twist, curve b: linear twist, curve c: no twist (E. Hau, 2006).

### 3.6.3 Rotor blade chord length

With certain simplifications, mainly neglecting the airfoil drag and tip vortex losses, the optimal chord length ( $c_{opt}$ ) along the blade can be solved analytically (Hau, 2006). This is useful for an approximate calculation of the blade contour and gives a hyperbolic function of the blade length:

$$c_{opt} = \frac{2\pi r}{z} \cdot \frac{8}{9} C_L \cdot \frac{U_{DW}}{\lambda U_{rel}} \quad (3-13)$$

where:

$U_{DW}$  = design wind speed [m/s]

$U_{tan}$  = peripheral speed [m/s]

$U_{rel} = \sqrt{U_{wind}^2 + U_{tan}^2}$  local effective flow velocity [m/s]

$U_{wind}$  = wind speed [m/s]

$\lambda$  = local tip speed ratio

$C_L$  = local lift coefficient (typically between 1.0 and 1.2)

$r$  = local blade length [m]

$z$  = number of rotor blades [z]

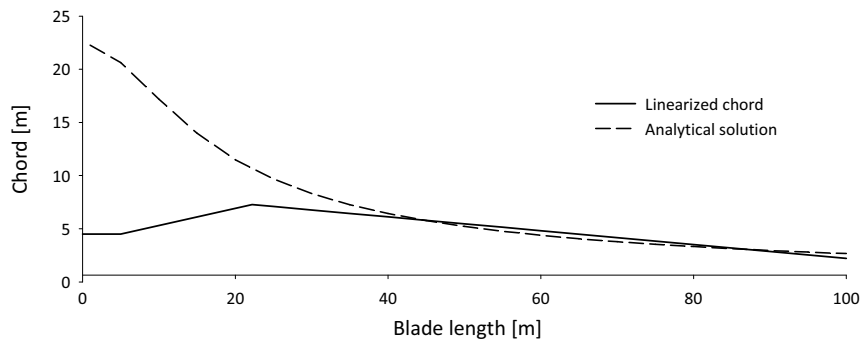


Figure 3-18 Chord distribution along a 100m blade given by Equation 3-13.

Equation 3-13 gives the chord length for an ideal rotor blade and Figure 3-18 shows the chord length along a 100 m blade with  $U_{DW} = 9 \text{ m/s}$ ,  $C_L = 1.0$  and  $75 \text{ m/s}$  as maximum tip-speed. For the inner sections, near the blade hub, this equation results in large airfoil sections. Since this part is of less significance in terms of power production, most manufacturers put aside the aerodynamic aspects of this section in favor of higher strength and greater simplicity in manufacturing (linearized chord in Figure 3-18). Often blades have a circular cross section near the hub, which also saves material and weight compared to having an aerodynamic optimal shape at the root. But the lower contribution by the root area to power production does not mean that it can be ignored without a noticeable change in power production. In special cases, it has been found that, regardless of the general rule, significant increases in performance were made possible by

using special shaping of the hub section of the blade ([www.enercon.de](http://www.enercon.de)). The German wind turbine manufacturer Enercon, has on its recent blades chosen to use a large chord length at the root, reflecting the optimal shape of a blade. Figure 3-19a shows how LM has sacrificed aerodynamics at the root section, whilst Enercon (Figure 3-19b) has chosen to optimize for aerodynamics at the root section. In a FEM analysis the chord distribution is often linearized for simplification.

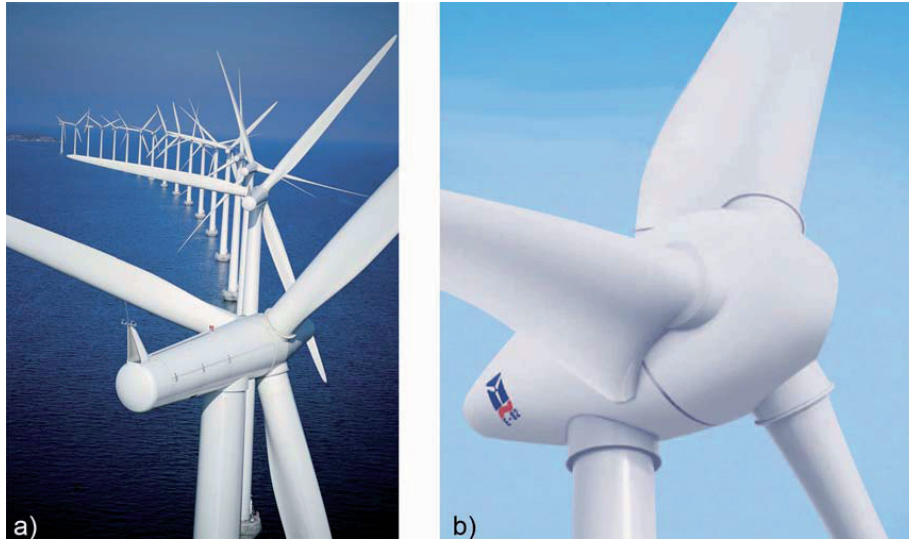


Figure 3-19 a) Root section of a LM blade b) Root section of an Enercon blade (LM and Enercon).

### 3.6.4 Thickness to chord ratio

The rotor blade thickness is a classical conflict between aerodynamical efficiency, rotor blade stiffness and strength requirements. From an aerodynamical point of view, the entire blade should be a thin high performance airfoil. Since most of the power is generated at the blades outmost section, aerodynamically efficient blade profiles are used near the blade tip. Typically these profiles have a thickness to chord ratio between 12-15 %. In contrast, structural requirements demand sufficiently thick cross sections for the load bearing elements. In general the main spar thickness influences the section stiffness to the third power, hence the requirements of good aerodynamic efficiency and structural stiffness counter each other. Thinner sections result in a less stiff structure, thereby more material has to be used, resulting in increased blade weight and cost. The optimum lies somewhere between good aerodynamic performance and blade weight.

The  $t/c$ -ratio for commercial blades are not easily available for obvious reasons. Figure 3-20 plots some ratios found for a Bonus 45 m blade (IIT, 2006) and information from Jensen et al. (2005). At the circular root section the  $t/c$  is defined as 100 %. A linearized distribution is also plotted for comparison.

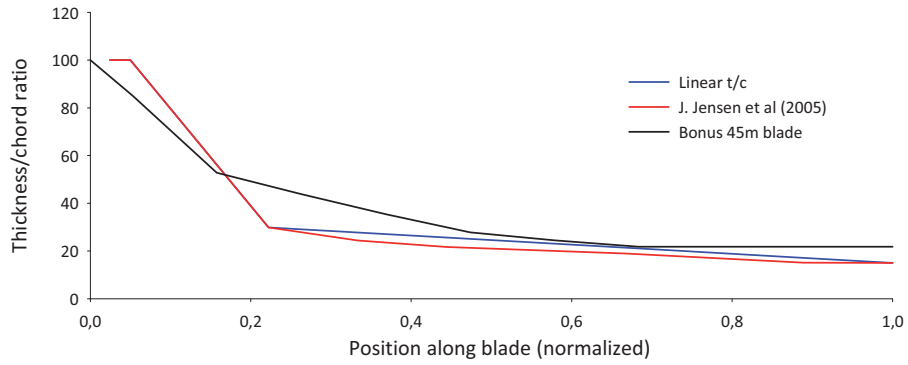


Figure 3-20 Thickness to chord ratio along the blade length.

### 3.6.5 Spar width

In order to develop the FE-models of a 100 m main spar in Chapter 8 it was necessary to know the spar width compared to the chord length. Also here, only limited data was available. Figure 3-22 shows data from J. Jensen et al. (2005). From 20 m to the tip of the blade, the average spar width was 33,5 % of the chord length. Measurements of pictures in B. F. Sørensen (2005) show a main spar width of approximately 30.4 %.

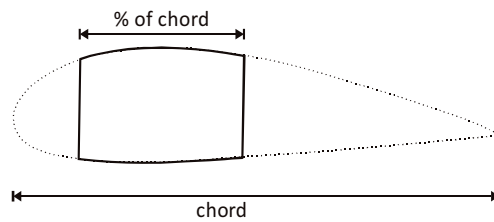


Figure 3-21 Definition of main spar width as a percentage of chord length.

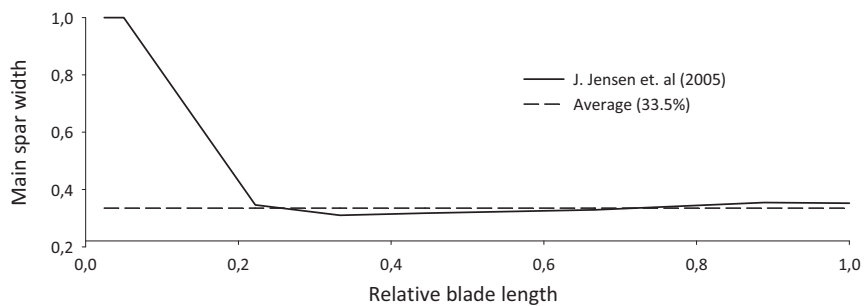


Figure 3-22 Main spar width along blade.



## 4 Loads on a wind turbine blade

A wind turbine is subjected to a series of different loads both from the wind, gravity and during operation. In general a wind turbine blade is subjected to the following loads:

- Flapwise and edgewise bending due to pressure load on the blade (symmetric and skew bending).
- Gravitational loads which change direction during the rotation and which mainly generate edgewise bending load
- Torsional loading because the shear resultant of the flap- and edgewise loads do not go through the center of the blade section (25 % of chord length from leading edge).
- Inertia forces due to the rotation of the blade.
- Relative small loads due to pitch de-accelerations and accelerations
- Loads from starting and stopping of the turbine. The loads are moderate during normal conditions, but in case of an emergency stop these loads can become large enough such that they have to be calculated for.

The three last loads have very little influence on the design and are often not taken into consideration. It is the flapwise and edgewise loads that determine the structural design and the blade cross section. The cross section in the outer  $2/3$  of the blade is determined by the aerodynamic shell, whilst at the root section the aerodynamic performance is sacrificed for structural performance. The flapwise loads are carried by the spar while the edgewise loads are carried by the leading and trailing edges of the blade profile with the aerodynamic shell transferring the shear loads.

### 4.1 Gravity and inertia loads

Whereas the aerodynamic loads on a wind turbine blade can be difficult to calculate, the loads from the mass of the components are relatively simple to calculate (Figure 4-1). The only challenge is that in the beginning of the design phase the mass of all the components is not known. The mass of the blade depends on the complete load spectrum (inertia and aerodynamic loads) and therefore one has to go through several design iterations before the complete mass of the system is known. First mass estimates can be done by comparing empirical data from existing blades.

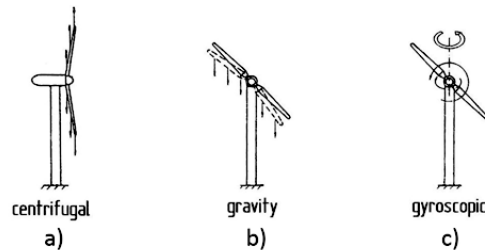


Figure 4-1 Gravitational and inertia forces on a wind turbine blade (E. Hau, 2006).

#### 4.1.1 Gravitational loads

The mass of the wind turbine blade generates cyclic tension and compression loads along the blade. Also large edgewise bending moments are generated, leading to variable tension-compression forces at the leading and trailing edge. The gravitational forces increase from the tip towards to root of the blade, i.e. in the opposite direction from the influence of the aerodynamic loads. A wind turbine is designed for 20 years of service, meaning that it has to withstand  $10^7$  to  $10^8$  cycles of these varying loads and bending moments. Together with wind turbulence, the gravitational loads have a dominating influence on the fatigue strength of a wind turbine blade. Defining the blade pointing straight up is as  $0^\circ$ , the alternating gravity loads are:

- $0^\circ$ : Compression forces on the entire blade
- $90^\circ$ : Blade profile's leading edge is subjected to compressive stresses and the trailing edge to tensile stresses. Edgewise bending moment.
- $180^\circ$ : Tensile forces on the entire blade.
- $270^\circ$ : Leading edge subjected to tensile load and trailing edge in compression load. Edgewise bending moment.

#### 4.1.2 Centrifugal loads

Because of the relatively low rotational speed, centrifugal forces are not very significant in wind turbines. Therefore these forces are neglected in the design phase of the wind turbine blade. This is in contrast to helicopter rotors, where the rotational speed generate high centrifugal forces and are important design factors. Since there is a restriction on blade tip speed ( $70 \text{ m/s}$  due to noise generated), the design of even larger blades will result in lower rotational speeds. This in turn will most likely make centrifugal forces even less important.

#### 4.1.3 Gyroscopic loads

Gyroscopic loads are created when the rotor is yawed into the wind. Fast yawing rates lead to large gyroscopic moments which manifest themselves as pitching moments on the rotor axis. Normally the yawing rates are relatively slow, so the practical effects are very small. Wind turbines are designed with so small yawing rates that the gyroscopic loads usually have no influence on the design (Hau, 2006).

### 4.2 Aerodynamic loads

Figure 4-2 shows the different aerodynamic loads that a wind turbine can be subjected to. The wind loads depicted here are considered normal during operation and do not propose any risk of exceeding the blades strength limit nor cause any excessive deflections of the blade. Wind turbulence causes a fluctuation of the blade loads and is therefore an important factor when determining the fatigue loads for a blade. Since the wind



will be less disturbed when going over water than landscape, offshore turbines might be subjected to less vertical wind shear and turbulence.

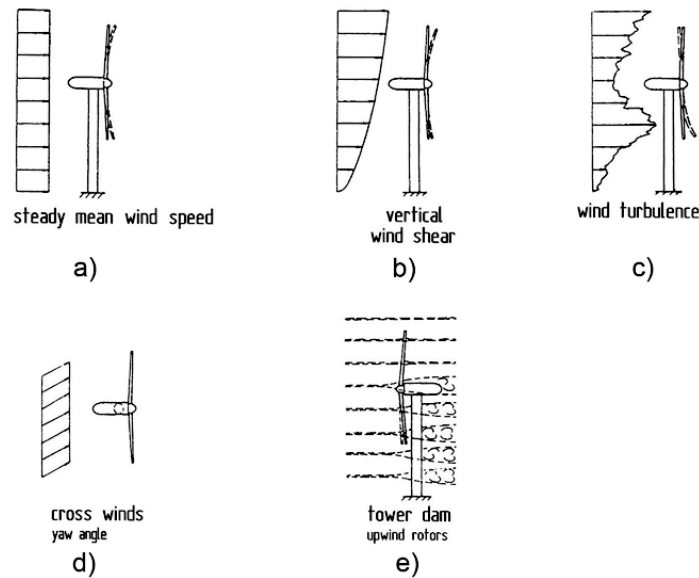


Figure 4-2 Different wind loads on a wind turbine blade (E. Hau, 2006).

### 4.3 Extreme wind loads

A wind turbine must be dimensioned such that it will survive the highest wind speed that can occur during its 20-year service life. The extreme wind model (EWM) in the IEC 61400-1-2005 standard specifies the following scenario:

The wind turbine has been parked due to winds above the turbine's cut-out speed of 25-30 m/s. The turbine is subjected to the reference wind speed ( $V_{ref} = 50 \text{ m/s}$ ) which is the maximum wind speed expected as a mean value over 10 minutes. With a 50-year occurrence the turbine is struck by a 70 m/s gust lasting 5 seconds before the wind speed returns to  $V_{ref}$ .

The 50-year gust will cause large flapwise bending moments for which the main spar needs sufficient strength and buckling resistance. In addition, the main spar has to be stiff enough avoid striking the tower. This would most likely damage the blade or in a worst-case scenario it could cause a collapse of the wind turbine tower. The criterion for tower clearance is presented in section 5.5.

The flapwise bending force is found by calculating the drag force  $D$  along the blade as the extreme gust strikes it perpendicularly. For an airfoil with cross section  $A$  (chord x blade length) the drag force is given by:

$$D = \frac{1}{2} \rho A C_D U^2 \quad (4-1)$$

where  $\rho = 1.25 \text{ kg/m}^3$  is the density of air and  $U = 70 \text{ m/s}$  is the speed of the 50-year gust. In section 3.4.2 it was shown how the coefficient of drag ( $C_D$ ) varied along the blade length and that it is necessary to include this distribution in order to get accurate predictions of the flapwise bending forces. Figure 4-3 shows the flapwise bending moment calculated for a 100 m long wind turbine blade of which the main spar will be studied by FEM analysis in Chapter 8. The forces were calculated in Excel by applying equation 4-1 together with the distribution of chord length and drag coefficient (Figure 3-18 and Figure 3-11).

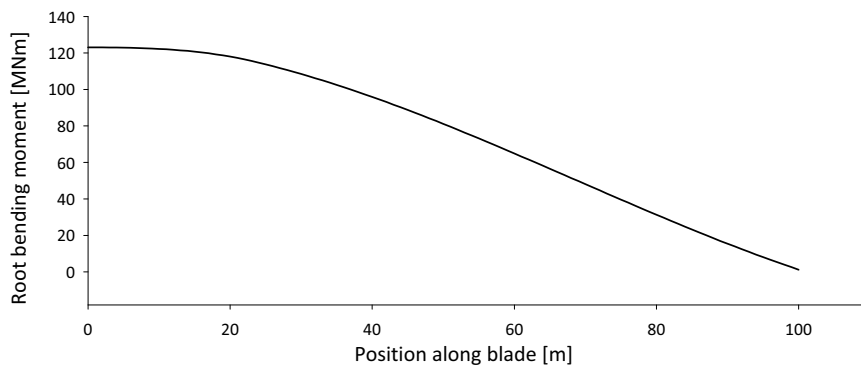


**Figure 4-3** Flapwise bending moment for the 100m blade.

The IEC 61400-1-2005 standard does not specify how the 50-year gust acts, but it is unreasonable to assume that it would act in a step-wise fashion as shown in Figure 4-4a. A more realistic shape can be found in the IEC 61400-1-2005 definition of the “Extreme Operating Gust” (Figure 4-4b), where the load is more gradually increased and decreased. Combining this with the 5 seconds of the 50-year gust, yields a more realistic wind speed curve in Figure 4-4c. The 5 seconds of the 50-year gust is most likely to be a large enough impulse for the blade to reach maximum deflection and it can therefore be modelled in a FEM analysis as a static load. The assumption is also that the turbines yaw system is operational and has turned the rotor into the wind. For a modern turbine with a backup power system (in case grid connection is lost) it is highly unlikely that the yaw system will fail during the 50-year gust and has therefore not been evaluated. If backup power is not provided, the blade would have to be dimensioned such that it could handle the  $70 \text{ m/s}$  gust from any direction.

The IEC 61400-1-2005 standard defines another interesting load case that needs to be evaluated in the design of the main spar (design load case 7.1). Annually the wind turbine is expected to be hit by a 1-year extreme gust of  $52.5 \text{ m/s}$ . Since this happens once a year, it is probable that it will happen during failure of the yaw system. Due to mechanical or electrical failure, the yaw system is unable to turn the turbine as the wind direction shifts during a storm. The blade therefore has to survive being struck by the  $52.5 \text{ m/s}$  gust from any direction. For the main spar, the worst case would be to be struck from the opposite direction of the 50-year gust. Laminates designed to be in tension on the pressure side of the airfoil, would now be in compression and in risk of experiencing

buckling failure. Composite materials have the great benefit of allowing engineers to highly optimize a structure for a given load case. A design that is optimal for one situation, can quickly become inadequate if the loads change. Ignoring the 1-year extreme gust in the design of the main spar could possibly lead to failure when being subjected to the 1-year extreme gust. A literature survey showed that the 1-year extreme gust has not previously been included in the design of the main spar (E. Lund et al., 2005, J.Jensen et al., 2005 and L. Kühlmeier, 2006).

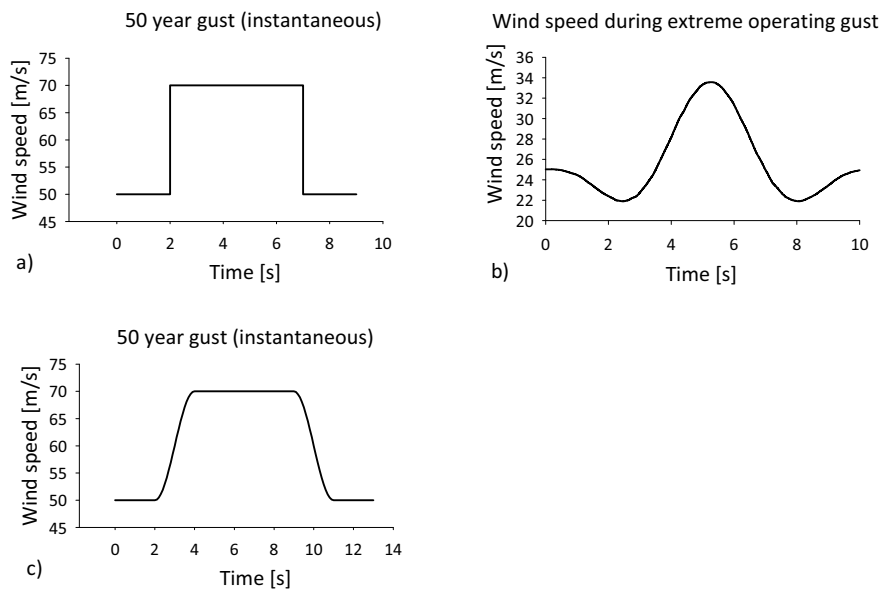


**Figure 4-4** a) Wind speed during 50-year gust. b) Wind speed during extreme operating gust for a wind turbine. c) A more realistic shape of the wind speeds during the 50-year gust.

In the FEM analysis presented in Chapter 8, the following two load cases are therefore used for the design of the main spar (Figure 4-5):

- *Primary load case*  
Wind turbine blade is struck by the 50-year extreme gust ( $70 \text{ m/s}$ ) bending it towards the tower. Suction side of blade is in compression and pressure side in tension.
- *Secondary load case*  
Wind turbine blade is struck by the 1-year extreme gust ( $52.5 \text{ m/s}$ ) in the opposite direction of the primary load case. Suction side is now in tension and pressure side in compression.

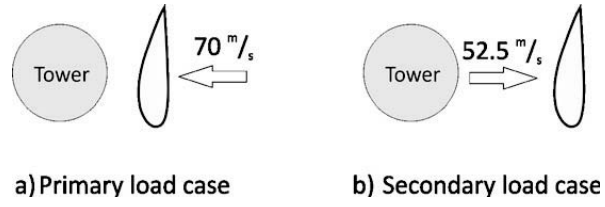


Figure 4-5 Load cases for FEM simulation of 100 m main spar

## 5 Wind turbine design criteria

When designing a wind turbine blade a wide range of criteria have to be met. The IEC 61400-1-2005 standard focuses on criteria regarding the entire wind turbine system. Tower clearance and load cases are specified, but criteria regarding materials are only briefly mentioned. The DNV-OS-J102-2006 standard focuses on criteria for composite materials used in a blade (ply failure, buckling, fatigue, etc) and is therefore used in this thesis.

### 5.1 Material safety factors

To account for the inherent variability in the characteristic material properties one needs to use material safety and strength reduction factors. The safety factors take into account the variability and assumes a certain annual probability of failure. The strength reduction factors take into account the weakening or non-statistical uncertainties in the materials. When compared to traditional metallic structures, the variation and environmental effects on the material characteristic strength can be quite significant for a composite material. This variation is mainly due to:

- variability in the constituent materials
- variability in the manufacturing process
- environmental effects such as temperature and moisture
- effects of cyclic loading
- local laminate details such as ply drops

To take these effects into account the material safety factor is a product of material safety factor and several partial strength reduction factors that take the above listed effects into account. The value of these partial safety factors can be determined by a dedicated test program. If such a test program has not been conducted one can use empirical values for the partial material safety factors as specified in DNV-OS-J102-2006. The partial material safety and strength reduction factors used in this thesis are:

$\gamma_{m1} = 1.3$  Base material factor

$\gamma_{m3} = 1.1$  Strength reduction factor for repeated loading/low cycle fatigue

$\gamma_{m4} = 1.1$  Strength reduction factor for size effects, temperature, ageing and degradation for UV radiation and humidity. Selected for epoxy resin system

$\gamma_{m5} = 1.1$  Strength reduction factor for effects of optional materials and manufacturing methods. Selected for prepreg or resin infusion with mainly unidirectional plies including ply drops

$\gamma_{m6} = 1.0$  Strength reduction factor for post curing with temperature control

The material safety factor ( $\gamma_m$ ) for stresses and strains then equates to:

$$\gamma_m = \gamma_{m1} \cdot \gamma_{m3} \cdot \gamma_{m4} \cdot \gamma_{m5} \cdot \gamma_{m6} = 1.73 \quad (5-1)$$

## 5.2 Composite failure criteria

Failure criteria for homogenous isotropic materials are well established (e.g. von Mises and Tresca criteria). Macro mechanical failure theories for composites have been developed by extending and adapting the isotropic failure theories in order to account for the anisotropy in stiffness and strength of the composite. In the recent years over 40 such failure theories have been developed for composites (I. M. Daniel et al., 1994). Almost all of these assume homogeneity and linear stress-strain behavior to failure. Some criteria account for interaction of stress components, while others do not. The criteria that do account for stress interaction often require additional strength parameters obtained from biaxial testing. Of all the failure criteria the following four ply failure criteria are the most widely used for composites:

1. Maximum stress criterion
2. Maximum strain criterion
3. Tsai-Hill criterion (deviatoric strain energy theory for anisotropic materials)
4. Tsai-Wu criterion (Interactive tensor polynomial theory)

The maximum stress and maximum strain criteria treat the stresses or strains in fiber direction and transverse to the fibers separately, i.e. they do not take into account interaction of the stress/strain components. Shear stress/strains are also treated separately. The difference between the two criteria is mainly caused by Poisson's effect coupling stress and strain. Since the strain to failure is independent of the fiber fraction while the strength is not, the maximum strain criterion is often easier to use. Both criteria are simple to use for describing fiber failure. The maximum stress criterion requires only tensile and compressive ply strength in fiber direction. Similarly, the maximum strain criterion requires ply strains at failure in fiber direction in tension and compression. The maximum stress or strain criteria can theoretically also be used to predict matrix failure. However, for this failure mechanisms the interaction of the various stress/strain components is important and other interactive failure criteria are recommended to be used (DNV-OS-C501-2003). Matrix cracking was not studied here in detail, so these criteria were not applied.

The Tsai-Hill and Tsai-Wu account for a much larger degree of stress interaction in the composite ply. One drawback with these two failure criteria is that they require numerous parameters to be determined by testing. In many cases the results from biaxial testing are not readily available for the relevant composite material. The main disadvantage though is that they do not distinguish between the failure mechanisms in the ply, fiber failure and matrix cracking are treated in the same way. These criteria can be used fairly well for predicting matrix failure.

The DNV wind turbine standard (DNV-OS-J102-2006) recommends using the maximum strain criterion to check against fiber failure. Other design criteria may be used if it is demonstrated that they are equivalent to or conservative relative to the maximum strain criterion. Figure 5-1 shows how the stiffness of a laminate containing 0°, 45° and 90° plies is reduced as a result of matrix cracking during tensile loading.  $E_{lin}$  is the initial stiffness modulus of the laminate and  $E_{nonlin}$  is the stiffness modulus for the laminate with matrix cracks. In order to account for this change in E-modulus, the FEM analysis needs to use a degradation model for the composite. If a degradation model is not included, using the maximum strain criterion will result in unrealistically high stress predictions. In this case a partial analysis factor should be used:

$$\gamma_A = E_{lin}/E_{nonlin} \quad (5-2)$$

The introduction of the partial analysis factor ( $\gamma_A$ ) can be thought of as a reduction of the effective strain to failure from  $\epsilon_{fail}$  to  $\epsilon_{corr}$ . In practice this alters the maximum strain criterion to a maximum stress criterion. The FEM analyses in this thesis do not employ a degradation model for the composite and therefore the maximum stress criterion has been used.

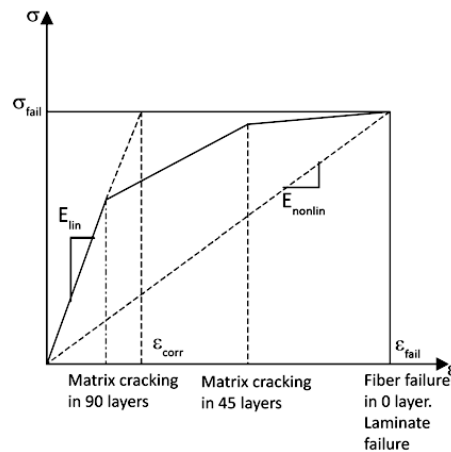


**Figure 5-1** Typical stress-strain relationship in laminate containing 0°, ±45° and 90° laminates.  $\epsilon_{corr}$  is the corrected failure strain for the 0° ply. This value is to be used in the maximum strain criterion if the analysis method does not account for ply degradation (reproduced from DNV-OS-J102-2006 standard).

### 5.3 Buckling analysis of wind turbine spar

Being the main load carrying structure of the blade, the main spar cannot be allowed to buckle when subjected to the ultimate design loads. Neither global nor local buckling of the spar is allowed and should be checked for. In this thesis both linear eigenvalue buckling and non-linear buckling analysis have been used to evaluate the structure. Linear eigenvalue analysis has the advantage of being very fast and easy to interpret (Figure 5-2). The FEM analysis calculates both the buckling loads and mode shapes. But a linear eigenvalue buckling analysis fails to include effects such as geometric and material non-

linearity. For structures experiencing large deflections, the exclusion of these effects can cause the linear analysis to overestimate the buckling load. A discussion of this is presented in section 8.7.1. A non-linear buckling analysis increases the load in small increments and for each increment calculates the change in geometry. This is a much more realistic analysis of the structure and shows how the structure fails. The drawback is that it takes a lot more computational resources compared to a linear analysis. A linear eigenvalue buckling analysis of the spar would take approximately 10 minutes whilst a non-linear buckling analysis needed approximately 3-5 hours. In this thesis both linear and non-linear buckling analysis was used in the design phase of the 100 m main spar. Further information about how non-linear analyses are performed in Abaqus is presented in section 8.6.

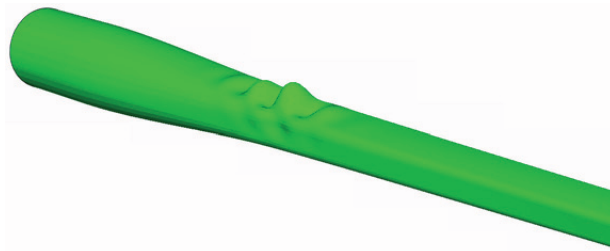


**Figure 5-2** Representative shape of the first linear eigenvalue buckling mode of a main spar.

The elastic buckling phenomena is commonly divided into two categories: bifurcation buckling and limit point buckling (DNV-OS-C501-2003). In bifurcation buckling the applied load at first results in deformations that are predominantly axial or in-plane. At a critical value, a new mode of deformation, which includes bending, is initiated. This critical load is commonly described as the “buckling load”. The DNV-OS-C501-2003 standard uses the term “elastic critical load” to describe this critical load. In this thesis the commonly used term “buckling load” has been adopted. Figure 5-3 illustrates three different post-buckling behaviors that are observed after reaching the buckling load. Deformations may develop in an unstable and uncontrolled way without any increase in load until failure (Figure 5-3a). This behavior is often described as a brittle type of failure. The post-buckling behavior can also be described as a plastic type of failure where the deformations grow with little or no increase in load, also known as neutral post-buckling behavior (Figure 5-3b). The third post-buckling behavior associated with bifurcation buckling is ductile failure. A new equilibrium state is found and the deformations are again able to develop gradually and in a controlled manner as the load is increased (Figure 5-3c).

In limit point buckling the structure becomes less stiff as the applied load is increased, i.e. one does not see the linear relationship between load and deformations as with bifurcation buckling (Figure 5-4). In limit point buckling the relationship between load and deformation reaches a smooth maximum (buckling load) at which the deformations increase in an uncontrolled way (brittle type of failure).



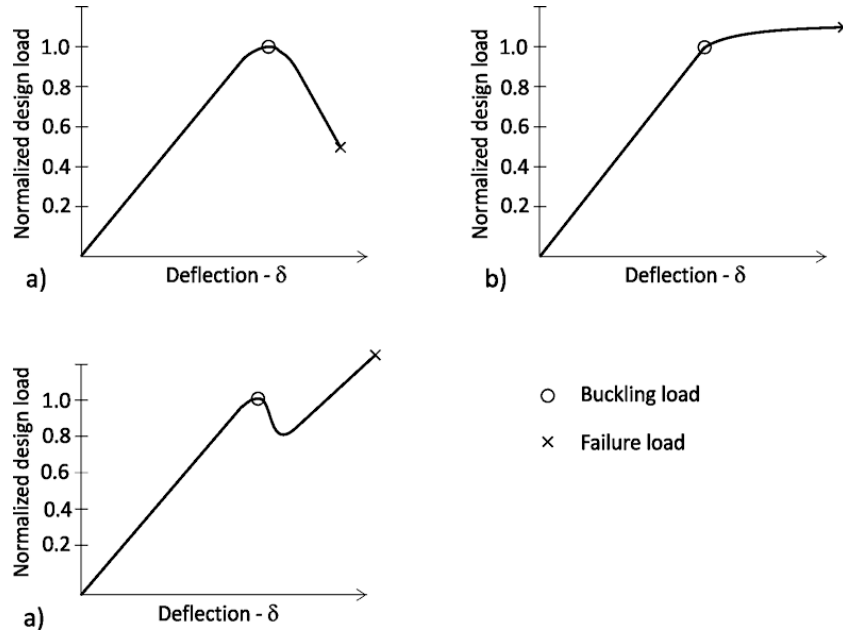


**Figure 5-3** Failure modes by bifurcation buckling. a) Unstable or brittle post-buckling behavior. b) Neutral post-buckling behavior (plastic failure). c) Stable post-buckling behavior (ductile failure).

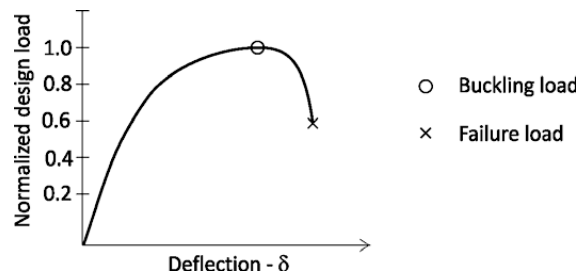


**Figure 5-4** Limit point buckling. Structure becomes less stiff with increased load and reaches a smooth maximum at which the deformations increase in an uncontrolled way.

Bifurcation buckling is mainly a feature of geometrically perfect structures. In such structures the applied load has no eccentricity and the geometry does not have any flaws such as out-of-straightness or out-of-roundness. Such an idealized structure is referred to as “geometrically perfect” and is often what one would have in a FEM analysis. In reality a structure will always have some imperfection and this leads to a situation where the compressive forces in the structure are not coincident with the neutral axis. Depending on the imperfection size, it can significantly influence the buckling behavior of the structure. The imperfection will destroy the bifurcation and cause the bending deformation to grow as the load is increased from zero, essentially chang-

ing the buckling behavior to limit point buckling. Also, structures with unstable post-buckling behavior can be highly sensitive to geometric imperfections. Such structures may experience a limit point buckling load that is significantly lower than the buckling load of a geometrically perfect structure.

In the FEM analysis presented in Chapter 8 the buckling load is defined to be the load where the structure experiences material failure according to the selected failure criterion. It should be noted that in all FEM analysis in this thesis, non-degraded linear material properties were used. This is further discussed in section 8.11. When buckling occurred near the root section of the blade, bifurcation buckling with unstable post-buckling behavior was often observed. But, when buckling occurred closer to the spar tip, limit point buckling behavior was more common. In this case it would be difficult to determine the exact buckling load. According to DNV standard DNV-OS-J102-2006 the local stresses are to be checked against the design criteria (fiber failure, matrix cracking, delamination) on a ply level. Deformations caused by the local buckling causes stresses and strains to rise and eventually violate the design criteria (Figure 5-5). During the buckling analysis, the Abaqus FEM software normalizes the applied design load. Results from both the linear and non-linear buckling analyses are given as ratios of the design load. If the structure is said to buckle at for example 0.6, it has reached 60% of the applied load case.

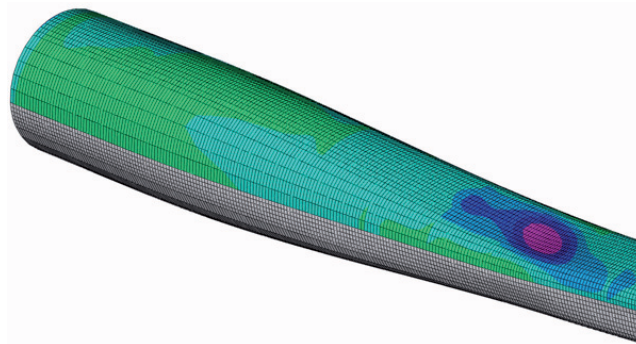


**Figure 5-5** Buckling load is defined as the load where ply stresses (checked on ply level) are above the design criteria for stresses (purple area).

Figure 5-6 shows the fiber stress at one node for a glass fiber  $\pm 45^\circ$  ply and a carbon fiber UD ply during a non-linear analysis. One can clearly see how the stress in the UD ply increases linearly whilst the stress in the  $\pm 45^\circ$  ply has a non-linear progress. In this case the buckling load will be defined when the carbon fiber UD ply reaches maximum compression stress at -555 MPa, corresponding to a buckling load of 1.12. In this analysis the stresses in the  $\pm 45^\circ$  ply increase rapidly and one can observe how the stress in the UD ply suddenly drops, caused by the flange buckling inwards. For a more realistic post-buckling analysis one needs to include a degradation model that takes into account when plies reach their maximum strength and thereby fail. A degradation model of material properties is not included in these studies since detailed post-buckling analysis is not within the scope of this work.

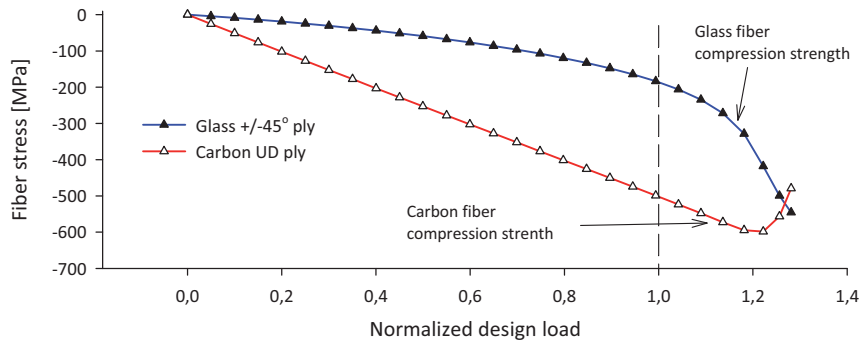


**Figure 5-6** Fiber stress in a UD carbon and  $\pm 45^\circ$  glass fiber ply for a node in the buckling region during a non-linear analysis.

### 5.4 Wrinkling of sandwich structures

Sandwich structures have additional failure mechanisms due to the interaction between the laminate and the core material (DNV-OS-C501-2003). The combination of stiff skins on a soft and lightweight core can fail in a local form of buckling where the support of the core is insufficient to stabilize the face sheets (Figure 5-7). This failure mode is often referred to as wrinkling. Most engineers use the formula derived by Hoff et al. (1945) when designing a sandwich structure against wrinkling failure. The critical face sheet stress at wrinkling is according to Hoff:

$$\sigma_{Hoff} = 0,5\sqrt[3]{E_f E_c G_c} \tag{5-3}$$

where  $E_f$  is the face sheet modulus and  $E_c$  and  $G_c$  are the core's E-modulus and shear modulus. The formula has been used in this thesis for the design against wrinkling failure because it is a conservative estimate and has been found to agree well with tests. Recent work in the field of wrinkling failure can be found in L. Fagerberg (2003) handling the effects of local bending stiffness, face sheet anisotropy, multi-axial loading and imperfection on wrinkling of sandwich panels.



**Figure 5-7** Wrinkling of sandwich structure (reproduced from DNV-OS-C501-2003).

### 5.5 Tower clearance

One of the most important criterion a blade has to comply with is that there should be no mechanical interference between the blade and the tower. It is crucial that the blade under no circumstances will hit the tower, since this most likely will result in catastrophic failure of the rotor blades and possibly of the entire wind turbine. When comparing the available tower clearance and maximum tip deflection, a minimum clearance must be met. The DNV standard DNV-OS-J102-2006 and the international standard IEC 61400-1-2005 take into account a variety of safety factors for loads, materials and consequence of failure.

$$D_d(\gamma_f F_k) \leq \frac{D_i}{\gamma_n \gamma_m} \quad (5-4)$$

$F_k$ :	Characteristic load
$D_d$ :	Largest tip deflection when passing tower
$D_i$ :	Smallest distance from blade tip to tower or other obstacles in the unloaded condition
$\gamma_f = 1.35$	Load factor
$\gamma_m = 1.1$	Material factor for stiffness. This can be reduced to 1.0 if the deflection analysis is carefully calibrated with a full scale static testing of the blade
$\gamma_n = 1.0$	Consequence of failure factor

The load case evaluated in this thesis is when the blade is struck by the 50-year gust ( $70 \text{ m/s}$ ), causing a flapwise bending of the blade towards the tower. The IEC61400-1-2005 standard does not specifically mention this load case, but it states:

“The maximum elastic deflection in the unfavorable direction shall be determined for the load cases in Table 2 using the characteristic loads.”

According to this table, which specifies the different design load cases (DLC), it is the case DLC 6.2 which would be the most critical. During the 50-year storm a loss of the electrical power network is assumed, disabling the yaw system. If there is no back-up power for the yaw system, one has to evaluate a change of wind direction up to  $\pm 180^\circ$ . Depending on how the blade is pitched relative to the plane of rotation, the blade is either free to deflect or could strike the tower (Figure 5-8).

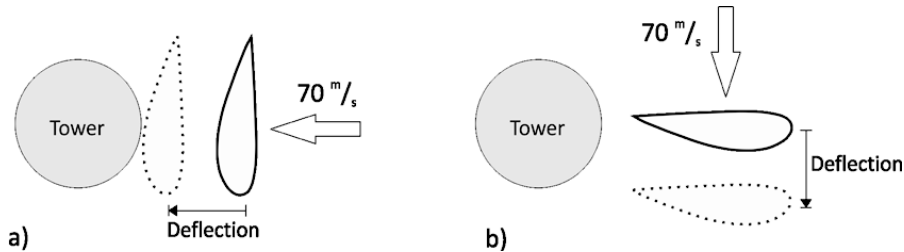


**Figure 5-8** Blade deflection when hit by the 50-year gust ( $70 \text{ m/s}$ ). Depending on the blade pitch it is either in danger of striking the tower (a) or free to deflect (b).

The standard does not discuss the pitch of the blade. As Figure 5-8 shows the blade can be pitched such that it would not strike the tower during the 50-year storm. In other available literature (J. Jensen et al., 2005 and O. T. Thomsen, 2006) it is assumed that the blade is pitched such that it could strike the tower. This is the absolute worst case scenario, assuming that control over yaw and pitch is lost due to either mechanical or electrical failure. The finite element analysis presented later will focus on this load case.

Figure 5-9a shows a wind turbine with straight rotor blades and a horizontal rotor axis. It can be seen that the rotor blades are close to the tower, leaving little room for deflection of the blades. Figure 5-9b shows how the rotor plane can be tilted to increase the tower clearance. A tilt angle of about  $5^\circ$  between rotor axis and the horizontal plane is common (Jensen, 2005).

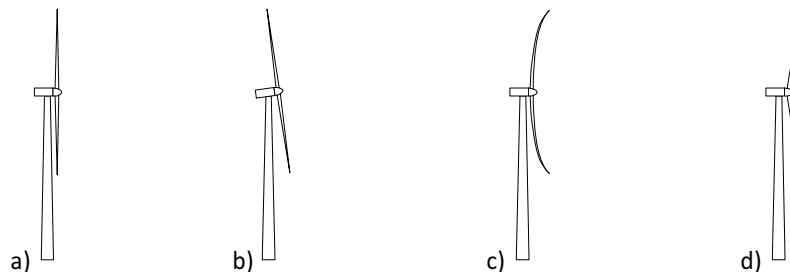


**Figure 5-9** a) Wind turbine without tilted or pre-bent rotor. b) Tilted rotor plane. c) Blade with pre-bending. d) Coned rotor.

Often blades will reach maximum allowable deflection long before the blade has reached its design limit of maximum allowable stress. By pre-bending the blades at production, it is possible to design the blades closer to maximum allowable stress (Figure 5-9c) (LM, 2002). Ideally, maximum allowable stress is reached at the same time when maximum allowable deflection is reached. For large blades this pre-bending increases gradually along the blade, typically resulting in 1.5 m pre-bending for a 50 m long blade.

Another technique is to cone the blades at a certain angle, thereby allowing the blades to deflect more (Figure 5-9d). This is very much the same as pre-bending, but the blades are bent at the root rather than gradually. A cone angle of  $3^\circ$  is common (Jensen, 2005).

For the 100 m blade analysis the tower diameter is assumed to be 6 m at the tip height and the distance between the tower center and hub center is also 6 m. The blade's plane of rotation is tilted  $5^\circ$  and a coning angle of  $3^\circ$  is used (J. F. Jensen et al., 2005, analysis of 90 m wind turbine blade). In an unloaded situation the distance between the tower and blade tip is:

$$D_i = (100\text{ m} \times \sin 8^\circ) + 6\text{ m} - \left(\frac{6\text{ m}}{2}\right) = 16.9\text{ m} \quad (5-5)$$

The maximum deflection for the blade is then:

$$D_d(1.35) = \frac{D_i}{1.1 \times 1.0} = 15.4\text{ m} \quad (5-6)$$

## 6 Composite manufacturing methods

The energy crisis in the early 1970s triggered small companies and grass-root organizations to start building wind turbines for energy production. Financial support from the Danish government encouraged utility companies to take up the challenge and develop larger wind turbines (M. Hansen, 2000). As the blades grew in size and larger numbers were produced, new manufacturing technologies were developed and implemented by the blade manufactures. Also, concerns about the working environment helped change the manufacturing method from the traditional wet and open mold process to prepreg technology and closed mold infusion techniques. The development of a 100 m long wind turbine blade will require composites with a higher performance and quality in order to reduce cost and weight. As the material properties of a composite are highly dependent on the manufacturing method used, a detailed and thorough understanding of the process parameters will be essential.

### 6.1 Wet hand lay-up

In the beginning, the manufacturing of glass fiber wind turbine blades was based on experience from GRP (Glass fiber Reinforced Plastic) boat building. The traditional wet hand lay-up technique was used in open molds where mainly chopped strand mats, with random fiber orientation were used. For increased strength and stiffness, woven fabrics, were sometimes added. The resin was applied by hand for each layer, using brushes and rollers (Figure 6-1).

After curing, the upper and lower shells were bonded together to form the airfoil shape of the blade. As the blades got longer (approaching 8 m), webs were inserted to support the airfoil, taking up bending and shear loads. The increasing length of the blades demanded higher stiffness and strength, introducing a more dedicated fiber orientation with increasing amount of fibers in the longitudinal direction of the blade. This was achieved either by using unidirectional fabrics or by laying down many parallel rovings<sup>1</sup> in the length direction of the blade between the chopped strand mats.

One worrisome drawback of this production method is personnel exposure to the resin, which can trigger serious allergic reactions. Expensive ventilation systems have to be built to limit airborne concentrations to legislative levels. Another main disadvantage is that the laminate quality is very dependent on the skill of the operator. Avoiding entrapped air in the laminate is difficult and typically a fiber volume fraction of only 35 % is achieved (DNV-OS-C501-2003).

---

1. Roving: long and narrow bundle of fiber.

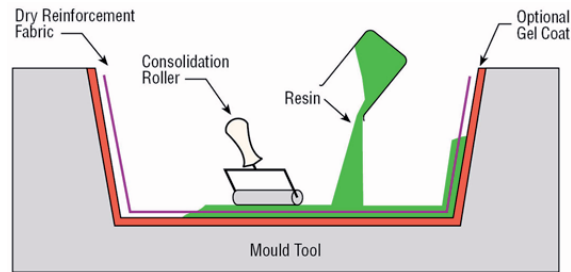


Figure 6-1 Concept of wet hand-lay-up (SP Systems, 2001.).

## 6.2 Filament winding

Support from the Danish government in the mid 1970s accelerated the development of wind turbines. Companies involved soon looked for a more rational way of manufacturing the blades, since the hand lay-up technique is very labor intensive and the laminate quality depends a lot on personnel skills. Filament winding is a rational way of placing high amounts of fibers in a controlled manner around a rotating concave shaped mandrel (Figure 6-2). But since the majority of the fibers have to be placed in the length direction, new techniques had to be developed.

Filament winding a wind turbine blade is a difficult challenge and can be solved in several ways. One can choose to make the spar and airfoils separately or the entire blade at once. Kaman Aerospace Corporation and Structural Composites Industries in the United States developed a technique for producing the whole blade. Three mandrels were used to build the airfoil with integrated shear webs. The first mandrel was used to wind the leading edge and forward shear web. A second mandrel was attached to the already wound leading edge structure to form the second shear web. Finally the third mandrel was attached and material wound to create the trailing edge. A big challenge for the filament winding technique is that as the blade length increases, it becomes difficult to build mandrels that are stiff enough to carry the weight of the blade without excessive deformation.

As mentioned, the majority of the fibers in a blade have to be placed in a longitudinal direction in order to achieve sufficient bending stiffness and strength. To achieve this, a special tape was developed where most of the fibers were placed in the transverse direction of the tape (Figure 6-3). In the late 1970's Risø National Laboratory and the Vølund company used tape for winding the spar of the Nibe wind turbines. The tape consisted of woven glass fiber with 90 % of the fibers in the transverse direction. The 20 cm wide tape was wound around the spar mandrel with an overlap of half the width of the tape. Because the spar was tapered towards the tip-end and the warp of the glass fibers could not stretch, it was necessary to insert and withdraw a wedge under the tape at the shear web position of the spar for each revolution in order to control and maintain straight fibers.



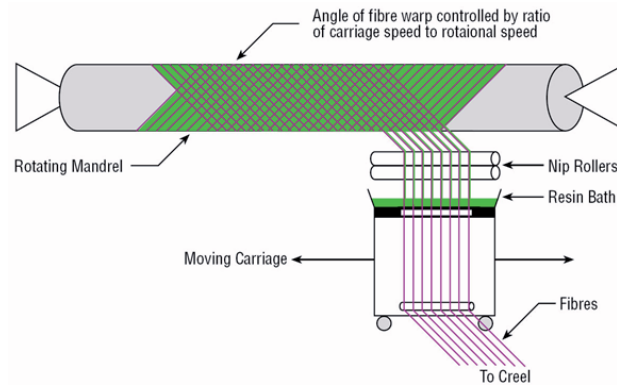


Figure 6-2 Concept of filament winding (SP Systems, 2001).

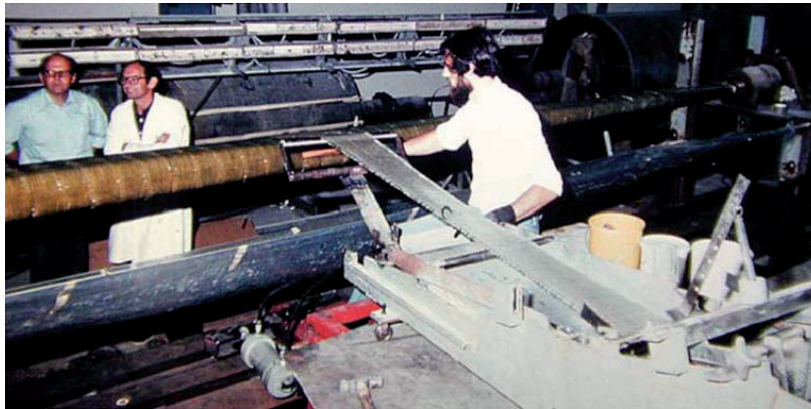


Figure 6-3 Filament winding at Risø using glass fiber tape (P. Brøndsted, 2005)

### 6.3 Prepreg technology

Prepreg technology has been adapted from aerospace technology to be used in building wind turbine blades. Prepreg is a semi-raw product where the fibers are impregnated with pre-catalyzed and B-staged (partially cured) resin. At room temperature the resin is like a tacky solid and sheets of prepreg can be stacked on top of each other to build a laminate. Prepreg is available in a variety of different combinations of fibers and resin, with processing and curing temperatures ranging from 70 to 225 °C. In order to keep process and equipment costs down, a processing temperature of 80 °C is often used for wind turbine blades. The prepreg laminate is covered by a polymer film and sealed along the edge of the mold (Figure 6-4). A vacuum is applied under the polymer film (vacuum bag) and the atmospheric pressure thereby compresses the vacuum bag and

prepreg layers towards the mold surface. The mold is placed in an oven, allowing the resin to become viscous and cure (Figure 6-5a). Even though the catalyst in the resin is largely latent at ambient temperatures, the shelf life for prepreg range from a few days to weeks, depending on the resin used. But by storing the prepreg at  $-18\text{ }^{\circ}\text{C}$ , shelf life can be extended up to 12 months.

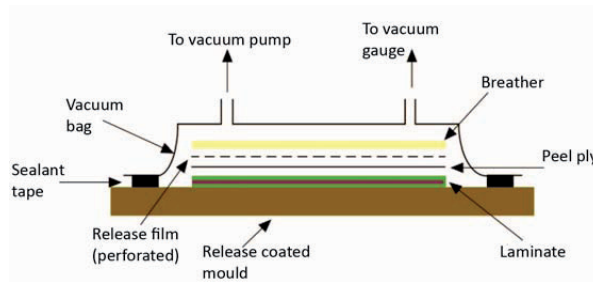


Figure 6-4 Vacuum consolidation of prepreg (SP Systems, 2001).

With prepreg there are several advantages. The fiber resin content and catalyst levels are accurately set by the prepreg manufacturer, making it easy to obtain a high fiber volume fraction. A higher fiber content results in higher specific stiffness and strength for the material, which in turn leads to lighter wind turbine blades. In an autoclave the temperature can be precisely controlled, providing optimal curing temperatures (Figure 6-5b). Also the pressure within the autoclave can be raised up to 7 atmospheres, providing a high compaction pressure. Prepreg cured within an autoclave gives the highest fiber volume fraction (up to 70 %) and a very low void content (below 1 %). Unfortunately the costs of making an autoclave that would fit a wind turbine blade or a spar are so high that it prevents many manufactures from using it.

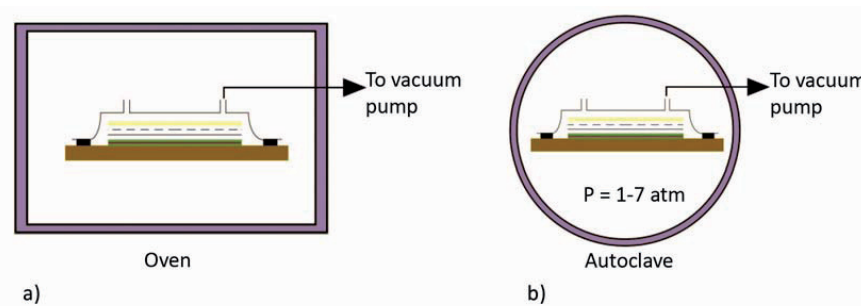


Figure 6-5 a) Consolidation of low temperature prepreg using only vacuum and an oven (SP Systems, 2001). b) Autoclave for consolidating of laminates (SP Systems, 2001).

One important disadvantage of prepreg is its very high cost and explains why it is mostly used by aero and space industry. It has found limited use in the wind turbine blade industry. To the author's knowledge, Vestas Wind Systems is the only wind turbine blade manufacturer using prepreg.

## 6.4 Resin infusion technology

This technology is known by different names and several variations of this process have been developed. The principle is to place dry fibers in a mold, encapsulate and seal off the fiber package (second mold tool or polymer film), inject liquid resin into the mold and let the component cure. This technology was developed in the 1950s, but was not adopted by the wind turbine industry before 1990s. The fibers, resins, equipment and the process have been intensively developed and resin infusion is now a widely used technology for producing composites.

The most important issue of this technology is making sure that all the fibers have been properly wetted. In the finished product there should be no areas with dry fibers, which would compromise its mechanical properties. Most developments of the resin infusion process have focused on this issue and several solutions have been developed:

- Fiber sizing with improved wettability to facilitate complete wetting without manipulating the rovings
- Fiber fabrics with special architecture to control flow pattern of the resin
- Resin with lower viscosity (at room or moderate temperature) to improve wettability and lower process time for larger components
- Resin that does not release volatiles under vacuum. Volatiles will create voids in the finished composite
- Accessories that help control resin flow pattern over large areas and ensure complete wetting of thick laminates (resin distribution mesh, special sandwich core, etc.)
- Equipment for continuous mixing of resin without introducing air
- Design of molds (placement of inlet and outlet for resin, sealing around the edge) to control resin flow to prevent entrapped area with dry fibers. Also heating and temperature control systems are incorporated into the mold to allow control of the cure temperature
- Sensors for monitoring the flow front
- Computer models for predicting and optimizing the flow pattern for a given component

The benefit of resin infusion technology, compared to wet hand lay-up, is that high fiber volumes of 50-60 % are obtained with a very low void content of 2 %. Another benefit is the increased safety and reduced exposure to resin for personnel, as the resin is enclosed in the mold, preventing fumes to fill the production facility. But when compared to prepreg materials, composites made by resin infusion have slightly lower properties. Whilst prepreg composites can achieve up to 70 % fiber volume fraction, resin infusion composites commonly achieve 50-55 %. The most important difference is that infused carbon fiber UD fabrics have a 30-40 % knockdown in compressive strength compared to carbon fiber prepreg. This is believed to be due to fiber waviness introduced by the stitching process of the fabrics and fiber wash-out from the resin as it flows through the laminate during an infusion process.

#### 6.4.1 Vacuum Assisted Resin Transfer Method (VARTM)

In a VARTM process the reinforcing fabrics are laid up dry in the mould as a preform. The mold and preform are then covered with a vacuum bag and air is removed from the preform with a vacuum pump (Figure 6-6). The preform will then be compacted by the atmospheric pressure acting on it. Once vacuum has been established in the preform, the resin is allowed to flow into the mould and impregnate the fibers. After a complete wet-out, the resin inlet is closed and the part set to cure. This can be done at either ambient temperature or in a oven at elevated temperatures for faster curing. In the case of wind turbine blades, a tent is often pulled over the newly infused blade and hot air is pumped into it in order to cure the blade at elevated temperatures. To prevent excess resin to reach the vacuum pump, a resin trap is used to collect resin that exits through the vacuum port. One of the great benefits with this process is that the working environment is drastically improved by it being a closed moulding process. Workers are not exposed to resin fumes (like during the wet hand lay-up process) and can work in a short-sleeve environment. A closed molding process eliminates the need for a high capacity and expensive ventilation system. The resin infusion method allows large components (wing turbine blades, boat hulls, etc.) to be infused rapidly and the need for only a single-sided mold reduces tooling costs and other capital investments (Figure 6-7). For wind turbine blades, the two airfoils and the shear webs are often manufactured separately and all the parts are adhesively bonded together to form a complete blade after the parts have been cured.

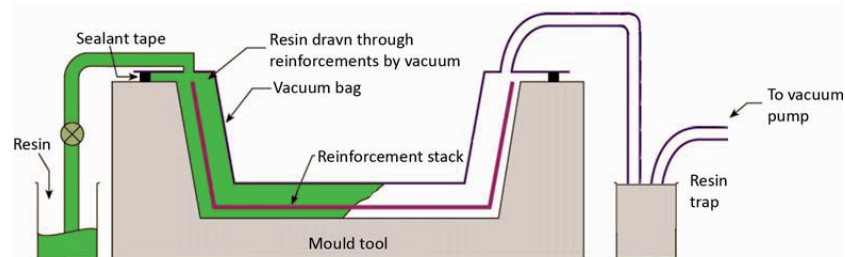


Figure 6-6 Concept of vacuum infusion (based on SP Systems, 2001).

In large structures, numerous resin inlets and vacuum parts are required for a successful infusion. The flow front can become quite complex and highly dependant on the sequence that inlets are opened. Large structures and complicated parts will often require the use of flow simulation tools in order to plan the placements of inlets. In theory, once the part is under full vacuum, one should only need to open the resin valve and let the resin fill the preform. In reality there will always be some air left in the preform, and it is very important to keep this in mind. As the flow front advances through the part, it pushes the remaining air in front of it. The vacuum ports should always be the last area where the resin arrives. Failing in doing so can create dry spots, where residual air is accumulated. This can happen if the vacuum ports are misplaced or if for example two flow fronts meet, trapping air between them with no place to escape. One solution to this situation is to penetrate the vacuum bag and perform a local extraction

of air, but any penetration of the vacuum bag during the process brings great risk of air entering the preform and rendering the entire part useless.



**Figure 6-7** Resin infusion of wind turbine blade (www.stanford.edu)

Highly important factors in the process are the permeability of the fiber and viscosity of the resin. For an infusion process the resin viscosity should be below 200 cP for it to be of practical use. A high viscosity resin (for example 600 cP) will flow slowly through the preform, creating too long processing times and a risk of resin cure before complete wet-through. Compaction of the fibers by the atmospheric pressure acting on the evacuated preform, drastically reduces the permeability of the fibers. Fiber permeability also depends on the fiber mat type (UD,  $\pm 45^\circ$ , chop) and direction of the flow front relative to the fiber direction. A unidirectional glass fiber fabric can be infused approximately 50 cm, whilst infusing perpendicular to the fibers will result in short infusion lengths of approximately 15-20 cm.

Simple estimations of the infusion time can be done by 1-D calculations using Darcy's law (eq. 6-1). It describes the flow of a fluid through a porous material and it was originally used to study water flowing through sand, but has since been adopted for describing resin flow. For complex parts with varying laminate thickness and fiber direction, flow simulations have to be done using Darcy's law in 2D and 3D. One such commercial software available is Polyworks, which has been successfully used by Umoe Mandal AS in the development of the new composite missile torpedo boat KNM Skjold (Polyworks website).

$$Q = \frac{-\kappa A (\Delta P)}{\mu L} \quad (6-1)$$

Q: Volume flow [m <sup>3</sup> /s]	$\kappa$ : Fiber permeability [m <sup>2</sup> ]
A: Cross sectional area to flow [m <sup>2</sup> ]	$\mu$ : Dynamic viscosity of resin [cP] <sup>1</sup>
$\Delta P$ : Pressure drop [Pa]	L: Length where pressure drop takes place [m]

1. 1 cP = 10<sup>-3</sup> Pa·s

To aid the resin flow and increase infusion lengths, different distribution media have been developed. One is the patented SCRIMP process (Seemans Composite Resin Infusion Moulding Process) which uses a surface distribution medium (Figure 6-8). The resin distribution medium has a very high permeability and is placed on top of the preform (Figure 6-9). The resin will first travel throughout the distribution medium and subsequently travel through the preform thickness. After cure the distribution medium is removed together with the peel-ply.

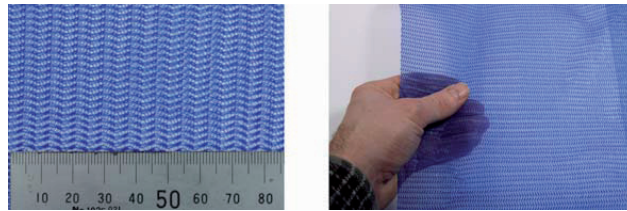


**Figure 6-8** Distribution medium manufactured by Aerovac.

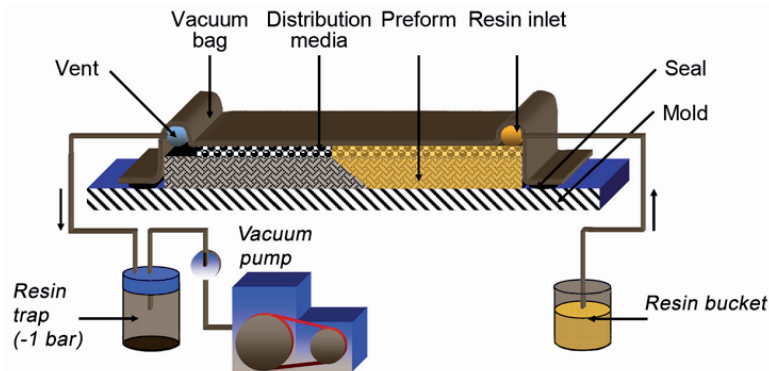


**Figure 6-9** SCRIMP infusion process using a distribution medium on top of the preform (based on Hughes,2005).

Another option is to use interlaminar distribution mediums like Coldbond's CFM (Continuous Filament Mat) glass fiber mat (Figure 6-10a). This mat is very similar to a chop strand mat, but is made of continuous fibers and with less density. It is placed within the laminate and compresses very little under vacuum, leaving a channel for the resin to flow through. Infusion tests done by the author showed that for a 4 ply laminate consisting of  $\pm 45^\circ$  glass fiber ( $600 \text{ g/m}^2$ ), the practical infusion distance was increased from 20 cm to one meter by using a single layer of CFM in the middle. Figure 6-10b shows the cross-section of a laminate where several layers of CFM have been used.

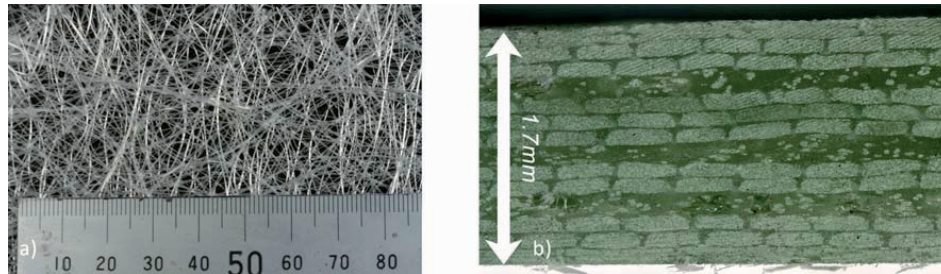


**Figure 6-10** a) CFM mat by Coldbond. b) Composite with CFM as interlaminar flow medium.

To increase the bending stiffness of a structure one can use core materials to create a sandwich structure. This will only slightly increase the weight, but will dramatically increase the laminate bending stiffness. These cores come in a variety of densities, thicknesses and finishes suitable for all kinds of composite processes. A global leader in sandwich core production, Diab, has developed a core suitable for the infusion process. To aid resin transport a grid pattern is milled on the core surface. These tracks are 2 mm wide and deep with 20 mm between tracks. The core thereby acts as a distribution medium by itself and eliminates the need of a surface distribution medium. Also, a regular pattern of holes penetrate the core, supplying the laminate on the backside with resin (Figure 6-11b).

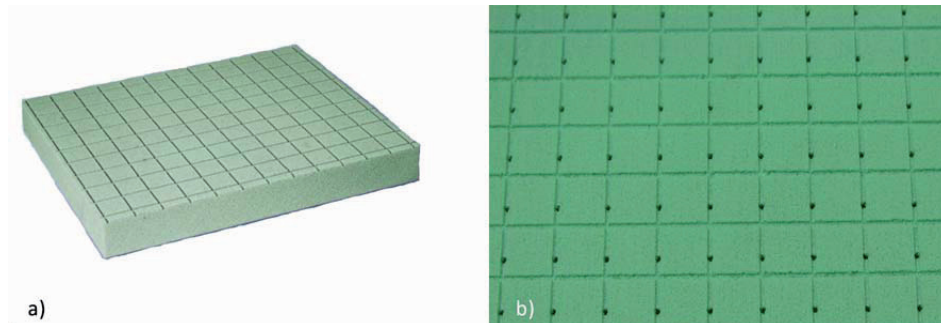


**Figure 6-11** a) Picture of Diab Core with resin tracks. b) Holes at resin track intersection.

The void content of a VARTM can be as low as 1.07 % (C. J. Hughes, 2005), but this is still above the levels of prepreg cured in an autoclave. An important factor in reaching low levels of voids is the degassing of resin before infusion. Mixing the resin will introduce air bubbles to the resin, when subjected to the vacuum in the preform these bubbles will grow many times in size and cause voids in the cured composite. Degassing is done by putting the resin bucket under vacuum and let the air be evacuated. Modern resin mixing equipment makes it possible to mix resin without introducing air.

Achieving the optimum fiber volume fraction in a composite can be challenging with the VARTM process. This is supported by the literature reporting inconsistent fiber volume fractions (50-56 %). In order to achieve high values of fiber volume fraction it is important to understand how the VARTM process works in detail. As mentioned earlier, the outside atmospheric pressure compresses the preform when vacuum is applied. The preform thickness can be compressed by as much as 30 %, packing the fibers tightly together. When the vacuum is removed, the preform expands again, returning to almost its original thickness. This is called fiber spring-back and plays a vital role in the fiber volume fraction in the composite. A common misconception is that the resin is sucked into the preform by the vacuum. In reality, it is the pressure difference between the resin bucket (exposed to the ambient pressure of 1 atm) and the preform (0 atm) that drives the resin into the fiber. During the VARTM process the resin separates the vacuum vent and resin inlet, causing a 1 atm pressure gradient to develop throughout the part. C. Niggemann et al. (2008) measured the pressure over the preform during infusion, confirming that a pressure gradient develops between the resin inlet and vacuum port (Figure 6-12). At the vacuum port (610 mm position) a pressure difference of almost 1 atm exists. Near the resin line (0 mm position), a pressure difference of 0.2 atm exist. The reason for this not being zero is that the resin bucket was placed approximately 1 m below the preform and caused a gravitational pressure drop.

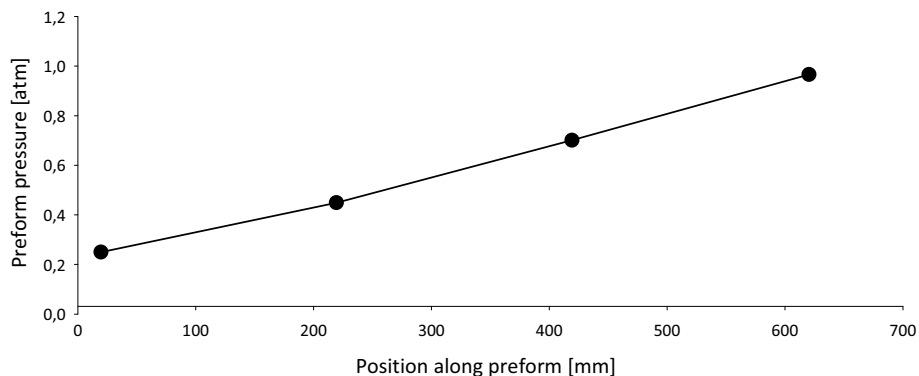


**Figure 6-12** Pressure distribution across preform directly after complete infusion (reproduced from C. Niggemann et al., 2008)

The reduced vacuum near the resin inlet results in the preform being less compacted by the outside atmosphere and allows fiber spring-back to take place. This causes a thickness gradient over there preform, with the thickest areas near the resin inlet and thinnest by the vacuum port. The fiber spring-back causes the preform volume to increase, giving more space for resin to fill and thereby lowering the fiber volume fraction. W. Li et al. (2004) used a laser scanner to measure the preform thickness before and during an infusion using the SCRIMP technology. Figure 6-13 shows that a substantial thickness gradient exists right after the infusion is complete.



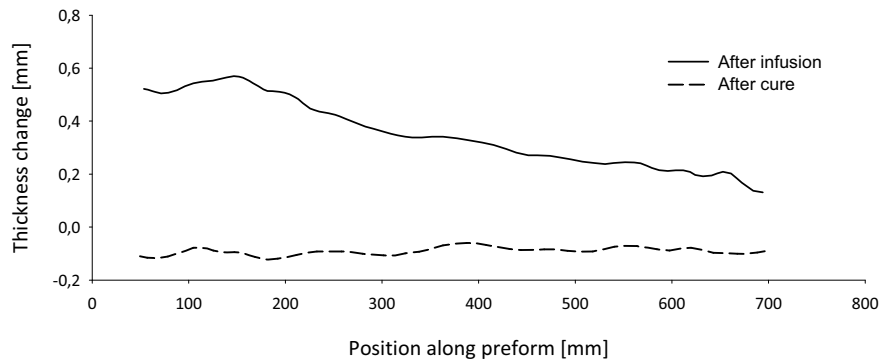


**Figure 6-13** Thickness change over the preform length after infusion and cure (reproduced from W. Li et al., 2004).

After infusion, the resin hose is closed, preventing any more resin entering the composite. If the resin cures shortly after infusion, the thickness gradients will be frozen in the part. If the resin cure is delayed for some time after the infusion, the resin will redistribute itself, reducing the pressure and thickness gradients. Figure 6-13 shows a significant reduction in thickness gradients for the cured part. Due to the pressure gradient during the infusion, it is clear that some spring-back has taken place, causing the preform to take up excessive resin. By letting the resin bleed out through the vacuum port (into the resin trap) the laminate can be further compacted, increasing fiber volume fraction. But, the time for this to take place depends on fiber permeability, resin viscosity, resin pot-life, part size and the location of the vacuum ports. The author has also experienced that excessive resin bleeding can lead to resin starved areas near the vacuum port.

With the VARTM process, fiber volume fractions of 50-53 % can be easily obtained. But getting optimal properties ( $V_f = 55-60\%$ ) is challenging due to the many factors involved. It demands skillful planning and experience.

#### 6.4.2 Vacuum Assisted Process (VAP)

The VAP method was developed and patented by EADS (European Aeronautic Defense and Space Company) in 2000 and presented a significant advance for resin infusion technology (German Patent WO 01/68353 A1). The method makes use of an air/gas permeable membrane to allow for a continuous vacuum distribution over the entire part during infusion and curing. Figure 6-14 shows the set-up of a infusion using the VAP membrane. The composite part (preform) is covered with a breather-bleeder fabric which acts like a resin distribution medium due to its high permeability. The VAP membrane then covers the composite part and is sealed against the mould. A new layer of breather-bleeder fabric is laid on top of the VAP membrane before the entire set-up is covered with a vacuum bag. The resin hose penetrates both bags and delivers resin to the inner distribution medium. The vacuum hose penetrates the vacuum bag and together with the outer breather-bleeder cloth ensures an even vacuum over the entire part. The micro porous VAP membrane allows air/gas within the preform to exit, but

acts like a barrier for the resin. After all the air is evacuated from the composite part, the resin hose is opened and resin is allowed to enter the part. In this setup the resin travels from the top towards the mold.

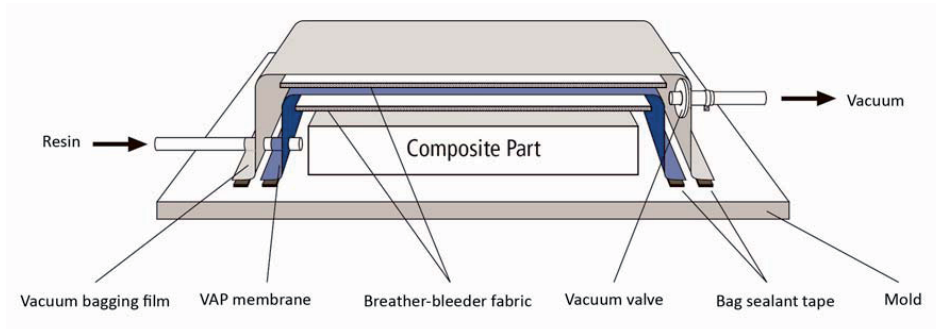


**Figure 6-14** Infusion setup using the Saertex VAP membrane ([www.saertex.de](http://www.saertex.de)).

The micro porous membrane was developed together with W. L Gore & Associates and consists of a thin sheet of PTFE (teflon) layer that is reinforced with a thin layer of nylon weave on one side (Figure 6-15a). Figure 6-15b shows a sketch of how the membrane works by allowing the air/gas to pass whilst retaining the resin. A SEM (Scanning Electron Microscope) picture of the membranes porous structure is shown in Figure 6-15c. Basically, the VAP membrane is a special edition of the fabric used to make Gore-Tex clothing.

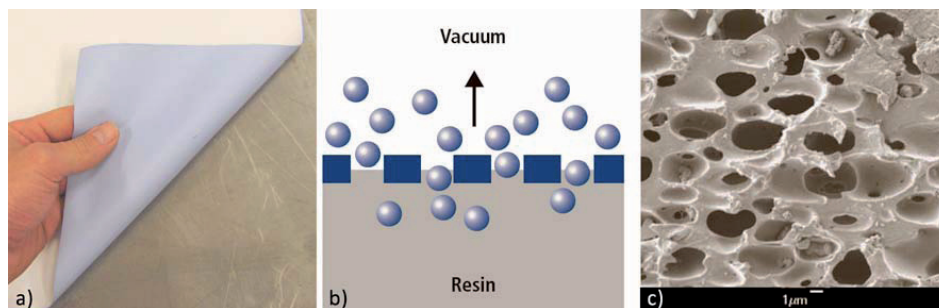


**Figure 6-15** a) The Saertex VAP membrane. White side is the PTFE membrane and light blue is the reinforcing nylon layer. b) The pores of the VAP membrane are so small that only air and gas can escape ([www.saertex.de](http://www.saertex.de)). c) SEM picture of the membrane (Hughes, C.J., 2005)

The VAP method was originally developed as a low-cost method of constructing primary aircraft structures of carbon fiber. The VAP method has also shown to give good results when using glass fiber and has gained acceptance in other industries than aero and space. In 2003, the Saertex company received a license to distribute the technology to all other areas than aero and space, such as automotive, marine and wind turbine industry.

The VAP method offers several advantages:

- An even vacuum distribution over the entire part during infusion and curing. Only one vacuum outlet is needed and a resin trap is not needed since the resin is retained by the membrane.
- The evenly distributed vacuum also results in a homogenous fibre volume fraction across the entire component cross section. This means also that the part has good dimensional tolerances with little thickness variation.
- It is a robust method since resin flow channels do not have to be planned in detail, often saving the cost of having to perform infusion flow simulations.
- The method is suitable for infusing very thick laminates. In a wind turbine blade the components can be up to 50 m long and 100 mm thick. Airbus has successfully infused a 150 mm thick carbon fiber laminate using the VAP method ([www.saertex.com](http://www.saertex.com), 2008).
- The membrane allows for continuous degassing of the component during infusion and curing. This results in a very low void content. W. Li et al. (2004) reports void content of 0.23 % (std. dev. 0.2 %), which fulfills aerospace requirement of void content below 1 %.
- When using methods like VARTM or SCRIMP, there is a risk of creating dry spots (see section 6.4.1). The VAP method more or less eliminates dry spots because of the continuous degassing over the entire part.

The VAP method also presents several challenges. The membrane prevents the user from seeing how the infusion progresses. Unless one uses a glass/acrylic mold, there is no way of seeing how the infusion is progressing. However, advances in sensors for flow and cure sensing (D. Heider, 2000) can overcome this disadvantage.

As with other VARTM processes, it seems that also for the VAP method, achieving the optimum fiber volume can be a challenge. Literature reports varying amounts of fiber volume fraction ranging from 52 % (Hughes, 2005) to 56.7 % (Saertex VAP information brochure). This variation in fiber volume fraction is most likely due to different knowledge levels in how to achieve the most optimum results from the VAP process. According to Saertex one should weigh the amount of placed fiber and calculate the exact resin amount needed to obtain desired fiber volume ratio. When the calculated amount of resin is injected into the preform, the resin inlet is closed even though the part is not completely wet-through. As the resin is set to cure, it should redistribute itself and end up evenly distributed in the finished composite part.

To gain some experience with this method the author made several test laminates of glass fiber and epoxy using the VAP membrane. The test plates consisted of 50 plies of Devold L1200 UD glass fibers measuring 300x300 mm. The laminate was infused on a glass plate such that the arrival of the resin at the mold tool could be monitored. It took approximately 45 minutes for a complete wet through, and after cure the laminate had a thickness of approximately 45 mm. After cure, cross-sections were cut from the laminate using a water-cooled diamond tipped table saw to check the result of the infusion. Figure 6-16 shows that the laminate is completely saturated with resin throughout the

thickness. Areas with dry fibers or encapsulated air would show as darker and less transparent areas in the cross section.

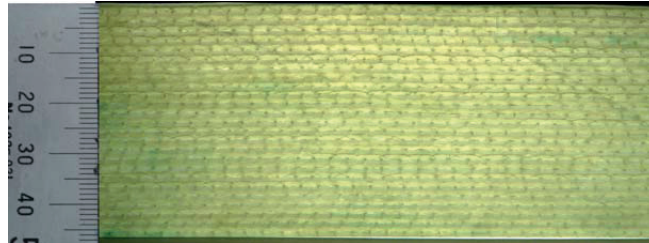


**Figure 6-16** Cross-section of the 50 ply test plate showing a complete wet-through.

Unlike other VARTM processes, the VAP process is not continued until complete wet-through of the preform. Once the calculated amount of resin is injected, the resin hose is closed. A test laminate was allowed to take up resin until resin gelation and cure. A substantial resin flow into the laminate was observed even after complete wet-through. This is explained by the spring-back effect taking place, increasing preform thickness (and thereby its volume), thus taking in more resin. This shows that the VAP process also needs careful preparation by weighting all the placed fiber and calculating the proper amount of resin needed in order to obtain optimum results.

#### **6.4.3 Controlled Atmospheric Pressure Resin Infusion (CAPRI)**

The Boeing Corporation patented early in 2008 a new infusion method named CAPRI (US Patent 7,334,782 B2) which is a variant of the VARTM method. This method brings several improvements to the VARTM method and promises to improve variability and increase fiber volume fraction. While increasing the complexity of the infusion process, CAPRI provides a low-cost alternative to autoclave processing. Today the CAPRI process is used by the Boeing Corporation to fabricate aerospace components, but could also be an alternative in the production of wind turbine blades where good mechanical properties are needed.

Prior to infusion, the preform is subjected to several debulking cycles. During each debulking cycle, vacuum is applied to the preform, giving a compaction pressure of 85 kPa for 30 seconds and then decreased to 15 kPa for 30 seconds. Debulking promotes nesting of the fiber and reduces the spring-back effect of the preform, resulting in a thickness reduction of the preform. What happens during nesting is that the rovings of a fiber mat are massaged together and flattened. Most likely it is not the length of compaction pressure that matters, but the number of cycles that are important. For each cycle, the circular rovings are more flattened, reducing the gaps between the rovings. Reduction of the spring-back effect most likely reduces the thickness gradient of the preform during infusion, thereby improving the dimensional tolerances and fiber volume fraction. C. Niggemann et al. (2008) studied how the number of debulking cycles affected the preform thickness. Figure 6-17 shows the thickness reduction of 15 layers with E-glass (810 g/m<sup>2</sup>, plain weave) undergoing debulking cycles. After 400 cycles the preform thickness was decreased by 5 %.

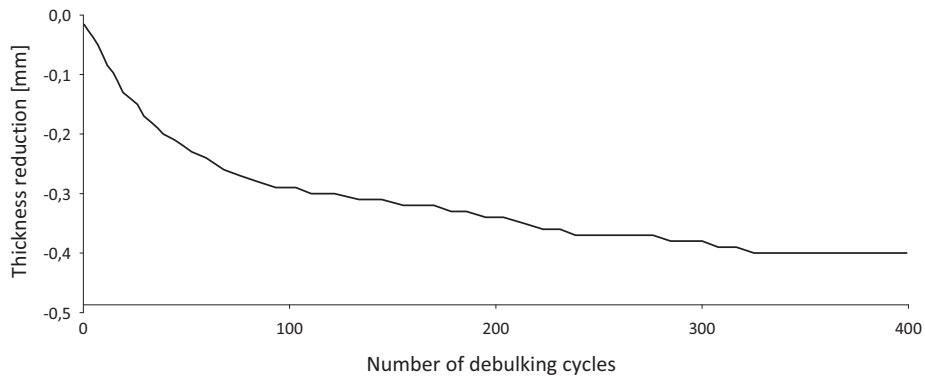


**Figure 6-17** Thickness reduction of preform during debulking (Reproduced from C. Niggemann et al, 2008).

Another feature of the CAPRI infusion process is the use of a partial vacuum in the resin bucket. Figure 6-18 shows the CAPRI setup with a separate vacuum pump creating 50 % vacuum at the resin bucket. This reduces the resin driving pressure by 50 %, but retains a net compaction pressure of 0.5 atm on the preform during the entire infusion and cure. Also this feature reduces the spring-back, hence increasing the fiber volume fraction of the composite.

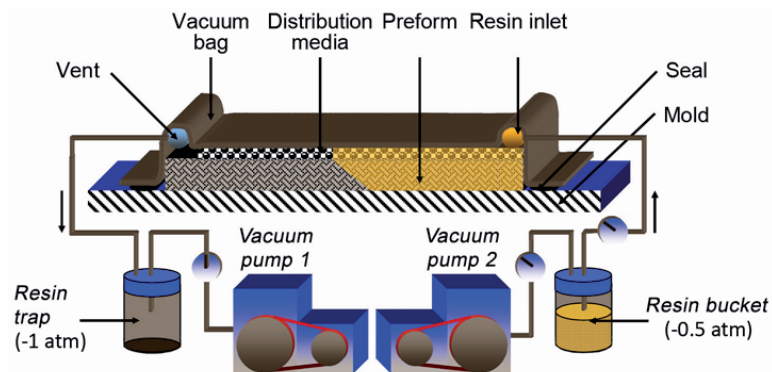


**Figure 6-18** Setup of Boeing's controlled atmospheric pressure resin infusion process (Hughes, 2005).

A literature search did not reveal any prior available work reporting the fiber volume fraction of composites made by the CAPRI process. A test plate was therefore made, consisting of 3 plies of UD L1200 Devold E-glass and epoxy resin. Five burn-off tests (ASTM D-2584) were performed revealing a fiber volume fraction of 59.6 % with a standard deviation of 0.3 %. The CAPRI process clearly improves the fiber volume fraction compared to prior VARTM processes. Literature references about void content in composites made using CAPRI process could not be found. It is reasonable to assume that it should be close to the same levels of other VARTM processes (1-2 %).

The CAPRI process also introduces some new challenges. Due to the debulking of the preform, its permeability can be reduced by as much as 40 %, thereby increasing infusion time. Also the reduced driving pressure of the resin (from 1 atm to 0.5 atm) increases infusion times by as much as 400 % (C. Niggemann, 2008). Resin and vacuum lines have to be recalculated for existing products and the increased infusion time can be challenging when dealing with large structures such as wind turbine blades. The infusion must be complete before the resin starts curing, demanding resins with long pot-life. Together, the debulking process and increased infusion times will increase cycle time and most likely increase production costs compared to other VARTM methods. Whether the increase in production cost of a wind turbine blade is balanced by the reduced weight (due to higher fiber volume fraction) is unknown to the author.

### 6.5 Future development of composite manufacturing process

Composites made by prepreg material and processed in an autoclave yield today the best quality. With high repeatability and mechanical properties, this is the preferred method within the aero and space industry. For the wind turbine blade industry, having an autoclave that fits an entire blade would be far too expensive and is therefore not feasible. Few blade manufacturers use prepreg because of its much higher cost compared to resin infusion, but as blade length increases, this might force the manufacturers to use carbon fiber for increased stiffness. In this case, carbon fiber prepreg has the advantage of having a 30-40 % higher compressive strength compared to carbon fiber composites made by resin infusion. For this reason, manufacturers who already today use carbon fiber in their blade design, use carbon fiber in prepreg and not in an infusion process (G. Gardiner, 2007)

Composites made by infusion processes have today too much variability (compared to the autoclave process) for it to be adopted by the aero/space industry. But the much lower cost of the VARTM process makes it a very attractive process and there is therefore a motivation for further improvements of this technology. Slightly lower mechanical properties are acceptable, if the infusion method maintains its low cost, but with higher repeatability (Hughes, 2005). Such advances in the infusion technology would greatly benefit the wind turbine blade industry. They will allow design limits to be pushed even further by allowing the characteristic values of material properties to be determined with greater accuracy. This would also help manufacturers limiting the weight of the blades and reduce material costs. Improvements like these will be important in the development of even longer wind turbine blades.

For wind turbine blades made by resin infusion the key areas for improvement will most likely be:

- Development of low viscosity resins without sacrificing performance. This will increase the infusion speed, thereby reducing production time.
- Improved stitching patterns to reduce fiber waviness. This will improve the compression strength and fatigue properties, especially for carbon fiber composites.

## 7 Mechanical properties of composite materials in FEM analysis

When performing a FEM analysis, choosing what mechanical properties to use can be quite challenging for composite materials. The fiber, resin and production process all have an influence on the mechanical properties. Also, the mechanical characterization of a composite can be extensive due to its anisotropic nature. A complete characterization requires numerous tests to determine fiber volume fraction, stiffness and strength in various directions, both during compressive and tensile load. As part of this PhD project, work was done on experimental characterization of glass fiber specimens produced by resin infusion (Figure 7-1). Specimens were made from Devold AMT glass fiber and Araldite ESR3 epoxy. Morten. R. Jacobsen (2008) measured modulus and strength for glass fiber composites loaded in tension or compression. The results from these tests were used in the FEM analysis in this thesis and are listed in Table 7-1. Mechanical properties that were not determined by the in-house testing are collected from available literature. Table 7-2 lists the mechanical properties of carbon fiber used in the FEM analysis. These are based on both literature (DNV-OS-C501-2003, I. M. Daniel et al., 1994 and S. W. Tsai, 2008) and calculations such that they represent a carbon fiber composite made by resin infusion. The properties of the carbon fiber composite are based on a Toho Tenax STS high strength carbon fiber in an epoxy matrix. In Table 7-3 the properties of the sandwich core material are listed. These properties are supplied by the manufacturer Diab (“Divinycell H-grade Technical Manual”, [www.diabgroup.com](http://www.diabgroup.com)).



**Figure 7-1** Tensile testing of glass fiber specimen at NTNU/SINTEF fatigue laboratory.

## 7.1 Mechanical properties of glass fiber composite

**Table 7-1** Mechanical properties of glass fiber composite.

Property	Glass fiber composite	Comment
$V_f$ [%]	55	Experimentally determined at NTNU
$\rho$ [kg/m <sup>3</sup> ]	1890	Experimentally determined at NTNU
$E_1$ [GPa]	41	Experimentally determined at NTNU
$E_2$ [GPa]	9	Experimentally determined at NTNU
$E_3$ [MPa]	9	Chosen as the same value as $E_2$
$G_{12}$ [GPa]	4.1	S. W. Tsai, 2008
$G_{13}$ [GPa]	4.1	Chosen as the same value as $G_{12}$
$G_{23}$ [GPa]	3.3	C. T. Herakovich, 1997
$\nu_{12}$	0.3	DNV-OS-C501-2003
$\nu_{13}$	0.3	DNV-OS-C501-2003
$\nu_{23}$	0.35	DNV-OS-C501-2003
$F_{1t}$ [MPa]	1200	Experimentally determined at NTNU
$F_{1c}$ [MPa]	-840	Experimentally determined at NTNU
$F_{2t}$ [MPa]	40	Experimentally determined at NTNU
$F_{2c}$ [MPa]	-120	Experimentally determined at NTNU
$S_6$ [MPa]	90	I. M. Daniel et al., 1994



## 7.2 Mechanical properties of carbon fiber composite

**Table 7-2** Mechanical properties of carbon fiber composite.

Property	Carbon fiber composite	Comment
$V_f$ [%]	58	L. P. Kollár, 2003
$\rho$ [kg/m <sup>3</sup> ]	1560	Calculated based on $V_f$
$E_1$ [GPa]	139	Calculated based on $V_f$
$E_2$ [GPa]	9	S. W. Tsai, 2008
$E_3$ [MPa]	9	Chosen as the same value as $E_2$
$G_{12}$ [GPa]	5.5	S. W. Tsai, 2008
$G_{13}$ [GPa]	5.5	S. W. Tsai, 2008
$G_{23}$ [GPa]	4.4	C. T. Herakovich, 1997
$\nu_{12}$	0.32	DNV-OS-C501-2003
$\nu_{13}$	0.32	DNV-OS-C501-2003
$\nu_{23}$	0.32	DNV-OS-C501-2003
$F_{1t}$ [MPa]	2400	I. M. Daniel et al., 1994
$F_{1c}$ [MPa]	-960	I. M. Daniel et al., 1994
$F_{2t}$ [MPa]	57	I. M. Daniel et al., 1994
$F_{2c}$ [MPa]	-228	I. M. Daniel et al., 1994
$S_6$ [MPa]	71	I. M. Daniel et al., 1994

### 7.3 Mechanical properties of core material

**Table 7-3** Mechanical properties of DIAB Divinycell H80 and H200 core material. Properties are from “Divinycell H-grade Technical Manual” by Diab ([www.diabgroup.com](http://www.diabgroup.com)).

Property	Divinycell H80	Divinycell H200
$\rho$ [kg/m <sup>3</sup> ]	80	200
$E_1$ [MPa]	95	250
$E_2$ [MPa]	95	250
$E_3$ [MPa]	95	250
$G_{12}$ [MPa]	27	85
$G_{13}$ [MPa]	27	85
$G_{23}$ [MPa]	27	85
$\nu_{12}$	0.35	0.35
$\nu_{13}$	0.35	0.35
$\nu_{23}$	0.35	0.35
$F_{1t}$ [MPa]	2.50	7.10
$F_{1c}$ [MPa]	1.40	4.80
$F_{2t}$ [MPa]	2.50	7.10
$F_{2c}$ [MPa]	1.40	4.80
$S_6$ [MPa]	1.15	3.50

# 8 FEM analysis of a 100 m main spar during extreme load

## 8.1 Introduction

Currently the largest wind turbine blade available has a length of 61.5 m, allowing the turbine to generate up to 5 MW of power (LM web link-02, 2008). There is a growing interest in putting wind turbines offshore where wind resources are better and the installation will have lesser environmental impact. Offshore installation costs will most likely be relatively independent of the turbine size and one would therefore want to install as large as possible turbines at each site. The author believes that this could become an important design driver for even larger turbine blades, reaching 80 m or even 100 m of length. In this chapter the main spar of a 100 m long blade is studied by finite element analysis. The load case to be studied is the extreme wind case where a gust of wind hits the blade at  $70 \text{ m/s}$ , causing flapwise bending of the blade towards the tower. Such a wind occurs only once every 50-years, but wind turbine design standards (IEC 64100-2005 and DNV-OS-J102-2006) require the blade to have sufficient strength and enough stiffness to prevent interference with the tower during these extreme conditions. A thorough discussion of the relevant load cases was presented in Chapter 4.

The aerodynamic loads on the blade result in edgewise and flapwise bending of the blade as well as torsional loading. The edgewise loads are carried by the leading and trailing edges of the blade, whilst the two latter loads are carried by the main spar (Figure 8-1). Being the main load carrying structure of the blade, the main spar needs enough global stiffness to prevent it from striking the tower during extreme flapwise bending loads. On a local scale, the main spar together with the stiffness of the outer shells ensures that the aerodynamic profile of the blade is kept as stable as possible. Also, the main spar flanges need sufficient local stiffness to resist buckling. When subjected to flapwise loading, the loads are mainly carried by the flanges in the main spar. The FEM analyses focus on the design of the flanges. Shear webs are designed with sufficient strength and stiffness, but are not studied in detail.

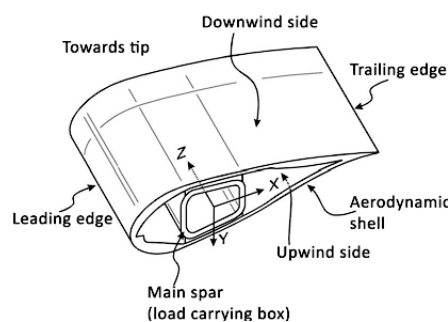


Figure 8-1 Wind turbine blade with aerodynamic outer shell and main spar (Jensen et al., 2005).

Even for the simple load case of flapwise load only, the turbine has to comply to several criteria. In addition to stiffness, the stresses in the structure must be within required material safety factors and the structure has to resist buckling (DNV OS-J102-2006). An optimal design of the main spar requires an understanding of how these criteria affect the solution.

#### *Maximum deflection*

The wind turbine blades today need sufficient stiffness such that the blade does not hit the tower during the 50-year gust ( $70 \text{ m/s}$ ). Compared to the turbine's design wind speed of approximately  $9 \text{ m/s}$ , the gust will require large amounts of UD plies in the main spar flanges to prevent excessive deflection. To explore how the required stiffness affected the spar, two designs were done:

- *Stiffness criterion:*  
Maximum tip deflection of 15.4 m for the 100 m main spar as specified by the IEC 61400-1-2005 and DNV OS-J102-2006 standards (see section 5.5). The structure also has to comply to strength and buckling criteria.
- *No stiffness criterion:*  
The structure only has to comply to strength and buckling criteria.

#### *Efficient use of material*

There are several possible approaches that can be used to determine the distribution and placement of UD plies. In this work the following two design philosophies have been used:

- The same material safety factor is used throughout the model.  
The top and bottom flanges are treated separately, adding UD plies in those areas where the longitudinal fiber stress is above the chosen safety factor. Since carbon and glass fiber composites have different strength in axial tension and compression, it will result in different designs for the top and bottom flanges. The compression strength for carbon fiber composite is typically half of the tensile strength. Figure 8-2a shows how the top flange, being in compression during the 50-year gust, will become thicker than the bottom flange in tension. Such design will be referred to as unsymmetric.
- UD plies are added symmetrically in both the top and bottom flange.  
When subjected to the extreme flapwise load, the compression stresses in the top flange governs the identification of the sections where material has to be added. In this approach the same amount of plies will be added in both flanges, resulting in the UD plies in the top and bottom flanges being equally thick (Figure 8-2b). Compared to the previous approach, material from the thick top flange is moved to the bottom flange, giving more global stiffness since the plies are moved further away from the neutral axis of the spar. On the downside, a thinner top flange will be more susceptible to buckling failure, thereby requiring more  $\pm 45^\circ$  plies for stability.

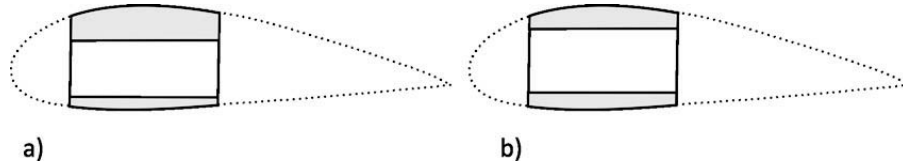


**Figure 8-2** a) Asymmetric distribution of UD plies in top and bottom flange. b) Symmetric distribution of UD plies in flanges.

#### *Choice of material*

As discussed in Chapter 2, the various blade manufacturers have different opinions on which materials to use in a wind turbine blade. LM still uses mainly glass fibers in their blades and have not publicly announced that this will change for longer blades in the near future (G. Gardinger, 2007). Vestas on the other hand uses carbon fiber in their 40 m blades, arguing that in addition to a stiffer and lighter blade, the added cost of carbon is justified by the lighter blade generating savings in the remaining structure of the wind turbine. It was therefore decided to evaluate three different concepts of material usage in the main spar.

- Carbon fiber main spar. Both the flanges and shear webs are made of carbon.
- Glass fiber main spar. Both the flanges and shear webs are made of glass fiber.
- Hybrid main spar. UD plies in flanges are made of carbon fiber and the  $\pm 45^\circ$  anti-buckling plies are glass fiber. Shear webs are also made of glass fiber composite.

The choice of material should have a substantial influence on the laminates generated by the FEM analysis. The solutions using UD carbon fiber in the flanges, will need less UD plies than the glass fiber solution to be sufficiently stiff. A thinner laminate will in return be more susceptible to buckling, thereby needing additional  $\pm 45^\circ$  plies for stability. It is therefore difficult to foresee what will be the most weight saving solution. Based on this, 12 FEM models were developed for the study of different design philosophies and material choices affected (Figure 8-3). All models had to comply to a minimum safety factor of 1.73 for material strength and be able to resist buckling failure (section 5.1). Figure 8-3 also includes the labels used to identify the different FEM models. The first letter denotes if it is a Symmetric/Unsymmetric design, the second letter if the model has to comply to a Stiffness/No Stiffness criterion and the last letter denotes the material used to design the spar (Carbon/Glass/Hybrid).

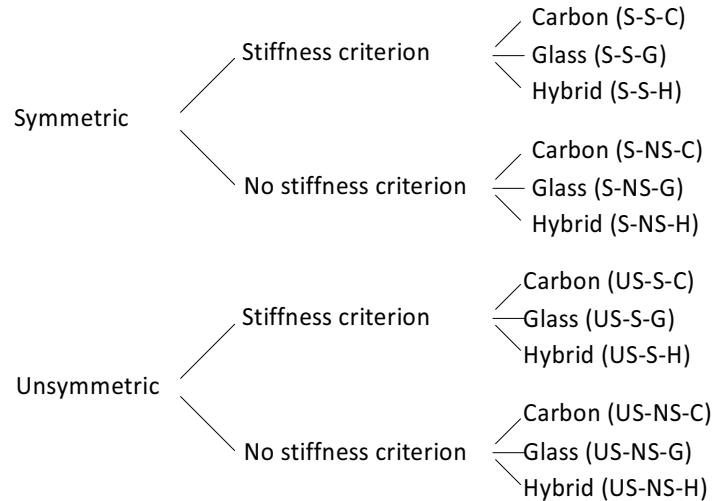


Figure 8-3 Modelling matrix for the 100m main spar.

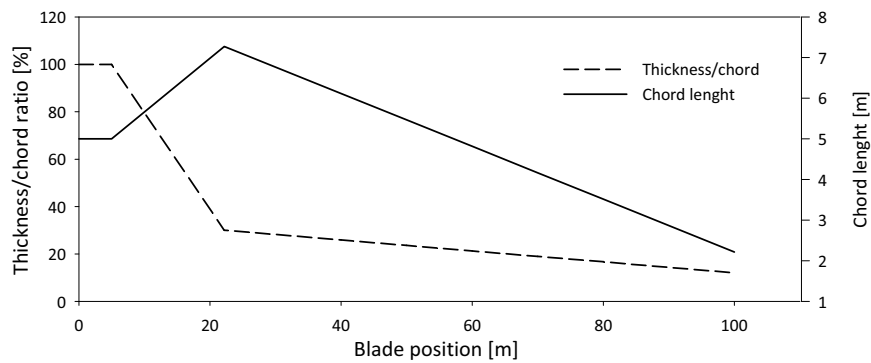
## 8.2 Main spar geometry

Defining the shape of a wind turbine blade is a complex task with numerous parameters affecting the outcome. The number of blades, design wind speed, blade length, aerodynamic efficiency and cost are some of the important factors that have to be balanced. For an introduction to basic airfoil theory and blade design the reader is referred to Chapter 2. Manufacturers invest a lot of research into developing high performance blade geometries. LM Glasfiber has recently built their own wind tunnel in order to be able to more intensively develop new airfoils and validate their CFD simulations (LM web link 01, 2008). Naturally, there is little publicly available information on the geometries of large blades, as this is well protected by the industry. The geometry used in this work is based on publicly available literature and the general wind turbine theory presented in Chapter 2.

The 100 m long blade analyzed here is for a three bladed turbine designed for a mean wind speed of  $9 \text{ m/s}$ . Table 8-1 presents the chord and thickness definitions for the blade and are shown graphically in Figure 8-4. The circular profiles at the root (0 to 5m) gradually change into an airfoil shape in the transition zone of the blade (5 to 22m). After the transition zone both the chord and thickness-to-chord ratio decrease linearly towards the blade tip. Closest to the root, airfoils with a thickness ratio of 30 % are used to provide structural stiffness. Towards the tip of the blade, thin airfoils (12-15 %) are used for high aerodynamic efficiency.

**Table 8-1** Geometric properties of 100 m blade FEM model

Local blade length [m]	Chord length [m]	Thickness to chord ratio [%]	Profile shape
0	4.5	-	Circular root
5	4.5	-	Circular root
22.2	7.27	30.0	Airfoil
30	6.77	28.2	Airfoil
40	6.12	25.9	Airfoil
50	5.47	23.6	Airfoil
60	4.82	21.3	Airfoil
70	4.17	18.9	Airfoil
80	3.52	16.6	Airfoil
90	2.87	14.3	Airfoil
100	2.22	12.0	Airfoil

**Figure 8-4** Definition of chord length and thickness to chord ratio for the 100m wind turbine blade.

The blade's aerodynamic profiles were generated using the java based software JavaFoil by Dr. Martin Hepperle (Hepperle, 2007). NACA<sup>1</sup> 64-series 6-digit airfoils were chosen and the profiles were generated by defining the thickness to chord percentage. The airfoil shape was described by 101 points and exported by JavaFoil as a text file. The exported coordinates were normalized between 0 and 1 and then scaled to the correct chord length in Excel. The scaled coordinates were then imported into the CAD software SolidWorks where the shape of the airfoil was generated by a spline curve through the

1. National Advisory Committee for Aeronautics, USA.

points (Figure 8-5a). Figure 8-5b illustrates that the spar width was defined as 33.5 % of the chord length (see Chapter 2 for background information).

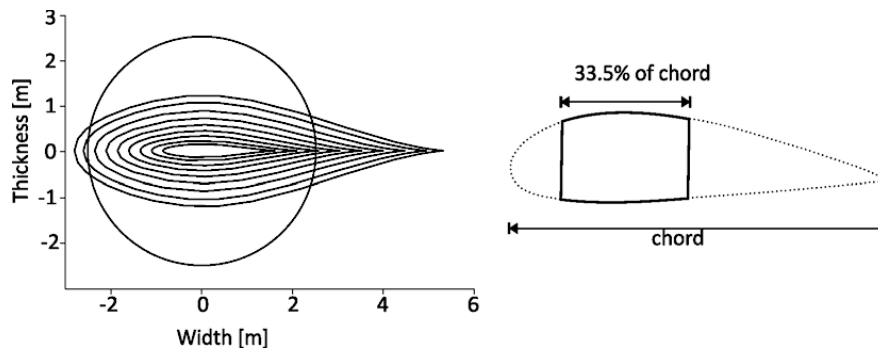


**Figure 8-5** NACA 64-series wing profiles used to define the wind turbine blade. b) Definition of main spar width.

Based on collected blade literature (E. Hau, 2006 and M. O. Hansen, 2000) and correspondence with aerodynamic engineers at IFE<sup>1</sup>, it was decided to give the blade a linearly distributed twist of 0 degrees at 22 m and 15 degrees at 100 m. Figure 8-6a shows how the main spar profiles are twisted towards the spar tip. It should be noted that an exact and detailed description of the aerodynamic profile is not within the scope of this work. The geometric properties and profiles are chosen such that an evaluation of the structural properties can be done on a representative spar geometry.

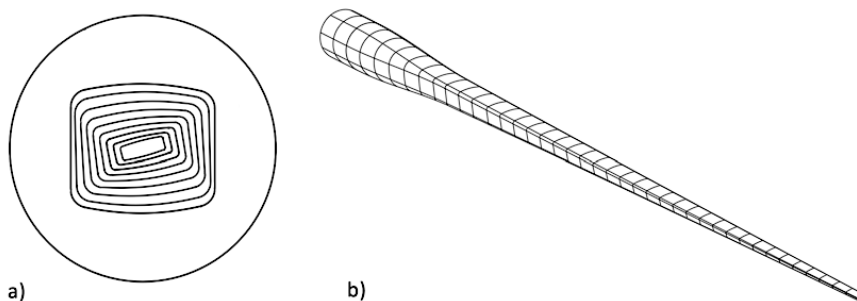


**Figure 8-6** a) Main spar sections. b) CAD model of main spar created in SolidWorks.

The profiles were used to generate a surface model of the main spar in SolidWorks. When generating the surfaces, the “Boundary Surface” function was used to ensure surface tangency between the sections. This way, a high quality surface could be generated without a sharp transitions between the profiles. Because the distribution of composite plies in Abaqus CAE is done by choosing regions, the main spar was divided into 40 sections along its length (Figure 8-6b), which would allow a fairly detailed distribution of the plies. After completion of the main spar geometry, it was exported to Abaqus for

1. Institutt for Energiteknikk (Institute for Energy Technology), Norway.



analysis via the IGS file format. Detailed information about the spar geometry is presented in Appendix A.

### 8.3 Loads and boundary conditions

The load case studied here is the extreme wind condition specified in the IEC 64100-1-2005 standard. The wind turbine has been shut down due to high winds during a storm when it is suddenly struck by a gust at  $70 \text{ m/s}$ . This extreme wind is only expected to happen once every 50-years and a detailed description is presented in section 4.3. It is assumed that the gust hits the blade perpendicularly and causes flapwise bending of the blade towards the tower. The bending of the blade will result in the suction side of the blade being loaded in compression and the pressure side loaded in tension. The spar flanges provide the blade with global bending stiffness such that it does not deflect into the tower. It is also highly important that the spar flanges do not buckle, because it will most likely lead to a fatal collapse of the blade and possibly the entire turbine. This load case will be referred to as the *primary load case*.

Annually the turbine can expect to be stuck by what is called the 1-year extreme gust with a wind speed of  $52.5 \text{ m/s}$ . It is likely that the turbine will experience this load during a failure of the yaw system and therefore one has to design the blade such that it can handle the load from any direction (IEC 61400-1-2005 Design load case 7.1). For the main spar the most critical direction would be the opposite direction of the primary load case. If one were to design the spar using only the primary load case, there would be no need for buckling resistance in the bottom flange because it would only be subjected to tension loads. But when subjected to the 1-year extreme gust, the bottom flange would be in compression and therefore needs sufficient buckling resistance. Summarizing the two load cases used in these FEM analyses (Figure 4-5):

- *Primary load case*  
Wind turbine blade is struck by a  $70 \text{ m/s}$  wind bending it towards the tower.
  
- *Secondary load case*  
Wind turbine blade is struck by the 1-year extreme gust ( $52.5 \text{ m/s}$ ) in the opposite direction of the primary load case. Suction side is now in tension and pressure side in compression

The loads were applied on the Abaqus CAE model as a variable pressure force along the length of the blade and equally distributed between the top and bottom flange (Figure 8-7). The nodes at the root of the blade were constrained in all six degrees of freedom, representing it being attached to the turbine hub.

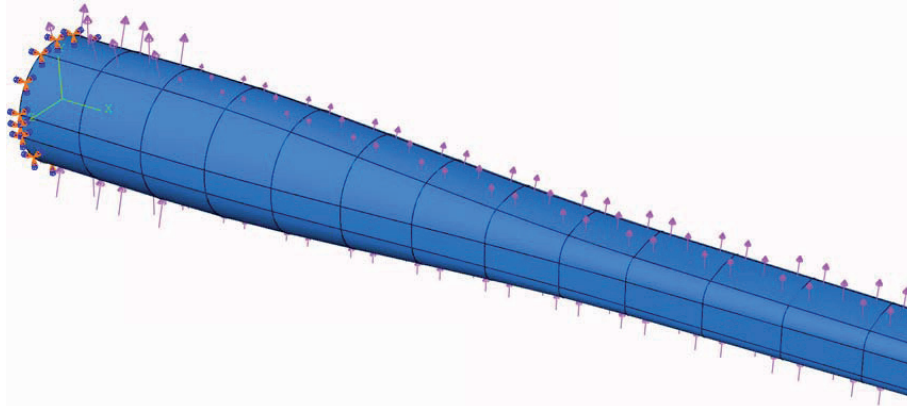


**Figure 8-7** Boundary conditions at main spar root and pressure load on upper and lower surfaces. Purple arrows show the applied pressure load on the top and bottom flanges. Orange and blue arrows show the boundary conditions at the root, where nodes are restrained in all six degrees of freedom

#### 8.4 Mesh

The 100 m spar was meshed using shell elements. Abaqus provides a wide range of different shell elements to choose from. The shell elements can be placed in one of three categories: general-purpose shells, thin shells and thick shells. The general-purpose shells are capable of deformations due to transverse shear stress whilst the thin shells should only be used when transverse shear deformations are negligible. The thick shells take transverse shear deformation into account and should be used when this deformation is important for the analysis. Transverse shear deformation were not thought to be highly important in the spar analysis and therefore general-purpose elements were chosen as candidates for meshing the spar. Small-strain elements are not capable of changing their thickness during the analysis, whilst finite-strain elements are capable of doing so. In order to obtain a fully non-linear analysis finite-strain elements must be used. When the shell elements in the analysis experience bending it is recommended to use curved shell elements (Abaqus theory manual). For this reason the 4-node doubly curved shell element S4R with reduced integration was chosen for meshing the 100 m spar. Using a shell element with reduced integration will reduce the amount of CPU time necessary for analysis of the spar. Due to the reduced number of integration points, the S4R element can experience hourglassing. Abaqus therefore has a hourglass stabilization feature built into the S4R element that will check for possible hourglass mode shapes.

A mesh refinement study was performed in order to find the necessary density of shell elements needed to determine the stresses and linear buckling eigenvalue with sufficient accuracy and to limit the computational resources needed. Element length along the spar was varied, as well as the number of elements across the flange, shear webs and in the corners. Figure 8-8 shows some of the results from the mesh refinement study. It can be seen how the axial and shear stress change as the number of elements

are varied. Based on these studies it was decided to use 6 elements across the shear web, 5 elements across the spar corners and 10 element across the spar flanges (Figure 8-9). Considerable time was spent in specifying the element size along the length of the spar. Element size was constantly varied along the spar, with a length of 0.5 m at the root and 0.14 m near the spar tip. An element aspect ratio of less the 3 was achieved in the spar flanges. The final spar mesh consisted of 41 600 elements and 250 000 degrees of freedom. The results of this model deviated less than 5 % from a model containing approximately 100 000 elements and required substantially less computational resources. This mesh is used in all the main spar analyses throughout this thesis.

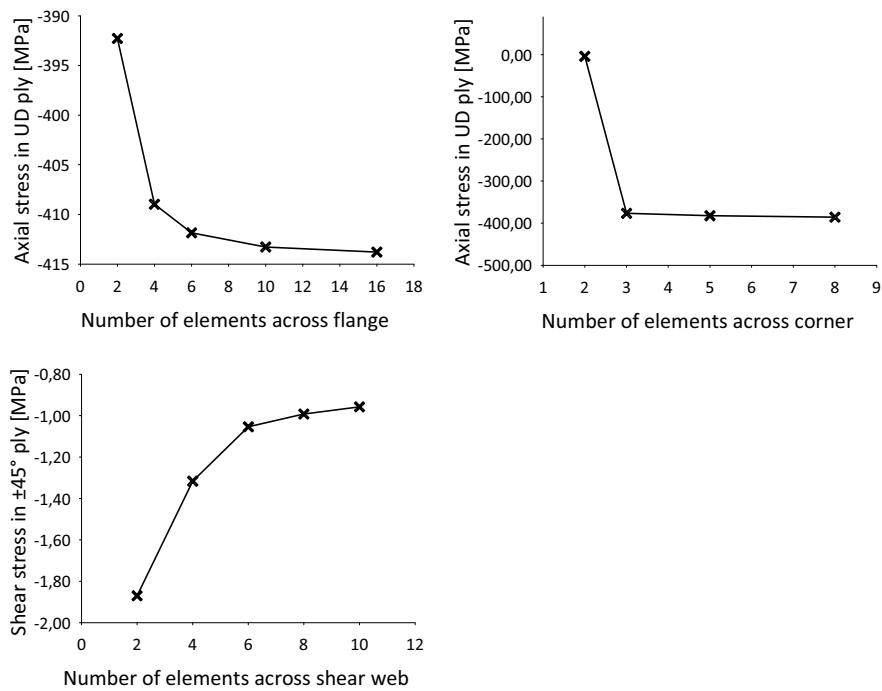


**Figure 8-8** Mesh refinement study of 100 m spar. Number of elements across the flange, spar corners and shear web is varied.

## 8.5 Composite lay-up modelling in Abaqus CAE

The composite lay-up was defined using the “composite lay-up editor” in Abaqus CAE. The editor is a graphical interface with a table where composite plies can be defined. It functions as a tool for defining the section properties of the shell elements in the spar analysis. For each ply its name, material, thickness, orientation, number of integration points and region is assigned. The ply regions can be assigned by directly selecting them from the Abaqus CAE viewport. Before creating the lay-up, the geometry needs to be partitioned in order to create the different regions to which plies will be assigned. Ply

orientation can be defined by selecting a coordinate system for the entire laminate or for the individual ply. Great care should be taken in ensuring that each individual ply has the correct orientation. This can be done in the composite ply editor by specifying that the ply orientation is to be shown on the geometry in the viewport. As the different plies are selected, the relevant ply orientation is shown and can be checked. Figure 8-10 depicts how plies at  $45^\circ$  and  $0^\circ$  were shown on the 100 m spar. Abaqus will also fail to define a ply in a selected region if the shell normal makes a sharp transition through an angle of  $90^\circ$  or greater, for example in a corner (Figure 8-11a). In these cases the solution is to model the region as separate plies as shown in Figure 8-11b. It might also be necessary to define a local coordinate system to ensure proper ply orientation. For the 100 m spar it was possible to use the part coordinate system for all ply definitions.

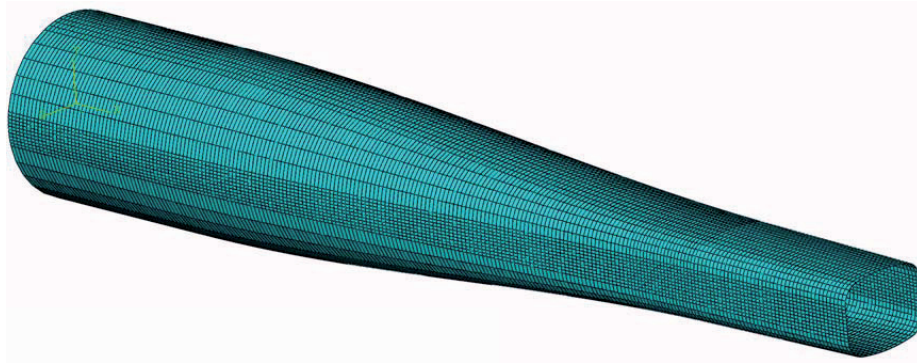


Figure 8-9 100 m spar mesh at the root area.

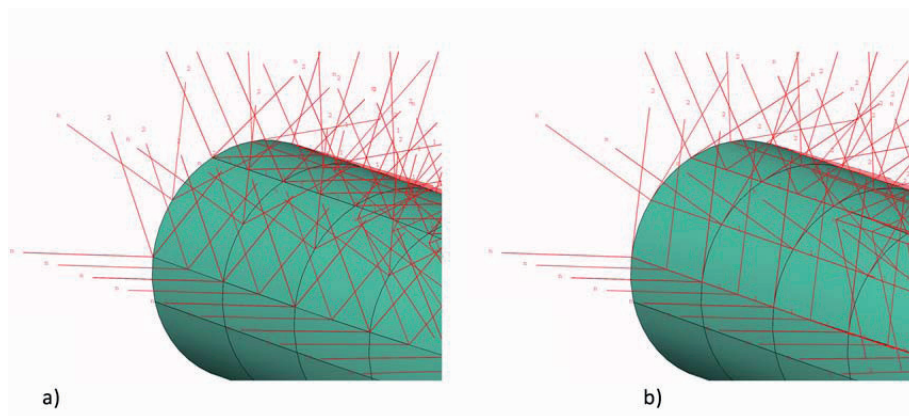
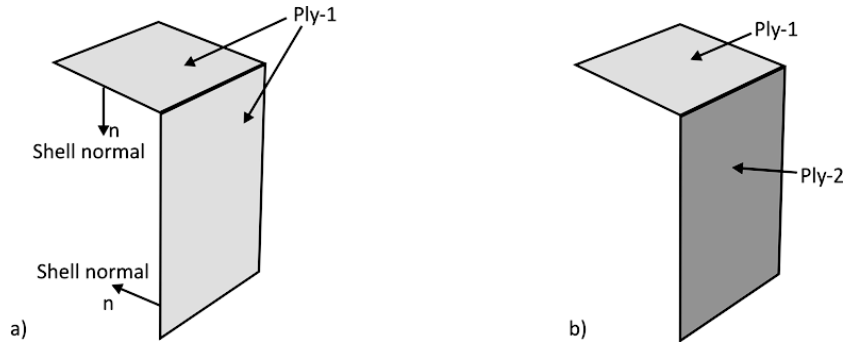


Figure 8-10 Abaqus ply editor is used to check ply orientation of the top flange in the 100 m spar analysis. a)  $45^\circ$  ply orientation b)  $0^\circ$  ply orientation.



**Figure 8-11** a) A sudden change in shell normals will cause Abaqus to fail in applying a single ply in the selected region. b) At sharp corners a single ply needs to be divided into two individual plies in order to achieve correct shell section definitions.

## 8.6 Non-linear analysis in Abaqus

In simple cases a linear eigenvalue analysis can be sufficient for design evaluation. It has the advantage of being fast and is easy to interpret (see section 5.3). But if there is a concern about geometric nonlinearity prior to buckling, such as the large deflections of a wind turbine spar, a load-deflection analysis should be performed. In Abaqus this analysis is known as the “modified Riks method”. The modified Riks method uses the load magnitude as an additional unknown and solves simultaneously for loads and displacements. This method can provide solutions even in cases of complex nonlinear and unstable response, such as shown in Figure 8-12. Since the load magnitude is treated as an unknown, Abaqus uses the “arc length”  $l$  along the equilibrium path in the load-displacement space to measure the progress of the solution. This will yield a solution regardless of whether the response is stable or unstable. Performing an analysis with the modified Riks method will require substitutionally more computational resources than a linear eigenvalue analysis.

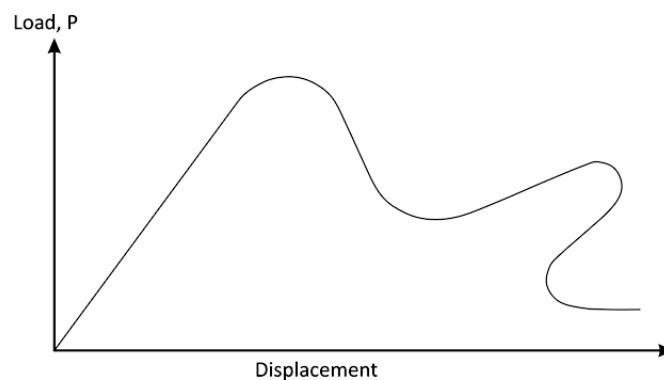


**Figure 8-12** Equilibrium path during a typical unstable static response.

Abaqus uses Newton's method to solve the nonlinear equilibrium equations. Since many problems involve history-dependent response, the solution is obtained as a series of increments. Within each increment, iterations are done in order to obtain equilibrium. Sometimes the increments have to be kept small (rotations and strain increments are kept small) to ensure correct modelling of history-dependent effects. Often the increment size is a matter of computational efficiency since large increments will require more iterations. Also, since the Newton's method has a finite radius of convergence, a too large increment can prevent obtaining a solution because the initial state is too far away from the equilibrium state being sought. For further information and in depth knowledge of the modified Riks method the reader is referred to section 2.3.2 in the Abaqus Theory Manual.

## 8.7 Design of 100 m main spar

### 8.7.1 Distribution of reinforcements

The design of a wind turbine blade is a highly iterative process influenced by numerous parameters. First the blade's aerodynamic shape has to be determined, complying to demands for power output, size and structural considerations. When the outer aerodynamic shape is set, the process of designing the inner structure can start. Criteria for deflection, buckling, strength, torsion, etc. all have to be met. The different criteria affect each other and after one criteria is satisfied another might be violated, requiring adjustments of plies. Figure 8-13 gives an overview of the process involved in developing a design for the main spar in this thesis.

The process of ply distribution starts by distributing the UD plies along the top and bottom flange during the primary load case. One ply is added to the flanges and a linear static FEM analysis is done to compute the axial fiber stress. During this first distribution a minimum allowable material safety factor of 1.73 (section 5.1) is used to evaluate the results. A new ply is then added in those areas where the stress levels are too high and a new static FEM analysis is performed. Enough plies have been added when there are no more areas in the spar flanges that are below the chosen safety factor. If a stiffness criterion exists, the deflection of the spar tip is checked. If the deflection is less than the maximum allowable deflection, the UD ply distribution is complete.

If not, the stiffness of the structure is increased by artificially increasing the material safety factor (e.g. from 1.73 to 2.0) and a new ply distribution is done. The material safety factor is manually adjusted until the deflection of the spar fulfils the stiffness criterion. Figure 8-14 shows a plot of the relatively even stress distribution of a UD ply on the top flange after the composite plies have been optimized. Figure 8-15 is a graph of the axial stress along an imaginary center line of this UD ply and more clearly illustrates the relatively even stress distribution along the length of the main spar that is present after the ply optimization procedure. When the maximum load is reached, failure should ideally happen at several locations. The spikes in the graph indicate the UD ply drops along the spar.

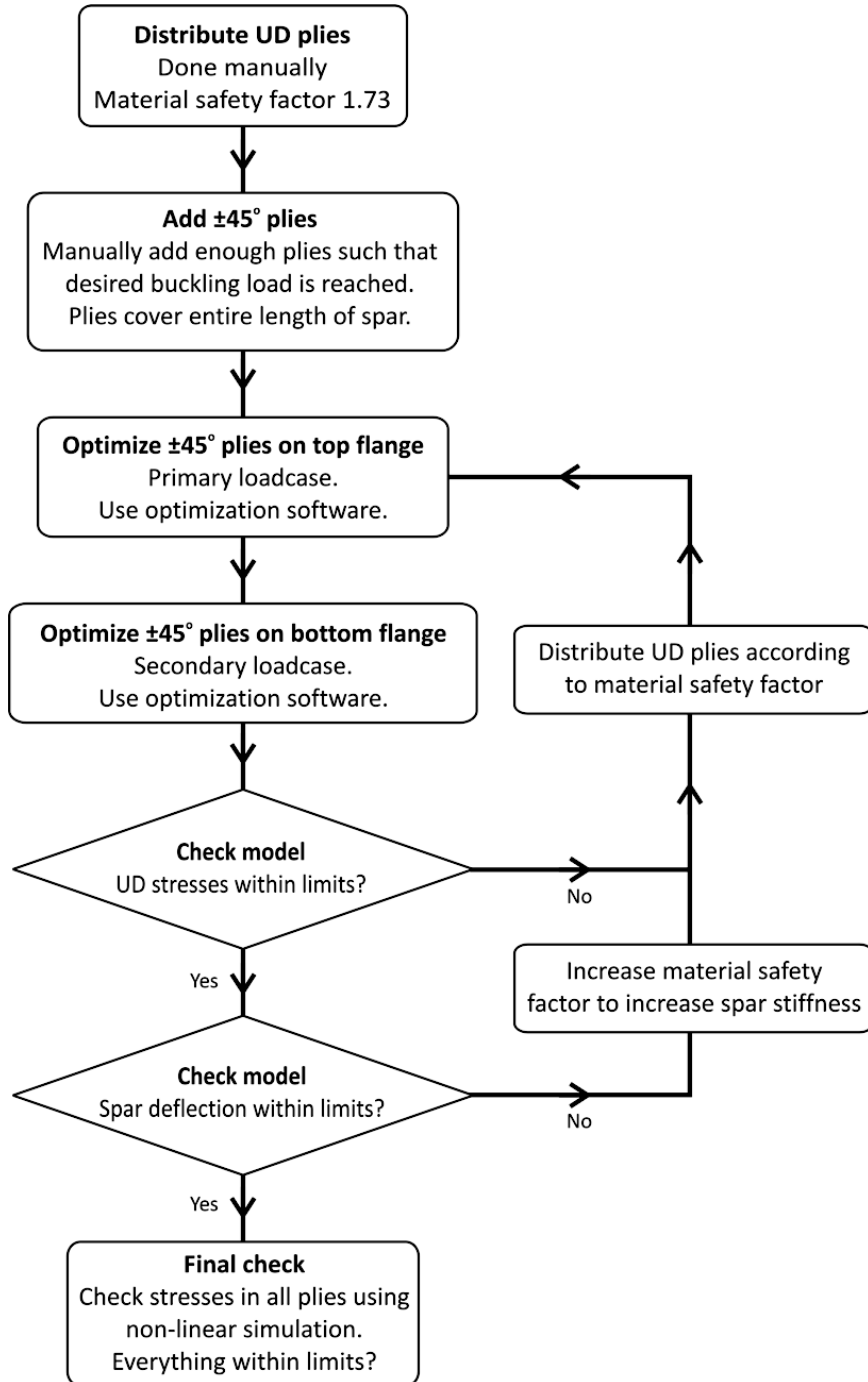
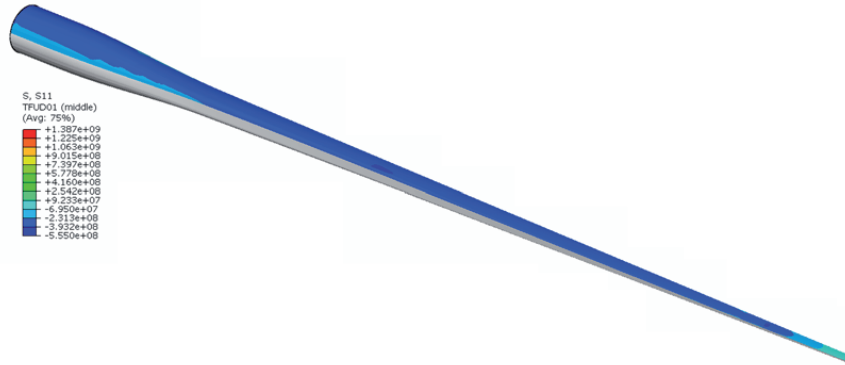
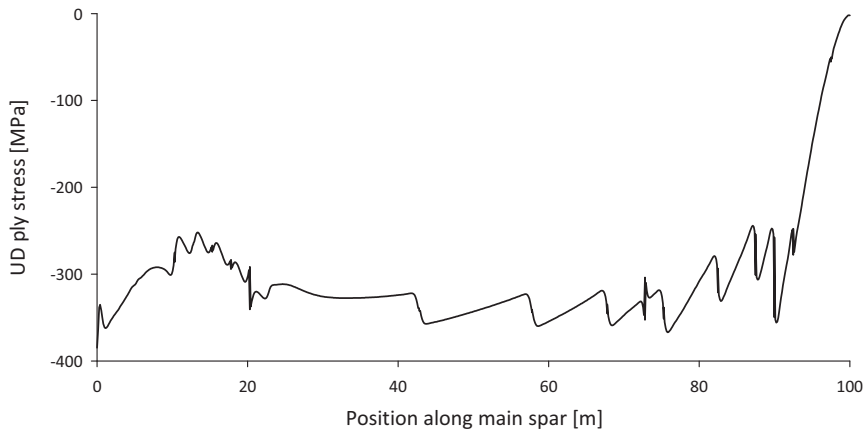


Figure 8-13 Design procedure of a main spar.



**Figure 8-14** Stress plot of UD ply on the top flange of the main spar. Spar is subjected to the 70 m/s extreme gust primary load case and plies have been optimized. Spar deflections have been removed for clarity.



**Figure 8-15** Axial compressive stress along the length of the spar for a UD ply. Spikes indicate location of UD and  $\pm 45^\circ$  ply drops.

Figure 8-16a shows a typical plot of compressive stress in a UD ply on the top flange during the ply distribution procedure. Areas with stresses above the chosen safety factor are colored pink and a continuous ply is then added in this area. Figure 8-16b shows another UD stress plot that was observed during ply distribution. In this case the strength criterion is violated in two separate areas. One could choose to place plies only in those areas violating the strength criterion (one ply 0-5 m and another ply 10-78 m), but this would result in highly localized ply definitions. From a production point of view this would be highly impractical and increase production time. For example Figure 8-17 shows how continuous plies are laid down at LM Fiberglass either manually or automatic.



Based on this, it was decided to only place continuous plies in the flanges. In the case of Figure 8-16b, the next ply would be placed from 0-78 m. During the initial UD ply distribution each ply was defined as 2 mm thick. Depending on the material (carbon or glass fiber), this would result in a total of 10-20 UD plies in the flanges. In order to reduce the amount of plies needed to be distributed, ply thickness was adjusted such that a maximum of 10 UD plies were needed in the flanges. Often after major thickness adjustments a new ply distribution was needed. The next step was to add  $\pm 45^\circ$  plies on both sides of the UD plies to provide buckling resistance.

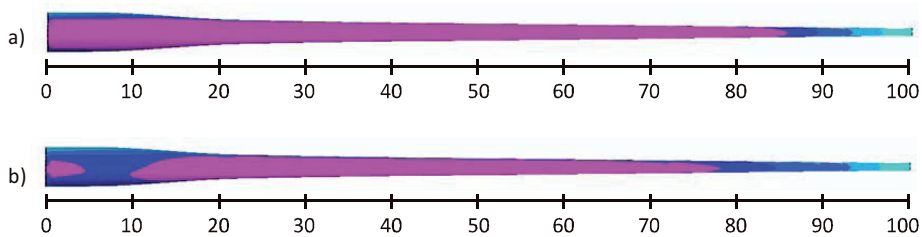


**Figure 8-16** a) Continuous areas violating strength criterion in UD ply (pink color). b) Separate areas violating the strength criterion.



**Figure 8-17** Manual and automatic placement of plies for a wind turbine blade at LM Fiberglass (Plastics Technology, 2008).

Performing a buckling analysis of the main spar proved to be a challenging task. A linear eigenvalue buckling analysis was easily performed and took approximately ten minutes. But when this model was analyzed by a non-linear analysis, the structure buckled at about half the load. In the non-linear analysis the structure was defined to buckle when the stress levels in any ply were above the minimum safety factor of 1.73 (according to DNV-OS-C501-2003). During the non-linear analysis the load is increased in small increments and deformation of the geometry is updated in each increment. Such an analysis is more realistic, but it demands considerably more computational resources. Typically a non-linear analysis of the main spar would take up to five hours. Using a non-linear analysis to distribute the  $\pm 45^\circ$  layers would be time consuming and highly unpractical. The

difference in buckling load found by linear and non-linear analysis is explained by the large deflections of the main spar. The results presented later show that tip deflections vary between 15-45 m for a 100 m main spar. Deflections above 10 % of beam length are regarded as large deflections and non-linear effects become significant (Irgens, 1999). This causes the predicted linear buckling load to deviate from the non-linear solution. The difference was confirmed by preliminary models of a carbon fiber and a glass fiber spar who were subjected to 100 % and 50 % of the primary load case and studied by both linear and non-linear buckling analysis. The amount of UD plies was kept unchanged in each load case, whilst the amount of  $\pm 45^\circ$  plies was adjusted to yield a linear buckling load of approximately 2.0<sup>1</sup>. The UD plies had been distributed along the length of the spar, whilst the  $\pm 45^\circ$  anti-buckling plies covered the entire length of the spar. Table 8-2 compares the linear and non-linear buckling analysis for the four different models. Compared to the non-linear analysis, the linear analysis overestimates the buckling load by a factor 1.59-1.91 in the examples calculated in this thesis. Note that for both the carbon and glass fiber solutions, the models with less deflection show a better agreement between the linear and non-linear buckling analysis. This is to be expected, because non-linearity is critical for large deformations.

When using the much quicker linear buckling analysis to distribute the  $\pm 45^\circ$  anti-buckling plies, a design factor  $\beta=2.0$  was introduced. This means that the structure was designed to handle a linear buckling load of 2.0. This would ensure that the final spar design, when checked by non-linear analysis, would have a buckling load of at least 1.0. This was a practical empirical approach to reduce the computational resources needed, but only non-linear analysis should be used for the final design evaluation.

**Table 8-2** Comparison of linear eigenvalue buckling and non-linear buckling analysis. Main spar made of either carbon or glass fiber is subjected to 100 % and 50 % of primary load case. Buckling loads are normalized (see footnote 1).

Material	Load [%]	Deflection [m]	Linear buckling analysis	Non-linear buckling analysis	Linear/non-linear
Glass	100	36.1	2.10	1.21	1.74
	50	19.2	2.15	1.35	1.59
Carbon	100	19.1	1.87	0.98	1.91
	50	9.72	2.68	1.46	1.83

### 8.7.2 Automatic anti-buckling ply distribution

The distribution of the anti-buckling plies started by adding enough anti-buckling plies on both sides of the UD plies until the main spar had a linear eigenvalue buckling load above 2.0. All plies covered the entire length of the spar. Unlike the UD plies, stress values from linear static analysis could not be used to distribute the anti-buckling plies. Stresses in an area could be well below the limits, but if an anti-buckling ply was

---

1. Abaqus CAE automatically normalizes the predicted buckling load. If a structure is found to buckle at a load of 1.0, it has reached the applied design load.

removed from one section, the area could suddenly become buckling critical. This is explained by the fact that buckling is an instability problem. The anti-buckling plies were optimized by incrementally shortening them along the main spar's 40 sections (Figure 8-6b) until a linear buckling load close to 2.0 was reached. If the linear buckling load dropped below 2.0, the  $\pm 45^\circ$  ply was extended by one section. After each change a new linear buckling analysis had to be performed to see how the change affected the linear buckling load. This optimization had to be done for each anti-buckling ply and therefore, finding the optimal distribution of the anti-buckling plies was a very time consuming task. In addition to the time needed for the simulation, the manual interpretation of results and ply adjustment was a labor intensive and time consuming task. A Matlab procedure that interacts with Abaqus was developed in order to automate this process. The surfaces in the CAD model were divided into 40 sections along the length of the main spar. In Abaqus the sections in the bottom and top flanges were then given unique names, such that Matlab could identify which sections to optimize. Figure 8-18 shows how the optimization software operated. After distribution of the UD plies, enough  $\pm 45^\circ$  plies were added manually to provide sufficient buckling resistance. These plies were placed symmetrically about the UD plies and covered the entire length of the spar. Ply definitions were exported to Matlab to define a starting point for the optimization. The desired linear buckling load of 2.0 was specified and the optimization software was initiated. The software starts by optimizing the anti-buckling plies closest to the UD plies and works its way outwards. Starting at the main spar tip, one section at a time was removed from the anti-buckling ply definition until the specified buckling value was violated, in this case a linear buckling load below 2.0. One section was then added to the ply in order to get the previously valid ply definition. The same procedure was then repeated at the root of the blade to complete the optimization of this anti-buckling ply. This procedure was repeated for each anti-buckling ply until all plies had been optimized.

The primary load case was used for the optimization of the anti-buckling plies in the top flange, and the secondary load case was used for the bottom flange. After the linear buckling optimization was complete, the ply definitions were exported as an Excel file and used to update the ply definitions in Abaqus. The great advantage of this procedure was that it was fully automatic and thereby greatly time saving. Often an optimal anti-buckling ply distribution could be found within 5-10 hours. After optimization of the anti-buckling plies, a static analysis was done to check stress levels and deflection of the blade. When adding or removing anti-buckling plies, the positions of the UD plies are shifted, thereby affecting the stress levels and deflection of the main spar. Often a new distribution of the UD layers had to be performed after the initial buckling optimization.

Experience with the procedure showed that running the model three times through the optimization process (distribution of UD and anti-buckling plies) was sufficient for a solution to converge. Figure 8-19 illustrates the anti-buckling plies of the top flange before and after their optimization. The  $\pm 45^\circ$  plies (blue lines) are distributed along the flange to yield an even distribution of the buckling load. Once the buckling load is reached, the spar should experience buckling failure at several locations.

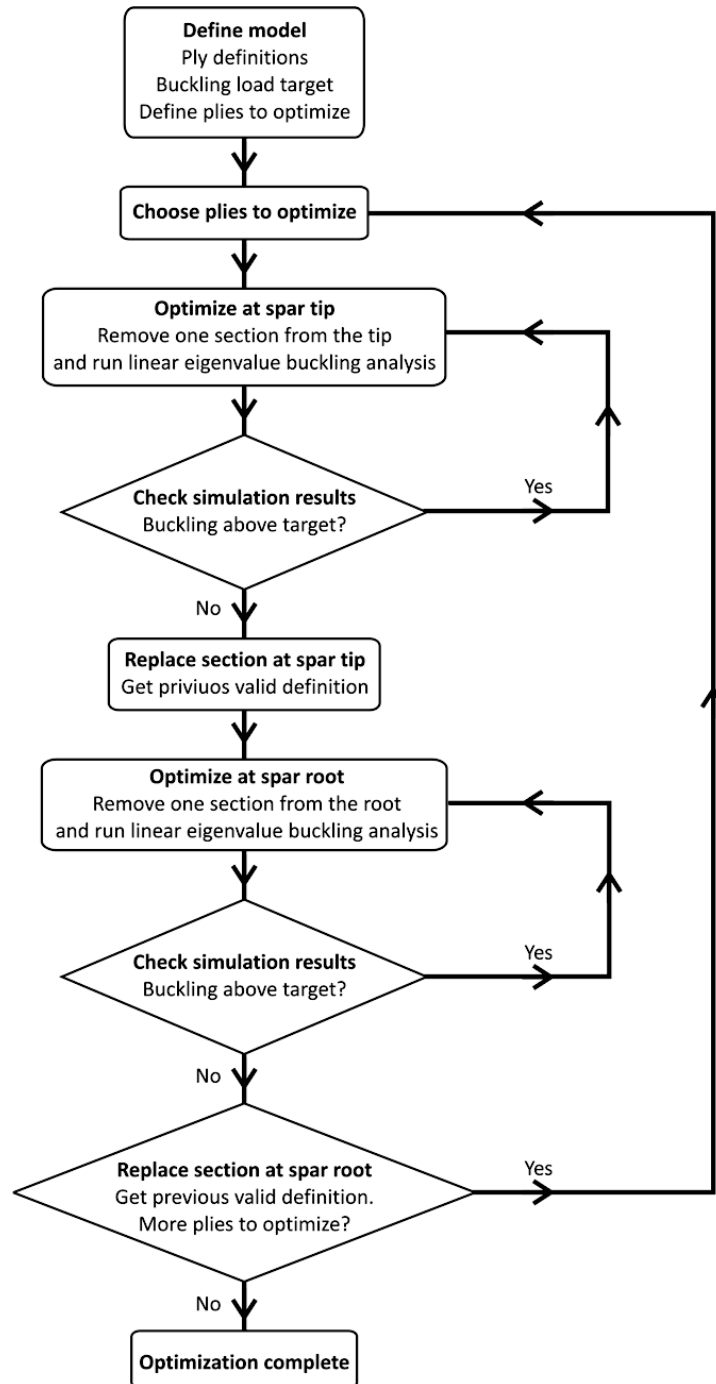
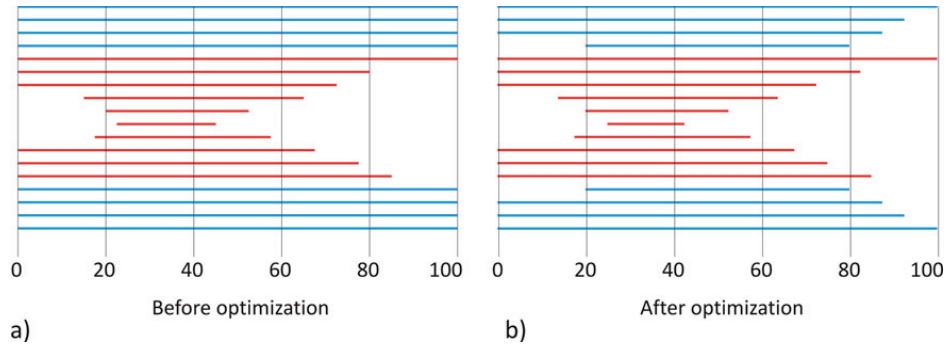


Figure 8-18 Procedure of optimization software for distribution of  $\pm 45^\circ$  anti-buckling plies.



**Figure 8-19** Distribution of  $\pm 45^\circ$  and UD plies before and after optimization of a flange. Blue lines are  $\pm 45^\circ$  plies and red lines are UD plies.

### 8.8 Results of 100 m main spar design

The 12 different FEM models were successfully optimized with regards to UD and  $\pm 45^\circ$  ply distribution. Already after the first iteration, it was clear that the models using a unsymmetric ply distribution were heavier and experienced larger deflections than the models using a symmetric ply distribution. As expected, this design approach resulted in a very thick top flange and a thinner bottom flange (Figure 8-2a). The thick top flange caused UD plies to be placed closer to the center of the spar, thus contributing less to global spar stiffness. It can be concluded that when designing a main spar, the UD plies should be placed equally in the top and bottom flange (Figure 8-2b). In this way each UD ply will be placed where it contributes the most to bending stiffness, thereby limiting deflections and stresses in the most efficient way. In the further work of this thesis only the models with a symmetric design are used.

The six FEM models with a symmetric design were developed and ply distribution optimized with regards to strength and buckling resistance. Ply distribution for these models are included in Appendix B. Table 8-3 presents the deflections and buckling loads for the six models during the primary and secondary loads. Comparing the models with no stiffness criteria shows that the two models with UD carbon fibers have deflections of 23-24 m, whilst the glass fiber model (S-NS-G) has nearly twice the deflection (44.6 m). The deflections of the two carbon models (S-NS-C and S-NS-H) are basically the same and confirms that the UD carbon plies are carrying the flapwise load and that there is little contribution from the  $\pm 45^\circ$  plies. The hybrid model has a slightly larger deflection than the full carbon model, which is due to the larger amount of  $\pm 45^\circ$  plies, thereby moving the UD plies closer to the spar center. In Figure 8-20 spar deflections are plotted for carbon spars with and without stiffness criterion and the glass fiber spar with no stiffness criterion. The plot clearly illustrates how much larger the deflections are for a glass fiber spar when there is not stiffness criterion applied. Appendix C.1 through C.3 contains plots of the axial stresses in the UD plies for the three spars plotted in Figure 8-20.

**Table 8-3** Properties of FEM model using symmetric design. No  $\pm 45^\circ$  plies needed for S-S-G model. The thick UD plies alone had sufficient buckling resistance.

Model	Primary load			Secondary load		
	Tip deflection [m]	Linear eigenvalue buckling	Non-linear buckling analysis	Tip deflection [m]	Linear eigenvalue buckling	Non-linear buckling analysis
S-NS-C	23.5	2.05	1.04	13.2	2.06	1.43
S-NS-H	24.5	2.01	1.04	13.8	2.04	1.27
S-NS-G	44.6	2.03	1.09	25.1	2.00	1.35
S-S-C	15.6	2.04	1.17	8.8	2.06	1.32
S-S-H	15.4	2.13	1.19	8.7	2.04	1.33
S-S-G	15.2	2.46	1.46	8.6	2.02	2.01

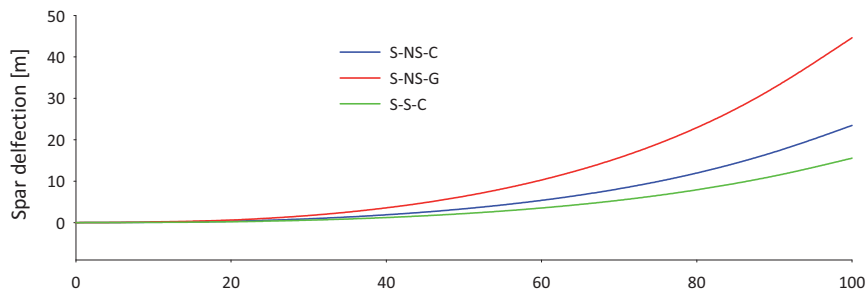


**Figure 8-20** Spar deflection of carbon fiber spar with no stiffness criterion (S-NS-C), carbon spar with stiffness criterion (S-S-C) and glass fiber spar with no stiffness criterion (S-NS-G).

For all the models with no stiffness criterion (S-NS-models) the predicted buckling load by non-linear analysis is very close to 1.0 for the primary load case. This confirms the assumption of a design factor  $\beta=2.0$  between the buckling loads found by linear and non-linear analysis for large deflection cases. For the S-NS-models during the secondary load case and for all the load cases of the S-S-models (excluding S-S-G because this model contains no  $\pm 45^\circ$  plies) the predicted buckling load by non-linear analysis is 1.17-1.43 suggesting that a factor of  $\beta=2.0$  is too large for these cases. This is explained by the smaller deflections in these analysis, thus resulting in a better agreement between a linear and non-linear buckling prediction. For these models the buckling factor  $\beta$  could have been reduced, thereby achieving a buckling load closer to 1.0 when performing a non-linear analysis. There is no need for a buckling load above 1.0 since the UD plies are designed to fail at this load. A smaller factor would also reduce the amount of anti-buckling plies used in the design, thereby saving additional weight. The results show that

linear eigenvalue buckling analysis can be used to distribute the  $\pm 45^\circ$  anti-buckling plies. By using a design factor  $\beta$  one can take into account that a linear buckling analysis over-predicts the buckling load for large deflection problems. This factor should be adjusted to the specific load case by comparing linear and non-linear buckling analysis.

The weight of the UD and  $\pm 45^\circ$  plies used in the flanges were extracted from the FEM analysis and are presented in Table 8-4. It is clear that there is a very large weight difference between the two glass fiber models. The deflection criterion causes the weight of the glass fiber spar to increase from 67.4 tons (S-NS-G) to 114.5 tons (S-S-G). The stiff glass fiber spar needed such large amounts of UD plies that there was no need for  $\pm 45^\circ$  anti-buckling plies. This confirms that the stiffness criterion has a large impact on spar weight for the glass fiber option. For both the carbon and hybrid spar, the deflection criterion resulted in no significant change of weight. Naturally the models without a stiffness criterion required less UD carbon plies, but these laminates were more susceptible to buckling failure and thus needed more  $\pm 45^\circ$  anti-buckling plies, resulting in little net weight change. Studying the weight of the carbon fiber spar in more detail one can see that it becomes 1.1 tons heavier with a stiffness criterion. There is a 79 % weight increase of the UD plies and 32 % weight reduction of the  $\pm 45^\circ$  anti-buckling plies, suggesting that there is not a linear relationship between the amount of UD and  $\pm 45^\circ$  plies needed. The hybrid model on the other hand became 2.6 tons lighter with the stiffness criterion. This is a somewhat surprising result because one would expect an increase in spar weight due to the stiffness criterion. The reduction in weight can be explained by the increased amounts of UD carbon fiber plies to be placed in the hybrid spar. This in turn reduced the amount of  $\pm 45^\circ$  glass fiber plies needed to prevent buckling, resulting in an overall weight reduction. Both the carbon and hybrid solutions use nearly the same amount of UD plies in the spar flanges. But, Table 8-4 also shows that a hybrid spar is considerably heavier than a carbon spar due to almost twice the amount of  $\pm 45^\circ$  plies needed.

**Table 8-4** Weight of UD and  $\pm 45^\circ$  plies in the different models.

Model	Weight of UD plies in flanges [ton]	Weight of $\pm 45^\circ$ plies in flanges [ton]	Total weight of flanges [ton]
S-NS-C	12.6	27.5	40.1
S-NS-H	12.1	53.3	65.4
S-NS-G	20.6	46.8	67.4
S-S-C	22.5	18.7	41.2
S-S-H	23.3	39.3	62.6
S-S-G	114.5	0.0	114.5

### 8.9 Simple cost estimate of spar flanges

The results from the 100 m main spar show a large difference in the amount of material used for the pure carbon or the pure glass solutions. For the wind turbine industry the fabrication cost is of great importance because it can be related to cost/watt. The blades stand for 10 % of the total turbine cost and a cost reduction of blades is therefore important (E. Hau, 2006). Devold AMT, a leading manufacturer of reinforcements for the wind turbine industry, operates with 2 €/kg for glass fiber and 34 €/kg for carbon fiber. Over the last six years the price of carbon fiber has risen dramatically. Due to increased demand it has more than quadrupled since 2003. One major reason for the increased demand has been the development of the new jetliners from Boeing (787) and Airbus (A350) which use large amounts of carbon fiber in their wing and fuselage structures in order to reduce weight and thereby fuel consumption (USA Today, 2007). In a court settlement in 2008, Toray (a leading producer of carbon fiber) agreed to pay the US Government 15.25 million US dollar to settle a lawsuit alleging that they had conspired to fix prices of carbon fiber. This is one of several settlements where Toray together has paid 62 million US dollars. It is therefore reasonable to believe that the price on carbon fiber is currently artificially high and that it can be expected to drop in the future.

The challenge for the wind turbine industry is that they are competing about the same medium quality carbon fiber as the aircraft industry. High tow industrial grade carbon fiber has been tried in the wind turbine blade industry, but has not generated the promised weight savings due to large knock-down factors on compression strength (G. Gardinger, 2007).

Only the flanges of the main spar are included in the cost analysis and a fiber volume fraction of 55 % with 3 €/kg epoxy is assumed. An initial estimate of the production time of the spar flanges was done in order to estimate the cost of labor. Assuming that each ply is 1 mm thick, the total number of plies was calculated. Further it was assumed that a 100 m ply could be laid down in three minutes and one additional minute was added for each ply, allowing for trimming and cutting before the next ply is laid down. These rough estimates showed that a carbon flange could be made in approximately 6 hours whilst 18 hours was needed for the glass fiber flange. Estimating that four people are needed in this operation, the cost of labor was found insignificant compared to the material cost. The cost of labor has therefore not been included in the price comparisons presented in Table 8-5.

The price of a carbon fiber spar is very little affected by the stiffness criterion. Both models have a material cost close to one million Euro. Glass fiber naturally yields the cheapest solutions (153 and 259 k€), has a weight of 114.5 ton, 73.3 ton more than a carbon fiber spar. The weight of the hybrid model is almost not affected by the stiffness criterion, but results in a cost increase from 404 k€ to 630 k€. The graph in Figure 8-21 shows how the cost of carbon fiber will affect the price of the stiff carbon and hybrid models (S-S-C and S-S-H). As a reference, the cost of the stiff glass fiber flange is also plotted. The price of the carbon and hybrid options will break even with the price of the glass fiber spar at carbon price of 8 € and 10 €. The latter corresponds approximately to the price levels in 2002. It is very unlikely that prices will drop to this level in the nearby



future due to the currently high demand for carbon fiber. Most likely the carbon and hybrid models will break even at a higher carbon fiber cost than predicted here due to the reduction of blade weight, which in turn generates savings throughout the rest of the turbine.

**Table 8-5** Deflection, weight and price of flanges for the symmetric models.

Model	Deflection of spar tip [m]	Weight of flanges [tons]	Material cost of UD plies in flanges [k€]	Material cost of DB plies in flanges [k€]	Material cost of flanges [k€]
S-NS-C	23.5	40.1	292	639	930
S-NS-H	24.5	65.4	282	121	403
S-NS-G	44.6	67.4	47	106	153
S-S-C	15.6	41.2	522	433	955
S-S-H	15.4	62.6	541	89	630
S-S-G	15.2	114.5	259	0	259

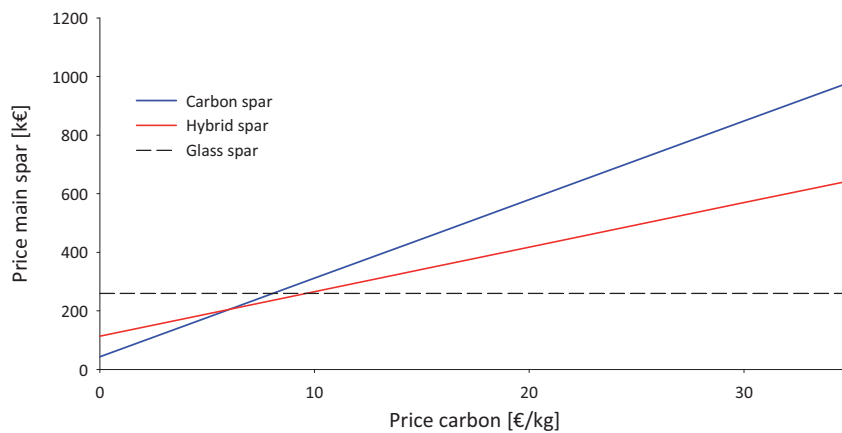


**Figure 8-21** Price of carbon spar (S-S-C model) and hybrid spar (S-S-H model) as a function of carbon price. The price of a stiff glass fiber spar (S-S-G model) is plotted for comparison.

## 8.10 Blades with pitch control

The largest wind turbines today use pitch control to optimize blade performance and to limit loads. In a large wind turbine there will most likely be a backup power unit such that if grid connection is lost, the turbine is still able to control the pitch and yaw of the blades. It is highly unlikely that the turbine will experience a failure of pitch and yaw control during the 50-year gust and designing the turbine for this scenario would be too

conservative. The analysis in section 8.8 also shows that the deflection criterion leads to very heavy designs for the glass fiber solution (114 tons). During the 50-year storm the turbine is shut down and put in emergency mode. The blades are pitched  $90^\circ$  to minimize the load on the turbine and the rotor-brake is applied (L. Kühlmeier, 2006). According to the IEC 61400-1-2005 standard (DLC 6.1<sup>1</sup>) one has to account for a yaw misalignment of  $\pm 15^\circ$  when hit by the  $70 \text{ m/s}$  gust. Assuming that the blade is hit at an angle that produces the highest possible lift, this will generate large flapwise bending forces (Figure 8-22a). There is no danger of the blade hitting any structure, but it needs sufficient strength and buckling resistance. In the case of the 1-year extreme gust ( $52.5 \text{ m/s}$ ), it is still regarded as likely that the turbine will experience this wind during a failure of the pitch/yaw system. Therefore a yaw misalignment of  $0$  to  $\pm 180^\circ$  has to be considered (Figure 8-22b and c). Regarding tower interference, the worst case scenario would be a blade pitch of  $0^\circ$  and the  $52.5 \text{ m/s}$  gust hitting the blade perpendicularly, causing flapwise bending towards the tower. For a wind turbine with blade pitch control and backup power the three load cases for designing the main spar are:

*Load case 1*

Blade is pitched at  $90^\circ$  angle and hit by the  $70 \text{ m/s}$  gust from a direction that causes maximum lift. Blade needs sufficient strength and buckling resistance.

*Load case 2*

Failure of turbine pitch and yaw system. Blade is struck perpendicularly by the 1-year extreme gust ( $52.5 \text{ m/s}$ ), causing deflection towards tower. Blade needs to be stiff enough to avoid striking the tower in addition to sufficient strength and buckling resistance.

*Load case 3*

As load case 2, but in the opposite direction. Now the suction side of the blade is in tension and the pressure side in compression load. Blade needs sufficient strength and buckling resistance, but there is no limit on deflection.

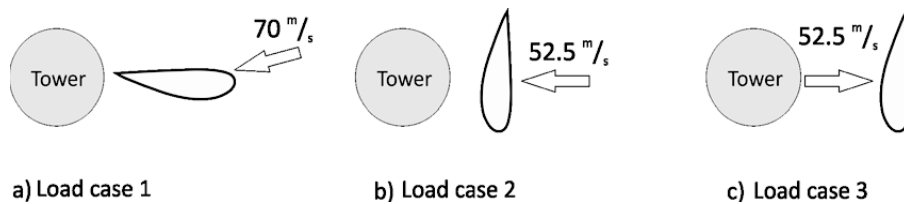


Figure 8-22 Load cases for a 100m pitch controlled wind turbine blade.

For *Load case 1* it is assumed that all airfoils along the main spar are characterized by the performance curve from the airfoil Risø-B1-18 (P. Fuglsang, 2004). This airfoil was developed at Risø for the use on large wind turbines and is therefore a reasonable assumption of airfoil lift performance. Experimental data of the airfoil's coefficient of lift

---

1. DLC: Design Load Case

( $C_l$ ) vs. angle of attack is shown in Figure 3-7. Due to blade twist the airfoils at the blade tip generate the highest lift and decreases towards the blade root. The performance data from Risø-B1-18 were applied from the blade tip at 100 m to the start of the transition zone at 22 m. Here blade cross section changes from an airfoil to a circular cross section at 5 m. From 22 m and to the blade root (0 m) it is assumed that no lift is generated by the cross sections. Together with the twist and chord distribution, the bending moment on the main spar could be found (Figure 8-23). By using pitchable blades the root bending moment during extreme load is reduced from 87.6 MN to 67.9 MN (23 % reduction). Load cases 2 and 3 are calculated the same way as the “Secondary load case” used previously.

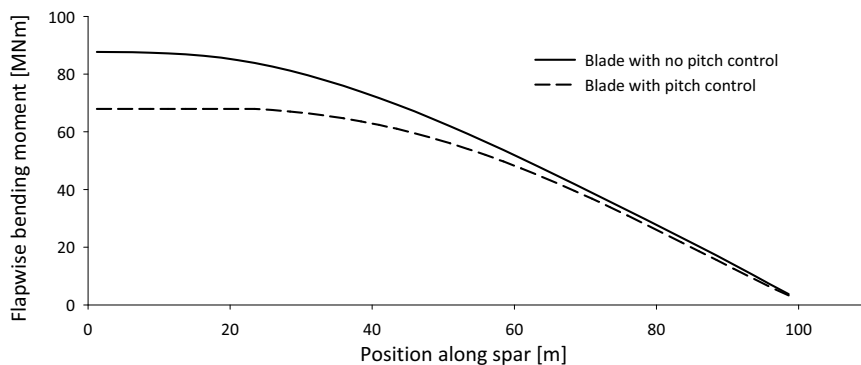


**Figure 8-23** Flapwise bending moment along main spar for blade with and without pitch control during 50-year extreme gust.

**Table 8-6** Properties of 100 m main spar with pitch control, resulting in reduced loads. NLC: New Load Carbon, NLH: New Load Hybrid, NLG: New Load Glass.

Model	Tip deflection [m]	Weight UD [ton]	Weight DB [ton]	Weight flanges [ton]	Price UD [k€]	Price DB [k€]	Price flanges [k€]
NLC	11.62	14.6	25.5	40.2	340	592	932
NLH	11.51	15.6	49.9	65.5	363	113	476
NLG	15.62	49.8	25.8	75.6	113	58	171

Table 8-6 presents the deflection, weight and material cost of a carbon, hybrid and glass fiber solution for blades using pitch control to limit the extreme loads. For both the carbon and hybrid solutions (NLC and NLH), Load case 1 proved to be the dimensioning load for the distribution of UD plies. For the glass fiber solution (NLG) the large amounts of UD glass fiber plies needed to provide enough strength during Load case 1 were insufficiently stiff when subjected to Load case 2. Hence, for the glass fiber solution Load case 2 was the dimensioning load. Consequently the carbon and hybrid solutions are dimensioned by stress (minimum material safety factor of 1.73) and the glass fiber solution is dimensioned by stiffness. In Figure 8-24 the deflections of the spar are plot-

ted while subjected to the 50-year gust (Load case 1). The deflections of the spars with UD carbon fiber in their flanges (NLC and NLH) have practically identical deflections. In the Appendix C.4 through C.6, plots are included showing the stresses in the top and bottom flanges for all three models. Both the carbon and hybrid solutions are too stiff (11.51 m and 11.62 m) when compared to the blade's maximum allowable deflection of 15.4 m. For the glass fiber solution there is a large reduction of flange weight (34 %) due to the reduced loads. The all carbon spar has 7.9 tons less UD plies, but needs 6.9 tons more  $\pm 45^\circ$  plies for buckling stability, resulting in a weight reduction of only 1 ton. Surprisingly the hybrid model ended up being 2.9 tons heavier than the hybrid blade with no pitch control. Also here the required amount of UD carbon plies is less (7.7 tons), but the hybrid model experiences a weight penalty due to the increased amount of  $\pm 45^\circ$  glass fiber needed to provide sufficient buckling resistance (10.6 tons). The full carbon spar still has a material cost close to one million Euro. Compared to a stiff hybrid spar (S-S-H), the reduced loads resulted in a cost reduction from 630 k€ to 476 k€. For a glass fiber spar the pitch control resulted in a material cost reduction from 259 k€ to 171 k€.

Plotting the flange price as a function of the price of carbon fiber shows that for pitch controlled blades the material costs now breaks even at 4 €/kg for the carbon model and 5 €/kg for the hybrid model which is very unrealistic for the nearby future (Figure 8-26).

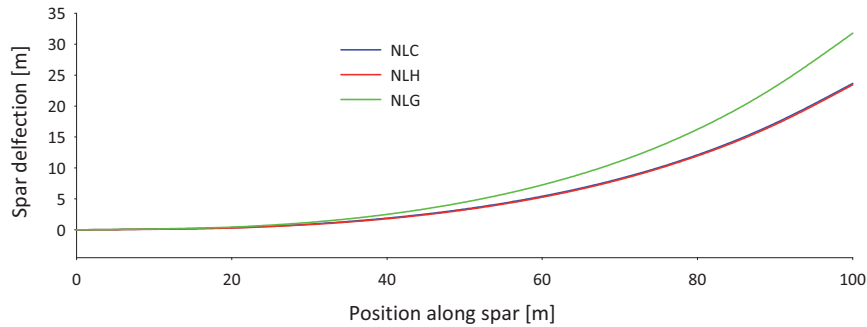


Figure 8-24 Deflection of spar with pitch control during 50-year extreme gust ( $70 \text{ m/s}$ ).

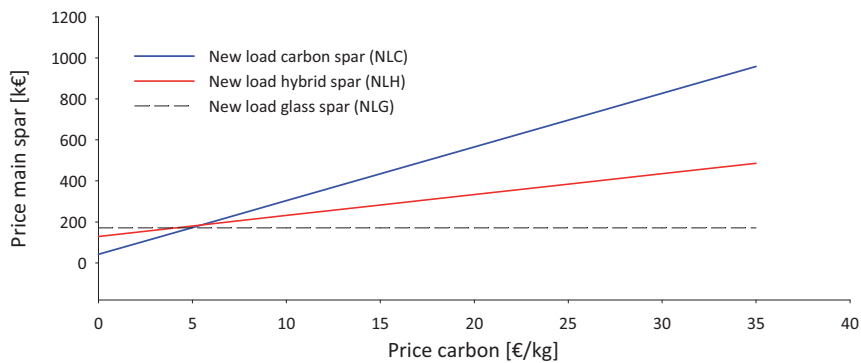


Figure 8-25 Price of main spar flanges as a function of carbon price for blades with pitch control.

With the currently high demand for carbon fiber it is unrealistic to expect the price to drop from today's 34 €/kg to below 10 €/kg. Even though the carbon and hybrid models are promising solutions regarding weight, the high carbon price makes them a very expensive option. Also the buckling performance of the UD carbon plies in the flanges needs to be increased in order to reduce the amount of  $\pm 45^\circ$  plies needed. To explore how price and buckling resistance would affect the carbon and hybrid models two assumptions were made:

- The price of carbon fiber is reduced to the half due to increased production capacity.
- The buckling resistance of the flanges is increased by 100 % and thereby reduces the amount of  $\pm 45^\circ$  plies needed. L. Kühlmeier (2006) showed how the use of optimization software increased the buckling resistance of the  $\pm 45^\circ$  anti-buckling plies by optimizing ply angles and stacking sequence. Another possible way of increasing buckling resistance would be the use of core materials in the flanges as suggested by J. Jensen et al (2005). In their work the weight of a 90 m main spar was reduced by 22.3 % through the use of sandwich materials in the flanges. Also, the results from the models using UD carbon fiber in the flanges show that these models are too stiff when compared to the maximum allowable deflection of 15.4 m. Additional buckling resistance could be gained by altering ply angles and stacking of the UD plies. This would increase main spar deflections, but there is room for increasing the deflections by 3.9 m before the deflection criterion is violated.

Table 8-7 shows how these assumptions will affect the weight and price of the main spar flanges. Note that the cost presented for the models with reduced amount of  $\pm 45^\circ$  plies does not include increased production cost due to a more advanced design. To reach a clear conclusion it would be necessary to evaluate how blade weight affects the cost of the rest of the wind turbine system. But it is clear that reducing the amount of  $\pm 45^\circ$  plies needed will have a significant effect on the blade weight and price. For the carbon blade both the weight and price was reduced by 33 % and for the hybrid model, weight and price was reduced by 38 % and 17 %. The glass fiber model has the lowest cost, but is more than twice as heavy as the carbon fiber option (63 tons vs. 27 tons). If carbon prices are reduced by 50 %, the carbon option will be twice the cost of glass fiber, but half the weight.

**Table 8-7** Weight and price for carbon and hybrid models assuming that the price of carbon is reduced by 50 % and that the amount of  $\pm 45^\circ$  is also reduced by 50 %. NLG contains only glass fiber and is not affected by carbon fiber price. Numbers in parenthesis are percentage change compared to the model with all of its  $\pm 45^\circ$  plies and full price carbon.

Model	100 % $\pm 45^\circ$ plies			50 % $\pm 45^\circ$ plies		
	Spar weight [tons]	Full carbon price [k€]	Half carbon price [k€]	Spar weight [tons]	Full carbon price [k€]	Half carbon price [k€]
NLC	40	932	487 (-48 %)	27 (-33 %)	626 (-33 %)	332 (-64 %)
NLH	66	476	303 (-36 %)	41 (-38 %)	419 (-12 %)	246 (-48 %)
NLG	76	171	-	63 (-17 %)	142 (-17 %)	-

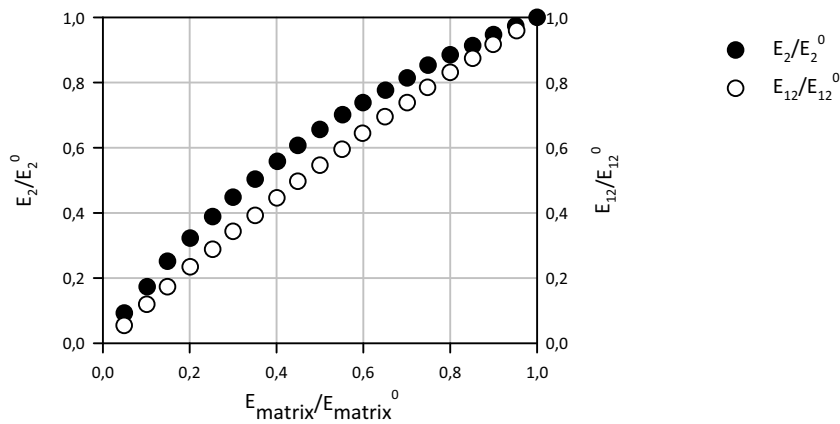
### 8.11 Degradation of composite ply properties

The mechanical properties used in the FEM analyses of 100 m long spars represent those of composite materials right after their production. Wind turbine blades are subjected to a very high amount of cyclic loads during their 20-year service life. For a composite material the modulus of elasticity tends to reduce under the effect of cyclic loading. The main reason for this is the formation and accumulation of matrix cracks due to axial/transverse tensile fatigue loads. The DNV offshore standard for wind turbines (DNV-OS-J102-2006) addresses the effect of material stiffness degradation due to cyclic loading, but does not give any suggestions by how much the stiffness is reduced. These can be found in the DNV offshore standard for composite components (DNV-OS-C501-2003) and are listed in Table 8-8. For both glass and carbon fiber composites the modulus of elasticity in main fiber direction ( $E_1$ ) is expected to drop by 10 %. In the transverse direction the modulus ( $E_2$ ) may drop to 0 in tension, but with no change in compression. Both the shear modulus ( $G_{12}$ ) and Poisson's ratio ( $\nu_{12}$ ) are only expected to experience a slight drop, but these values are not specified in the standard. Reducing the transverse modulus to 0 in tension can be considered to be a conservative approach since the matrix in the ply will not be totally degraded by the cyclic loads. This large reduction transverse modulus will also most likely cause numerical challenges in a FEM analysis due to the extreme anisotropy of the laminate (convergence problems)

**Table 8-8** Change of modulus of elasticity under cyclic loading. Reproduced from DNV-OS-C501-2003.

Property	Description	Comment
$E_{1\text{fiber}}$ UD-ply	Modulus of elasticity in main fiber direction	10 % reduction for glass and carbon fiber.
$E_{2\text{matrix}}$ UD-ply	Modulus of elasticity transverse to main fiber direction	Drops to 0 in tension. No change in compression.
$G_{12\text{linear}}$	In plane shear modulus in the linear range	Slight drop (unknown)
$\nu_{12}$	Ply major Poisson's ratio	Slight drop (unknown)

In S. W. Tsai (1988) a micro mechanical approach was used to determine the effect of matrix cracking in a laminate. It is thought that lowering the transverse and shear modulus to nearly zero is not a reasonable approach because the plies with matrix cracks are not totally disintegrated. Instead it is recommended to replace the plies containing matrix cracks with a quasi-homogenous ply with reduced matrix modulus. Micro mechanics analysis is then used to calculate the degree of transverse and shear modulus reduction. The observed stiffness reductions in Figure 8-20 are for a CFRP T300/5208 laminate and are shown in dimensionless quantities. References S. W. Tsai (1988) and S. W. Tsai (2008) are recommended for further reading about matrix degradation models.

**Figure 8-26** Relative reduction in transverse and shear modulus due to reduction in matrix Young's modulus for CFRP T300/5208 baseline ply (reproduced from S. W. Tsai,1988).

The effect of ply properties degradation in a wind turbine spar is not within the scope of this thesis, but it is a highly important issue regarding blade design for wind turbines. Four non-linear analyses were done in order to explore how material degradation would

affect the performance of a 100 m spar. The hybrid spar for a blade with pitch control (NLH analysis) was selected for this study and Table 8-9 shows how the ply properties in the flanges of the hybrid spar were gradually degraded. The spar was subjected to Load case 1, representing the 50-year gust (see Section 8.10). The flanges of the spar were gradually degraded in order to see how each change affected spar deflection and buckling load. The results from the analyses are shown in Table 8-9 and Figure 8-27.

**Table 8-9** Non-linear analysis of hybrid spar (NLH) with gradually degrading ply properties.

Model	Description	Buckling load	Deflection at 50-year gust
1	NLH blade with properties of virgin material	1.057	22.75 m
2	NLH blade with 10 % reduction of $E_1$ in flange	1.060 (+0.3 %)	24.7 m (+8.6 %)
3	Model 2 with $E_2$ in flange reduced to 10 % of original value	1.052 (-0.5 %)	25.07 m (+10.2 %)
4	Model 3 with shear modulus $G_{12}$ in flange reduced to 10 % of original value	0.703 (-33.5 %)	not available

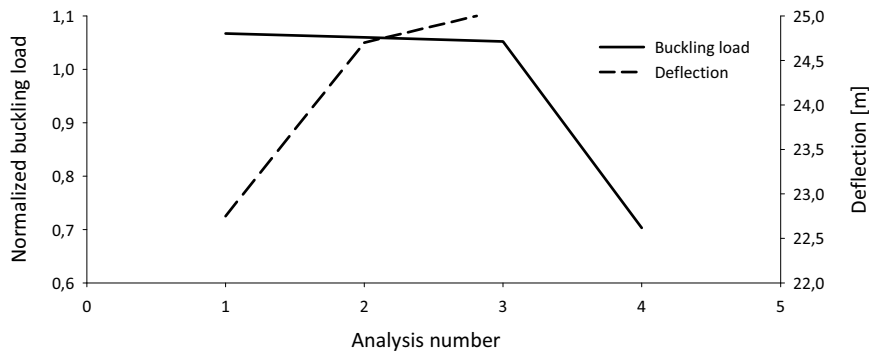


**Figure 8-27** Spar buckling load and deflection as material properties are increasingly degraded in analysis 1 through 4. In analysis 4 (reduction of  $G_{12}$ ) the spar failed to reach design load and a deflection result is therefore not included.

The 10 % reduction in axial stiffness ( $E_1$ ) resulted in a 8.6 % increase in deflection and did not affect the buckling load. Neither did the reduction in transverse stiffness ( $E_2$ ) resulted in any significant changes. The largest change was found when reducing the shear modulus ( $G_{12}$ ) in the flanges. Buckling load was reduced by 33.5 %, causing the spar to fail before reaching full load. It should be noted that when the transverse modulus ( $E_2$ ) was reduced to 1000th of its original value the buckling load was reduced by 6.7 %. An equal reduction in flange shear modulus ( $G_{12}$ ) resulted early termination of analysis due to convergence problems. This confirms the numerical challenges associated with reducing transverse and shear modulus close to zero. The large reduction in



buckling load due to reduction in shear modulus ( $G_{12}$ ) shows that the shear modulus is critical for structural integrity. These results show that the effect of material degradation on spar performance should be evaluated in future studies.

### 8.12 Conclusions from FEM analysis of 100m main spar

The results show that the UD plies contribute the most to spar stiffness when they are equally placed in both top and bottom flanges. The linear buckling analysis tends to overestimate the buckling capacity for the large deflections caused by the 50-year extreme wind load. For models with large deflections it was found that the linear eigenvalue analysis overestimated the buckling load by about approximately a factor 2 compared to non-linear results. Linear eigenvalue analysis can be used to distribute the  $\pm 45^\circ$  anti-buckling plies, but should be correlated with a non-linear analysis.

Pitch control of the blades is found to reduce the loads on the blade and thereby the weight and cost of the material needed (except for the hybrid model). For a 100 m blade using UD carbon fiber to limit deflections, the UD plies can be distributed according to the minimum allowable material safety factor (1.73). This gives the blade sufficiently stiffness but causes it to become more susceptible to buckling. Large amounts of  $\pm 45^\circ$  plies are needed to prevent the UD plies from buckling. Improving the buckling performance of the laminate will be important in order to reduce both weight and cost of the spar. This might be achieved by optimizing ply angles and stacking sequence. Another possible way of improving buckling resistance is the usage of core materials in the flanges, as suggested by J. Jensen et al. (2005). The current price of carbon fiber (34 €/kg) would make the blades too costly and therefore hampers its use in wind turbine blades. If future prices are lowered and combined with optimization of anti-buckling plies, a carbon or hybrid spar might become the most cost efficient choice due to large weight reductions. In order to reach a conclusion on material choice, it will be necessary to combine the results from these simulations with a cost model that can predict how blade weight affects the system cost of the wind turbine. Tor A. Nygaard (1999) presented a cost model for wind turbines based on work by Harrison and Jenkins (1993). This model predicts how the cost of gear, brakes, tower, nacelle, etc are affected by the blade's length, weight and predicted power output. The model was, however, developed for onshore wind turbines and needs to be modified in order to accurately represent the cost picture for offshore wind turbines. Cost of transportation, installation, tower and foundation are most likely very different for an offshore wind turbine.

The analyses developed in this chapter have used composite material properties representing those of right after manufacturing. In order to develop realistic analyses and ply definitions, material degradation models should be used to account for the cyclic fatigue load a spar experiences during its 20-year service life.



## 9 Optimizing buckling resistance

The FEM analysis in Chapter 8 focused on how load and choice of material affects the design, weight and material cost of a 100 m main spar. Unidirectional plies gave flapwise bending stiffness and  $\pm 45^\circ$  plies provided buckling resistance. It became clear that one way of reducing spar weight would be to improve the buckling resistance of the main spar. If the plies are used in their most efficient way, it could reduce the amount of anti-buckling plies needed and thereby save additional weight. Using double bias plies (e.g.  $\pm 30^\circ$ ,  $\pm 45^\circ$  or  $\pm 60^\circ$ ) in equal amounts on both sides of an UD ply is regarded as a standard way of increasing a laminate's buckling resistance. Generally this works quite well, but might not be the optimal solution for the given load case. E. Lund (2005) and L. Kühlmeier (2006) studied how the anti-buckling plies of a flange could be optimized and found that there was a potential of improving the buckling performance of the main spar by 10-20 % by altering ply angles and stacking sequence. The results from Chapter 8 show that the hybrid spar with pitch control (NLH model) has the largest potential for weight saving. If the buckling resistance of the hybrid spar is doubled, this would lead to a 38 % weight reduction (25 tons) of the spar. This increase in buckling performance might be achieved by optimizing the lay-up of both the glass fiber  $\pm 45^\circ$  anti-buckling plies and the UD carbon plies.

Optimizing a structure made of composite materials can be a very challenging task because of the many variables involved. Ply angle, thickness, stacking sequence and choice of material affect the structural behavior. In the daily design process engineers use a combination of calculations, experience, parametric studies and testing to search for the optimal solution. For an engineer, optimization software can be a powerful tool, allowing for fast and efficient determination of the optimal result for a given problem. Another benefit is that it can yield results that are far from intuitive and have superior performance compared to more traditional solutions (L. Kühlmeier, 2006). The outcome of an optimization study is greatly affected by the boundary conditions. Failing to realize this can yield a solution that is optimal in one situation, but greatly insufficient in another. For an introduction to optimization techniques the reader is referred to Arora (1989). L. Kühlmeier (2006) and E. Lund (2005) studied the compression flange of the main spar and developed different algorithms to optimize it against buckling. L. Kühlmeier (2006) modelled a section of the top flange, whilst E. Lund (2005) modelled a section of the upper half of the blade (Figure 9-1). In both studies the model was loaded by an axial compression force and linear bifurcation buckling simulation was used to determine the buckling load. Within certain constraints, the optimization software was allowed to change ply thickness and angle.

### 9.1 Optimization models

Since the focus of this work was not to develop an optimization software, it was decided to use a brute-force approach and solve for all possible solutions for a given problem. Matlab was used to create a matrix containing all possible combinations of variables and to generate the Abaqus input files. After completion of all the analysis, the results were automatically written to an Excel file.

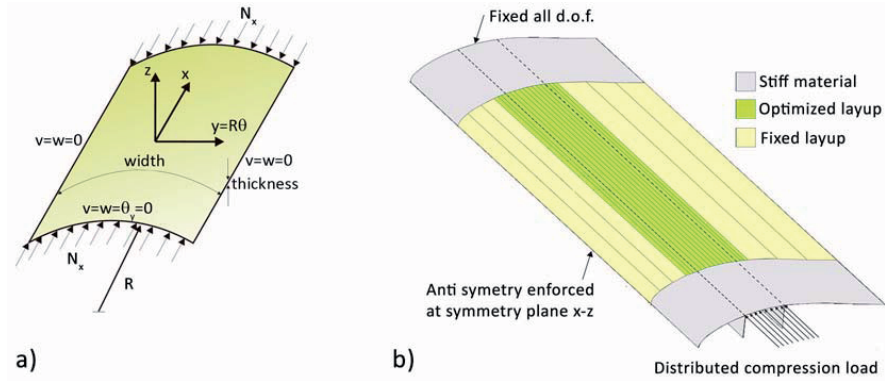


**Figure 9-1** Buckling optimizations models for the top flange by a) L. Kühlmeier (2006) and b) E. Lund (2005).

Three different sections of the 100 m main spar were studied to see how curvature and size affected the optimal solution (Figure 9-2). The sections were picked from 22, 50 and 90 m of spar length. Some small simplifications were made to the original sections in order to create symmetric sections. Symmetric sections were preferred such that the buckling mode would not be biased towards one side of the section.

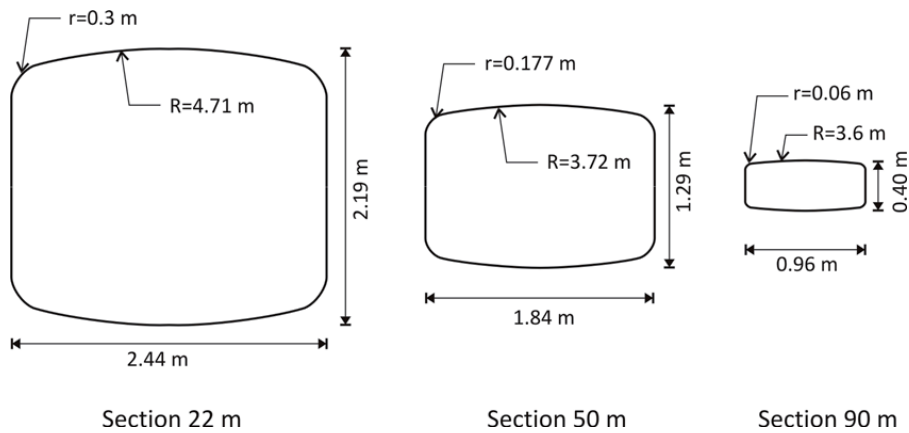


**Figure 9-2** Sections from 22, 50 and 90 m used in the optimization study.

### 9.1.1 Bending model

In order to replicate the bending moments and stresses experienced in the top flange during flapwise bending loads, an evenly distributed pressure load was applied over a simply supported beam (Figure 9-3a). A distributed pressure load was chosen because this would gently introduce the bending moment and ensure that buckling appeared in the middle of the spar. The distributed pressure load was increased until the stresses in

the top flange were close to those levels found in the 100 m main spar simulation. The boundary conditions were created by defining a reference point at each end of the spar and linking the spar edges rigidly to these reference points such that they would act as hinges (Figure 9-3b). Both reference points could rotate about the z-axis and were restrained from rotating about the x and y-axis. All translations were restrained for the left reference point, while the right reference point was free to move in x-direction. In order to reduce the size of the model the length-to-width ratio was set to approximately 20 for all models. For the 22 m and 50 m sections this resulted in a 50 m long beam model and a 20 m beam for the 90 m section.

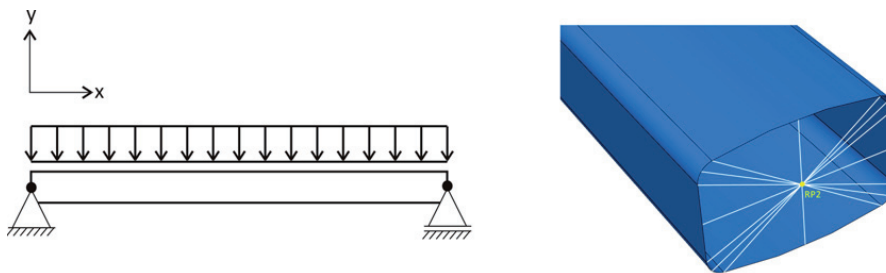


**Figure 9-3** a) Load distribution of model. b) Linking beam edges to the reference point.

Four-node shell elements with reduced integration were used in the model. A discussion on element properties is provided in Chapter 8. A mesh refinement study was performed for all three models to minimize the amount of elements needed and to make sure that the buckling load was predicted with sufficient accuracy. A discussion on element properties is provided in Chapter 8. An eigenvalue buckling analysis with a very fine mesh was performed on all models and functioned as a benchmark for the mesh optimization. The fine mesh used an element length of 0.05 m and resulted in 92 000 elements (672 684 DOF). Figure 9-4 shows the shape of the first buckling mode for the bending model. The buckling shape is mainly present in the center of the spar and in order to further reduce the number of elements needed, the middle 10 m of the spar used a finer mesh than the outer parts of the beam. This refinement also ensured a minimum of 12 elements across the wavelength of one buckling mode shape, as recommended in DNV-OS-C501-2003 standard. During the mesh size study, both element length and width were adjusted. Five elements were used across the corners and six elements across the shear webs. Table 9-1 shows the resulting mesh definitions for the bending models and how much the predicted linear buckling load deviated from the high mesh resolution analysis.

**Table 9-1** Mesh definition in bending models. Linear buckling load is compared to the linear buckling load predicted in an analysis with a high mesh density.

Model	Element length in middle section	Element length in outer sections	Number of elements	DOF	Deviation in linear buckling load [%]
22 m	0.4	0.5	5880	35 628	0.81
50 m	0.4	0.5	5880	35 628	0.76
90 m	0.1	0.3	7504	45 372	0.97

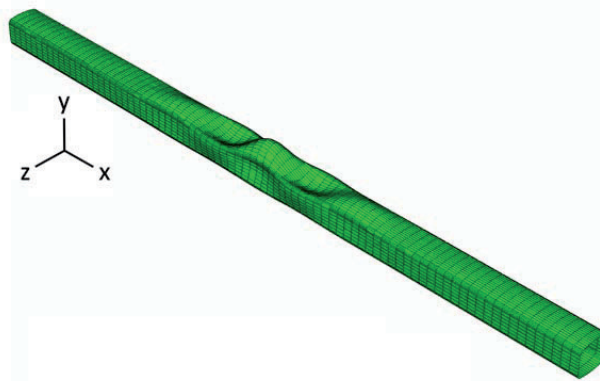


**Figure 9-4** Linear eigenvalue buckling shape of the bending model simulation of the 50 m section. Buckling shape is present only in the middle of the spar.

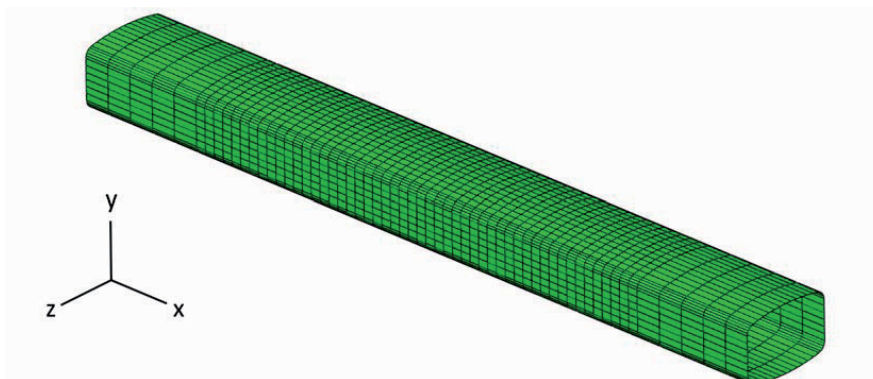


**Figure 9-5** Mesh refinement at the middle of the spar beam (some elements from the outer parts have been removed for clarity).

### 9.1.2 Compression model

Based on the work by L. Kühlmeier (2006) and E. Lund (2005) it was decided to develop a model of the top flange where buckling was introduced by axial compression of the flange. Comparison between the bending and compression model would show how the optimization results are affected by the simplification of the geometry and boundary conditions. The geometry of the bending model was modified by removing the shear webs and bottom flange, leaving the top flange and corners. Figure 9-6 shows that the nodes at both ends are fully restrained (translation and rotation). The lengthwise edges were translational restrained in the y and z direction. The compression load was introduced by displacing the nodes at end B by 0.19 m, resulting in stress levels in the UD carbon plies that were comparable to those found in the 100 m NLH model in Chapter 8. An edge load could also have been used, but initial studies showed that this resulted in stress concentrations at the edge. Figure 9-7 shows that the compression model exhibited a different buckling shape than the bending model. The shape of the first buckling mode appears over the entire length of the flange and with a much shorter wavelength. Equal element length had to be used over the entire flange to ensure the minimum of 12 elements across one buckling mode wavelength. As with the compression model a mesh refinement study was done to limit the number of elements needed and to determine the accuracy of the model. The benchmark analysis with a very fine mesh used an element length of 0.05 resulting in 46 000 elements with 282 282 DOF. Table 9-2 shows the mesh definitions for the compression models.



Figure 9-6 Boundary conditions of compression model.

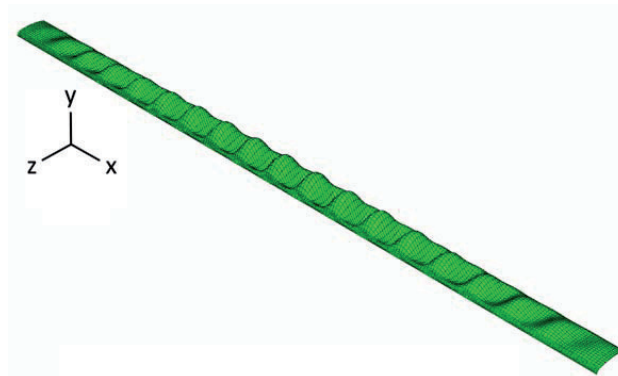


Figure 9-7 Shape of the first linear buckling mode of the compression model. The buckling mode appears almost across the entire flange. Constraints are not included for clarity.

**Table 9-2** Mesh definition in bending models. Linear buckling load is compared to the linear buckling load predicted in an analysis with a high mesh density.

Model	Element length in middle section	Element length in outer sections	Number of elements	DOF	Deviation in linear buckling load [%]
22 m	0.20	0.20	5500	34 638	1.54
50 m	0.17	0.17	6490	40 848	1.19
90 m	0.08	0.08	5522	34 776	1.58

## 9.2 Optimizing the glass fiber anti-buckling plies

In the hybrid spar the flanges consist of 15.6 ton UD carbon fiber and 49.9 ton  $\pm 45^\circ$  glass fiber. This is a very large amount of glass fiber just to provide enough buckling resistance for the load carrying UD carbon plies. If the anti-buckling plies could be optimized for the given load cases, valuable weight reductions could possibly be achieved.

### 9.2.1 Defining the optimization analysis

The number of plies, variations in ply angle, stacking sequence and thickness will generate a very large amount of possible solutions. In order to reduce the number of solutions, the lay-up of the flanges was simplified. Figure 9-8 shows an example of the lay-up used in the flanges. It consists of one ply of unidirectional carbon fiber, providing the spar with bending stiffness, and two plies of glass fiber on both sides of the UD ply, giving it buckling resistance. This laminate simplification has also been used by L. Kühlmeyer (2006) and will allow for easy comparison of results. Ply thicknesses for the carbon and glass fiber at the relevant sections are collected from the hybrid model (NLH) in Chapter 8. The thickness of the  $\pm 45^\circ$  glass fiber plies was reduced until the beam buckled at half of the rated load. This was done to ensure that beam failure is governed by buckling and not by laminate strength. During the optimization of the flanges the following rules were applied:

- Angle and thickness of unidirectional carbon fiber layer is kept unchanged.
- The total amount of glass fiber is kept constant, but the ratio of distribution between the top and bottom plies is varied between 10-90 % by 10 % increments (9 variables).
- The angles of the top and bottom layers ( $\theta_1$  and  $\theta_2$ ) are independently varied between  $0^\circ$  and  $90^\circ$  in  $10^\circ$  increments.  $45^\circ$  is also included, giving a total of 11 variables. The laminate is kept balanced.
- Ply definition of spar corners and shear webs is kept unchanged.



This resulted in the possible number of solutions being:  $N = 9 \times 11 \times 11 = 1089$

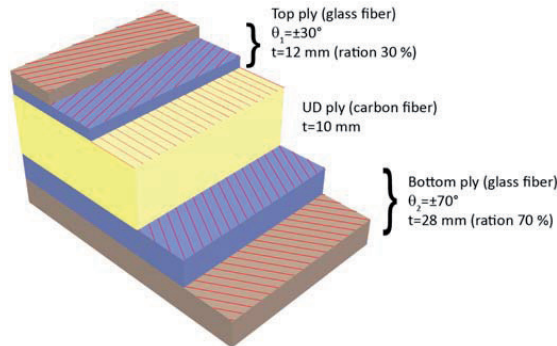


**Figure 9-8** Example of top flange ply definition. UD carbon ply in the middle covered by four glass fiber plies for buckling resistance.

A coordinate system was placed in the middle of each model to ensure correct ply orientations. A discussion on ply orientation in Abaqus is provided in Section 8.5. An example of how ply properties were defined in the analysis input file is provided in Appendix E. Input files were generated from Matlab and passed to Abaqus for linear eigenvalue buckling analysis. With this limited number of possible solutions it was possible to solve all of them within 24 hours. Figure 9-9 together with Table 9-3, 9-4 and 9-5 shows the ply definitions for all the FEM models.

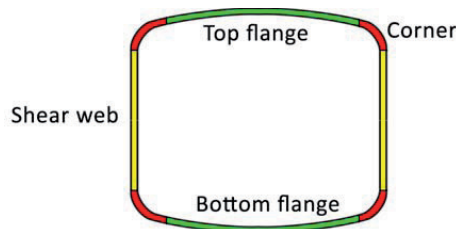


**Figure 9-9** Color coding of the ply definition of the spar.

**Table 9-3** Web ply definitions for FEM model of sections at 22, 50 and 90 m before optimization.

Ply angle	Material	Section 22m ply thickness [mm]	Section 50m ply thickness [mm]	Section 90m ply thickness [mm]
45°	Glass fiber	6	4	1
-45°	Glass fiber	6	4	1
0°	Diab H200 core	10	10	10
-45°	Glass fiber	6	4	1
45°	Glass fiber	6	4	1

**Table 9-4** Corner ply definitions for FEM model of sections at 22, 50 and 90 m before optimization.

	Ply angle	Material	Section 22m ply thickness [mm]	Section 50m ply thickness [mm]	Section 90m ply thickness [mm]
	45°	Glass fiber	8	7.2	5
	-45°	Glass fiber	8	7.2	5
	-45°	Glass fiber	8	7.2	5
	45°	Glass fiber	8	7.2	5

**Table 9-5** Flange ply definitions for FEM model of sections at 22, 50 and 90 m before optimization.

	Ply angle	Material	Section 22m ply thickness [mm]	Section 50m ply thickness [mm]	Section 90m ply thickness [mm]
	45	Glass fiber	8	7.2	5
	-45	Glass fiber	8	7.2	5
	0	Carbon fiber	24	21	3
	-45	Glass fiber	8	7.2	5
	45	Glass fiber	8	7.2	5

### 9.2.2 Results from the anti-buckling ply optimization

For each model the standard lay-up with equal amounts  $\pm 45^\circ$  glass fiber anti-buckling plies on both sides of the UD ply is set as a reference to which all results are compared to. Table 9-6 and Table 9-7 presents the results from the linear buckling optimization study, showing the lay-up that yielded the highest buckling load for each section and the percentage of improvement. A supplementary table containing the actual eigenvalue is included in Appendix D, Table D.1. For the bending model there is an improvement of 7.6-13.0 % of the buckling load and the compression model yields similar improvements (5.1-12.4 %). It should be noted that for the bending models, the largest improvements were made for the cross sections located at 22 and 50 m of the spar. These cross sections are fairly square and have a width/height-ratio between 1.1 and 1.4. For the section at 90 m, which is more rectangular (width/height-ratio 2.4), the improvement was only 7.67 %. The compression model on the other hand made its largest improvement at the 90 m section (12.43 %), whilst the buckling load for the 22 and 50 m sections was only improved by approximately 5 %.

The bending (Table 9-6) and compression (Table 9-7) models yield a very different distribution ratio of the glass fiber anti-buckling plies. In the compression model, 60-80 % of the glass fiber plies are placed on top of the UD carbon ply. This agrees well with the

findings from L. Kühlmeier (2006), which suggested a ratio of 75 %. For the bending model the most optimal lay-up places only 20-30 % of the anti-buckling plies on top of the UD carbon ply. These very different results clearly show how the boundary conditions of the optimization model affects the outcome. Figure 9-10 illustrates the differences between the optimal solution from the bending and compression model for the 50 m section. All the bending models resulted in a top ply with an angle of 90°. The angle of the bottom ply was kept unchanged, except for the 90 m section where it was reduced to 30°. The compression model yielded very similar results with high angles for the top ply (50-70°) and only small adjustments for the bottom ply in the 90 m section (45-50°).

**Table 9-6** Optimal anti-buckling ply angles and ratio for the three different sections optimized by the bending model.

Section	Angle top ply ( $\theta_1$ )	Angle bottom ply ( $\theta_2$ )	Ratio anti-buckling plies on top [%]	Change linear eigenvalue buckling [%]
22 m	90	45	30	11.79
50 m	90	45	30	13.04
90 m	90	30	20	7.67

**Table 9-7** Optimal anti-buckling ply angles and ratio for the three different sections optimized by the compression model.

Section	Angle top ply ( $\theta_1$ )	Angle bottom ply ( $\theta_2$ )	Ratio anti-buckling plies on top [%]	Change linear eigenvalue buckling [%]
22 m	70	45	60	5.93
50 m	60	45	60	5.05
90 m	50	50	80	12.43

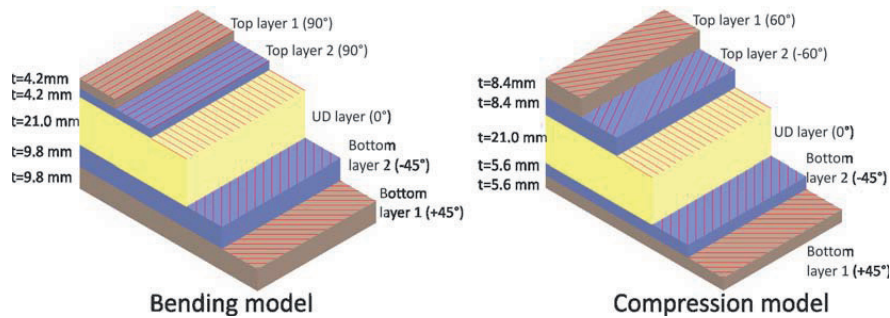


**Figure 9-10** Optimal ply definitions of the 50 m section from the bending and compression model. Images of the 22 m and 90 m sections are included in Appendix D.

When designing and optimizing long and slender beams by linear analysis, it can lead to an inadequate design due to the neglect of non-linear effects. When a long and slender beam is subjected to bending, the tensile and compressive loads will tend to flatten or ovalize the section. This non-linear effect was first described by Brazier, who studied the ovalization of thin-walled steel tubes loaded in bending (Brazier, 1927). The Brazier effects originates from the transverse components of the membrane forces which will compress the cross section and result in a reduction of the beam's moment of inertia  $I$  (Figure 9-11). As the curvature increases, the ovalization also increases and can result in premature buckling of the beam due to large reduction in beam bending stiffness. Figure 9-12a shows the cross section of a long and slender beam designed by using linear analysis. The top flange consists of UD laminates for bending stiffness and  $\pm 45^\circ$  plies for buckling resistance. Bottom tension flange is made up of only UD plies. According to a linear eigenvalue analysis, buckling failure is predicted to appear in the top flange when the beam reaches its rated load. When the same beam is analyzed by a non-linear method, the beam fails at a considerably lower load due to Brazier buckling of the tension flange (Figure 9-12b). For this reason the results from a linear optimization study should always be analyzed by non-linear methods as a final verification.

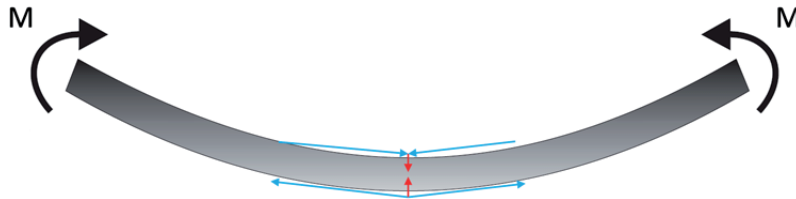


**Figure 9-11** The Brazier effect causes ovalization or flattening of the beam cross section (reproduced from L. Kühlmeier, 2006).

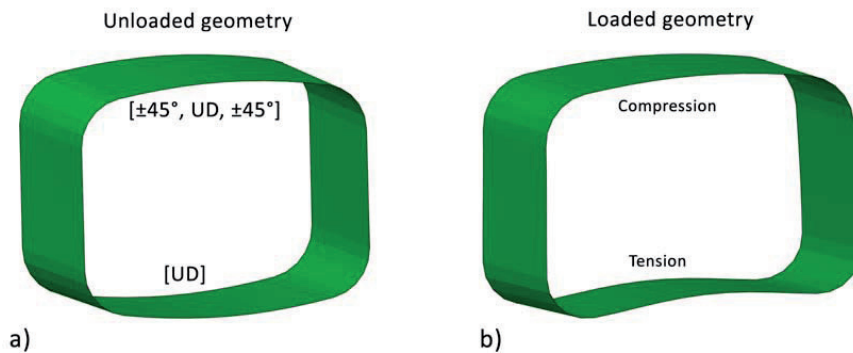


**Figure 9-12** Brazier buckling on beam cross section with insufficient amount of  $\pm 45^\circ$  plies in the tension flange.

### 9.2.3 Non-linear analysis of optimized laminates

In the previous analyses the beam models have been assumed to be perfect, i.e. without any geometric imperfections. In reality all structures contain some imperfections and their influence depends on their size, shape and location. Therefore, no general guideline can be given on how to account for imperfections. One common way of performing imperfection sensitivity studies is to use the shape of the first eigenvalue buckling mode as an imperfection field. The nodal displacements from the linear eigenvalue buckling analysis are used to offset the nodes in the geometry for the non-linear analysis. The size of the imperfection is adjusted by scaling the eigenvector. Very limited information could be found on which imperfection sizes are used when evaluating a wind turbine blade. L. Kühlmeier (2006) used an imperfection size of 0.4 mm based on production tolerances related to the production of a 9 m long blade section used for destructive testing. Three different imperfection sizes (0.1, 0.5 and 1 mm) were applied to the geometry of the bending and compression model. The sensitivity to these imperfections were studied by non-linear analyses. It should be noted that these analyses use linear material properties and are used to include structural non-linear behavior due to large deflections as discussed in Section 8.7.1.

**Table 9-8** Non-linear analysis of bending model with optimized plies. Table shows % improvement in buckling load compared to a standard  $\pm 45^\circ$  anti-buckling ply lay-up.

Bending model					
Section	Non-linear no imperfection [%]	Non-linear 0.1 mm imperfection [%]	Non-linear 0.5 mm imperfection [%]	Non-linear 1.0 mm imperfection [%]	Linear eigenvalue buckling [%]
22 m	2.71	10.75	10.27	10.50	11.79
50 m	17.17	4.73	9.03	8.88	13.04
90 m	-3.07	2.48	2.10	1.85	7.67

**Table 9-9** Non-linear analysis of compression model with optimized plies. Table shows % improvement in buckling load compared to a standard  $\pm 45^\circ$  anti-buckling ply lay-up.

Compression model					
Section	Non-linear no imperfection [%]	Non-linear 0.1 mm imperfection [%]	Non-linear 0.5 mm imperfection [%]	Non-linear 1.0 mm imperfection [%]	Linear eigenvalue buckling [%]
22 m	0.20	-0.18	1.24	0.85	5.93
50 m	3.08	2.26	0.42	0.59	5.05
90 m	5.69	3.48	-26.08	-24.50	12.43

Table 9-8 shows the results from the non-linear analysis of the bending model. Results from the linear eigenvalue buckling analysis have also been included for comparison. There is no good agreement between the non-linear analysis of a perfect geometry and those containing an imperfection. Amongst the models with imperfections there is a good agreement between the results. The only exception is the 50 m section with 0.1 mm imperfection which predicts less improvement of the buckling load (4.7 %) compared to the models with 0.5 and 1.0 mm imperfection (8.9 %). It can be seen that there is a very good agreement between the analyses with 0.5 and 1.0 mm imperfection. This indicates that a critical imperfection size has been passed between 0.1 and 0.5 mm. For both the 22 and 50 m sections the results from the non-linear analysis with larger than 0.5 mm imperfection agree well with the predicted improvement of the linear buckling value. For the 90 m section the non-linear imperfection analysis predicts a smaller improvement (approximately 2 %) than the linear buckling analysis (7 %). The non-linear analysis (with and without imperfection) of the compression model agree fairly well for the 22 and 50 m sections and no significant improvements in buckling load was made (Table 9-9). Analysis of the 90 m section, with 0.5 and 1 mm imperfection, experienced a drastic reduction (-25 %) of the predicted buckling load, meaning that the optimized lay-up is highly sensitive to imperfections. There was also poor agreement between the non-linear and linear results of the compression model.

#### 9.2.4 Implementing optimized anti-buckling plies in 100 m main spar

To compare the validity of the optimization models, the optimal solution from both the bending and compression model was implemented in a FEM analysis of a 100 m hybrid main spar (NLH-model, section 8.10). In Load case 1 ( $70 \text{ m/s}$  wind) the main spar is designed to fail by both buckling and fiber failure. For this load case it would therefore be difficult to determine the cause of ply failure. Instead Load case 3, with  $52.5 \text{ m/s}$  wind was chosen to ensure that the failures in the UD plies would be due to buckling and not large deflections. In this load case the bottom flange laminate is designed to fail by buckling at  $52.5 \text{ m/s}$  wind, but the UD plies have enough strength to handle a  $70 \text{ m/s}$  wind due to the symmetric distribution of UD plies between the top and bottom flanges.

The three models compared are:

- NLH model with standard  $\pm 45^\circ$  glass fiber anti-buckling plies equally distributed on both sides of the UD carbon fiber plies. This model is set as the base line to which the other models are compared.
- Optimal solution from the bending model is applied to the NLH spar.  $90^\circ$  glass fiber on top of the UD plies and  $\pm 40^\circ$  plies underneath the UD plies. 30 % of the anti-buckling plies are placed on top of the UD carbon plies.
- Optimal solution from the compression model is applied to the NLH spar.  $\pm 60^\circ$  glass fiber on top of the UD plies and  $\pm 45^\circ$  plies underneath the UD plies. 60 % of the anti-buckling plies are placed on top of the UD carbon plies.

Naturally the lay-up from the bending model resulted in a stiffer spar since only 30 % of the anti-buckling plies are placed on top of the flange (Table 9-10). This shifts the UD carbon plies away from the spar center, resulting in increased stiffness. Likewise the lay-

up from the compression model increased spar deflection due to the larger percentage (60 %) of anti-buckling plies on tip of the flange. According to the linear buckling analysis, none of the optimized lay-up resulted in a significant increase of the buckling load. The non-linear analysis on the other hand yielded a 7.4 % increase for the bending model and only a 2.3 % increase for the compression model. This suggests that the bending optimization model more correctly replicates the loads and boundary conditions of the main spar. In Figure 9-13 and Figure 9-14 axial stress plots from the root of the spar are presented. The images are taken from the non-linear analysis at the moment of material failure. Figure 9-13 presents the spar using solution from bending model and Figure 9-14 presents spar using solution from compression model. Additional plots showing the entire spar are included in Appendix D.5. Both spars experience material failure in the UD carbon plies located in the transition area of the spar.

**Table 9-10** Buckling load for a 100 m main spar with optimized lay-up from bending and compression models. Numbers in parenthesis show percentage improvement compared to the standard solution. Abaqus CAE automatically normalizes the predicted buckling load. If a structure is found to buckle at a load of 1.0, it has reached the design load.

Model	Deflection [m]	Linear eigenvalue analysis	Non-linear analysis
NLH Standard solution	11.51	2.01	1.59
Bending model optimal solution	10.92	2.07 (2.67 %)	1.71 (7.41 %)
Compression model optimal solution	12.01	2.04 (1.12 %)	1.63 (2.34 %)



**Figure 9-13** Axial stress plots of top flange for a 100 m spar with ply lay-up based on results from bending model. a) UD ply. b)  $\pm 45^\circ$  ply.



**Figure 9-14** Axial stress plots of top flange for a 100 m spar with ply lay-up based on results from compression model. a) UD ply. b)  $\pm 45^\circ$  ply.

It is difficult to reach a clear conclusion on which optimization model is most accurate one, due to large differences between the results from the optimization models and the analysis of the 100 m spar. It is also questionable whether linear buckling analysis should be used in the buckling optimization of plies for composite beams. A linear analysis will fail to include non-linearities such as the Brazier effect, which is relevant for long and slender beams subjected to bending loads. Further improvements can be made if the optimization procedure uses a non-linear analysis to evaluate the buckling performance of a laminate. The FEM analysis should also include an imperfection that is representative for the imperfections found in the manufacturing process. This will avoid generating an optimized lay-up that is sensitive to imperfections.

### 9.3 Optimization of the UD carbon plies

The pitch controlled hybrid spar developed in section 8.10 had a maximum flapwise deflection towards the tower of 11.51 m, meaning that the design is too stiff when compared to the maximum allowable deflection of 15.4 m. This extra stiffness could give room for improving the buckling resistance of the UD plies by sacrificing some of their stiffness. One intuitive way of doing this would be to place the UD plies at a small angle (i.e.  $\pm 15^\circ$ ), which would decrease the axial stiffness, but might increase the buckling resistance of the UD plies.

Another possible way of increasing flange buckling resistance was proposed by J. Jensen et al. (2005). The 100 m main spars designed in Chapter 8 use a traditional single skin design in the flanges. J. Jensen et al. (2005) suggested increasing the buckling resistance by adding core material to the flanges (Figure 9-15). The addition of core material to the flanges reduced the amount of  $\pm 45^\circ$  plies needed and resulted in a 22.3 % weight reduction for a 90 m glass fiber spar. It should be noted that Jensen’s study did not use safety factors and the spar was designed with a linear eigenvalue buckling load of 1.0.



**Figure 9-15** a) Traditional single skin design of flanges. b) Sandwich concept by J. Jensen et al. (2005).



The buckling optimization in the previous section showed how increase in buckling performance can be made by optimizing the angle and thickness of the anti-buckling plies. In this study a traditional lay-up was used with  $\pm 45^\circ$  glass fiber plies placed on either side of the UD carbon fiber plies (Figure 9-16a). Such a design creates a very sharp division between the stiff UD carbon plies and the relatively soft  $\pm 45^\circ$  glass fiber plies and may not be an optimal design. It has been found through analytical analysis and experience that plies should be dispersed as much as possible throughout the laminate in order to create a more homogenized laminate (S. W. Tsai, 2008). This might complicate the production of wind turbine blades somewhat, but should result in increased strength and toughness of the laminate (Figure 9-16b).

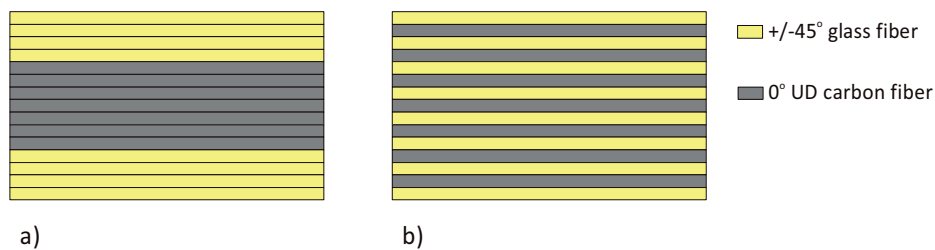


**Figure 9-16** a)  $\pm 45^\circ$  plies surrounding the UD plies. B.) Homogenized laminate with  $\pm 45^\circ$  plies distributed amongst the UD plies.

### 9.3.1 Defining the UD ply optimization analysis

The geometry and mesh of the bending model (section 9.1) was used for the optimization of the UD carbon plies. Ply definitions of the corners and shear web remained the same whilst the ply definition of the flanges was changed. The amount of fiber in the flanges is kept constant, but ply numbers were increased in order to get a more realistic representation of the laminate. The new flange laminate lay-up and ply thicknesses are listed in Table 9-11. The thickness notation used was introduced by L. Kühlmeier (2006).

**Table 9-11** Flange laminate lay-up and thicknesses for the UD ply optimization models of the 22, 50 and 90 m sections. Superscripts G and C denote Glass fiber and Carbon fiber.

Model	Section 22 m	Section 50 m	Section 90 m
Lay-up	$[(\pm 45)_8^G, 0_4^C]_s$	$[(\pm 45)_8^G, 0_4^C]_s$	$[(\pm 45)_8^G, 0_4^C]_s$
Ply thickness [mm]	$[2.0^G, 3.0^C]_s$	$[1.75^G, 2.63^C]_s$	$[1.0^G, 0.375^C]_s$

The buckling resistance of the UD plies was improved by using three different approaches:

- UD ply angle is varied from 0 to  $\pm 30^\circ$  in  $5^\circ$  increments
- Diab H200 core material is added to the flanges. Laminate thickness is increased by up to 200 %. Hoff's criterion (equation 5-3) is used to prevent sandwich wrinkling failure.
- Homogenization of the laminate. The  $\pm 45^\circ$  plies are evenly distributed amongst the UD plies. This is applied to the most promising solutions from the approaches listed above

Buckling analysis by both linear and non-linear methods were performed. The non-linear analyses were done with a perfect geometry and with a 0.5 mm imperfection based on the shape of the first eigenvalue buckling mode.

### 9.3.2 Results from UD carbon ply optimization

The angle of the UD carbon fiber ply was adjusted from 0-30° in 5° increments for all three sections. Figure 9-17 and Figure 9-18 shows how this affected the linear eigenvalue buckling load and deflection. It can be seen that only small increases in buckling values can be achieved and it results in an exponential increase in deflections due to the reduction of axial stiffness. The non-linear analysis of the 22 and 50 m sections resulted in no increase of the buckling load (Figure 9-19). Only the 90 m section showed an increase of 6-13 % for angles 20-30°. Tables with complete results can be found in Appendix D.2. The marginal gains in buckling load and large increase in deflection confirms that altering UD ply angle is not a good approach for increasing the buckling load of the spar.

The second approach to increase buckling load, was to add core material to the spar flanges. In the 22 and 50 m sections, core thickness was varied from 0-100 mm and in the 90 m section the core added had a thickness of 0-30 mm. For all sections this corresponded up to a 200 % increase in laminate thickness. The linear buckling analysis shows that the buckling loads increased for all sections, with the most dramatic effect for the 90 m section which increased by 170 % (Figure 9-20). The 22 and 50 m sections had a slight decrease in buckling load below 20 mm core thickness, but after this a linear increase can be observed. In contrast to the altering of UD ply angle, the addition of core material only increased deflections slightly (Figure 9-21). For the 22 m section the change in deflection was insignificant and for the 50 and 90 m sections there was a 15 % increase. The non-linear analysis confirms that buckling load can be doubled by the addition of core material (Figure 9-22). The effect is higher than observed in the linear buckling analysis and for all sections a steady increase in buckling load can be observed. It can also be seen in Figure 9-22 that the buckling load for the 90 m section levels off after the addition of 20 mm core material. This is due to the UD carbon fiber plies reaching their static design load limit and fail by compression stress.

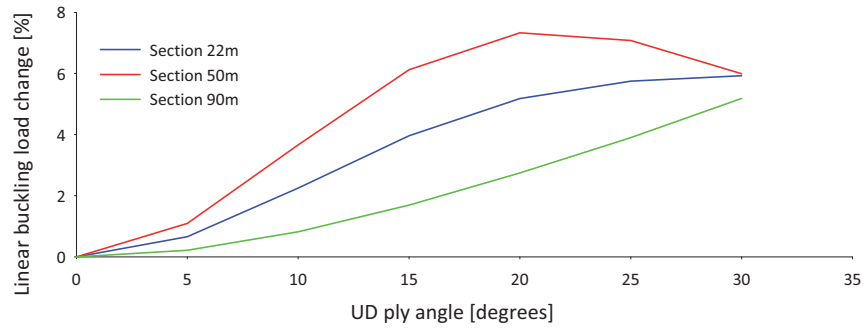


Figure 9-17 Change in linear eigenvalue buckling load due to UD carbon fiber ply angle.

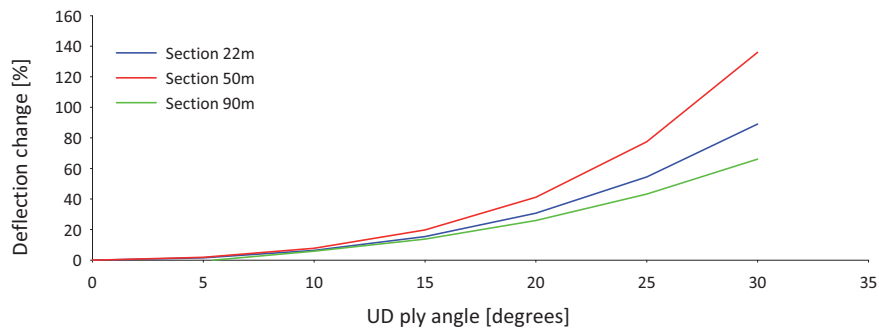


Figure 9-18 Change in deflection due to UD carbon fiber ply angle.

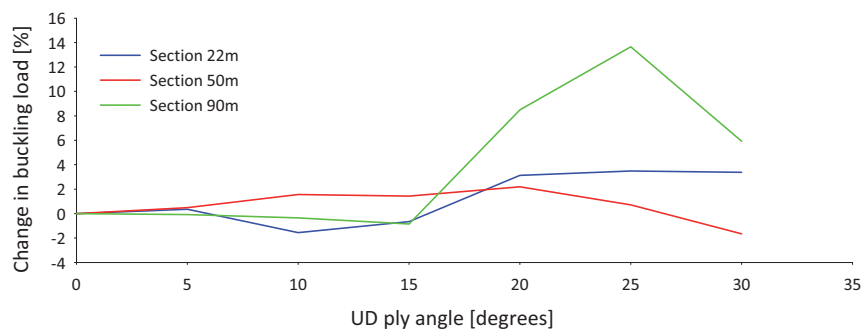


Figure 9-19 Change in buckling load (0.5 mm imperfection) due to UD carbon fiber ply angle. Buckling load is found by using nonlinear analysis.

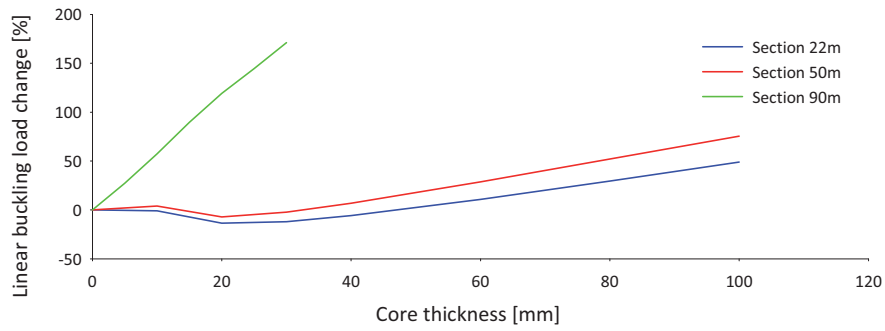


Figure 9-20 Change in linear eigenvalue buckling load due to addition of core material in flange.

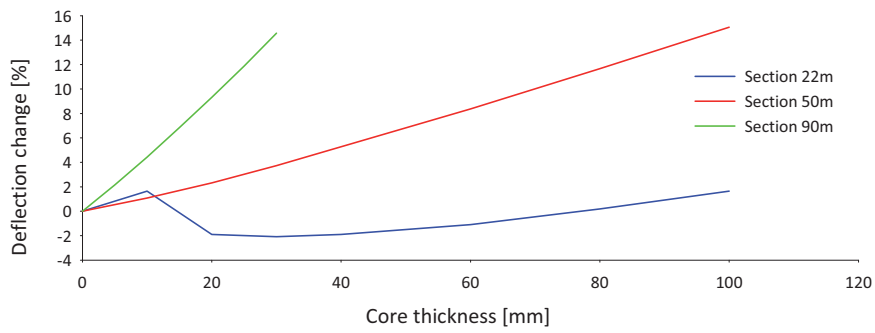


Figure 9-21 Change in deflection due to addition of core material in flange.

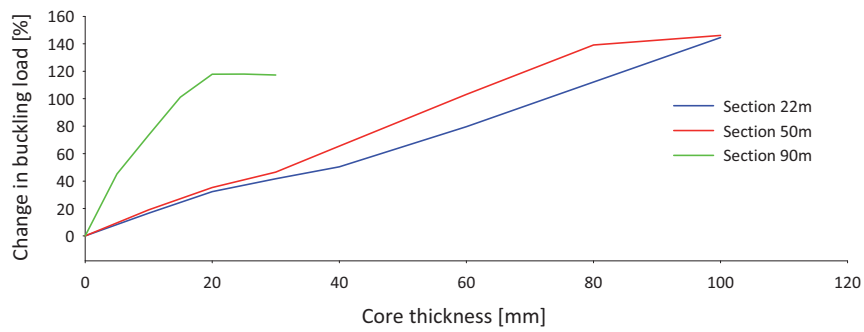


Figure 9-22 Change in buckling load (0.5 mm imperfection) due to addition of core material in flange. Buckling load is found by using nonlinear analysis.

Ply homogenization was evaluated on sections with a single skin design and on sections with core material in their flanges. All flanges had UD carbon fiber at 0° for stiffness and ±45° glass fiber for buckling resistance. The amount of core material added to each section is listed in Table 9-12.

**Table 9-12** Core material added to the flanges of the 22, 50 and 90 m sections.

Section	22 m	50 m	90 m
Core thickness	30 mm	30 mm	10 mm

For the single skin design it can be seen in Figure 9-23 that the laminate homogenization had no effect on the 22 m section. The buckling load was slightly reduced for the 50 m section (-4.1 %) whilst the 90 m section showed an increase of 12.2 %. All the sections with a sandwich flange experienced an increase of the buckling load by the distribution of the ±45° plies. The 90 m section increased by only 2.6 %, which is negligible, but the 22 and 50 m sections had a noteworthy increase of approximately 19 %.

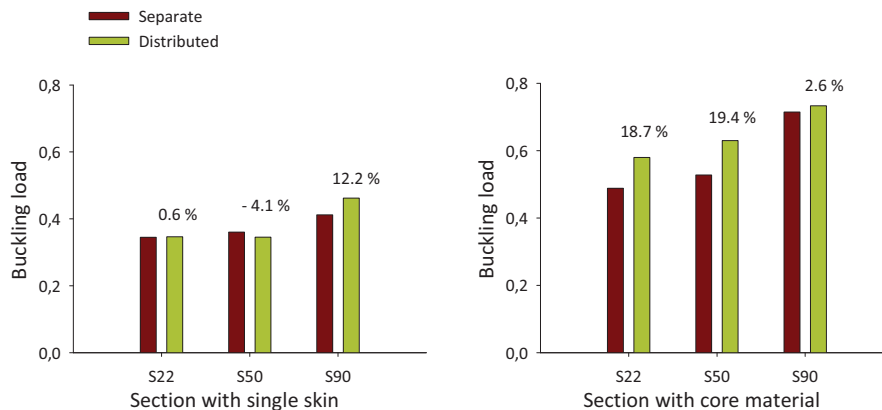


**Figure 9-23** Buckling load found by non-linear analysis (0.5 mm imperfection) for sections with and without homogenization of the laminate. Percentage above bars show change in buckling load due to homogenization.

The results show that homogenization of the laminate can significantly improve the buckling load. This optimization of the stacking sequence is virtually done for free, with no additional increase in material cost or weight. The production of the laminate will be slightly more complicated due to frequent change of fiber mats, but this may not represent a significant increase in production costs.

### 9.3.3 Implementing optimized UD plies in a 100 m main spar

The optimization study of the UD carbon plies confirmed that adding core material to the main spar flanges will greatly increase the buckling load and only slightly increase spar deflections. To verify the validity of the optimization models used, the results were applied to a FEM analysis of a 100 m hybrid main spar. As with the previous validation analysis (section 9.2.4), Load case 3 is applied to ensure that laminate failure is by buckling. This load case puts the bottom flange in compression and therefore only the bottom flange is altered. Shear web and top flange are kept unchanged. The addition of core material to the bottom flange was done in the following steps.

1. The amount of  $\pm 45^\circ$  plies are reduced and redistributed over the main spar by non-linear buckling analysis such that the main spar has a buckling load of approximately 0.6. At this load, buckling failure should occur at multiple places in the flange.
2. Flange laminate is homogenized by evenly distributing the  $\pm 45^\circ$  glass fiber plies amongst the UD carbon fiber plies.
3. Core material is only added to the middle of the bottom flange. Main spar corners are kept unchanged. The only exception are the first 4 corner sections at the root, where some core material was needed to prevent buckling (Figure 9-24). Using non-linear buckling analysis, 4 plies of core material with 20 mm thickness are roughly distributed such that a buckling load of at least 1.2 is achieved.
4. Using non-linear analysis, the plies of core material are incrementally shortened until material failure occurs and a detailed distribution of the core material is obtained.

For comparison, a main spar with single skin design and a buckling load of 1.2 was also developed by non-linear buckling analysis.

Figure 9-24 shows the distribution of core material in the bottom flange. As expected, an increasing amount of core material is needed towards the root area. Some core material (20 mm) had to be added to the corners at the root in order to prevent buckling. Detailed information about ply and core distribution are included in Appendix D.3.

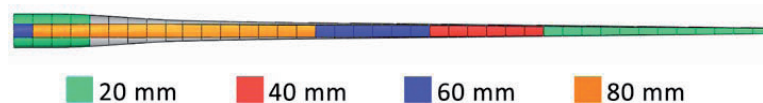


**Figure 9-24** Distribution of core material in the bottom flange of hybrid (NLH) spar. Core material is placed in flanges only except for the corners at the 4 root sections.

In Table 9-13 the single skin design and the sandwich design are compared. The usage of core material allowed for a substantial weight reduction of the bottom flange (5.89 tons). Comparing the weight of the anti-buckling plies in the single skin design with the sandwich design, the amount of anti-buckling plies was reduced by 47%. Deflections were only slightly increased by the use of core material and are still lower than the maximum allowable deflection of 15.4 m. These results confirm that core

material in the flanges can considerably reduce the weight of the main spar and thereby support the findings by J. Jensen et al (2005).

**Table 9-13** Comparison of 100 m main spar with bottom flange using a single skin design or the sandwich concept.

Model	Weight of bottom flange [tons]	Weight of $\pm 45^\circ$ plies [tons]	Weight of core material [tons]	Main spar deflection [m]	Buckling load by nonlinear analysis
NLH-model with single skin design	19.91	12.58	0	11.72	1.34
NLH-model with core material and homogenized laminate	14.02	4.89	1.79	12.28	1.21

#### 9.4 Discussion of optimization results

Several approaches were tried in order to increase the buckling load of the spar flange. The anti-buckling ply angle and distribution were optimized by linear eigenvalue analysis of three different sections from the 100 m hybrid spar. Neither the bending or compression model resulted in a significant increase of the linear buckling load for the 100 m spar, but in a non-linear analysis the bending model showed an increase in buckling load by 7.4 %. It is questionable if linear analysis can be used for the buckling optimization of the flanges in a spar. Buckling is non-linear by nature and a linear analysis will fail to include non-linear effects such as Brazier buckling. Also, when optimizing a laminate, imperfections should be included in order to avoid a design that is imperfection sensitive. The results for the linear optimization were found by simply solving all possible solutions within a given solution space. This practice works well for linear analysis of small models, but will be too time consuming if non-linear analyses are used. A search algorithm (e.g. genetic) should be used in order to reduce the number of analyses needed and to quickly find the global maximum within the given solution space.

The most efficient way of increasing flange buckling resistance was found to be the addition of core material to the spar flanges and thereby confirming the findings of J. Jensen et al. (2005). The distribution of anti-buckling plies amongst the UD plies and homogenization of the laminate, proved to have a synergetic effect together with the core material. For a 100 m hybrid spar the amount of anti-buckling plies were reduced by 50 %, resulting in a 5.9 ton weight reduction of the bottom flange. For the evaluation of sandwich wrinkling failure, Hoff's criteria was used due to its ease of use and conservative estimate. But this criterion should not be used in the further optimization of the sandwich structure because it does not take the face sheet stiffness into account. According to Hoff, the way to increase wrinkling resistance is to use a core material with higher stiffness. This is straightforward, but carries with it a cost and weight penalty.

Recent work on wrinkling of sandwich structures (L. Fagerberg, 2003) recommends using the equations derived by F.J. Plantema (1966) because it takes the face sheet bending stiffness into account.

The results show that small models can be used for studying trends and speed up the optimization. In the case of a wind turbine main spar it is recommended that several representative sections are used, as geometric aspect ratios will affect the results. Care should also be taken to develop a model that as closely as possible replicates the loads and boundary conditions of the original analysis. In the analyses presented here, torsional loads on the spar were not included. The main spar provides the wind turbine blade with a major part of its torsional stiffness. A reduction in the amount of  $\pm 45^\circ$  anti-buckling plies or a change in their angles and distribution, will affect the torsional stiffness of the spar. Future spar optimization studies should therefore include torsional loads and a stiffness criterion.

When optimizing a composite structure it is important to keep in mind how it will be produced and limitations given thereby. In the production of blades, continuous plies are rolled out either manually or by robots. Highly localized ply definitions might yield the optimal result, but in the case of a wind turbine spar it will be too time consuming to place a range of plies at very specific angles.



## 10 Testing of a 6 m scaled main spar section

The use of finite element analysis is a powerful engineering tool and the previous chapter shows how it can be used in the optimization of a wind turbine main spar. Being able to explore and test new designs in a FEM analysis, can save the time and cost of having to build several prototypes. But, FEM analysis results should be interpreted with great caution. The realism of the simulation depends on the choice of elements, material models and on the degree of simplification of geometry and boundary conditions. The sinking of the concrete base for the Sleipner A offshore platform outside Stavanger, Norway, in 1991 is an example of the possible consequence of a wrongly defined FEM analysis. Due to inaccurate finite element approximation in Nastran, the shear stresses in parts of the concrete structure were underestimated by 47 %. During a controlled ballasting operation of the concrete base, failure in the cell walls caused severe leakage, resulting in the entire structure sinking. The impact with the ocean floor 100 m below caused a seismic event registering 3.0 on the Richter scale, leaving nothing but a pile of debris at 220 m depth and a loss of \$700 million.

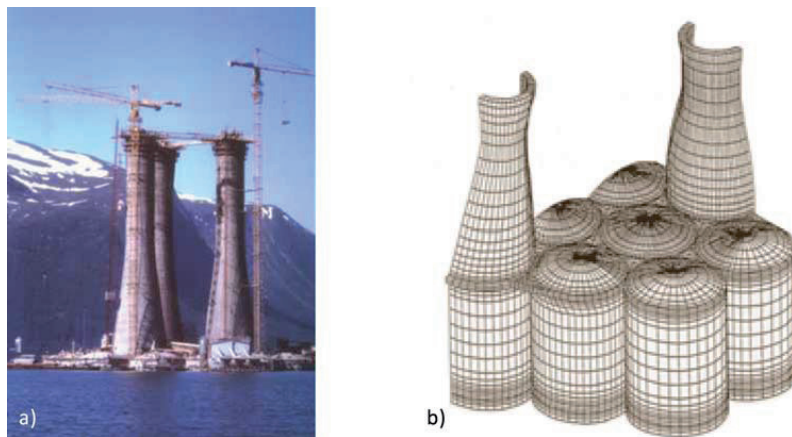


**Figure 10-1** a) Concrete base of Sleipner A offshore platform. b) Finite Element model of concrete base.

When developing a FEM analysis, it is therefore necessary to understand the limitations of the model. Experimental testing is an important step towards verifying the results of a FEM analysis and building confidence in the model. Based on this, it was decided to build a 6 m long spar and conduct a 4-point bending test with the aim of correlating test data with the FEM analysis presented later in this thesis. The specimen was designed to fail by buckling in the top flange and tested destructively. Much effort has been put into planning, building and testing the specimen.

### 10.1 Geometry definition

In order to fit the available test facilities, the spar was scaled to a length of 6 m and a cross section representing the middle of a 100 m spar was chosen. The cross section is based on a NACA 64-series 6-digit airfoil with a 780 mm chord length and a thickness to chord ratio of 21 %. For the sake of simplicity and generality, the spar did not taper or twist as it would in a real spar. Also, to avoid the buckling failure being biased to either side, the cross section of the spar was made symmetric (Figure 10-2). The spars developed in Chapter 8 are based on a spar made on a mandrel, but for reasons of ease of production, it was chosen to build the test specimen using a spar cap construction (see section 2.3). The UD plies are included in the two airfoil shells and then bonded around two shear webs. Detailed information about the cross section is included in Appendix F and ply definitions are included in Figure 10-2. The spar flanges have a single skin design whilst the shear webs include core material for additional stiffness.

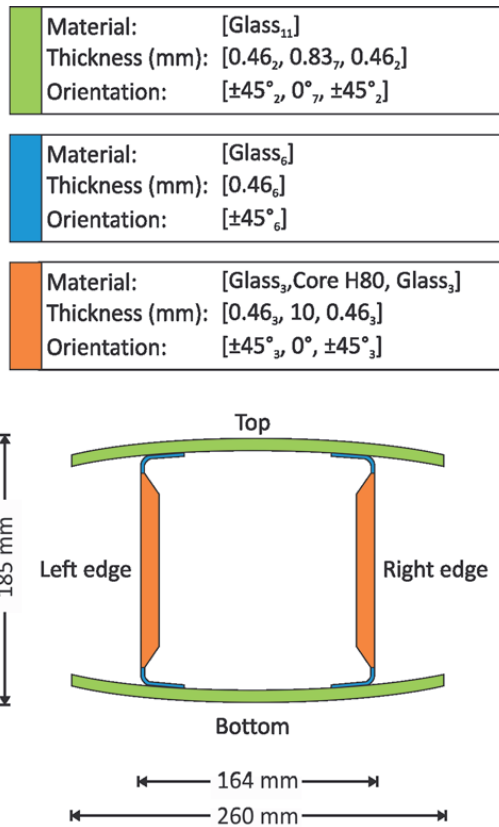


Figure 10-2 Cross section of 6 m spar.

Very limited information could be found on the practical design of a wind turbine blade. In the first prototypes of the shear web, the core material had a 45° draft angle. Inspection of the shear web revealed that the glass fiber laminate did not follow the steep

draft angle of the core, which resulted in resin rich areas in the corners of the shear web. In an article by F. M. Jensen et al. (2006) on the testing of a 34 m wind turbine blade, an image of the cross section of a spar shows how the sandwich core of the shear webs is tapered towards the corners of the spar. Analysis of this image yielded a  $25^\circ$  draft angle of the core, and it was therefore decided to use this on the shear webs for the 6 m spar as well. Post-molding inspection confirmed that the laminate followed the transition from a sandwich design into the corners of the shear web, thereby improving laminate quality.



**Figure 10-3** Tapering of core material in shear web of wind turbine spar (reproduced from F. M. Jensen et al., 2006).

In order to control the location of the buckling failure, an imperfection was added to the top flange by adding an extra UD ply, 100 mm wide, between the outer  $\pm 45^\circ$  plies and the remaining plies (Figure 10-4). The intention was to create a small kink in the UD plies in order to initiate buckling at this location. Measurement after production showed that this extra ply increased the flange thickness by 0.83 mm.

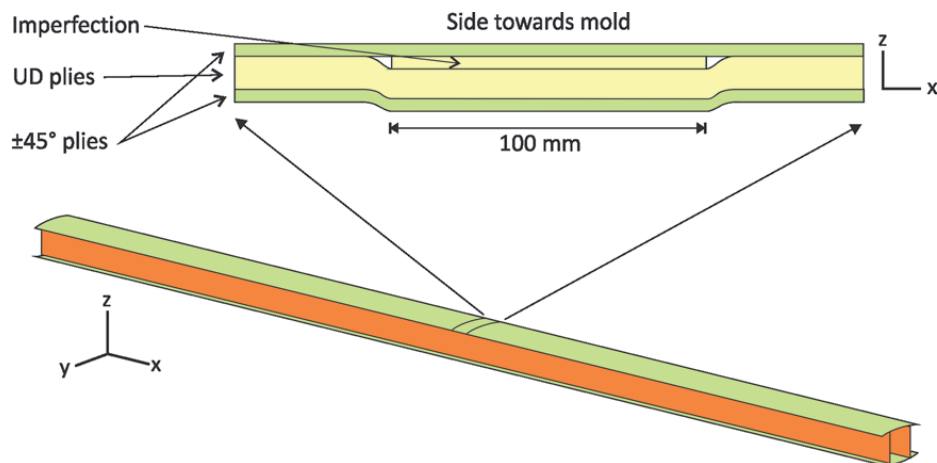


**Figure 10-4** Introduction of imperfection in top flange by adding an extra ply of 100 mm wide UD ply.

## 10.2 Manufacture of specimen

The entire manufacturing of the 6 m spar was done using available in-house resources. The mold plug was constructed by CNC machining sections of Ebalta 60 tooling block and assembled together on a level frame. After applying several coats of release agent, the surface was covered by a tooling gel-coat followed by several layers of hand laminated glass fiber. After cure, a frame was mounted on the backside of the mold for support and stiffness.

The production of the 7.6 mm thick flange by resin infusion proved to be challenging and initial trials on 400 x 400 mm laminates resulted in air inclusions and thereby inadequate wetting of the fiber. Figure 10-5a shows the initial infusion set-up with flow medium covering the entire laminate. For thin laminates this set-up works well, but on the 7.6 mm laminate the resin reached the vacuum outlet, sealing it off, before the resin has had time to propagate through the thickness of the laminate. With the vacuum line blocked, residual air had no way to escape and thereby remained in the laminate. The problem was solved by creating a break zone at the vacuum outlet and to switch to a through-thickness infusion by adding an extra layer of flow medium (Figure 10-5b). The break zone was created by ending the two layers of flow medium 50 and 100 mm from the vacuum outlet. Resin would enter the laminate and very quickly distribute through the flow medium. The progress of the resin front was slowed down by the break zone, preventing it from prematurely blocking the vacuum outlet. Resin would then progress through the thickness of the laminate while allowing residual air to escape, resulting in a laminate with complete wet-through. The spar flanges and shear webs were infused using glass fiber from Devold AMT and Araldite ESR3 infusion epoxy. They were both successfully infused within 20 minutes and cured in a hot air tent at 50 °C, resulting in a high quality glass fiber composite. Using a matrix burn off test (ASTM D-2584), the fiber volume fraction was found to be 52 %.

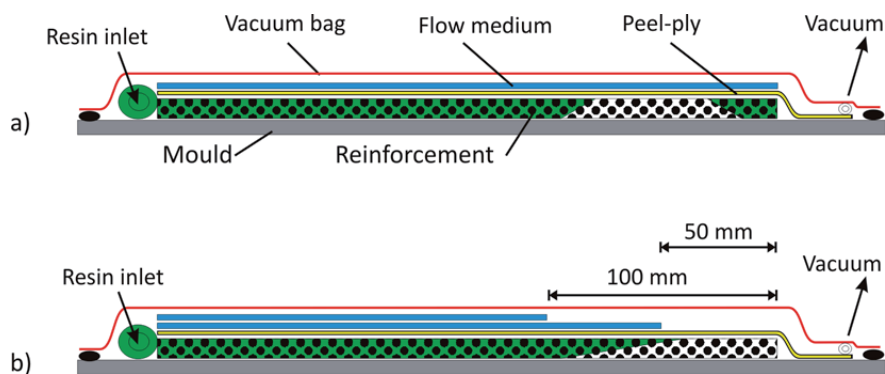


**Figure 10-5** a) In-plane resin infusion with blockage of air. b) Through thickness infusion with break-zone.

The flanges and shear webs were bonded together using 3M DP460 epoxy adhesive. During production of the flanges and shear webs, all bonding surfaces were covered in peel-ply, yielding a textured and resin rich surface. This would ensure good adhesion in

the subsequent bonding of the spar. The outer edge of the bond between the shear web and flange was covered with the structural filleting adhesive Crestomer Advantage 10 by Scott Bader. This urethane acrylate adhesive should provide some stress relief in the primary bond between the shear webs and flanges. Prior to the production of the 6 m long specimen, a 1 m specimen with the same cross section had been made in order to verify the production and assembly methods. A simple 3-point bending test was performed on the 1 m specimen to confirm that the bonds had sufficient shear strength. The mini-spar was loaded to 150 % of the expected shear stress in the 6 m spar before the test was terminated. No failures were observed.

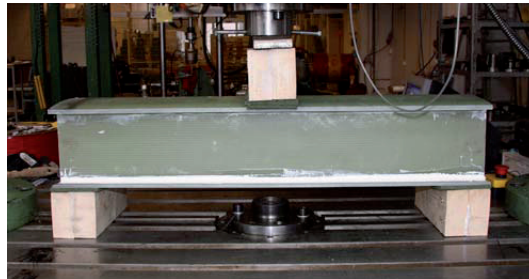


Figure 10-6 3-point bending test of 1 m long spar in order to verify shear strength of bonds.

### 10.3 Experimental setup for the 6 m spar

The 6 m spar was tested in a 4-point bending configuration with the top flange in compression, subjecting the middle 1.3 m of the specimen to a constant bending moment. Figure 10-7 is a sketch of the test set-up with loads and boundary conditions. A picture from the actual test is shown in Figure 10-8. The loads on the specimen were applied by cables pulling on two loading yokes on the spar. A schematic of a loading yoke is shown in Figure 10-9. Blocks of medium-density fiberboard (MDF) had been cut to shape such that they would fit the curvature of the flange. A 5 mm thick sheet of EVA foam was put between the specimen and MDF blocks in order to evenly distribute the load. Underneath each loading yoke, a load cell was mounted to monitor the force applied by the pulling cable. Each end of the spar was placed on a hinge/roller fixture to allow the spar ends to rotate and move towards the spar center as it deflects. Stoppers were placed at each end of the spar to prevent it from moving too far sideways in case of an unforeseen event. A horizontally mounted 100 kN Instron hydraulic actuator provided the pulling force on the yokes by cables running through pulleys beneath the spar (Figure 10-10a). Both yokes were connected by the same cable and a pulley on the actuator cross-head equalized the pulling force on the yokes (Figure 10-10b).

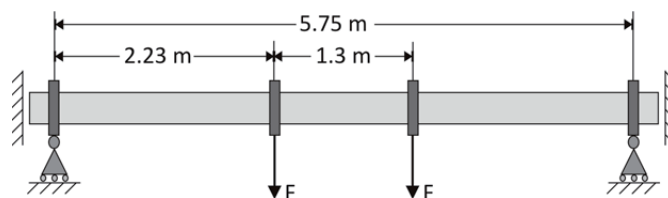


Figure 10-7 4-point bending test set-up of 6 m spar.

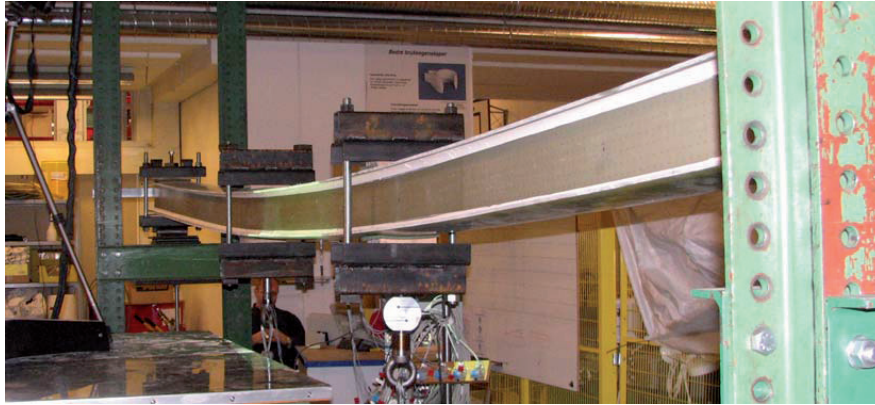


Figure 10-8 Experimental setup of the 6 m spar at the NTNU/SINTEF fatigue laboratory.

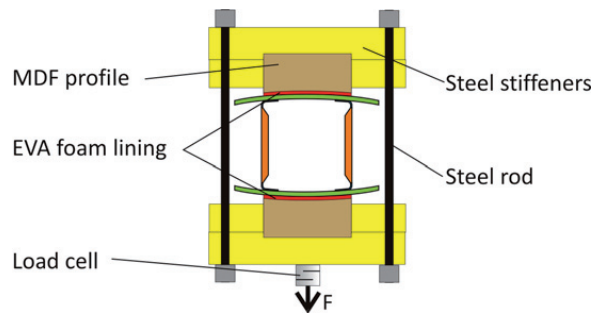


Figure 10-9 Loading yoke on the 6 m spar.

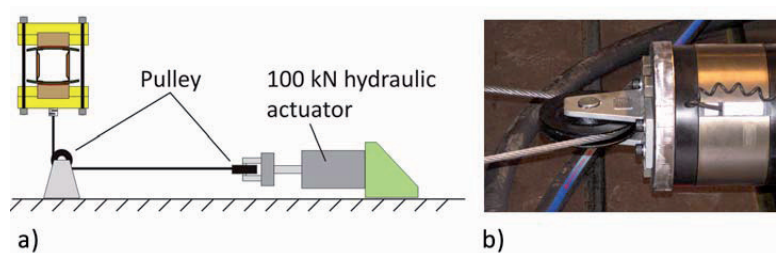


Figure 10-10 a) Placement of spar, pulleys and actuator. b) Pulley mounted on hydraulic actuator cross head.

### 10.4 Measuring equipment

Altogether, 25 strain gages were mounted on the main spar and Figure 10-11 schematically shows the placement of strain gages on the top flange. The distance between the strain gages was determined on the basis that three gages should cover a half wave of the predicted buckling mode shape. A preliminary linear eigenvalue buckling analysis showed that the wavelength of a buckling mode would be 300 mm, equating to 75 mm between the strain gages. A total of 13 strain gages were placed along the centerline of the top flange to measure axial strain. In the center of the test section, three axial strain gages were placed along the left and right edges to check if the axial strains were symmetric. Five strain gages were also placed at 90° to measure transverse strain. One strain gage was placed underneath the spar to check if axial strain was equal on the top and bottom of the spar.

The displacement of the spar was measured by attaching a draw wire underneath the center of the spar. Measurements were collected by a total of six HBM Spider8 data acquisition units connected to a laptop. A laptop was purposely used because this would ensure that no data was lost in the case of a power failure. Each Spider8 unit has 8 channels available for collecting readings from strain gages, load cells, thermocouples, etc. A sampling rate of 5 Hz was used during the test and the software “Catman” by HBM was used for data storage.

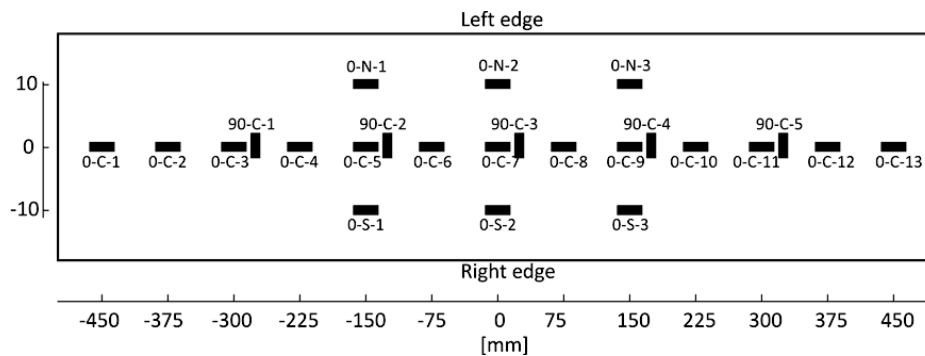
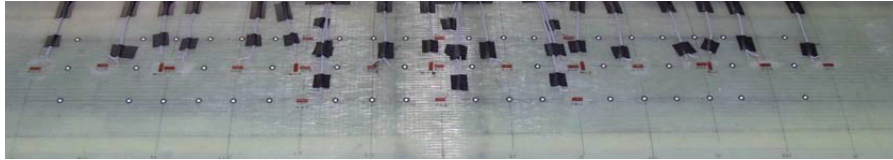


Figure 10-11 Strain gages on the top flange seen from above.

As a supplement to the strain gages, a 3D digitizer was used to measure the shape and deformation of the top flange. The 3D digitizer, Atos by Optical Measuring Techniques ([www.gom.com](http://www.gom.com)), uses 2 cameras and a projected fringe pattern to accurately measure the surface of any given object. The system is capable of digitizing the entire surface within its field of view, but in the case of the 6 m spar, the measurements would be incomplete and distorted due to all the strain gages and their wires. Instead 48 circular white/black circular stickers were attached on the top flange, allowing the Atos system to track these points with great accuracy. Figure 10-12 is a picture of the middle section of the spar, showing the strain gages and tracking points mounted on the top flange. The digitizer needed three seconds to perform a measurement, during which the specimen had to remain completely still. The test was halted every 5 kN to measure the tracking points.



**Figure 10-12** Strain gages and tracking points mounted on to top flange of the spar. Circular marks are used by the 3D digitizer to measure their position in space.

### 10.5 Test data

The load was gradually increased by displacement control of the hydraulic actuator and halted every 5 kN for optical measurements. The maximum combined pulling force on the specimen at the moment of collapse was 49.7 kN, which corresponds to a constant bending moment of 58.0 kNm over the middle 1.3 m of the spar. The plot in Figure 10-13 shows how the load from the two load cells increased with deflections and confirms that equal load was applied to each of the loading yokes. The plot in Figure 10-14 compares readings from the two strain gages placed on the top and bottom flange in the middle of the specimen (at 0 mm). It can be seen that both flanges contributed equally in carrying the loads. A linear regression analysis of the top and bottom strains confirms that the strain increased linearly with the load, yielding  $R^2$  values of 99.9. The difference between the maximum top and bottom strains is only 3.8 %.

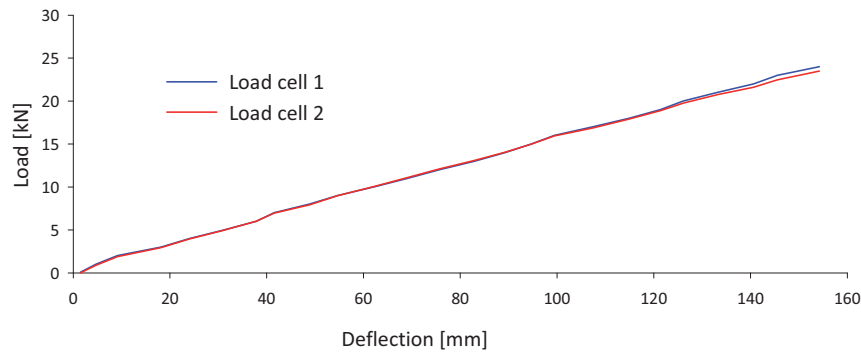


**Figure 10-13** Spar deflection vs. load from the two load cells.

In Figure 10-15, the axial strains along the spar centerline are plotted in 2 kN intervals. As the load increases, a M-shaped pattern clearly develops in the middle of the spar, with compressive strains decreasing in the center of the imperfection. To verify that this pattern is not caused by miscalibrated strain gages, the axial strains at the left and right edge of the spar are plotted in Figure 10-16. The readings from the strain gages at the



left and right edge coincidence well with the gages placed along the spar centerline, confirming that the M-shaped pattern appears over the entire width of the top flange. Both the location and symmetry of the pattern strongly suggests that it is caused by the imperfection situated here.

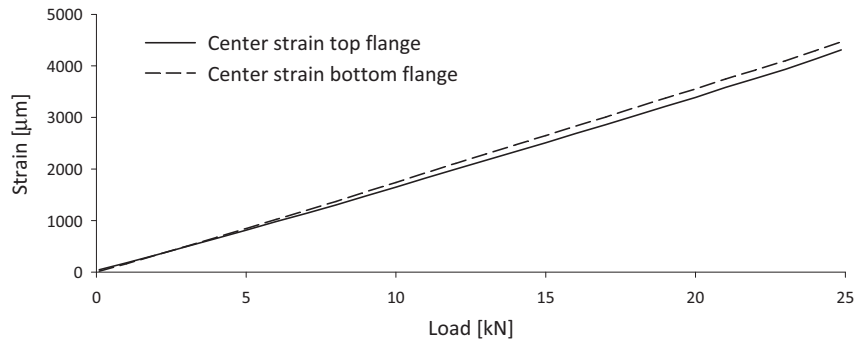


Figure 10-14 Comparison of strain on top and bottom flange in the middle of the specimen.

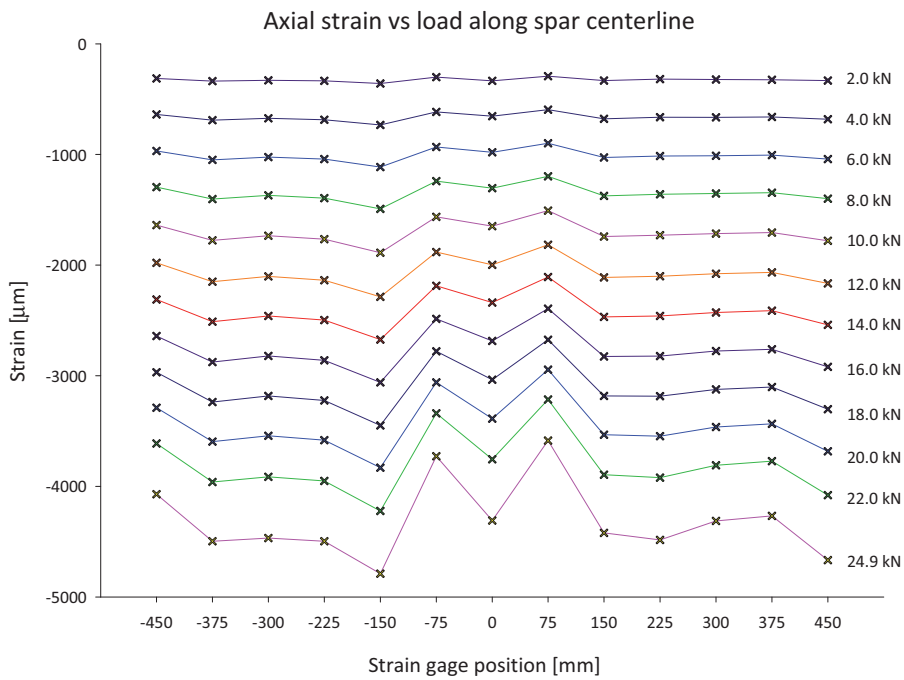


Figure 10-15 Axial strains along spar centerline.

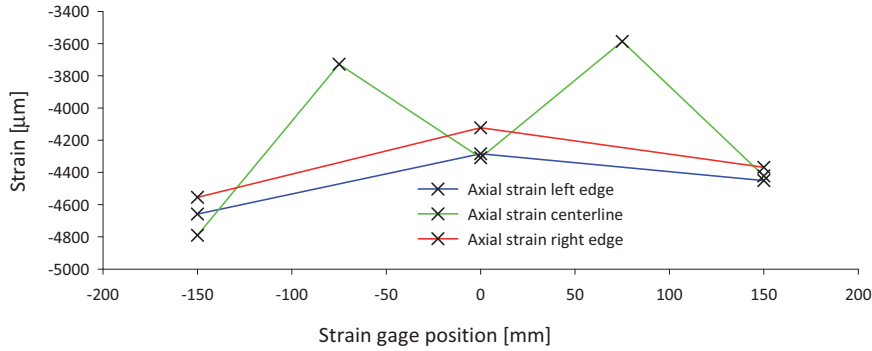


Figure 10-16 Comparing axial strains above and below the spar centerline (ref. Figure 10-11).

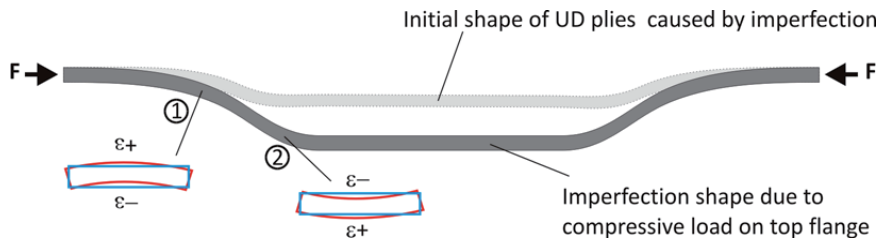


Figure 10-17 Tensile and compressive strains caused by the imperfection in the top flange. See also Figure 10-4 for information about imperfection.

The reduction of the axial compressive strain at locations -75 mm and +75 mm could be explained by how the compressive load in the top flange affects the imperfection (Figure 10-17). At zero the UD plies are shifted 0.83 mm towards the spar center by the 100 mm wide imperfection, causing a small and stable buckling shape in the top flange. As the compressive load in the top flange rises, the size of the imperfection is increased and causes additional strains to develop. At point 1 in Figure 10-17, the curvature of the imperfection will cause tensile strain on the surface of the flange and result in a reduction of the compressive strain at -75 mm and +75 mm. As the imperfection starts to level of at point 2, the magnitude of the compressive strains are partially restored (at location 0 mm), resulting in the observed M-shaped strain pattern.

The plot in Figure 10-18 shows the data collected from the 5 strain gages measuring transverse strain along the spar centerline. At first the transverse strain increases linearly, but after approximately 10 kN, the plot becomes increasingly non-linear and starts to level off. The exception is the transverse strain measured in the center of the imperfection (at location 0 mm) which progresses in a non-linear way from the start. The declining slope indicates that there is a reduction of the spar stiffness and that it is due to the Brazier effect. The transverse component in the membrane forces will try to

flatten the flanges and thereby cause additional compressive and tensile strains in the flanges (Figure 10-19). On the surface of the top flange, the Brazier effect will result in transverse compressive strains, thereby explaining the reduction of the slopes in Figure 10-18. Taking into account how the imperfection affects the shape of the top flange (Figure 10-17), the imperfection will most likely locally increase the Brazier effect and thereby explain the non-linear progression of the transverse strain at 0 mm.

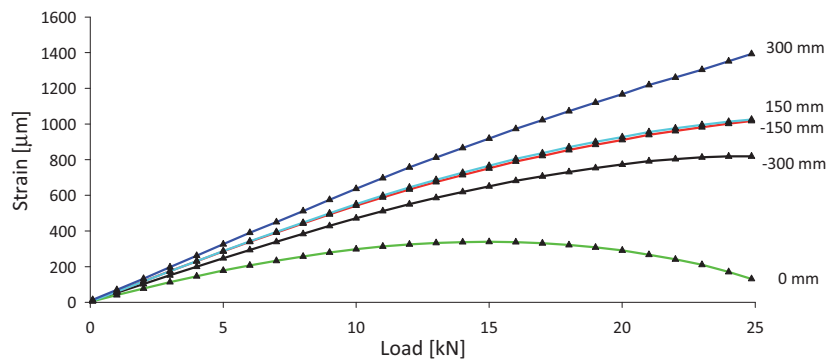


Figure 10-18 Transverse strain of 6 m spar.

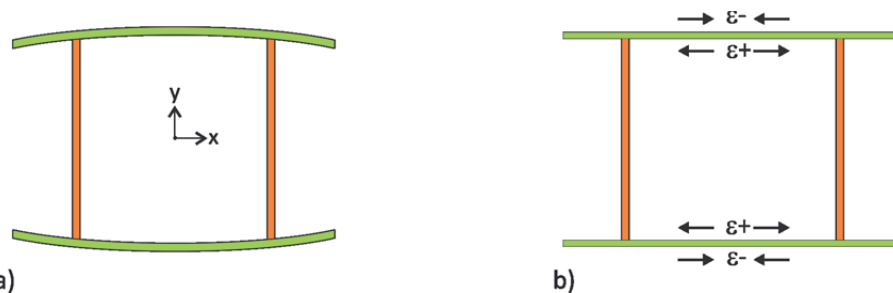


Figure 10-19 a) Spar cross-section when unloaded. b) Spar cross-section as load is increased. The Brazier effect will try to flatten the flanges, thereby causing additional transverse strains in the flanges.

The reduction of spar stiffness is confirmed by the plot of the measured ratio between transverse and axial strain along the spar (Figure 10-20), where a linear decrease takes place. This ratio should stay constant under linear conditions but can change due to nonlinear effects like buckling. Also in this plot the data from the center of the imperfection deviates from the other locations. At 0 mm the strain ratio is both lower and has a steeper declining slope. Unfortunately this could not be confirmed by the measurement from the 3D digitizer due to calibration errors. As the spar was pulled down and away from the digitizer, calibration was lost and therefore yielded measurements with inadequate accuracy. To ensure that accurate data are collected the digitizer should have been recalibrated every time the test was halted.

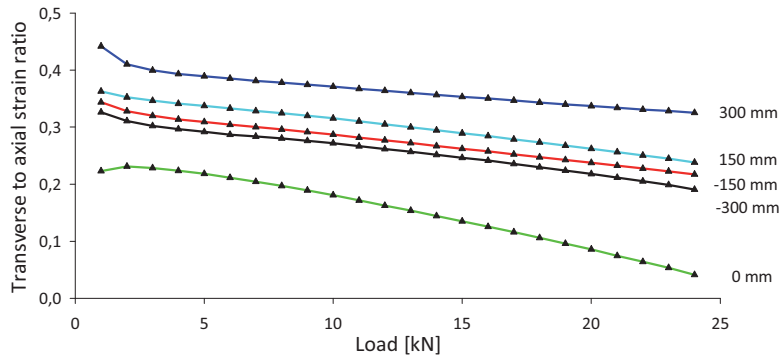


Figure 10-20 Transverse to axial strain ratio with increasing load.

Unfortunately, the spar did not fail by buckling of the upper flange. At a bending moment of 58.1 kNm, at 60% of the rated load, the bond between the shear web and flanges failed prematurely and caused a sudden collapse of the spar (Figure 10-22). There were no prior warnings with regards to cracking noises from matrix/bond failure or any visual clues. It was not possible to identify the starting point of the bond failure, but it most likely initiated at one of the supported ends or at the imperfection. Post-failure inspection of the spar showed that the bond had failed 3/4 of the spar length, spanning from the left side to 1.5 m from the right side. The inspection of the bond also revealed several areas with insufficient amount of adhesive between the parts. The explanation for this is twofold. Insufficient tolerances in the manufacturing and assembly of the spar parts caused an inconsistent bond thickness. In some areas of the spar, the shear web was close to the flange (Figure 10-21a), whilst in other areas there was a up to 3 mm gap (Figure 10-21b). The epoxy adhesive used, DP460 by 3M, had insufficient thixotropy to fill in these large gaps, causing it to drain away from the bonding surfaces as it hardened and result in inadequate bonding of the parts. This could most likely have been prevented by having greater production tolerances and using an adhesive with a higher thixotropy.



Figure 10-21 a) Ideal bonding of shear web and flange. b) Large gap between parts causing the adhesive to drain away due to insufficient thixotropy.



**Figure 10-22** Failure of bond between shear web and flange at the left side of the spar.

As a buckling pattern started to develop in the top flange, this would cause some parts of the flange to be pulled away from the shear web. This would introduce peel-stresses in the bond and could have contributed to the premature failure. It is therefore important to take this failure mode into account when designing a composite bond for a spar.

In Figure 10-22 it can be seen that the shear webs at the left side of the spar experienced a failure of the sandwich core. This failure mode was only found at the left side of the spar and progressed about 30 cm towards the center of the spar. This is most likely a 2nd order damage due to failure of the bond line. A likely scenario is that the bond failure initiated at the center of the spar and traveled towards the left and right sides. As the failure progressed, the remaining shear web (with its bonding intact) would have to carry a rapidly increasing shear load. With the bond failure progressing all the way to the left side of the spar, this resulted in a failure of the sandwich core at the outer 30 cm.

Chapter 10 Testing of a 6 m scaled main spar section

# 11 FEM analysis of 6 m main spar section

A FEM analysis of the 6 m spar was developed using the software Abaqus. The aim was to reproduce the boundary conditions and results from the 4-point bending test. This will allow for a deeper understanding of how the structure behaved and which factors influenced the collapse. Previous work by L. Kühlmeier (2006) and F. M. Jensen (2008) shows that correlating theoretical and experimental results can be quite challenging, as production methods, process control and assembly can influence the geometry and material properties of the specimen. By tuning and improving the FEM analysis such that it reproduces the experimental results, confidence is built in the model that allows for optimization studies. Although developing a FEM analysis can be extremely time consuming, it can save cost by reducing the number of prototypes having to be built.

## 11.1 Geometry, materials and boundary conditions

### 11.1.1 Geometry

The cross section of the 6 m spar was simplified by neglecting the corners of the shear webs (Figure 11-1). This was done because the quadratic 4-node shell elements used would not allow for a detailed analysis of the bond between the shear webs and spar flanges. Section definitions are shown in Figure 11-1, using ply notation introduced by L. Kühlmeier (2006). Subscripts denote the number of plies the relevant property applies to. In the bond area, the plies from both the flange and shear web are included in the section, assuming a perfect bond between them. The bonding adhesive is not included in the analysis due to the simplification of the shear web corners. In Abaqus each  $\pm 45^\circ$  ply was modelled as two discrete UD plies placed at  $+45^\circ$  and  $-45^\circ$ . The 6 m spar ply definitions used in the Abaqus input files are provided in Appendix G. A coordinate system was placed in the middle of the spar to ensure correct ply orientations. A discussion on ply orientation in Abaqus is provided in Section 8.5. Figure 11-2 illustrates how the shell element reference plane was offset by half of the flange element thickness in order to abstract the geometry.

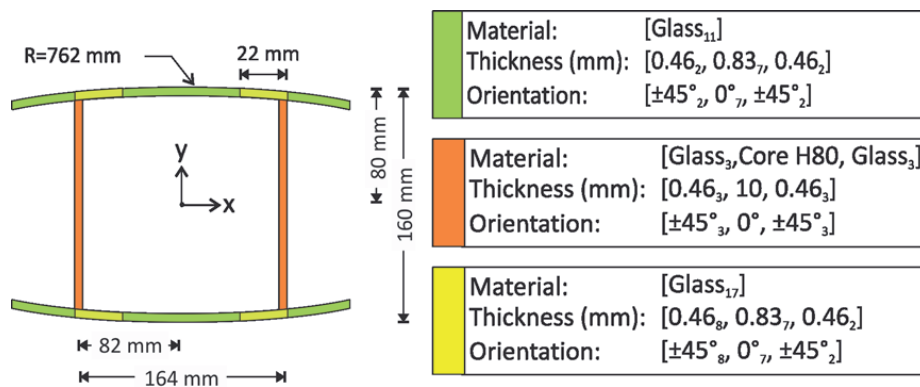


Figure 11-1 Dimensions and material definition of spar cross section shell model.

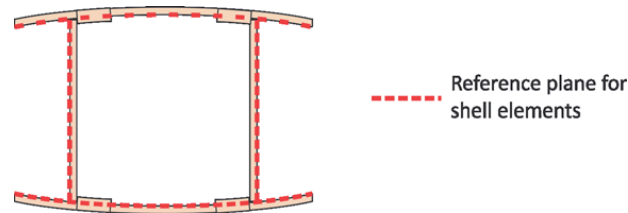


Figure 11-2 Shell element reference plane offset in order to abstract the spar geometry.

### 11.1.2 Boundary conditions

A symmetry-plane was established in the middle of the 6 m spar in order to reduce the number of elements needed in the analysis (Figure 11-3). This would greatly reduce the computational resources needed, especially when performing non-linear analysis. Figure 11-4a is a close-up picture of the boundary conditions in the middle of the spar. The nodes are restrained from moving in the z-direction and have no rotation about the x and y-axis.

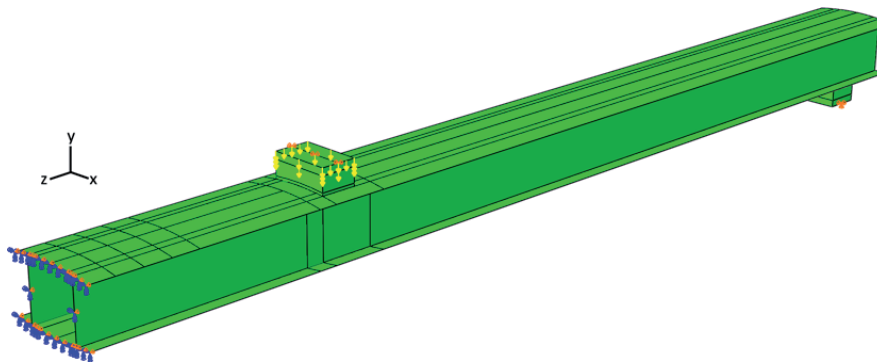


Figure 11-3 Overview of FEM geometry of 6 m spar with boundary conditions. Loading blocks are included in the analysis in order to correctly apply the end support and load. Details of boundary conditions are shown in Figure 11-4.

To ensure realistic load and support conditions of the spar, the MDF loading blocks were included in the analysis. The interaction between the loading block and top flange was simplified as a frictionless contact. The MDF loading block was modelled as an isotropic material with E-modulus=2 GPa and Poisson's ratio of  $\nu=0.3$  (R. M. Rowell, 2005). Figure 11-4b shows how the upper center line of the loading block was restrained in the x and z-direction. To avoid stress concentration and loads that follow nodal rations due to spar deflection, the 24.85 kN load was applied to the MDF loading block as a body force in the y-direction. This was the load registered at the moment spar failure during the 4-point bending test presented in Chapter 10.

The end support of the spar was replicated by restraining the MDF block at the end of the spar in the x and y-direction (Figure 11-4c). By also allowing it to rotate about the x-



axis, it would resemble the hinge/roller fixture used in the experiment. In the experiment a 5 mm thick sheet of EVA foam was put between the specimen and MDF blocks in order to evenly distribute the load. Initial FEM analysis included this EVA sheet, but it was removed because the relatively soft foam elements experienced large distortions. This caused the analysis to run very slow or to prematurely terminate due to convergence issues. The removal of the foam did not introduce any stress concentrations between the MDF loading blocks and spar flanges.

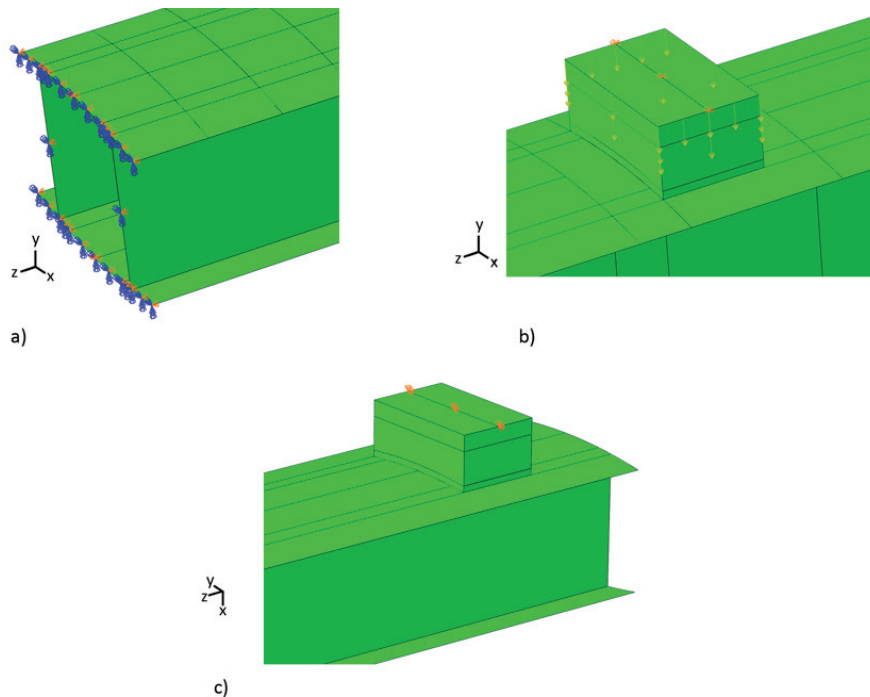


**Figure 11-4** a) Boundary conditions at the symmetry plane of the spar. Zero displacement are prescribed for the nodes in the z-direction together with no rotation about the x and y-axis.  
 b) MDF loading block restrained in the x and z-direction. Force is applied as a body load.  
 c) MDF support block at spar end. No translation in x and y-direction for the centerline. Note that spar is rotated 180° about z-axis for clarity.

### 11.1.3 Mesh

Quadratic four-node shell elements with reduced integration were used to mesh the spar. A discussion on element properties is provided in Chapter 8. Care was taken to partition the geometry in such a way that element nodes would be present along the spar centerline at the locations of the strain gages used in the experimental testing. A mesh refinement study was done to ensure that stress predictions were accurate, but also at the same time limit the amount of elements needed. The axial stress at a node on the spar flange and the shear stress at a node on the shear web were monitored as the element size was adjusted. The base line for comparison were the results from an analysis

with a high mesh density of 70 064 elements. Figure 11-5 shows how adjusting element size affected the stresses monitored. The adjustments of element size had very little effect on the axial stress predicted in to top flange (less than 1 %). The largest changes were found for the shear stress when adjusting the number of elements across the shear web. Adjusting the size to 0.016 (10 elements across shear web) resulted in under predicting the shear stresses by 7 %, which was acceptable since the focus in this analysis was the axial stresses in the top flange. The final spar mesh used a mesh width of 0.01 across the spar flanges and an element length of 0.02 along the spar. Further reductions in element numbers were gained by adjusting element length to 0.05 in the outer parts of the spar. The final spar analysis consisted of 16 470 elements (83 796 DOF). These reductions in computational costs were very beneficial when performing the more computational demanding non-linear analysis. Figure 11-6 shows the mesh and boundary conditions at the center of the spar. At the right end of the spar it can be seen how element length is increased at the outer portions of the spar.

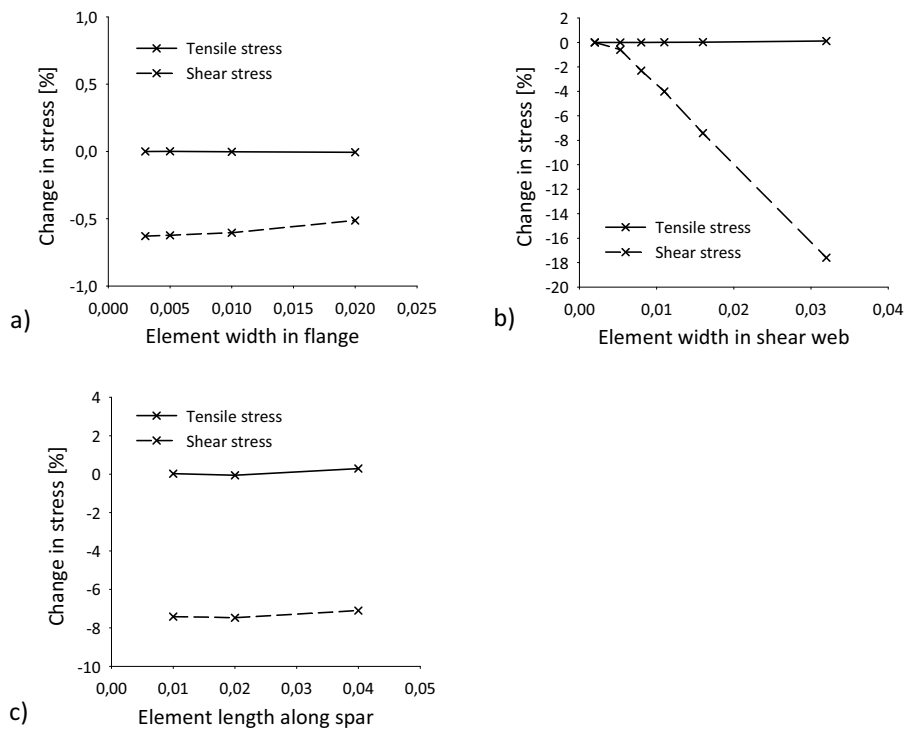


**Figure 11-5** Mesh refinement study of spar. a) Adjustment of element width across spar flange. b) Adjustment of element width across shear web. c) Adjustment of element length along spar.

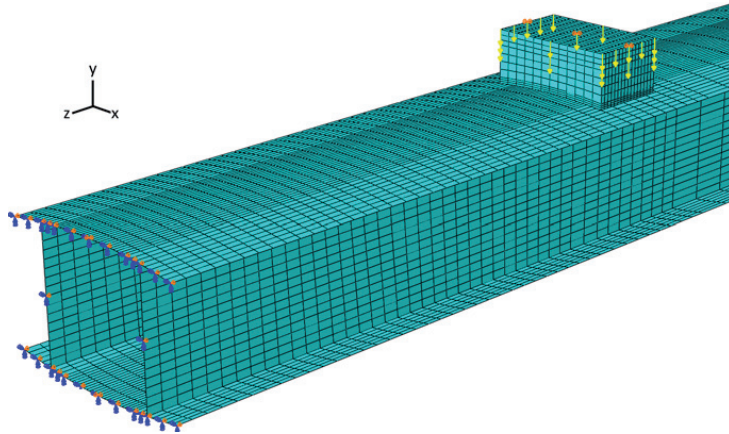


**Figure 11-6** Mesh of the middle part of the 6 m spar. Boundary conditions at the spar center and loading block are shown as small arrows.

### 11.2 Initial FEM analysis

The FEM analysis was run using linear and non-linear solvers which both predicted the global spar deflection very well (Figure 11-7 and Figure 11-9a). Figure 11-7 shows the shape of the deflected spar at a load of 24.85 kN. Figure 11-8 presents a field plot of the minimum axial stress in the spar. It can be seen how the compressive stresses in the top flange gradually increase towards the spar center. Towards the spar center it is the middle portion of the spar flange that experiences the largest compressive stresses. Figure 11-9b plots the axial strain in the middle of the spar on the top flange (position 0 mm centerline). Initially the FEM analysis follows the spar experiment perfectly, but after approximately 15 kN it does not reproduce the non-linear development seen in the experiment. A linear regression analysis of the FEM strain results in  $R^2=1$ , confirming that the FEM analysis predicts a linear increase of strain. By comparing the axial strain along the spar centerline with the experimental results (Figure 11-10a), we see that the FEM analysis does not reproduce the strain pattern in the area of the imperfection. Also, the predicted compressive strain at the outer parts of the test region (150-300 mm) are slightly lower. In Figure 11-10b the transverse strain at the center of the top flange is plotted. Here as well, the non-linear analysis does not reproduce the results from the spar experiment.

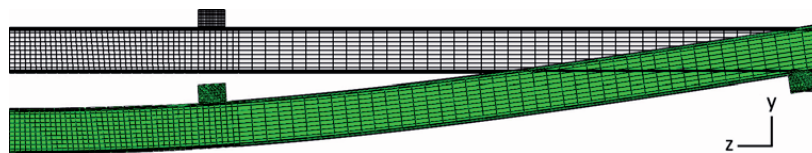


**Figure 11-7** Deflection of 6 m spar at 24.85 kN load. The transparent plot shows the shape of the unloaded spar for comparison.

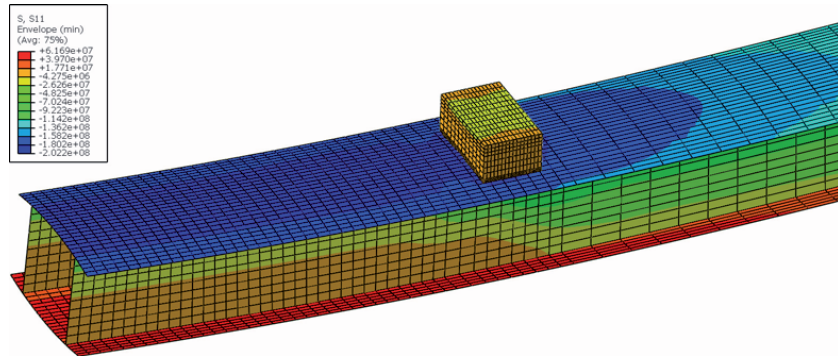


**Figure 11-8** Field plot of minimum axial stress in 6 m spar. Note that at the center of the spar the middle part of the top flange experiences the largest compressive stresses.

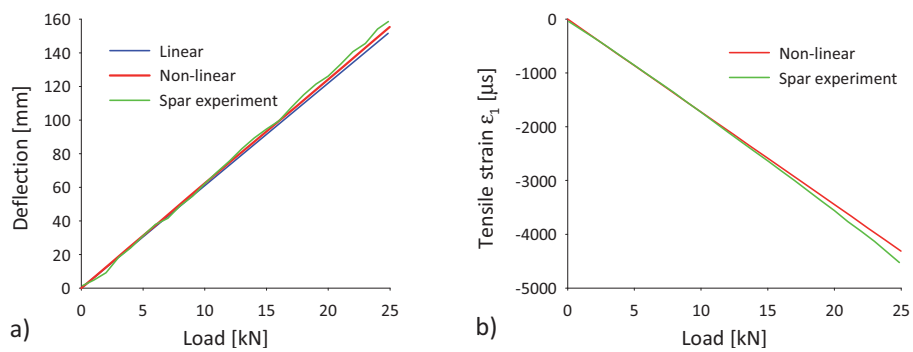


**Figure 11-9** a) Spar deflection from experiment and FEM analysis. b) Compressive strain on top flange in the middle of the spar.

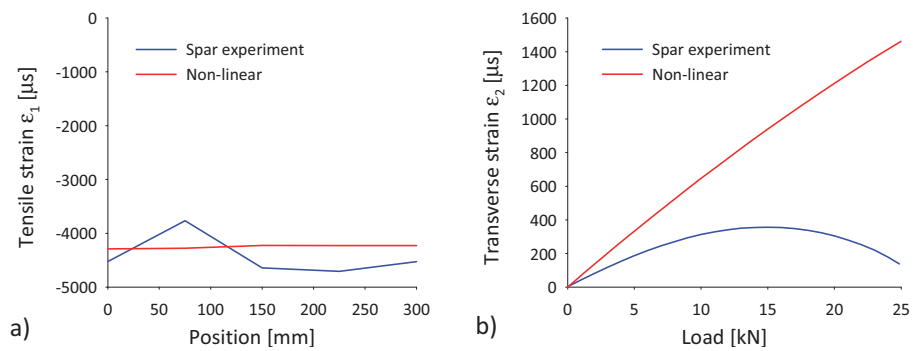


**Figure 11-10** a) Axial strain along spar centerline. b) Transverse strain at location 0 mm on top flange.

### 11.3 Calibration of FEM analysis

The initial FEM analysis of the 6 m spar predicted the global deflection and strains quite well. This confirms that the general abstraction of the spar geometry and material was fairly accurate. On a local level the FEM analysis did not accurately reproduce the strain pattern in the region of the imperfection and indicates that the model needed to be calibrated to the experimental results. Geometric simplifications, the absence of imperfections and uncertainties in material properties are all contributing factors to the difference between a FEM analysis and a real-life test.

#### 11.3.1 Corner stiffness

At the intersections between the shear web and the flange, the shell elements of the cross section share a common node (Figure 11-11a). Naturally the rotational stiffness of this node is affected by the ply definition of both the flange and shear web. In the initial FEM analysis, the shear web was simplified by defining all of it as being a sandwich structure made of glass fiber and core material (see Figure 11-1). The sandwich structure of the shear web imposes a big rotational stiffness on the shared node and thereby resists flattening of the spar flanges which is caused by the Brazier effect. In reality, the shear web goes from a sandwich structure to a monolithic laminate at the shear web corners (see fig Figure 10-2 and Figure 10-3). In order to increase the compliance in the intersection between the shear web and flange, the outer 10 mm of the shear web was partitioned and given a new ply definition. The laminate here consists of the same amount of  $\pm 45^\circ$  glass fiber plies as in the rest of the shear web, but without the core material. This more realistic laminate should lessen the restraint on the spar corners and result in increased flattening of the flange by the Brazier effect.

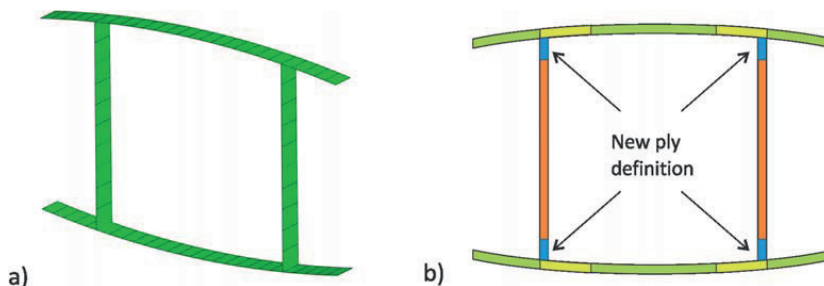


**Figure 11-11** a) Spar cross section represented by shell elements. b) New definition of shear web in order to increase the compliance of the corners of the shell element model. See also Figure 11-14.

Figure 11-12a shows that the axial strain along the spar centerline was increased by the compliant corners. The FEM analysis still fails to predict the strain pattern caused by the imperfection, but the axial strains in the region away from the imperfection are more correctly predicted. In Figure 11-12b, the relative displacement of the top flange, compared to the flange/shear web corner is plotted. It confirms that the compliant corners allowed for an increased flattening of the flanges. The increased compliance of the corner had however very little effect on the transverse strain  $\varepsilon_2$  (Figure 11-13).

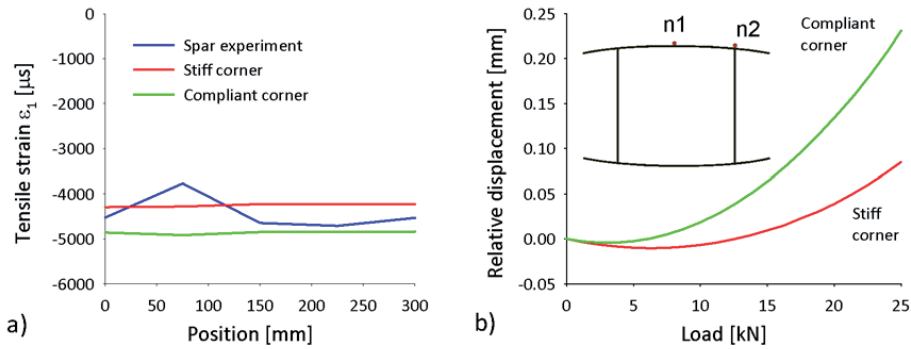


Figure 11-12 a) Axial compressive strain ( $\epsilon_1$ ) along spar centerline and the effect of corners with increased compliance. b) Relative displacement of node on top flange (n1) compared to node at flange/web intersection (n2).

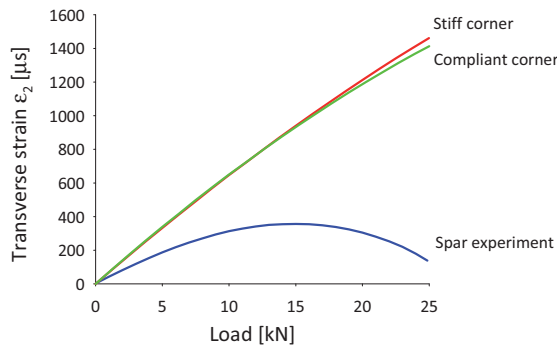
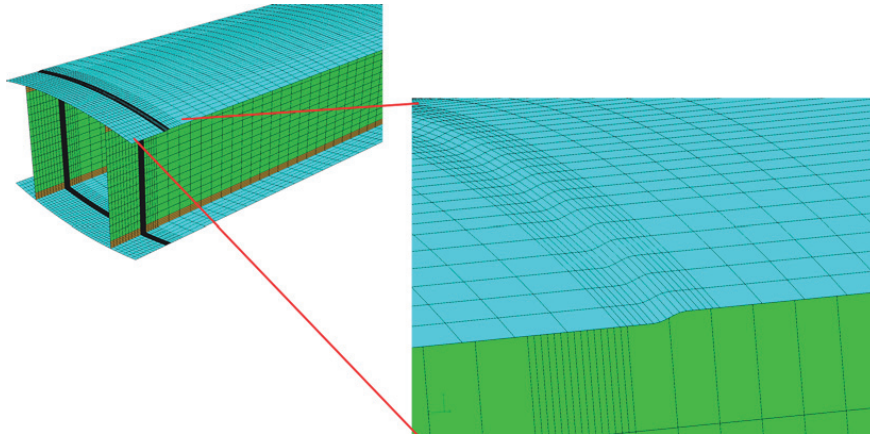


Figure 11-13 Influence of corners with increased compliance on transverse strain  $\epsilon_2$ .

### 11.3.2 Including the imperfection

The FEM analyses so far have not been able to reproduce the strain pattern observed in the area of the imperfection. This is most likely due to the absence of the imperfection which was present in the 6 m spar. As previously illustrated in Figure 10-4, the added UD ply increased the flange thickness by 0.83mm and caused a kink in the remaining UD plies. The imperfection was included in the FEM analysis by displacing the nodes over a length of 3 mm at the relevant location. A sine function was used to generate the shape of the imperfection (Figure 11-14). This way of implementing the imperfection is a conservative one since it assumes that all plies are displaced by 0.83 mm. Closer inspection of the spar laminate at the imperfection site shows that the kink is evened out through the thickness of the laminate (Figure 11-15). For this reason several imperfection sizes (0.83, 0.6 and 0.4 mm) were studied to see which one fitted the experimental results the best.



**Figure 11-14** Displacement of nodes in order to reproduce the imperfection (50 mm from spar center).

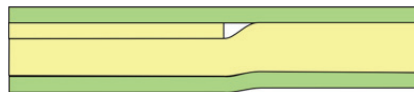


**Figure 11-15** A more realistic representation of how the imperfection affects the UD plies. The 0.83 mm displacement of the UD plies at the imperfection is evened out through the thickness of the laminate.

Figure 11-16 shows axial stress for UD plies in the spar flanges at the spar center. Comparison with Figure 11-8 shows that a stress concentration is introduced in the top flange by including the imperfection in the FEM analysis. The axial strains along the spar centerline are plotted in Figure 11-17 and clearly illustrate how including the imperfection in the FEM analysis influences the strain. Even though the compressive strain at 0 mm is overpredicted, the strain pattern observed in the 6 m spar experiment is reproduced very well. The plot also confirms that assuming that all UD plies are moved by 0.83 mm is a conservative approach. The best fit is found by using an imperfection size of 0.6 mm. Including the imperfection in the analysis also results in a better prediction of the transverse strain (Figure 11-18) with 0.83 mm coming very close to the experimental results. Since the correct prediction of the axial strains are of greater importance, an imperfection size of 0.60 mm will be used in the following FEM analysis.

It should be noted that having the experimental results available allowed for this method of fine-tuning the analysis. If the experimental results had not been available, using an imperfection size of 0.83 mm would yield conservative results and can be considered as a safe approach.

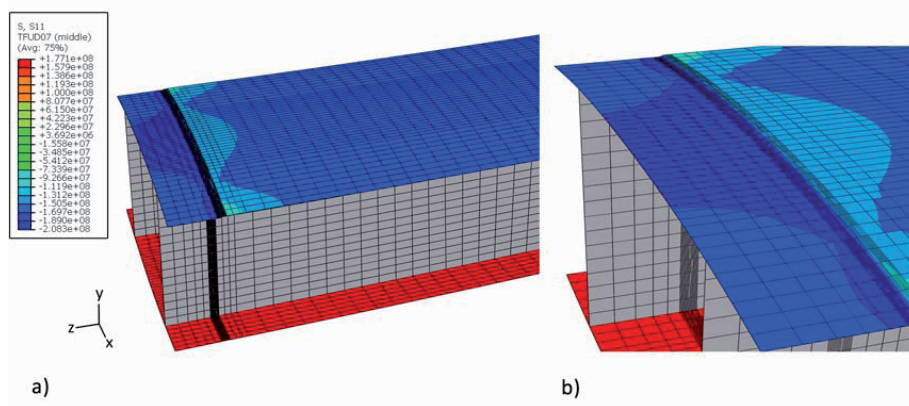


Figure 11-16 a) Axial stresses of UD plies in flanges at moment of spar failure (24.85 kN). An imperfection size of 0.6mm is used. b) Close-up of increased compressive stresses at imperfection.

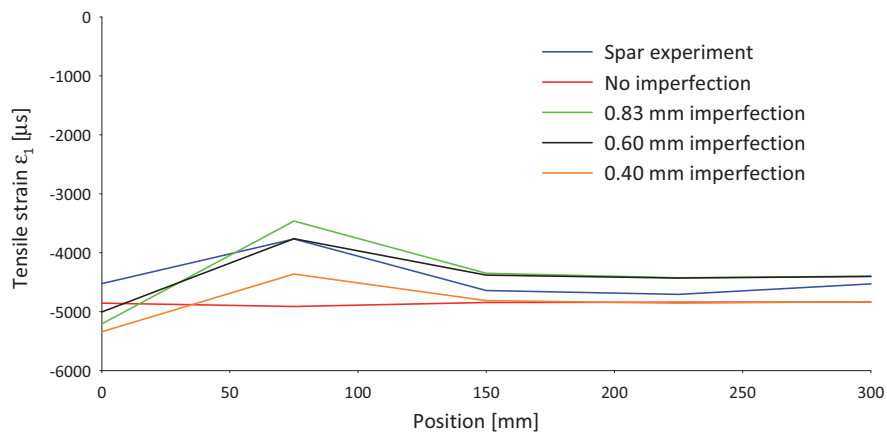


Figure 11-17 The effect of imperfection size on the axial strain pattern.

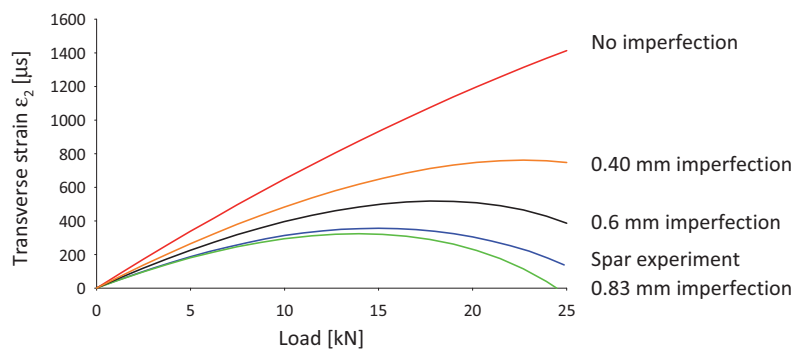


Figure 11-18 Effect of imperfection on the prediction of the transverse strain  $\epsilon_2$ .



### 11.3.3 Poisson's ratio

In the preceding FEM analyses of the 6 m spar, a Poisson's ratio of  $\nu=0.3$  has been used on the individual UD ply level. Literature reveals that the Poisson's ratio for a glass fiber composite can range from 0.20 to 0.30 (L. P. Kollár et al., 2003 and DNV-OS-C501-2003). Factors that affect the Poisson's ratio are the type of resin used in the composite, the production method used and degree of process control. Tensile tests on glass fiber UD laminates done during this thesis yielded a Poisson's ratio of  $\nu=0.22$ . Figure 11-19 shows how the FEM analysis with  $\nu=0.3$  overpredicted the transverse strains. This model has corners with increased compliance and includes a 0.6 mm imperfection. In order to better predict the transverse strains, the Poisson's ratio was gradually reduced such that it would fit the results from the 6 m spar experiment. At  $\nu=0.235$  it is seen that the predicted axial strain agrees very well with the experimental results. The reduction of the Poisson's ratio had negligible effect on the axial strain, which were reduced by only 0.7 %.

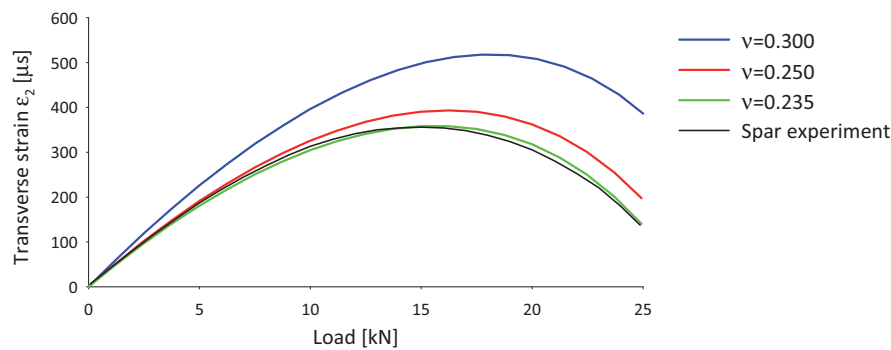
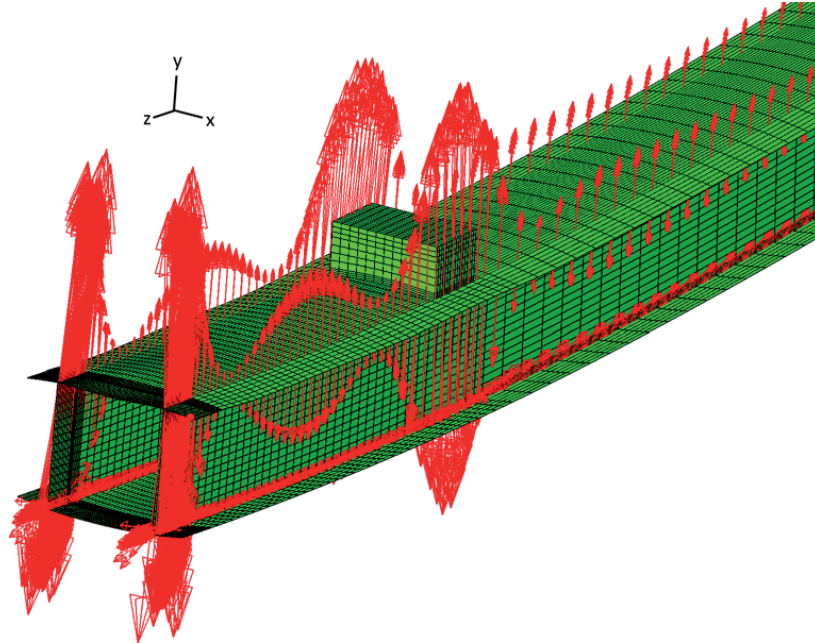


Figure 11-19 The effect of adjusting the Poisson's ratio on the transverse strains ( $\epsilon_2$ ).

### 11.3.4 Peel-strain in bond

In Chapter 10 it was hypothesized that the buckling shape of the top flange might have introduced peel-strains in the bond between the top flange and shear webs, thereby contributing to the premature failure of the spar. The geometry and elements used in this analysis are not suitable for a detailed analysis of the bond. For this, one would have to use three-dimensional elements and include the corners of the shear webs. In Figure 11-20 the vectors of the maximal in-plane strain are plotted for the nodes that intersect between the flanges and shear webs. The vectors in the gage area of the spar strongly suggest that peel-strains were present due to the buckling shape of top flange. The analysis does not quantify the peel-stain, but it shows its presence and that peel-strain should be accounted for when designing bonds.



**Figure 11-20** Maximum in-plane strain at the intersection between shear web and top flange. The strain vectors suggest that peel-strains were present in the bond between the top flange and shear webs due to the buckling shape of the top flange.

#### 11.4 Comments on the FEM analysis

A FEM analysis of the 6 m spar was successfully developed and tuned such that it would reproduce fairly accurately the results from the 4-point bending test. The analyses showed that using the actual dimension of the defect gave a slight overprediction of strains, i.e. conservative results. The Poisson's ratio is important for the accurate calculations of the transverse strains in the spar flanges. The development of this analysis confirms the value of combining both experimental and theoretical results. Trying to match the experimental and theoretical results yields a better understanding of which factors affect the result and how the structure behaves. The work also shows how analysis simplifications and material properties affect the results. A major challenge with composite materials are their sensitivity to manufacturing methods and process control. A good understanding of the production processes and materials involved will aid in the development of the FEM analysis.

## 12 Conclusions and future work

### 12.1 Overall conclusions

The main spar geometry for a 100 m wind turbine blade was established and analyzed by FEM. The spar was subjected to the maximum flapwise bending loads expected to occur during the 1-year and 50-year extreme gust. Carbon, glass and hybrid composite spars were developed, assuming both pitch control and failure of pitch control during the extreme gusts. If pitch control is maintained during the gusts, the root bending loads are reduced by 23 %. It was found that the most effective design was achieved by placing the UD plies where they contribute the most to global spar stiffness. For blades with pitch control the carbon, hybrid and glass fibers spars had a weight of 40, 66 and 76 ton respectively. Safety factors were included in the design optimization.

Traditional design of a wind turbine spar uses a monolithic laminate in the spar flanges. Using  $\pm 45^\circ$  plies on both sides of a UD ply for buckling resistance yields good results, but can be further optimized. It was found that the use core material in the spar flanges, employing a sandwich design, can reduce the need of  $\pm 45^\circ$  plies by 50 %. Further gains are achieved by homogenization of the laminate. When optimizing a composite spar for buckling resistance, non-linear analysis should be used. Linear simplifications and optimization can in worst-case lead to non-optimal designs.

A 6 m scaled glass fiber spar was produced by resin infusion and tested in a 4-point bending rig. A FEM analysis of the spar was developed and calibrated, yielding very good agreement between experimental and theoretical results. Including production defects in a FEM analysis is important in order to accurately predict the behavior of a composite laminate.

### 12.2 Detailed conclusions

Offshore wind turbines have access to stronger winds with less wind turbulence and hence the productivity of each unit is increased. These turbines will also most likely have lesser environmental impact than land based systems. The installation cost for an offshore wind turbine is believed to be relatively independent of turbine size and will therefore encourage the development of bigger turbines. In this thesis the main spar for a 100 m long wind turbine blade was studied.

The main spar geometry for a 100 m wind turbine blade was established and analyzed using the FEM software Abaqus. The main focus was the spar flanges as the blade is subjected to ultimate loads during its 20-year service life. Three different versions of the main spar were developed using carbon, glass or hybrid composites. In the hybrid spar the UD plies are made of carbon fiber whilst the  $\pm 45^\circ$  anti buckling plies are made of glass fiber. The spar flanges consisted of a lay-up with the UD plies placed in the middle of the laminate and surrounded by equal amounts of  $\pm 45^\circ$  plies [ $\pm 45^\circ/0^\circ/\pm 45^\circ$ ]. Ply distribution was done using both linear static and linear buckling analyses. Using buckling analysis for ply distribution was found to be very labor intensive and time consuming. A

Matlab-program that could interact with the FEM software was therefore written in order to automate the distribution of the  $\pm 45^\circ$  anti-buckling plies. This proved to be very effective and time saving in the design phase. For structures which experience large deflections during ultimate loads, linear buckling analysis tends to overestimate the buckling capacity. When compared to non-linear buckling analysis, the spar with the largest deflections overestimates the buckling load up to a factor 2. Compared to non-linear buckling analysis, a linear buckling analysis is much faster and therefore the preferred method during the design phase. But a scaling factor should be used together with the linear buckling analysis in order to ensure sufficient buckling capacity. Finally, promising solutions should be checked by nonlinear analysis.

When distributing the UD plies along the spar flanges, two different philosophies were tried: one is to place UD plies in areas with high stress, the other is to symmetrically place plies in the bottom and top flanges of the spar. It was shown that the symmetric design philosophy was considerably more effective. It can be concluded that the UD plies should be placed where they contribute the most to global spar stiffness. The ultimate loads during the 1-year and 50-year extreme gust were calculated for blades with pitch control and for blades experiencing a failure of pitch control. Assuming that the wind turbine experiences pitch failure during the 50-year gust, the carbon, hybrid and glass fiber spars had a weight of 41, 63 and 115 ton respectively. For the glass fiber spar, the assumption of pitch failure leads to a conservative and very heavy design. Large amounts of UD glass fiber plies are needed in order to prevent blade-tower interference. If one assumes that the wind turbine system manages to maintain pitch control, being able to turn the profile out of the wind during the 50-year gust, the maximum root bending loads are considerably reduced (23 %). For the glass fiber spar this led to a significant weight reduction, whilst the weight of the carbon and hybrid spars remained practically unchanged. The reduced root bending loads resulted in thinner UD carbon plies for global stiffness. The thinner UD carbon plies require larger amounts of  $\pm 45^\circ$  plies for buckling resistance, hence resulting in no net weight reduction. For the blades with pitch control the carbon, hybrid and glass fibers spars had a weight of 40, 66 and 76 ton respectively.

A simple cost analysis of the spars was done, considering only the material cost of the composites used. The carbon blade was the most expensive one with a cost of nearly one million Euro. The hybrid and glass fiber spars had a price of 476 k€ and 171 k€. Even though the carbon fiber spar is considerably more expensive than the glass fiber spar, it might be a viable option because of its low weight. Reduced weight will decrease the demands on the remaining components in wind turbine and might therefore bring the total system cost down.

It was explored whether the lay-up described above could be further optimized with regards to weight and buckling resistance. The 100 m hybrid spar was identified as the solution with the most weight saving potential. The relatively thin UD carbon plies for global stiffness required large amounts of  $\pm 45^\circ$  glass fiber plies in order to avoid buckling. Sub-models of spar cross sections were established with the aim of reducing weight and increase buckling resistance of flange laminate. While keeping the total amount of  $\pm 45^\circ$  glass fiber plies constant, their ply angles and thickness were optimized by linear buckling analysis. This approach did not result in a significant increase in the

buckling load. Also altering the ply angles of the UD carbon plies did not yield any desirable results. Only non-linear analyses showed that the addition of core material in the top flange resulted in the largest increases in buckling load. Additional gain was achieved by ply homogenization, the even distribution of the  $\pm 45^\circ$  plies amongst the UD plies. For a 100 m spar the amount of anti-buckling plies in the bottom flange was reduced by 50 %. Using sub-models for optimization is a very computationally effective method for optimizing a structure. Due to large deflections, a wind turbine spar is subjected to several non-linear effects in addition to buckling, which itself is a non-linear phenomenon. A linear analysis will fail to include these non-linearities and optimization by linear methods will most likely result in a non-optimal result. Nonlinear analysis should therefore be used when optimizing a wind turbine spar against buckling failure.

An experimental program was done to check how well the FEM analysis can predict buckling. A 6 m scaled wind turbine spar was made of glass fiber composite and produced by resin infusion. The specimen was designed to fail by buckling in a 4-point bending test, with the middle 1.3 m subjected to a constant bending moment. To control the location of the buckling failure, a realistic imperfection was added to the top flange during production. The imperfection was an extra ply of UD fiber, 100 mm wide, causing a 0.83 mm kink in the remaining UD fibers. Altogether 25 strain gages measured the axial and transverse strains in the gage section of the spar. Axial strain measurements along the top flange centerline show that a buckling pattern developed at the location of the imperfection. Measurements of the transverse strain also confirm that the spar experienced Brazier buckling, which is expected in slender structures subjected to bending loads. The spar collapsed at 60 % of the rated load, experiencing a maximum bending moment of 58.1 kNm. Post-failure examination shows that the premature failure was most likely due to inadequate bonding between the shear webs and spar flanges. It is also believed that peel-stresses in the bond contributed to the collapse.

A FEM analysis of the 6 m spar was developed with the aim of reproducing the results from the experiment. This would also highlight some of the challenges involved when comparing experimental results and FEM analysis. A shell element analysis of the spar was run using both linear and non-linear methods. The initial analysis used a perfect geometry and managed to predict the global spar deflections, but failed to reproduce the strain pattern observed in the top flange. By including the imperfection in the analysis the shape of the strain pattern was replicated. Further adjustments to the size of the imperfection and stiffness of spar corners resulted in an analysis that reproduced the results from the experiments very well. Even though the model was not suitable for detailed analysis of the spar bonds, the strain readings from the shear webs strongly suggested that peel-strains were present in the bond and that this contributed to the premature failure of the spar.

### 12.3 Future work

Due to the computational resources needed, there is a limit to the level of detail one can include in a global FEM-model of a wind turbine blade. The global model is used as a basis for providing overall structural behavior, as e.g. buckling critical areas, deflections, areas of high stress, etc. By creating sub-models of the wind turbine blade, more

detailed analysis can be performed of critical areas. As stated in the conclusion, sub-modeling can be used in the optimization of composite laminates for a wind turbine spar. As of now, all published studies have used linear analysis in the optimization of the main spar laminate. The work in this thesis confirmed that a linear analysis fails to include the non-linear effects which are present in long and slender structures such as a wind turbine blade spar. One might therefore risk developing a composite laminate that is not optimal under real life operating conditions. Future studies are therefore recommended to use non-linear analysis in their optimization routines. To limit the number of iterations needed, search algorithms should be used (e.g. a genetic search algorithm). Even though non-linear analyses will be considerably more time consuming, the level of computing power available to an engineer today (with a reasonable budget) allows for such studies to be solved within reasonable time.

The combination of theoretical studies and actual laboratory testing is highly valuable. Such tests serve as an important verification of the FEM analysis and will allow for the development of powerful optimization tools. Laboratory experiments can be extremely time consuming and represent a significant cost. It is therefore important to learn as much as possible from the experiment. Strain gages are simple to use and give good data on the measured strain. But they give very local data and one would need a large amount of strain gages to get a good picture of the strain-field. Future studies should aspire to use optical strain measurements of the specimen in order to get better understanding of how the strain-field develops with increased load on a spar.

The FEM optimization done in this thesis showed that the amount of  $\pm 45^\circ$  laminate used for buckling resistance can be greatly reduced through the use of core material in the spar flanges. Additional gains in buckling resistance are also achieved through homogenization of the laminate. It is recommended that these findings are verified by experimental testing in order to confirm the validity of the optimization. Performing the testing on a structure similar to the 6 m spar would allow for good comparison of the results.

## References

**Berggreen, Christian** (2005). Application of load carrying sandwich elements in large wind turbine blades. O.T. Thomsen et al. (eds), *Sandwich Structures 7: Advancing with Sandwich Structures and Materials*, 947-956. Springer, ISBN-10 1-4020-34444-x (HB).

**Bertagnolio, Franck** (2001). Wind turbine airfoil catalogue. Risø-R-1280. Risø national laboratory, Roskilde, Denmark. ISBN 87-550-2910-8

**Brazier, L.** (1927). On the flexure of thin cylindrical shells and other "thin" sections. *Proceedings of the Royal Society of London. Series A, Containing Papers of a Mathematical and Physical Character*, 104-114.

**Brøndsted, Povl** (2005). Composite materials for wind power turbine blades. *Annu. re. mater. Res.* 2005, 35: 505-538.

**Brøndsted, Povl** (2005). Materials for Wind Turbine Rotor Blades and Their Fatigue Behavior. Coronet Regional seminar. RISØ National Laboratory, Denmark. <http://www.risoe.dk/afm/coronet-regional-seminar/Presentations/CORONET%20Povl%20Broendsted%20Risoe.pdf>

**DNV** (2003). Composite components. Det Norske Veritas. Offshore standard DNV-OS-C501.

**DNV** (2006). Design and manufacture of wind turbine blades, offshore and onshore wind turbines. Det Norske Veritas. Offshore standard DNV-OS-J102.

**DNV/RISØ** (2002). Guidelines for Design of Wind Turbines. 2nd edition, ISBN 87-550-2870-5.

**Fuglsang, Petter** (2004). Design and verification of the Risø-B1 Airfoil family for wind turbines. *Journal of solar energy engineering*, 2004, 126: 1002-1010.

**Fuglsang, Petter** (2004). Development of the Risø Wind Turbine Airfoils. *Wind Energy*, 7:145-163, 2004.

**Gardinger, G.** (2007). Carbon fiber in the wind. *High Performance Composites*, Volume 15, number 4.

**Gardiner, G.** (2008) Wind blade manufacturing, Part I: M and P innovations optimize production. *High Performance Composites*, Volume 16, number 6.

**Germanischer Lloyd** (1993). Regulation for the Certification of Wind Energy Conversion Systems, Chapter 1-10. 1993 Edition.

**Hansen, Martin O.** (2000) *Aerodynamics of Wind Turbines*. ISBN 1 902916 06 9.

## References

**Harrison, R. and Jenkins, G.** (1993). Cost modelling of horizontal axis wind turbines. Technical Report ETSU W/34/00170/REP. University of Sunderland.

**Hartman, Dave** (2006). Analysis of wind turbine blade failure modes. Presentation at Wind Energy Composites and Polycon, 2006. Owens Corning. <http://www.owenscorning.com/hiper-tex/pdfs/WindEnergyAnalysis.pdf>

**Hau, Erich** (2006). Wind Turbines: Fundamentals, Technologies, Application, Economics, 2nd ed. Springer. ISBN-10 3-540-24240-6.

**Hayman, B., Wedel-Heinen, J. and Brøndsted, P.** (2008). Materials Challenges in Present and Future Wind Energy. Materials Research Society. MRS Bulletin, 33: 343-353.

**Heider, D.** (2000). Automation and Control of Large Scale Composite Parts by VARTM Processing, In: Proceeding of the 45th International SAMPE Symposium Exhibition, Bridging the Centuries with SAMPE's Materials and Processes Technology, Long Beach, CA.

**Hepperle, Martin** (2007). JavaFoil application for generating airfoil cross sections. <http://www.mh-aerotoools.de/airfoils/javafoil.htm>

**Herakovich, C. T.** (1997). Mechanics of fibrous composites. John Wiley and Sons. ISBN-10: 0471106364

**Hoff, N. J. and Mautner S. E.** (1945). Buckling of sandwich type panels. Journal of Aeronautical Science, 12(3), 285-297.

**Hughes, C. J.** (2005). VARTM variability and substantiation. University of Delaware, Center for Composite Materials. <http://www.jams-coe.org/docs/Tuesday%20Afternoon05/Newton.pdf>

**IEC 61400-1** (2005). International standard. Wind Turbines - Part1: Design requirements

**IIT**(2006). Illinois Institute of Technology poster at IPRO Day exhibition Dec. 1st. [http://www.iit.edu/~ipro344f06/archive/derivables/IPRO344F06\\_Poster.pdf](http://www.iit.edu/~ipro344f06/archive/derivables/IPRO344F06_Poster.pdf)

**Irgens, Fridtjov** (1999). Fasthetslære. 6th edition. Tapir Forlag. ISBN 82-519-1522-8

**Isaac M. Daniel et al.** (1994). Engineering mechanics of composite materials. Oxford University Press. ISBN 0-19-515097-X.

**Jacobsen, Morten R.** (2008). Extremely large wind turbine blades. Masters Thesis. Norwegian University of Science and Technology, Department of Engineering Design and Materials.

**Jensen, Find M.** (2008). Ultimate strength of a large wind turbine blade. Department of Civil Engineering, Technical University of Denmark. ISBN 978-87-550-3634-5.



**Jensen, Jacob and Schultz, Jacob** (2005). Application of Load Carrying Sandwich Elements in Wind Turbine Blades. Master thesis. Technical University of Denmark, Department of Mechanical Engineering.

**Joncas, Simon** (2004). Preliminary Design of Large Wind Turbine Blades Using Layout Optimization Techniques. Delft University of Technology, Delft, The Netherlands.

**Kollár, L. P.** (2003). Mechanics of Composite Structures, Cambridge University Press, ISBN-10: 0521801656.

**Kühlmeier, L.** (2006). Large scale buckling experiment and validation of predictive capabilities. Department of Mechanical Engineering, Aalborg University, Denmark. ISBN 87-91464-00-5.

**Li, W.** (2004). Process and Performance Evaluation of the Vacuum Assisted Process. Journal of Composite Materials, 38:1803-1814.

**LM** (2002). LM newsletter April 2002. [http://www.lmglassfiber.com/uploadlmnews\\_200204\\_uk.pdf](http://www.lmglassfiber.com/uploadlmnews_200204_uk.pdf)

**LM** (2008). Web link-01: <http://www.lmglassfiber.com/Technology/Test/Aerodynamic%20test.aspx>. Copy of page in Appendix H.

**LM** (2008). Web link-02: <http://www.lmglassfiber.com/Products/Wing%20Overview/2000-5000/LM%2061.5.aspx>. Copy of page in Appendix H.

**Lund, Erik** (2005). Buckling optimization of laminated hybrid composite shell structures using discrete material optimization. 6th World COngress on Structural and multidisciplinary optimization.

**Lund, Erik** (2005). On Structural Optimization of Composite Shell Structures Using a Discrete Constitutive Parametrization. *Wind Energy*, 8:109-124, 2005.

**Manwell, J. F.** (2002). Wind energy explained - Theory, design and application. John Wiley & Sons, LTD. ISBN 0 471 49972 2.

**Mason, Karen F.** (2004). Carbon/glass hybrids used in wind turbine rotor blade design. Composites Technology. [www.compositesworld.com](http://www.compositesworld.com)

**NVE** (2007). Fornybar Energi 2007. ISBN 978-82-410-0632-6.

**Nygaard, Tor Anders** (1999). Optimization of wind turbine rotors. PhD thesis, Norwegian University of Science and Technology. ISBN 82-471-0472-5.

**Plastics Technology** (2008). Wind Power Blades Energize Composites Manufacturing *Plastics Technology*, 10, 2008.

## References

**Risø** (2001) Wind Turbine Airfoil Catalogue. Risø National Laboratory. ISBN 87-550-2911-6

**Roos, Ruud van** (2004) Design of airfoils for wind turbine blades. Delft University of Technology. [http://gcep.stanford.edu/pdfs/energy\\_workshops\\_04\\_04/wind\\_van\\_roos.pdf](http://gcep.stanford.edu/pdfs/energy_workshops_04_04/wind_van_roos.pdf)

**Rowell, R. M.** (2005). Handbook of wood chemistry and wood composites. ISBN 0-8493-1588-3.

**Scott, J.** (2003). Airfoils at high angle of attack. <http://www.aerospaceweb.org/question/airfoils/q0150b.shtml>. Copy of page in Appendix H.

**Sheldahl, R.E.** (1981) Aerodynamic characteristics of seven symmetrical airfoil section through 180-degree angle of attack for use in aerodynamic analysis of vertical axis wind turbines. Sandia National Labs report SAND80-2114.

**Spera, David A.** (1994) Wind turbine technology. American Society of Mechanical Engineers. ISBN 0-7918-1205-7.

**SP Systems** (2001). Guide to Composites. <http://www.bolton.ac.uk/CODATE/SPGuidetoComposites.pdf>

**Sørensen, N. N.** (2004). Drag prediction for blades at high angle of attack using CFD. Journal of Solar Energy Engineering, 126: 1011-1016: 2004.

**Sørensen, Bent F.** (2004). Improved design of large wind turbine blade of fibre composites based on studies of scale effects (Phase 1) - Summary Report. Risø-R-1390(EN).

**Sørensen, Bent F.** (2005). Improved design of large wind turbine blades of fibre composites (Phase 2) - Summary Report. Risø-R-1526(EN).

**Thomsen, Ole T.** (2006). Sandwich materials for wind turbine blades. Proceedings of the 27th Risø International Symposium on Materials Science: Polymer Composite Materials for Wind Power Turbines. Risø National Laboratory, Roskilde, Denmark, 2006.

**Toho Tenax** (2009). Web link-05: <http://www.tohotenax-eu.com/en/products/tenax/filament-yarn/sts.html>. Copy of page in Appendix H.

**Tsai, Stephen W.** (1988). Composites Design, 4th edition. Think Composites. ISBN 0-9618090-2-7

**Tsai, Stephen W.** (2008). Strength and Life of Composites. ISBN 978-0-9819143-0-5.

**USA Today** (2007). Web link-03: Aircraft orders put carbon fiber prices in steep climb. [www.usatoday.com/money/industries/manufacturing/2007-06-05-carbon-fibers-usat\\_N.ht](http://www.usatoday.com/money/industries/manufacturing/2007-06-05-carbon-fibers-usat_N.ht). Copy of page in Appendix H

**Veers, Paul S.** (2003). Trends in the design, manufacture and evaluation of wind turbine blades. *Wind Energy*, 6: 245-259, 2003.

**White, Frank M.** (1994). *Fluid Mechanics*. McGraw-Hill. ISBN 10 0072281928.

**Wonderly, C.** (2005). Comparison of mechanical properties of glass fiber/vinyl ester and carbon fiber/vinyl ester composites. *Composites Part B: Engineering*, 36: 417-426.

## References

## Appendix A 100 m main spar geometry

Table A.1 shows detailed information about section properties of the FEM model of a 100 m main spar. This information is used to generate the NACA 64-0XX profiles using the Java application JavaFoil (<http://www.mh-aerotoools.de/airfoils/javafoil.htm>).

**Table A.1** Geometric properties of 100m blade FEM model

Local blade length [m]	Chord length [m]	Main spar half width [m]	Twist angle	Shape	t/c [%]	Radius corner [m]
0	4.5		0.0	Circular	100.00	
5	4.5		0.0	Circular	100.00	
22.2	7.27	1.218	0.0	Box	30.00	0.300
30	6.77	1.133	1.5	Box	28.20	0.263
40	6.12	1.024	3.4	Box	25.88	0.219
50	5.47	0.916	5.4	Box	23.57	0.177
60	4.82	0.807	7.3	Box	21.25	0.142
70	4.17	0.698	9.2	Box	18.94	0.109
80	3.52	0.589	11.1	Box	16.63	0.081
90	2.87	0.480	13.1	Box	14.31	0.056
100	2.22	0.371	15.0	Box	12.00	0.037

Appendix A

## Appendix B Ply definitions from FEM analysis of 100 m main spar

### B.1 Symmetric-Stiff-Carbon spar (S-S-C)

Table B.1 Top flange and corners ply definitions

Ply #	Section start	Section stopp	Material	Thickness	Angle
1	1	40	Carbon	0.002	+45
2	1	40	Carbon	0.002	-45
3	1	39	Carbon	0.002	+45
4	1	39	Carbon	0.002	-45
5	1	37	Carbon	0.002	+45
6	1	37	Carbon	0.002	-45
7	9	29	Carbon	0.002	+45
8	9	29	Carbon	0.002	-45
9	1	36	Carbon	0.0045	0
10	1	33	Carbon	0.0045	0
11	6	27	Carbon	0.0045	0
12	8	17	Carbon	0.0045	0
13	7	23	Carbon	0.0045	0
14	5	30	Carbon	0.0045	0
15	1	35	Carbon	0.0045	0
16	1	40	Carbon	0.0045	0
17-24	Symmetric about last UD ply				

Appendix B

**Table B.2** Bottom flange and corners ply definitions

Ply #	Section start	Section stopp	Material	Thickness	Angle
1	1	40	Carbon	0.002	+45
2	1	40	Carbon	0.002	-45
3	1	38	Carbon	0.002	+45
4	1	38	Carbon	0.002	-45
5	1	36	Carbon	0.0045	0
6	1	33	Carbon	0.0045	0
7	6	27	Carbon	0.0045	0
8	8	17	Carbon	0.0045	0
9	7	23	Carbon	0.0045	0
10	5	30	Carbon	0.0045	0
11	1	35	Carbon	0.0045	0
12	1	40	Carbon	0.0045	0
13-16	Symmetric about last UD ply				

**Table B.3** Shear web ply definitions

Ply #	Section start	Section stopp	Material	Thickness	Angle
1	1	40	Carbon	0.002	+45
2	1	40	Carbon	0.002	-45
3	1	40	Diab H200	0.02	0
4-5	Symmetric about last UD ply				



## B.2 Symmetric-Stiff-Hybrid spar (S-S-H)

**Table B.4** Top flange and corners ply definitions

Ply #	Section start	Section stopp	Material	Thickness	Angle
1	1	40	Glass	0.002	+45
2	1	40	Glass	0.002	-45
3	1	39	Glass	0.002	+45
4	1	39	Glass	0.002	-45
5	1	38	Glass	0.002	+45
6	1	38	Glass	0.002	-45
7	1	37	Glass	0.002	+45
8	1	37	Glass	0.002	-45
9	1	35	Glass	0.002	+45
10	1	35	Glass	0.002	-45
11	7	31	Glass	0.002	+45
12	7	31	Glass	0.002	-45
13	9	27	Glass	0.002	+45
14	9	27	Glass	0.002	-45
15	1	37	Carbon	0.004	0
16	1	34	Carbon	0.004	0
17	6	30	Carbon	0.004	0
18	8	24	Carbon	0.004	0
19	7	19	Carbon	0.004	0
20	6	28	Carbon	0.004	0
21	1	32	Carbon	0.004	0
22	1	35	Carbon	0.004	0
23	1	40	Carbon	0.004	0
24-37	Symmetric about last UD ply				

Appendix B

**Table B.5** Bottom flange and corners ply definitions

Ply #	Section start	Section stopp	Material	Thickness	Angle
1	1	40	Glass	0.002	+45
2	1	40	Glass	0.002	-45
3	1	39	Glass	0.002	+45
4	1	39	Glass	0.002	-45
5	1	38	Glass	0.002	+45
6	1	38	Glass	0.002	-45
7	9	33	Glass	0.002	+45
8	9	33	Glass	0.002	-45
9	1	37	Carbon	0.004	0
10	1	34	Carbon	0.004	0
11	6	30	Carbon	0.004	0
12	8	24	Carbon	0.004	0
13	7	19	Carbon	0.004	0
14	6	28	Carbon	0.004	0
15	1	32	Carbon	0.004	0
16	1	35	Carbon	0.004	0
17	1	40	Carbon	0.004	0
18-25	Symmetric about last UD ply				

**Table B.6** Shear web ply definitions

Ply #	Section start	Section stopp	Material	Thickness	Angle
1	1	40	Glass	0.002	+45
2	1	40	Glass	0.002	-45
3	1	40	Diab H200	0.02	0
4-5	Symmetric about last UD ply				

### B.3 Symmetric-Stiff-Glass spar (S-S-G)

**Table B.7** Top flange and corners ply definitions

Ply #	Section start	Section stopp	Material	Thickness	Angle
1	1	39	Glass	0.015	0
2	1	35	Glass	0.015	0
3	5	31	Glass	0.015	0
4	7	27	Glass	0.015	0
5	9	17	Glass	0.015	0
6	8	24	Glass	0.015	0
7	6	30	Glass	0.015	0
8	1	33	Glass	0.015	0
9	1	37	Glass	0.015	0
10	1	40	Glass	0.015	0

**Table B.8** Bottom flange and corners ply definitions

Ply #	Section start	Section stopp	Material	Thickness	Angle
1	1	39	Glass	0.015	0
2	1	35	Glass	0.015	0
3	5	31	Glass	0.015	0
4	7	27	Glass	0.015	0
5	9	17	Glass	0.015	0
6	8	24	Glass	0.015	0
7	6	30	Glass	0.015	0
8	1	33	Glass	0.015	0
9	1	37	Glass	0.015	0
10	1	40	Glass	0.015	0

Appendix B

**Table B.9** Shear web ply definitions

<b>Ply #</b>	<b>Section start</b>	<b>Section stopp</b>	<b>Material</b>	<b>Thickness</b>	<b>Angle</b>
1	1	40	Glass	0.002	+45
2	1	40	Glass	0.002	-45
3	1	40	Glass	0.3	0
4-5	Symmetric about last UD ply				

## B.4 Symmetric-Unstiff-Carbon spar (S-S-C)

Table B.10 Top flange and corners ply definitions

Ply #	Section start	Section stopp	Material	Thickness	Angle
1	1	40	Carbon	0.002	+45
2	1	40	Carbon	0.002	-45
3	1	39	Carbon	0.002	+45
4	1	39	Carbon	0.002	-45
5	1	37	Carbon	0.002	+45
6	1	37	Carbon	0.002	-45
7	1	34	Carbon	0.002	+45
8	1	34	Carbon	0.002	-45
9	7	29	Carbon	0.002	+45
10	7	29	Carbon	0.002	-45
11	9	11	Carbon	0.002	+45
12	9	11	Carbon	0.002	-45
13	1	36	Carbon	0.0025	0
14	1	32	Carbon	0.0025	0
15	6	27	Carbon	0.0025	0
16	8	20	Carbon	0.0025	0
17	11	12	Carbon	0.0025	0
18	8	24	Carbon	0.0025	0
19	6	30	Carbon	0.0025	0
20	1	34	Carbon	0.0025	0
21	1	40	Carbon	0.0025	0
22-33	Symmetric about last UD ply				

Appendix B

**Table B.11** Bottom flange and corners ply definitions

Ply #	Section start	Section stopp	Material	Thickness	Angle
1	1	40	Carbon	0.002	+45
2	1	40	Carbon	0.002	-45
3	1	38	Carbon	0.002	+45
4	1	38	Carbon	0.002	-45
5	1	36	Carbon	0.002	+45
6	1	36	Carbon	0.002	-45
7	8	28	Carbon	0.002	+45
8	8	28	Carbon	0.002	-45
9	1	36	Carbon	0.0025	0
10	1	32	Carbon	0.0025	0
11	6	27	Carbon	0.0025	0
12	8	20	Carbon	0.0025	0
13	11	12	Carbon	0.0025	0
14	8	24	Carbon	0.0025	0
15	6	30	Carbon	0.0025	0
16	1	34	Carbon	0.0025	0
17	1	40	Carbon	0.0025	0
18-25	Symmetric about last UD ply				

**Table B.12** Shear web ply definitions

Ply #	Section start	Section stopp	Material	Thickness	Angle
1	1	40	Carbon	0.002	+45
2	1	40	Carbon	0.002	-45
3	1	40	Diab H200	0.02	0
4-5	Symmetric about last UD ply				

## B.5 Symmetric-Unstiff-Hybrid spar (S-S-H)

**Table B.13** Top flange and corners ply definitions

Ply #	Section start	Section stopp	Material	Thickness	Angle
1	1	40	Glass	0.003	+45
2	1	40	Glass	0.003	-45
3	1	39	Glass	0.003	+45
4	1	39	Glass	0.003	-45
5	1	37	Glass	0.003	+45
6	1	37	Glass	0.003	-45
7	1	35	Glass	0.003	+45
8	1	35	Glass	0.003	-45
9	6	30	Glass	0.003	+45
10	6	30	Glass	0.003	-45
11	8	26	Glass	0.003	+45
12	8	26	Glass	0.003	-45
13	1	36	Carbon	0.002	0
14	1	34	Carbon	0.002	0
15	5	31	Carbon	0.002	0
16	7	24	Carbon	0.002	0
17	9	17	Carbon	0.002	0
18	8	21	Carbon	0.002	0
19	7	28	Carbon	0.002	0
20	1	32	Carbon	0.002	0
21	1	35	Carbon	0.002	0
22	1	40	Carbon	0.002	0
23-34	Symmetric about last UD ply				

Appendix B

**Table B.14** Bottom flange and corners ply definitions

Ply #	Section start	Section stopp	Material	Thickness	Angle
1	1	40	Glass	0.003	+45
2	1	40	Glass	0.003	-45
3	1	38	Glass	0.003	+45
4	1	38	Glass	0.003	-45
5	1	36	Glass	0.003	+45
6	1	36	Glass	0.003	-45
7	7	30	Glass	0.003	+45
8	7	30	Glass	0.003	-45
9	1	36	Carbon	0.002	0
10	1	34	Carbon	0.002	0
11	5	31	Carbon	0.002	0
12	7	24	Carbon	0.002	0
13	9	17	Carbon	0.002	0
14	8	21	Carbon	0.002	0
15	7	28	Carbon	0.002	0
16	1	32	Carbon	0.002	0
17	1	35	Carbon	0.002	0
18	1	40	Carbon	0.002	0
19-26	Symmetric about last UD ply				

**Table B.15** Shear web ply definitions

Ply #	Section start	Section stopp	Material	Thickness	Angle
1	1	40	Glass	0.002	+45
2	1	40	Glass	0.002	-45
3	1	40	Diab H200	0.02	0
4-5	Symmetric about last UD ply				



## B.6 Symmetric-Unstiff-Glass spar (S-S-G)

Table B.16 Top flange and corners ply definitions

Ply #	Section start	Section stopp	Material	Thickness	Angle
1	1	40	Glass	0.002	+45
2	1	40	Glass	0.002	-45
3	1	39	Glass	0.002	+45
4	1	39	Glass	0.002	-45
5	1	38	Glass	0.002	+45
6	1	38	Glass	0.002	-45
7	1	37	Glass	0.002	+45
8	1	37	Glass	0.002	-45
9	1	35	Glass	0.002	+45
10	1	35	Glass	0.002	-45
11	1	32	Glass	0.002	+45
12	1	32	Glass	0.002	-45
13	6	27	Glass	0.002	+45
14	6	27	Glass	0.002	-45
15	8	21	Glass	0.002	+45
16	8	21	Glass	0.002	-45
17	1	34	Glass	0.0035	0
18	1	31	Glass	0.0035	0
19	7	26	Glass	0.0035	0
20	8	18	Glass	0.0035	0
21	7	23	Glass	0.0035	0
22	6	29	Glass	0.0035	0
23	1	33	Glass	0.0035	0
24	1	40	Glass	0.0035	0
25-40	Symmetric about last UD ply				

**Table B.17** Bottom flange and corners ply definitions

Ply #	Section start	Section stopp	Material	Thickness	Angle
1	1	40	Glass	0.002	+45
2	1	40	Glass	0.002	-45
3	1	39	Glass	0.002	+45
4	1	39	Glass	0.002	-45
5	1	37	Glass	0.002	+45
6	1	37	Glass	0.002	-45
7	1	35	Glass	0.002	+45
8	1	35	Glass	0.002	-45
9	7	28	Glass	0.002	+45
10	7	28	Glass	0.002	-45
11	1	34	Glass	0.0035	0
12	1	31	Glass	0.0035	0
13	7	26	Glass	0.0035	0
14	8	18	Glass	0.0035	0
15	7	23	Glass	0.0035	0
16	6	29	Glass	0.0035	0
17	1	33	Glass	0.0035	0
18	1	40	Glass	0.0035	0
19-28	Symmetric about last UD ply				

**Table B.18** Shear web ply definitions

Ply #	Section start	Section stopp	Material	Thickness	Angle
1	1	40	Glass	0.002	+45
2	1	40	Glass	0.002	-45
3	1	40	Diab H200	0.05	0
4-5	Symmetric about last UD ply				

## B.7 New-Load-Carbon spar (N-L-C)

**Table B.19** Top flange and corners ply definitions

Ply #	Section start	Section stopp	Material	Thickness	Angle
1	1	40	Carbon	0.002	+45
2	1	40	Carbon	0.002	-45
3	1	39	Carbon	0.002	+45
4	1	39	Carbon	0.002	-45
5	1	37	Carbon	0.002	+45
6	1	37	Carbon	0.002	-45
7	1	33	Carbon	0.002	+45
8	1	33	Carbon	0.002	-45
9	6	28	Carbon	0.002	+45
10	6	28	Carbon	0.002	-45
11	1	36	Carbon	0.003	0
12	1	32	Carbon	0.003	0
13	7	27	Carbon	0.003	0
14	9	19	Carbon	0.003	0
15	8	24	Carbon	0.003	0
16	6	30	Carbon	0.003	0
17	1	34	Carbon	0.003	0
18	1	40	Carbon	0.003	0
24-28	Symmetric about last UD ply				

Appendix B

**Table B.20** Bottom flange and corners ply definitions

Ply #	Section start	Section stopp	Material	Thickness	Angle
1	1	40	Carbon	0.002	+45
2	1	40	Carbon	0.002	-45
3	1	38	Carbon	0.002	+45
4	1	38	Carbon	0.002	-45
5	1	34	Carbon	0.002	+45
6	1	34	Carbon	0.002	-45
7	1	36	Carbon	0.003	0
8	1	32	Carbon	0.003	0
9	7	27	Carbon	0.003	0
10	9	19	Carbon	0.003	0
11	8	24	Carbon	0.003	0
12	6	30	Carbon	0.003	0
13	1	34	Carbon	0.003	0
14	1	40	Carbon	0.003	0
15-20	Symmetric about last UD ply				

**Table B.21** Shear web ply definitions

Ply #	Section start	Section stopp	Material	Thickness	Angle
1	1	40	Carbon	0.002	+45
2	1	40	Carbon	0.002	-45
3	1	40	Diab H200	0.02	0
4-5	Symmetric about last UD ply				

## B.8 New-Load-Hybrid spar (N-L-H)

Table B.22 Top flange and corners ply definitions

Ply #	Section start	Section stopp	Material	Thickness	Angle
1	1	40	Glass	0.002	+45
2	1	40	Glass	0.002	-45
3	1	39	Glass	0.002	+45
4	1	39	Glass	0.002	-45
5	1	38	Glass	0.002	+45
6	1	38	Glass	0.002	-45
7	1	37	Glass	0.002	+45
8	1	37	Glass	0.002	-45
9	1	35	Glass	0.002	+45
10	1	35	Glass	0.002	-45
11	1	32	Glass	0.002	+45
12	1	32	Glass	0.002	-45
13	6	29	Glass	0.002	+45
14	6	29	Glass	0.002	-45
15	7	26	Glass	0.002	+45
16	7	26	Glass	0.002	-45
17	9	21	Glass	0.002	+45
18	9	21	Glass	0.002	-45
19	1	36	Carbon	0.003	0
20	1	33	Carbon	0.003	0
21	7	28	Carbon	0.003	0
22	8	20	Carbon	0.003	0
23	8	24	Carbon	0.003	0
24	1	32	Carbon	0.003	0
25	1	34	Carbon	0.003	0
26	1	40	Carbon	0.003	0
27-44	Symmetric about last UD ply				

Appendix B

**Table B.23** Bottom flange and corners ply definitions

Ply #	Section start	Section stopp	Material	Thickness	Angle
1	1	40	Glass	0.002	+45
2	1	40	Glass	0.002	-45
3	1	39	Glass	0.002	+45
4	1	39	Glass	0.002	-45
5	1	38	Glass	0.002	+45
6	1	38	Glass	0.002	-45
7	1	35	Glass	0.002	+45
8	1	35	Glass	0.002	-45
9	6	29	Glass	0.002	+45
10	6	29	Glass	0.002	-45
11	9	14	Glass	0.002	+45
12	9	14	Glass	0.002	-45
13	1	36	Carbon	0.003	0
14	1	33	Carbon	0.003	0
15	7	28	Carbon	0.003	0
16	8	20	Carbon	0.003	0
17	8	24	Carbon	0.003	0
18	1	32	Carbon	0.003	0
19	1	34	Carbon	0.003	0
20	1	40	Carbon	0.003	0
21-32	Symmetric about last UD ply				

**Table B.24** Shear web ply definitions

Ply #	Section start	Section stopp	Material	Thickness	Angle
1	1	40	Glass	0.002	+45
2	1	40	Glass	0.002	-45
3	1	40	Diab H200	0.05	0
4-5	Symmetric about last UD ply				

## B.9 New-Load-Glass spar (N-L-G)

Table B.25 Top flange and corners ply definitions

Ply #	Section start	Section stopp	Material	Thickness	Angle
1	1	40	Glass	0.002	+45
2	1	40	Glass	0.002	-45
3	1	39	Glass	0.002	+45
4	1	39	Glass	0.002	-45
5	1	38	Glass	0.002	+45
6	1	38	Glass	0.002	-45
7	1	35	Glass	0.002	+45
8	1	35	Glass	0.002	-45
9	9	21	Glass	0.002	+45
10	9	21	Glass	0.002	-45
11	1	35	Glass	0.008	0
12	1	33	Glass	0.008	0
13	6	28	Glass	0.008	0
14	8	22	Glass	0.008	0
15	7	26	Glass	0.008	0
16	5	30	Glass	0.008	0
17	1	34	Glass	0.008	0
18	1	40	Glass	0.008	0
19-28	Symmetric about last UD ply				

Appendix B

**Table B.26** Bottom flange and corners ply definitions

Ply #	Section start	Section stopp	Material	Thickness	Angle
1	1	39	Glass	0.002	+45
2	1	39	Glass	0.002	-45
3	2	38	Glass	0.002	+45
4	2	38	Glass	0.002	-45
5	1	35	Glass	0.008	0
6	1	33	Glass	0.008	0
7	6	28	Glass	0.008	0
8	8	22	Glass	0.008	0
9	7	26	Glass	0.008	0
10	5	30	Glass	0.008	0
11	1	34	Glass	0.008	0
12	1	40	Glass	0.008	0
13-16	Symmetric about last UD ply				

**Table B.27** Shear web ply definitions

Ply #	Section start	Section stopp	Material	Thickness	Angle
1	1	40	Glass	0.002	+45
2	1	40	Glass	0.002	-45
3	1	40	Glass	0.05	0
4-5	Symmetric about last UD ply				



# Appendix C Stress plots from 100 m spar analyses

## C.1 S-NS-C

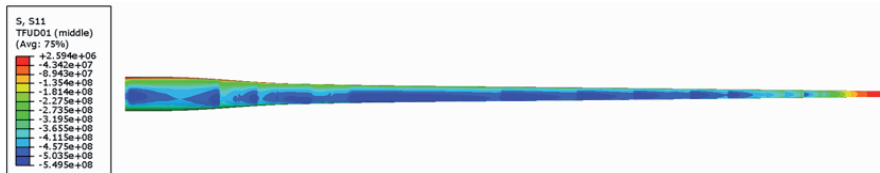


Figure 12-1 Axial stresses in UD carbon ply for carbon fiber spar with no stiffness criterion.

## C.2 S-S-C



Figure 12-2 Axial stresses in UD carbon ply for carbon fiber spar with stiffness criterion.

## C.3 S-NS-G



Figure 12-3 Axial stresses in UD glass ply for glass fiber spar with no stiffness criterion.

Appendix C

C.4 NLC

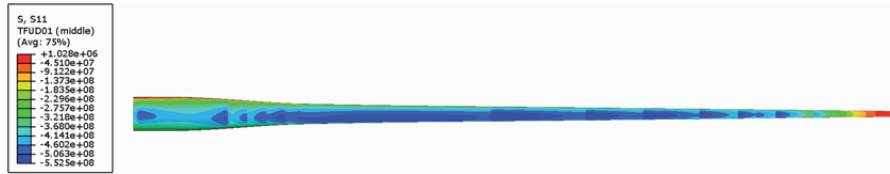


Figure 12-4 Axial stress in top flange UD ply during 50-year gust.



Figure 12-5 Axial stress in top flange  $\pm 45^\circ$  ply during 50-year gust.



Figure 12-6 Axial stress in bottom flange UD ply during 50-year gust.



Figure 12-7 Axial stress in bottom flange  $\pm 45^\circ$  ply during 50-year gust.

### C.5 NLH



Figure 12-8 Axial stress in top flange UD ply during 50-year gust.



Figure 12-9 Axial stress in top flange  $\pm 45^\circ$  ply during 50-year gust.



Figure 12-10 Axial stress in bottom flange UD ply during 50-year gust.

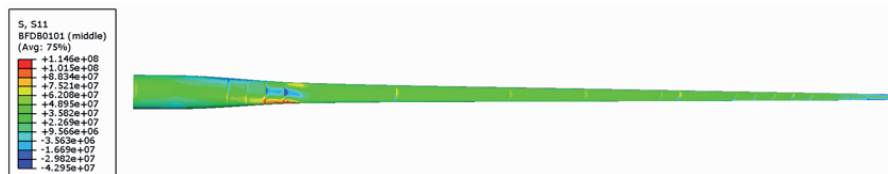


Figure 12-11 Axial stress in bottom flange  $\pm 45^\circ$  ply during 50-year gust.

Appendix C

C.6 NLG

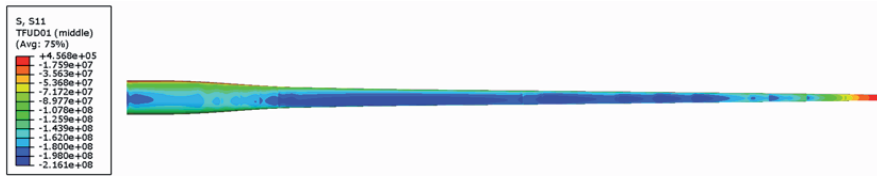


Figure 12-12 Axial stress in top flange UD ply during 50-year gust.



Figure 12-13 Axial stress in top flange  $\pm 45^\circ$  ply during 50-year gust.

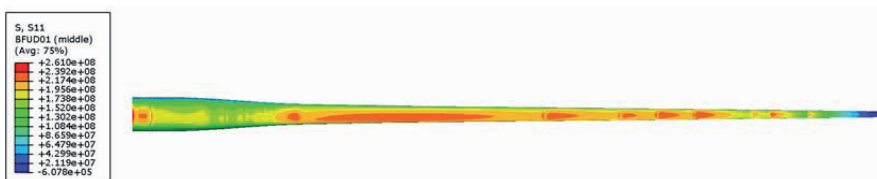


Figure 12-14 Axial stress in bottom flange UD ply during 50-year gust.



Figure 12-15 Axial stress in bottom flange  $\pm 45^\circ$  ply during 50-year gust.

## Appendix D Results from buckling optimization

### D.1 Optimizing glass fiber anti-buckling plies

**Table D.1** Optimal anti-buckling ply angles and ratio for the three different sections optimized by the bending and compression model. Eigenvalue of optimized lay-up/lay-up is compared to standard  $\pm 45^\circ$  lay-up.

Section	Model	Angle top ply ( $\theta_1$ )	Angle bottom ply ( $\theta_2$ )	Ratio buck. plies on top [%]	Lin. eigenvalue $\pm 45^\circ$ ply lay-up	Lin. eigenvalue optimal ply lay-up	Change lin. eigenvalue buckling [%]
Section 22m	Bending	90	45	30	0.489	0.547	11.79
	Compression	70	45	60	0.576	0.610	5.93
Section 50m	Bending	90	45	30	0.476	0.538	13.04
	Compression	60	45	60	0.594	0.624	5.05
Section 90m	Bending	90	30	20	0.490	0.527	7.67
	Compression	50	50	80	0.563	0.633	12.43

## Section 22 m

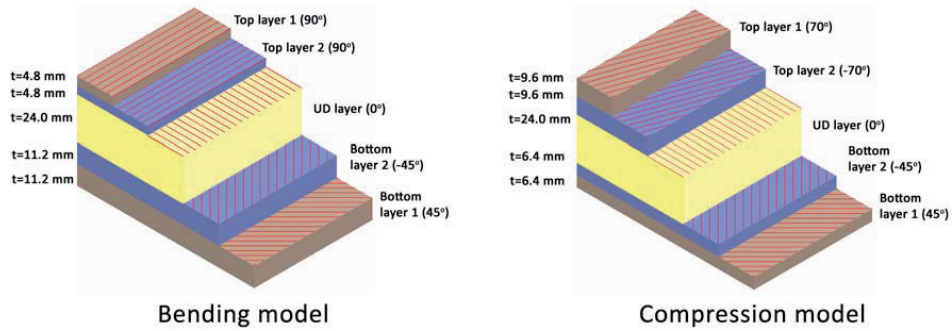


Figure D-1 Optimal ply definitions from the bending and compression model for the 22 m section.

## Section 50 m

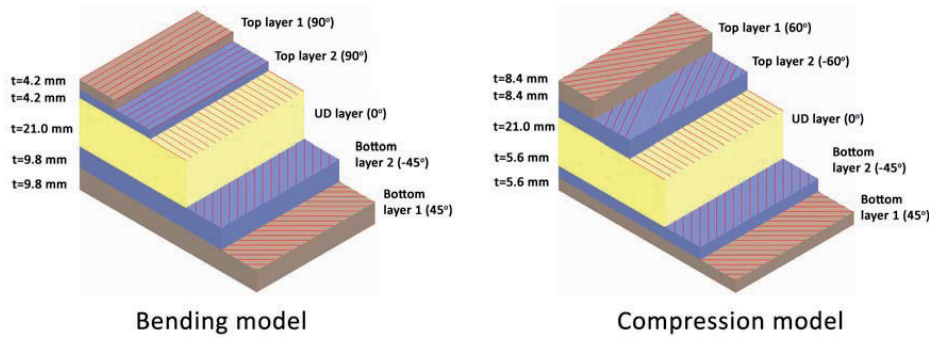


Figure D-2 Optimal ply definitions from the bending and compression model for the 50 m section.

## Section 90 m

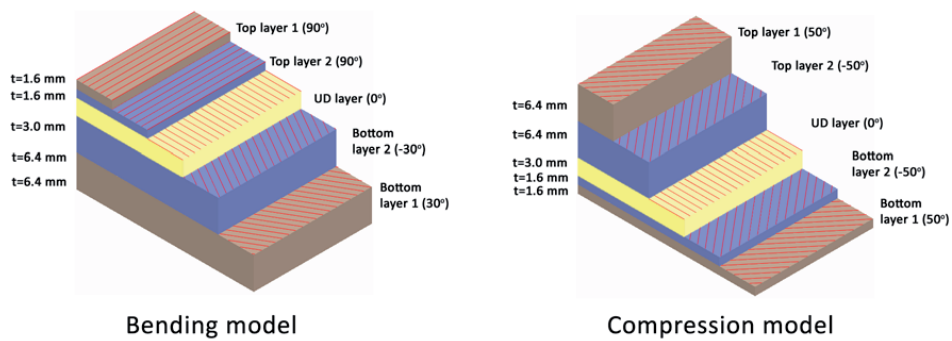


Figure D-3 Optimal ply definitions from the bending and compression model for the 90 m section.

**Table D.2** Non-linear analysis with perfect geometry of 22, 50 and 90 m sections

Section	Model	Non-lin. buckling $\pm 45^\circ$ ply with	Non-lin. buckling optimal ply	Change in non-lin. buckling [%]
22 m	Bending	0.374	0.384	2.71
	Compression	0.561	0.562	0.20
50 m	Bending	0.414	0.485	17.17
	Compression	0.591	0.610	3.08
90 m	Bending	0.463	0.449	-3.07
	Compression	0.645	0.681	5.69

**Table D.3** Non-linear analysis with 0.1 mm imperfection of 22, 50 and 90 m sections

Section	Model	Non-lin. buckling $\pm 45^\circ$ ply with 0.1 mm imperfection	Non-lin. buckling optimal ply 0.1 mm imperfection	Change in non-lin. buckling [%]
22 m	Bending	0.330	0.365	10.75
	Compression	0.561	0.560	-0.18
50 m	Bending	0.386	0.404	4.73
	Compression	0.595	0.609	2.26
90 m	Bending	0.381	0.390	2.48
	Compression	0.625	0.647	3.48

**Table D.4** Non-linear analysis with 0.5 mm imperfection of 22, 50 and 90 m sections

Section	Model	Non-lin. buckling $\pm 45^\circ$ ply with 0.5 mm imperfection	Non-lin. buckling optimal ply 0.5 mm imperfection	Change in non-lin. buckling [%]
22 m	Bending	0.321	0.354	10.27
	Compression	0.546	0.553	1.24
50 m	Bending	0.356	0.388	9.03
	Compression	0.594	0.596	0.42
90 m	Bending	0.393	0.401	2.10
	Compression	0.859	0.635	-26.08

**Table D.5** Non-linear analysis with 1.0 mm imperfection of 22, 50 and 90 m sections

Section	Model	Non-lin. buckling $\pm 45^\circ$ ply with 1.0 mm imperfection	Non-lin. buckling optimal ply 1.0 mm imperfection	Change in non-lin. buckling [%]
22 m	Bending	0.313	0.345	10.50
	Compression	0.523	0.527	0.85
50 m	Bending	0.345	0.376	8.88
	Compression	0.583	0.594	0.59
90 m	Bending	0.390	0.397	1.85
	Compression	0.851	0.642	-24.50

## D.2 Buckling optimization of UD carbon plies

### Effect of adjusting UD ply angle

#### Section 22 m

**Table D.6** Effect of adjusting UD carbon ply angle for the 22m section. Parenthesis shows percentage of change.

UD ply angle [degrees]	Deflection [m]	Linear buckling load	Non-linear buckling load	Non-linear buckling load with 0.5 mm imperfection
0	1.10	0.533	0.361	0.345
5	1.12 (1.55%)	0.537 (0.65%)	0.350 (-2.38%)	0.346 (0.35%)
10	1.17 (6.28%)	0.545 (2.25%)	0.360 (1.03%)	0.339 (-1.56%)
15	1.27 (15.3%)	0.554 (3.96%)	0.377 (4.48%)	0.342 (-0.65%)
20	1.44 (30.69%)	0.561 (5.18%)	0.358 (-0.75%)	0.355 (3.13%)
25	1.70 (54.46%)	0.564 (5.75%)	0.401 (11.35%)	0.357 (3.49%)
30	2.08 (89.07%)	0.565 (5.95%)	0.413 (14.45%)	0.356 (3.38%)



### Section 50 m

**Table D.7** Effect of adjusting UD carbon ply angle for the 50m section. Parenthesis shows percentage of change.

UD ply angle [degrees]	Deflection [m]	Linear buckling load	Non-linear buckling load	Non-linear buckling load with 0.5 mm imperfection
0	1.77	0.482	0.394	0.360
5	1.80 (1.81%)	0.487 (1.10%)	0.397 (0.59%)	0.362 (0.48%)
10	1.91 (7.81%)	0.499 (3.66%)	0.410 (4.08%)	0.366 (1.57%)
15	2.12 (19.81%)	0.511 (6.12%)	0.413 (4.85%)	0.365 (1.44%)
20	2.50 (41.20)	0.517 (7.33%)	0.404 (2.56%)	0.368 (2.18%)
25	3.14 (77.53%)	0.516 (7.08%)	0.442 (12.08%)	0.363 (0.71%)
30	4.17 (136.05%)	0.511 (6.00%)	0.443 (12.49%)	0.354 (-1.66)

### Section 90 m

**Table D.8** Effect of adjusting UD carbon ply angle for the 90m section. Parenthesis shows percentage of change.

UD ply angle [degrees]	Deflection [m]	Linear buckling load	Non-linear buckling load	Non-linear buckling load with 0.5 mm imperfection
0	0.87	0.519	0.461	0.412
5	0.87 (-0.53%)	0.520 (0.21%)	0.461 (-0.05)	0.411 (-0.09%)
10	0.93 (5.84%)	0.523 (0.82%)	0.474 (2.73%)	0.410 (-0.35%)
15	0.99 (13.75%)	0.528 (1.70%)	0.459 (-0.46%)	0.408 (-0.85%)
20	1.10 (25.89%)	0.533 (2.74%)	0.444 (-3.80%)	0.447 (8.49%)
25	1.25 (43.27%)	0.539 (3.90%)	0.483 (4.74%)	0.468 (13.66%)
30	1.45 (66.13%)	0.546 (5.18%)	0.481 (4.19%)	0.436 (5.93%)

### Effect of adding core material to flanges

#### Section 22 m

**Table D.9** Effect of adding core material (Diab H200) to the 22m section. Parenthesis shows percentage of change.

Core thickness [mm]	Deflection [m]	Linear buckling load	Non-linear buckling load	Non-linear buckling load with 0.5 mm imperfection
0	1.10	0.533	0.361	0.345
10	1.12 (1.64%)	0.528 (-1.04%)	0.469 (30.19%)	0.402 (16.66%)
20	1.08 (-1.91%)	0.461 (-13.47%)	0.472 (30.92%)	0.456 (32.35%)
30	1.08 (-2.09%)	0.469 (-12.03%)	0.526 (45.97%)	0.488 (41.73%)
40	1.08 (-1.91%)	0.502 (-5.92%)	0.644 (78.72%)	0.518 (50.43%)
60	1.09 (-1.09%)	0.591 (10.80%)	0.692 (91.84%)	0.619 (79.57%)
80	1.10 (0.187%)	0.691 (29.55%)	0.796 (120.87%)	0.731 (112.12%)
100	1.12 (1.64%)	0.794 (48.89%)	0.905 (151.07%)	0.843 (144.56%)

#### Section 50 m

**Table D.10** Effect of adding core material (Diab H200) to the 50m section. Parenthesis shows percentage of change.

Core thickness [mm]	Deflection [m]	Linear buckling load	Non-linear buckling load	Non-linear buckling load with 0.5 mm imperfection
0	1.77	0.482	0.394	0.360
10	1.79 (1.08%)	0.501 (3.94%)	0.455 (15.31%)	0.429 (19.13%)
20	1.81 (2.32%)	0.447 (-7.24%)	0.490 (24.32%)	0.488 (35.41%)
30	1.83 (3.74%)	0.471 (-2.25%)	0.562 (42.67%)	0.528 (46.47%)
40	1.86 (5.26%)	0.515 (6.82%)	0.589 (19.30%)	0.596 (65.52%)
60	1.92 (8.38%)	0.620 (28.68%)	0.727 (84.30%)	0.732 (103.13%)
80	1.97 (11.66%)	0.732 (52.00%)	0.879 (122.86%)	0.861 (139.12%)
100	2.03 (15.05%)	0.846 (75.54%)	0.869 (120.33%)	0.887 (146.08%)

### Section 90 m

**Table D.11** Effect of adding core material (Diab H200) to the 90m section. Parenthesis shows percentage of change.

Core thickness [mm]	Deflection [m]	Linear buckling load	Non-linear buckling load	Non-linear buckling load with 0.5 mm imperfection
0	0.87	0.519	0.461	0.412
5	0.89 (2.14%)	0.660 (27.22%)	0.581 (25.92%)	0.598 (45.22%)
10	0.91 (4.42%)	0.817 (57.33%)	0.745 (61.55%)	0.715 (73.55%)
15	0.93 (6.84%)	0.984 (89.54%)	0.927 (100.99%)	0.828 (101.02%)
20	0.96 (9.32%)	1.138 (119.22%)	0.933 (102.31%)	0.897 (117.79%)
25	0.98 (11.88%)	1.270 (144.60%)	0.925 (100.54%)	0.897 (117.86%)
30	1.00 (14.57%)	1.407 (171.13%)	0.904 (95.94%)	0.894 (117.19%)

### Effect of $\pm 45^\circ$ glass fiber ply distribution among UD carbon plies

#### Section 22 m

**Table D.12** Effect of  $\pm 45^\circ$  ply distribution on single skin flange and flange with core material. Parenthesis shows percentage of change.

Model	Deflection [m]	Deflection [m]	Linear buckling load	Non-linear buckling load	Non-linear buckling load with 0.5 mm imperfection
UD ply $0^\circ$	Seperate	1.10	0.533	0.361	0.345
	Distributed	1.16 (5.74%)	0.484 (-9.28%)	0.353 (-2.09%)	0.347 (0.61%)
UD ply $0^\circ$ 30 mm core material	Seperate	1.08 (-2.09%)	0.469 (-12.03%)	0.526 (45.97%)	0.488 (41.73%)
	Distributed	1.12 (2.28%)	0.693 (29.99%)	0.609 (68.97%)	0.580 (68.30%)

**Section 50 m****Table D.13** Effect of  $\pm 45^\circ$  ply distribution on single skin flange and flange with core material. Parenthesis shows percentage of change.

Model	Deflection [m]	Deflection [m]	Linear buckling load	Non-linear buckling load	Non-linear buckling load with 0.5 mm imperfection
UD ply $0^\circ$	Seperate	1.77	0.482	0.394	0.360
	Distributed	1.77 (0.34%)	0.463 (-3.85%)	0.380 (-3.73%)	0.345 (-4.13%)
UD ply $0^\circ$ 30 mm core material	Seperate	1.83 (3.74%)	0.471 (-2.25%)	0.562 (42.67%)	0.528 (46.47%)
	Distributed	1.83 (3.79%)	0.682 (41.60%)	0.655 (66.26%)	0.630 (74.85%)

**Section 90 m****Table D.14** Effect of  $\pm 45^\circ$  ply distribution on single skin flange and flange with core material. Parenthesis shows percentage of change.

Model	Deflection [m]	Deflection [m]	Linear buckling load	Non-linear buckling load	Non-linear buckling load with 0.5 mm imperfection
UD ply $0^\circ$	Seperate	0.87	0.519	0.461	0.412
	Distributed	0.87 (0.01%)	0.545 (4.97%)	0.510 (10.65%)	0.462 (12.23%)
UD ply $0^\circ$ 10 mm core material	Seperate	0.91 (4.42)	0.817 (57.33%)	0.745 (61.55%)	0.715 (73.55%)
	Distributed	0.91 (4.34%)	0.919 (77.07%)	0.767 (66.20%)	0.733 (78.04%)

### D.3 100 m hybrid spar with optimized bottom flange. Buckling load of 1.2 by non-linear analysis.

Table D.15 Top flange and corners ply definitions

Ply #	Section start	Section stopp	Material	Thickness	Angle
1	1	40	Glass	0.002	+45
2	1	40	Glass	0.002	-45
3	1	39	Glass	0.002	+45
4	1	39	Glass	0.002	-45
5	1	38	Glass	0.002	+45
6	1	38	Glass	0.002	-45
7	1	37	Glass	0.002	+45
8	1	37	Glass	0.002	-45
9	1	35	Glass	0.002	+45
10	1	35	Glass	0.002	-45
11	1	32	Glass	0.002	+45
12	1	32	Glass	0.002	-45
13	6	29	Glass	0.002	+45
14	6	29	Glass	0.002	-45
15	7	26	Glass	0.002	+45
16	7	26	Glass	0.002	-45
17	9	21	Glass	0.002	+45
18	9	21	Glass	0.002	-45
19	1	36	Carbon	0.003	0
20	1	33	Carbon	0.003	0
21	7	28	Carbon	0.003	0
22	8	20	Carbon	0.003	0
23	8	24	Carbon	0.003	0
24	1	32	Carbon	0.003	0
25	1	34	Carbon	0.003	0
26	1	40	Carbon	0.003	0
27-44	Symmetric about last UD ply				

Appendix D

**Table D.16** Bottom flange and corners ply definitions

Ply #	Section start	Section stopp	Material	Thickness	Angle
1	1	40	Glass	0.002	+45
2	1	40	Glass	0.002	-45
3	1	39	Glass	0.002	+45
4	1	39	Glass	0.002	-45
5	1	35	Glass	0.002	+45
6	1	35	Glass	0.002	-45
7	14	26	Glass	0.002	+45
8	14	26	Glass	0.002	-45
9	1	36	Carbon	0.003	0
10	1	33	Carbon	0.003	0
11	7	28	Carbon	0.003	0
12	8	20	Carbon	0.003	0
13	8	24	Carbon	0.003	0
14	1	32	Carbon	0.003	0
15	1	34	Carbon	0.003	0
16	1	40	Carbon	0.003	0
17-24	Symmetric about last UD ply				

**Table D.17** Shear web ply definitions

Ply #	Section start	Section stopp	Material	Thickness	Angle
1	1	40	Glass	0.002	+45
2	1	40	Glass	0.002	-45
3	1	40	Diab H200	0.05	0
4-5	Symmetric about last UD ply				

#### D.4 100 m hybrid spar with core material in bottom flange. Buckling load of 1.2 by non-linear analysis.

Table D.18 Top flange and corners ply definitions

Ply #	Section start	Section stopp	Material	Thickness	Angle
1	1	40	Glass	0.002	+45
2	1	40	Glass	0.002	-45
3	1	39	Glass	0.002	+45
4	1	39	Glass	0.002	-45
5	1	38	Glass	0.002	+45
6	1	38	Glass	0.002	-45
7	1	37	Glass	0.002	+45
8	1	37	Glass	0.002	-45
9	1	35	Glass	0.002	+45
10	1	35	Glass	0.002	-45
11	1	32	Glass	0.002	+45
12	1	32	Glass	0.002	-45
13	6	29	Glass	0.002	+45
14	6	29	Glass	0.002	-45
15	7	26	Glass	0.002	+45
16	7	26	Glass	0.002	-45
17	9	21	Glass	0.002	+45
18	9	21	Glass	0.002	-45
19	1	36	Carbon	0.003	0
20	1	33	Carbon	0.003	0
21	7	28	Carbon	0.003	0
22	8	20	Carbon	0.003	0
23	8	24	Carbon	0.003	0
24	1	32	Carbon	0.003	0
25	1	34	Carbon	0.003	0
26	1	40	Carbon	0.003	0
27-44	Symmetric about last UD ply				

Appendix D

**Table D.19** Bottom flange

Ply #	Section start	Section stopp	Material	Thickness	Angle
1	1	40	Glass	0.001	+45
2	1	40	Glass	0.001	-45
3	1	36	Carbon	0.003	0
4	5	37	Glass	0.001	+45
5	5	37	Glass	0.001	-45
6	1	33	Carbon	0.003	0
7	8	35	Glass	0.001	+45
8	8	35	Glass	0.001	-45
9	7	28	Carbon	0.003	0
10	20	30	Glass	0.001	+45
11	20	30	Glass	0.001	-45
12	8	20	Carbon	0.003	0
13	1	28	Diab H200	0.02	0
14	2	16	Diab H200	0.02	0
15	1	22	Diab H200	0.02	0
16	1	40	Diab H200	0.02	0
17	8	24	Carbon	0.003	0
18	20	30	Glass	0.001	+45
19	20	30	Glass	0.001	-45
20	1	32	Carbon	0.003	0
21	8	35	Glass	0.001	+45
22	8	35	Glass	0.001	-45
23	1	34	Carbon	0.003	0
24	5	37	Glass	0.001	+45
25	5	37	Glass	0.001	-45
26	1	40	Carbon	0.003	0
27	1	40	Glass	0.001	+45
28	1	40	Glass	0.001	-45



Table D.20 Bottom flange corners

Ply #	Section start	Section stopp	Material	Thickness	Angle
1	1	40	Glass	0.001	+45
2	1	40	Glass	0.001	-45
3	1	36	Carbon	0.003	0
4	5	37	Glass	0.001	+45
5	5	37	Glass	0.001	-45
6	1	33	Carbon	0.003	0
7	8	35	Glass	0.001	+45
8	8	35	Glass	0.001	-45
9	7	28	Carbon	0.003	0
10	20	30	Glass	0.001	+45
11	20	30	Glass	0.001	-45
12	8	20	Carbon	0.003	0
13	1	4	Diab H200	0.02	0
17	8	24	Carbon	0.003	0
18	20	30	Glass	0.001	+45
19	20	30	Glass	0.001	-45
20	1	32	Carbon	0.003	0
21	8	35	Glass	0.001	+45
22	8	35	Glass	0.001	-45
23	1	34	Carbon	0.003	0
24	5	37	Glass	0.001	+45
25	5	37	Glass	0.001	-45
26	1	40	Carbon	0.003	0
27	1	40	Glass	0.001	+45
28	1	40	Glass	0.001	-45

**Table D.21** Shear web ply definitions

Ply #	Section start	Section stopp	Material	Thickness	Angle
1	1	40	Glass	0.002	+45
2	1	40	Glass	0.002	-45
3	1	40	Diab H200	0.05	0
4-5	Symmetric about last UD ply				

### D.5 Stress plots from 100 m spar with optimized plies

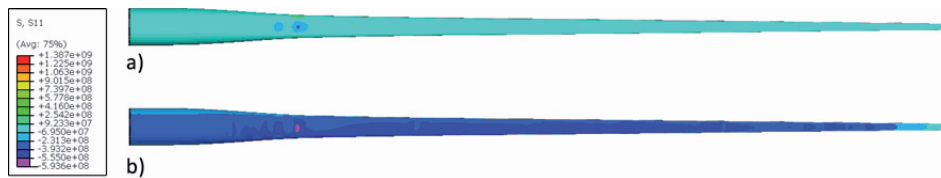


**Figure D-4** Stress distribution plots of top flange for 100 m spar with optimal ply distribution based on results from bending model. a)  $\pm 45^\circ$  glass fiber ply. b) UD carbon fiber ply.

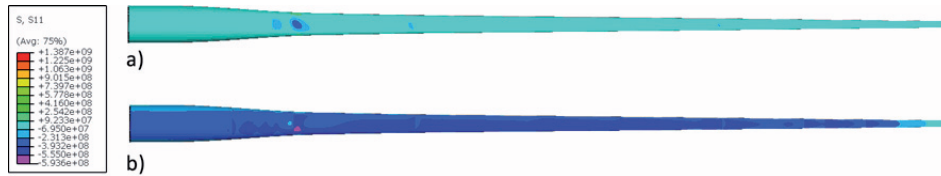


**Figure D-5** Stress distribution plots of top flange for 100 m spar with optimal ply distribution based on results from compression model. a)  $\pm 45^\circ$  glass fiber ply. b) UD carbon fiber ply.

## Appendix E Abaqus ply definition for optimization model

Composite ply definitions used to define shell sections for the optimization models in the Abaqus input file. The input lines define the following:

Thickness [m], number of integration points, Material name, ply orientation, ply name

\*Shell Section, elset=Flanges, composite, offset=0.5, layup=Flanges

0.0112, 3, "Glass UD infusion", 45., Flange-DB0101

0.0112, 3, "Glass UD infusion", -45., Flange-DB0102

0.024, 3, "Carbon UD infusion", 0., Flange-UD01

0.0048, 3, "Glass UD infusion", -90., Flange-DB0102-Copy1

0.0048, 3, "Glass UD infusion", 90., Flange-DB0101-Copy1

\*Shell Section, elset=Corners-1, composite, offset=0.5, layup=Corners

0.008, 3, "Glass UD infusion", 45., Corner-DB0101

0.008, 3, "Glass UD infusion", -45., Corner-DB0102

0.008, 3, "Glass UD infusion", -45., Corner-DB0102-Copy1

0.008, 3, "Glass UD infusion", 45., Corner-DB0101-Copy1

\*Shell Section, elset=Web, composite, offset=0.5, layup=Web

0.004, 3, "Glass UD infusion", 45., Web-DB0101

0.004, 3, "Glass UD infusion", -45., Web-DB0102

0.02, 3, "Diab Divinycell H200", 0., Web Core

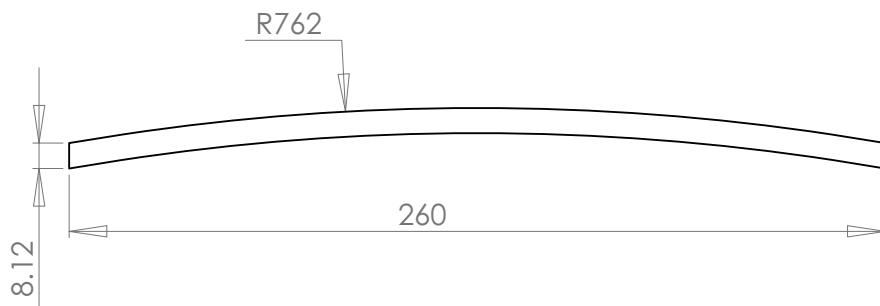
0.004, 3, "Glass UD infusion", -45., Web-DB0102-Copy1

0.004, 3, "Glass UD infusion", 45., Web-DB0101-Copy1

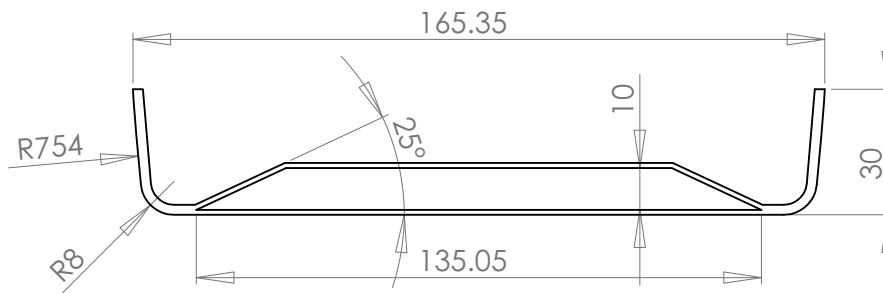
Appendix E

## Appendix F Geometry of 6 m spar

### Top and bottom flange



### Shear web



Appendix F

## Appendix G Abaqus ply definition for 6 m spar

### G.1 Ply definitions for spar flange

Composite ply definitions used to shell sections in the Abaqus input file. The input lines define the following:

Thickness [m], number of integration points, Material name, ply orientation, ply name

```
*Shell Section, elset=Flange-1, composite, orientation=Ori-1, offset=SNEG,
layup=Flange
0.0002292, 3, "Glass UD infusion", 45., TFDB0101
0.0002292, 3, "Glass UD infusion", -45., TFDB0102
0.0002292, 3, "Glass UD infusion", 45., TFDB0201
0.0002292, 3, "Glass UD infusion", -45., TFDB0202
0.00083, 3, "Glass UD infusion", 0., TFUD01
0.00083, 3, "Glass UD infusion", 0., TFUD02
0.00083, 3, "Glass UD infusion", 0., TFUD03
0.00083, 3, "Glass UD infusion", 0., TFUD04
0.00083, 3, "Glass UD infusion", 0., TFUD05
0.00083, 3, "Glass UD infusion", 0., TFUD06
0.00083, 3, "Glass UD infusion", 0., TFUD07
0.0002292, 3, "Glass UD infusion", -45., TFDB0202-Copy1
0.0002292, 3, "Glass UD infusion", 45., TFDB0201-Copy1
0.0002292, 3, "Glass UD infusion", -45., TFDB0102-Copy1
0.0002292, 3, "Glass UD infusion", 45., TFDB0101-Copy1
```

### G.2 Ply definitions for spar flange/web intersection

Composite ply definitions used to define the section where the flange and shear web is bonded together. A perfect bond is assumed and adhesive is therefore neglected.

```
*Shell Section, elset=Flange-web-1, composite, orientation=Ori-2, offset=-0.175827,
layup=Flange-web
0.0009166, 3, "Glass UD infusion", 45., TF-Web-0101
0.0009166, 3, "Glass UD infusion", -45., TF-Web-0102
0.0009166, 3, "Glass UD infusion", -45., TF-Web-0102-Copy2
0.0009166, 3, "Glass UD infusion", 45., TF-Web-0101-Copy3
0.0002292, 3, "Glass UD infusion", 45., TFDB0101
0.0002292, 3, "Glass UD infusion", -45., TFDB0102
0.0002292, 3, "Glass UD infusion", 45., TFDB0201
0.0002292, 3, "Glass UD infusion", -45., TFDB0202
0.00083, 3, "Glass UD infusion", 0., TFUD01
0.00083, 3, "Glass UD infusion", 0., TFUD02
0.00083, 3, "Glass UD infusion", 0., TFUD03
```

## Appendix G

0.00083, 3, "Glass UD infusion", 0., TFUD04  
0.00083, 3, "Glass UD infusion", 0., TFUD05  
0.00083, 3, "Glass UD infusion", 0., TFUD06  
0.00083, 3, "Glass UD infusion", 0., TFUD07  
0.0002292, 3, "Glass UD infusion", -45., TFDB0202-Copy1  
0.0002292, 3, "Glass UD infusion", 45., TFDB0201-Copy1  
0.0002292, 3, "Glass UD infusion", -45., TFDB0102-Copy1  
0.0002292, 3, "Glass UD infusion", 45., TFDB0101-Copy1

### G.3 Ply definitions for shear web

Composite ply definitions used to define the section representing the shear web.

\*Shell Section, elset=Web01-1, composite, orientation=Ori-3, offset=SPOS,  
layup=Web01  
0.0004583, 3, "Glass UD infusion", 45., Web0101  
0.0004583, 3, "Glass UD infusion", -45., Web0102  
0.0004583, 3, "Glass UD infusion", 45., Web0201  
0.0004583, 3, "Glass UD infusion", -45., Web0202  
0.01, 3, "Diab Divinycell H80", 0., Web Core01  
0.0004583, 3, "Glass UD infusion", -45., Web0202-Copy1  
0.0004583, 3, "Glass UD infusion", 45., Web0201-Copy1  
0.0004583, 3, "Glass UD infusion", -45., Web0102-Copy1  
0.0004583, 3, "Glass UD infusion", 45., Web0101-Copy1

### G.4 Ply definitions for shear web without core

Composite ply definitions used to define the section representing the shear web without the core material

\*Shell Section, elset=Web02-1, composite, orientation=Ori-3, offset=SPOS,  
layup=Web02  
0.0004583, 3, "Glass UD infusion", 45., Web0101  
0.0004583, 3, "Glass UD infusion", -45., Web0102  
0.0004583, 3, "Glass UD infusion", 45., Web0201  
0.0004583, 3, "Glass UD infusion", -45., Web0202  
0.0004583, 3, "Glass UD infusion", -45., Web0202-Copy1  
0.0004583, 3, "Glass UD infusion", 45., Web0201-Copy1  
0.0004583, 3, "Glass UD infusion", -45., Web0102-Copy1  
0.0004583, 3, "Glass UD infusion", 45., Web0101-Copy1



# Appendix H Web links

## LM Web link-01



lasterne som fx flaps.

### AERODYNAMISK TEST

LM Glasfibers vindtunnel er specialdesignet til at teste vindmøllevinger. Dette sofistikerede testværktøj giver vores aerodynamikere og udviklingsingeniører en unik mulighed for at udføre tests 24 timer i døgnet, 365 dage om året under forhold der svarer til driftsforholdene for vindmøllevinger i megawatt størrelsen.

[Se en kort præsentationsvideo om vindtunnelen](#)

Ved at have ubegrænset adgang til en vindtunnel kan vi arbejde med aerodynamisk design på en bred front. Vindtunnelen er skræddersyet til test af vindmøllevinger, så vi opnår en meget høj præcision i målingerne. Hastigheden i og størrelsen på testsektionen er beregnet til at genskabe dynamiske driftsforhold, fx fra stall ved forskellige indstrømningsvinkler. Hermed kan vi eftervise forskellige løsninger til aktiv kontrol af



### Test setup

Testprofilen er installeret på en fintfølende drejelig profilholder. Kolvandet lige bag testprofilen scannes med en sensor. I alt måler næsten 300 sensorer kræfterne inklusiv for eksempel tryksensorer og vejecellesystemer. Automatisk dataopsamling sikrer ensartethed mellem forskellige tests. Bearbejdning af data fra forsøgene giver yderligere 400 værdier.

### Vindtunnelens design

Vindkanalen er designet med et lukket retursystem og en kontraktionsratio på 10:1. En honeycomb og turbulens skærm sikrer luftstrømning af høj kvalitet i test sektionen. Et kølesystem fjerner overskydende varme fra den kraftige 1 MW blæser. Testsektionen måles 1,35 m i bredden, 2,70 meter i højden og 7 meter i længden. Det reducerer indflydelsen fra testsektionens vægge og gør det muligt at skabe et længerevarende kølvand.



### Reynolds tal

Resultater fra validering af vindtunnelen foretaget af eksterne specialister viser at maksimum hastigheden på 105 m/sekund opnås i testsektionen. Det giver et maksimalt Reynolds tal på mere end 6 millioner for et profil med en korde på 900 mm.

### Fakta:

Lukket retursystem  
 Testkammer dimensioner: (b) x (h) x (l): 1,35m x 2,70m x 7m  
 Vindhastighed: 375 km/t eller Mach 0,3  
 Blæseeffekt: 1000 kW  
 Lavturbulent  
 Reynoldstal: 6 mio. for et vingeprofil med 0,90 m korde  
 Konstant temperatur

## LM Web link-02



### VERDENS LÆNGSTE VINGER

LM 61.5 P er verdens længste vindmøllevinger. LM Glasfiber udviklede disse 61,5 meter lange vinger i tæt samarbejde med den tyske producent af verdens største vindmølle, REpower. Vingerne var på alle måder en stor udfordring for ingeniørerne, der har flyttet grænserne for vingeproduktion for at løse opgaven.

Se hvor imponerende det ser ud, når verdens længste vinger bliver støbt og monteret. [Se en kort film her.](#)

### Vægten afgørende

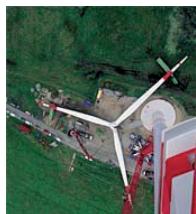
Jo større vingerne er desto vigtigere er det at fokusere på deres vægt for at reducere belastningerne på vindmøllen og dermed opnå betydelige besparelser på dimensioneringen af møllens øvrige komponenter. Ved hjælp af en videreudvikling af LM Glasfibers [FutureBlade teknologi](#) opnåede ingeniørerne at udvikle en vinge med en imponerende lav vægt, under 18 tons.

Udfordringen ved en stor vinge er ikke proportional med vingens længde. Når man fordobler længden på en vinge, er det ikke dobbelt så stor en udfordring udviklingsmæssigt. Det er derimod en langt større opgave at udvikle en stor vinge, der er optimeret på ydelse, vægt og pris. Matematisk gælder det som tommelfingerregel, at vingens vægt mindst stiger med forøgelsen af længden i tredje potens. Derfor har vægten været et vigtigt fokusområde under udviklingen af LM 61.5 P vingen, og en målrettet indsats har resulteret i, at denne regneregulering er blevet brudt.

### Smart engineering

I forbindelse med udviklingen af verdens længste vinger havde LM Glasfiber stor fokus på at vælge de rette materialer. Strategien, som LM Glasfiber i øvrigt altid arbejder efter, var at vælge det bedste materiale til hver eneste lille del af den store vinge uden at gøre vingerne unødigt omkostningskrævende.

[Læs mere om vores materialeforskning](#)



Sidelebende med materialevalg og -udvikling krævede det store udviklingsprojekt en videreudvikling af produktionsprocesserne. Således anvendte vi f.eks. en såkaldt glasrobot til udlægning af de glasmatter, der udgør det bærende laminat i vingen og som skal monteres uhyre præcist.

[Læs mere om automatisering af vores produktionsprocesser](#)

### Nabo til atomkraftværk

Det første sæt LM 61.5 P prototypevinger er moteret på 5M prototype møllen ved Brunsbüttel i Nordtyskland. Der har de uden problemer produceret strøm til nettet siden slutningen af 2004.

Se flash animation med alle data og få et hurtigt overblik over denne store vinge (på engelsk)

[Se animationen her](#)



## USA Today Web link-03

## Aircraft orders put carbon fiber prices in steep climb

Updated 7/3/2007 6:53 PM | Comments 3 | Recommend 5 | E-mail | Save | Print | Reprints & Permissions | [RSS](#)

By Chris Woodyard, USA TODAY

Booming demand for new jetliners is driving up the cost of carbon fiber, a high-tech material used in products ranging from cars to hockey sticks.

Prices for carbon fiber now run as high as \$20 a pound, compared with as little as \$5 a pound three or four years ago, says Mike Musselman, managing editor of *High Performance Composites* magazine. Spot shortages have developed, too. Carbon fiber manufacturers are boosting production, but it may be another year before all the new lines are running.

Carbon fiber is a woven synthetic that, helped by resins, hardens into a solid plastic, stronger yet lighter than many metals.

Lower weight is making Boeing's new 787 jetliner a hit, with 584 on order. Half the weight will be from carbon fiber and other composites in the fuselage, wings and tail that will cut fuel use by up to 20%.

Airbus plans to use carbon-fiber wings on the 787 rival, the A350. Qatar Airways said last week it will boost its A350 orders to 80, an increase of 20.

**FIND MORE STORIES IN:** [Internet](#) | [California](#) | [Boeing](#) | [Airbus](#) | [Irvine](#) | [Saleen](#) | [Cannondale](#) | [Industry News](#)

"Boeing and Airbus are scarfing up what's available," Musselman says. "The rest of the folks get what's left."

Carbon fiber supplier Zoltek has tripled capacity over the past year to service the growing market. "We've been able to raise prices significantly in a two-year time frame," CFO Kevin Schott says.

Where the carbon fiber crunch is showing up:

**Cars and accessories.** Specialty sports carmaker Saleen in Irvine, Calif., says the costs of the carbon fiber that it uses in the body of its \$580,000 S7 supercar have more than doubled over the past year. It raised the 2007 price by \$25,000 because of it.

Illstreet.com, an Internet business that sells carbon fiber car hoods to automotive enthusiasts, has seen costs almost double. It's had to switch to a higher grade of carbon fiber to avoid shortages it faced last year. "It was taking three to four weeks for product to come in," owner Chris Osborne says. He says he hasn't increased prices.

**Bicycles.** Bike makers use carbon fiber for lightweight frames. "Without a doubt, they've seen increased prices, but that's been going on for some time," says Megan Tompkins of *Bicycle Retailer and Industry News*. Trek and Cannondale lined up supply in advance of the crunch and haven't had to raise prices. "We kind of hedged our bet," Trek's Jim Colegrove says.

**Hockey sticks.** Easton Sports has tested new carbon fibers over the past few years. Some of the sticks have had "subtle redesigns" to accommodate the new grades of fibers, says Ned Goldsmith, senior vice president. But prices weren't increased, and, "It has been seamless for the customers," he says.

[Mixx it](#)  
Other ways to share:  
[Digg](#)  
[del.icio.us](#)  
[Newsvine](#)  
[Reddit](#)  
[Facebook](#)  
What's this?

High angles of attack: Web link-04



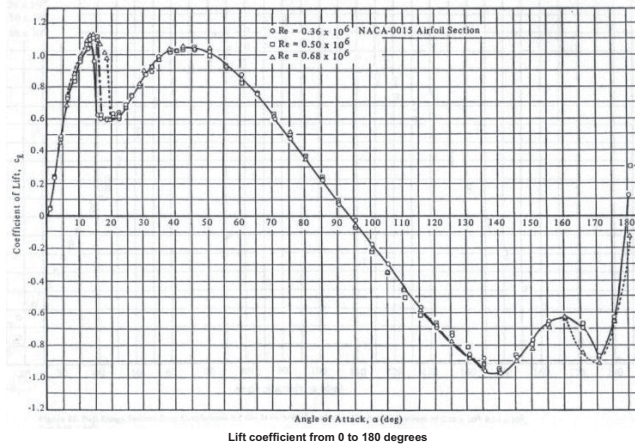
Location: Home > ask a rocket scientist > airfoils > q0150b

Search This Site for  Go

## Airfoils at High Angle of Attack

I need to know the lift and drag of a symmetric airfoil as a function of the angle of attack from 0 degrees to 90 degrees. I have seen tables for  $0^\circ < \alpha < 15^\circ$ , but I need it up to 90 degrees. Where can I find these tables?  
 - question from Ramon

Finding tables of airfoil lift and drag characteristics up to angles of attack of  $90^\circ$  is pretty unusual. As you suggest in your question, most tables or graphs of airfoil aerodynamic behavior only go up to the stall angle or a little higher and usually end between  $15^\circ$  and  $20^\circ$ . However, Sandia National Labs conducted some tests in which they collected lift coefficient ( $c_l$ ) and drag coefficient ( $c_d$ ) data for seven different airfoils up to angles of attack of  $180^\circ$ . Shown below are the  $c_l$  and  $c_d$  for the symmetric NACA airfoil section 0015, and the general trends are representative of all the airfoils tested.



You'll notice that both coefficients behave much like a flat plate. In fact, beyond the stall angle, all airfoils behave in essentially the same manner as a flat plate. Since the flow becomes separated and the boundary layer is very thick, the actual shape of the airfoil has little or no effect on its aerodynamics in the stalled region. Flat plate aerodynamics predict that the lift coefficient reaches a maximum of 1.2 at  $45^\circ$  before decreasing to 0 at  $90^\circ$ . It is therefore not surprising that the lift curve shown above also indicates a

Toho Tenax: Web link-05

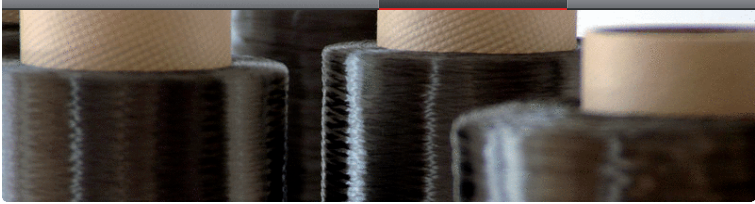
STS - Toho Tenax Europe GmbH

•Homepage • Products • Tenax • Filament yarn • STS

**TEIJIN**

Contact | Jobs | Sitemap | Imprint | Search | Print

Home About us **Products** News



**Filament yarn STS**

Tenax® STS carbon fiber is a newly developed low-cost yarn (compared to HTS and HTA), suitable for modern industrial applications, featuring similar properties as the prominent HT type whilst retaining excellent processing properties for all common fiber processing methods.

The Tenax® STS carbon fiber is bound to open the door for new high-performance applications in industry, such as the wind energy, automotive, and building industries and many others. This type is only available in high low counts (24K).

**Downloads (PDF-Files)**

- [Delivery programme and characteristics](#)
- [Standard make-up and packing](#)

**Safety data sheets**

- [STS safety data sheets](#)

**Products**

- What's carbon fiber?
- Tenax
  - Filament yarn
  - HTA & HTS
- STS
  - UTS
  - IMS

<http://www.tohotenax-eu.com/en/products/tenax/filament-yarn/sts.html> (1 of 2) [13.02.2010 18:54:31]

Appendix H